



**Titre:** On the Role of Chemical Affinity on the Dispersion, Self-Assembly,  
and Interfacial Behavior of Colloidal Cellulose Nanocrystals

**Auteur:** Charles Bruel  
Author:

**Date:** 2020

**Type:** Mémoire ou thèse / Dissertation or Thesis

**Référence:** Bruel, C. (2020). On the Role of Chemical Affinity on the Dispersion, Self-Assembly, and Interfacial Behavior of Colloidal Cellulose Nanocrystals [Ph.D. thesis, Polytechnique Montréal]. PolyPublie. <https://publications.polymtl.ca/5401/>

 **Document en libre accès dans PolyPublie**  
Open Access document in PolyPublie

**URL de PolyPublie:** <https://publications.polymtl.ca/5401/>  
PolyPublie URL:

**Directeurs de recherche:** Marie-Claude Heuzey, Pierre Carreau, & Jason Robert Tavares  
Advisors:

**Programme:** Génie chimique  
Program:

**POLYTECHNIQUE MONTRÉAL**

affiliée à l'Université de Montréal

**On the role of chemical affinity on the dispersion, self-assembly, and interfacial  
behavior of colloidal cellulose nanocrystals**

**CHARLES BRUEL**

Département de génie chimique

Thèse présentée en vue de l'obtention du diplôme de *Philosophiæ Doctor*  
Génie chimique

Août 2020

**POLYTECHNIQUE MONTRÉAL**

affiliée à l'Université de Montréal

Cette thèse intitulée :

**On the role of chemical affinity on the dispersion, self-assembly, and interfacial  
behavior of colloidal cellulose nanocrystals**

présentée par **Charles BRUEL**

en vue de l'obtention du diplôme de *Philosophiæ Doctor*  
a été dûment acceptée par le jury d'examen constitué de :

**Abdellah AJJI**, président

**Marie-Claude HEUZEY**, membre et directrice de recherche

**Pierre CARREAU**, membre et codirecteur de recherche

**Jason Robert TAVARES**, membre et codirecteur de recherche

**Marc LAVERTU**, membre

**Alain DUFRESNE**, membre externe

**DEDICATION**

*À mes parents,  
Merci d'avoir toujours  
encouragé ma curiosité.*



## ACKNOWLEDGMENTS

Cette dissertation représente l’accomplissement d’un travail de trois ans et demi et d’un cheminement que je n’aurai pas été capable de parcourir seul. Et puisque les défis à surmonter ne furent pas tous de nature scientifique, ces remerciements s’adressent non seulement à ceux qui ont apporté un soutien direct au projet, mais aussi à ceux, plus nombreux encore, qui m’ont permis de garder le cap à travers vents et marées.

Je souhaiterais naturellement débiter par ma directrice, Marie-Claude, et mes co-directeurs, Jason et Pierre, qui ont su travailler en parfaite intelligence pour m’offrir une supervision unie et cohérente. Je ne saurai dire à quel point j’ai apprécié le degré d’autonomie et de confiance que vous m’avez accordé. La fluidité de nos échanges et votre degré de disponibilité auront été exceptionnels : du premier article que vous m’avez renvoyé annoté et corrigé en moins de 12 heures à cette dissertation qui vous aura demandé moins de 4 jours. Vous avez su me faire bénéficier d’un confort matériel, financier, administratif et humain qui ont fait de moi le facteur limitant de cette thèse : son rendu reflète mon potentiel plus que l’environnement de travail dans lequel j’ai évolué. Cela dénote d’une qualité de supervision et d’anticipation que je ne peux qu’espérer retrouver ailleurs.

Je poursuivrais avec mes stagiaires : Salomé Queffeuilou, Tom S. Davies, et Theron Darlow. Faire un stage de recherche nécessite d’assimiler en quelques semaines des concepts qui dépassent (parfois de loin) son niveau académique et de travailler sur des objectifs dont la formulation précède, et dont l’échéance dépasse, la période du stage. Vous m’avez tous trois impressionné, chacun à votre façon, par la maestria avec laquelle vous avez relevé ce défi. Vous avez fait preuve de sérieux, de motivation, de dédication et de créativité. Vous avez joué un rôle de catalyseur et il suffit pour mesurer votre contribution de voir que trois des publications liées de près ou de loin à cette thèse portent vos noms. Je suis sûr que les qualités dont vous avez fait preuve durant vos stages respectifs sauront vous porter loin par la suite. (Tom & Theron : all of this to say “thanks” ! If you wonder how a single English word can summarize a full paragraph in French, please keep in mind that concision is probably English’s greatest asset).

Au rang des contributeurs directs viennent s’ajouter les autres membres du groupe « nanocellulose » et affiliés : Mélanie Girard, Quentin Beuguel, Mojtaba Mohammadi, Helia Sojoudiasli, Dhriti Khandal, Wissam Nakhle, Bahareh Zakeri, et Davood Bagherials. J’ai eu la chance de faire partie d’un projet plus grand que moi et je ne saurai assez vous remercier pour nos discussions. Quentin, cette thèse repose entièrement sur le travail exploratoire que tu as

effectué juste avant mon arrivée. Mélanie, j'ai trouvé en toi une interlocutrice et une amie exceptionnelle pendant l'essentiel de mon doctorat.

Je souhaiterai également remercier le Dr. Mohammad Latifi et le Pr. Jamal Chaouki de m'avoir apporté leur aide en début de doctorat : j'ai frappé à vos portes au jour 1 de mon doctorat avec une idée de collaboration et vous m'avez permis d'accéder à vos laboratoires dès le jour 2! Même si l'évolution des objectifs de recherche n'a malheureusement pas permis à notre collaboration d'aboutir, c'est votre réactivité qui m'a permis d'aborder ce projet du bon pied et je vous suis reconnaissant d'avoir contribué à instaurer une dynamique qui m'aura accompagné jusqu'au bout. Un projet similaire de collaboration avec le Pr. Jean-Marie Raquez et le Dr. Antoniya Toncheva (de l'Université de Mons) n'a pu, non plus, être mené à son terme dû à des contraintes de temps. Je souhaiterai néanmoins les remercier d'avoir considéré cette collaboration et de nous avoir envoyé des nanocristaux de cellulose produits par leurs soins.

Ce travail n'aurait pas été possible sans les gracieuses contributions : du Dr. Wadood Hamad (FPInnovations) à la révision des différents articles produits dans ce projet et pour son rôle de coordinateur avec le partenaire industriel ; des Prs. Theo van de Ven (McGill University) et Charles Dubois (Polytechnique Montréal), jurys lors de l'examen pré-doctoral ; des Prs. Alain Dufresne (Grenoble INP - Pangora) et Marc Lavertu (Polytechnique Montréal), jurys lors de l'examen doctoral ; et du Pr. Abdellah Ajji (Polytechnique Montréal), président du jury lors des examens pré-doctoral et doctoral. Le rôle des relecteurs, anonymes, dans le processus de revue par les pairs des articles présentés dans cette thèse est salué : leurs commentaires ont significativement contribué à la qualité des manuscrits.

À ce stade, je souhaiterai remercier nos partenaires industriels et institutionnels : Cellulforce (Windsor, Québec, Canada) pour son soutien matériel et pour l'enthousiasme stimulant qu'ils ont pu manifester à chacune de nos rencontres ; FPInnovations (Pointe-Claire, Québec, Canada) pour avoir initié et financé ce projet ainsi que pour avoir organisé ces forums d'échange sur la nanocellulose lors des conférences BIOFOR/Paperweek 2018 et 2019 ; PRIMA Québec et le Conseil National de Recherches Canada (NSERC) pour leur soutien financier au projet ; le Fond de Recherche du Québec – Nature et Technologies (FRQNT) pour m'avoir alloué une bourse dans le cadre du Programme de bourses d'excellence pour étudiants étrangers (PBEEE).

Une thèse c'est aussi une armée de travailleurs de l'ombre dont la contribution, bien qu'essentielle à la mécanique universitaire, est rarement soulignée dans les publications. Je pense ici aux personnels permanents du département : associés de recherche, techniciens de laboratoire, personnels administratif. Je citerai nommément Matthieu Gauthier, Wendell Raphaël, Gino

Robin, Martine Lamarche, Sylvie Taillon, Robert Delisle, Daniel Pilon, Claire Cerclé, Richard Silverwood, Alexandre Bréard, Mariia Kopach, Brigitte Langevin, Élise Saint-Jacques, Carole Savoie, et je pense fort aux autres. Vous êtes l'âme et la structure du département : ce sont vos rôles de conseil et de soutien technique/scientifique/administratif qui m'auront permis d'avancer au quotidien et de bénéficier d'un environnement propice à mes recherches.

L'un des avantages d'avoir trois superviseurs est la taille des groupes de recherche et le nombre de personnes avec qui il est possible d'interagir. Je souhaiterai ainsi remercier mes amis et collègues des groupes de Rhéologie et PhotoSEL. Puisqu'on en arrive aux remerciements personnels, j'ai également une pensée pour mes amis de l'université, ceux de mes troupes de théâtre (Pains Perdus et Poly-Théâtre), et ceux d'au-delà ! C'est grâce à vous que j'ai su trouver une seconde maison à Montréal : ça en prend de la chaleur humaine pour tempérer le climat d'ici !

J'ai bien sûr gardé ma famille pour la fin, vous dont le soutien précède et supplante tous les autres ! Depuis mes premiers « Et pourquoi . . . ? (*voix de petit garçon un peu pénible*) », vous avez toujours su fournir un environnement propice à ma curiosité et les outils pour la satisfaire. Aujourd'hui que j'ai appris à chercher des réponses par moi-même, on peut se retourner et se dire qu'on a parcouru du chemin. Loin des yeux, près du cœur : vous savez à quel point ces dernières années ont pu être difficiles par moments, j'étais absent et c'est votre investissement qui y a suppléé et qui m'a offert l'opportunité de finir cette thèse. Merci.

## RÉSUMÉ

Les nanocristaux de cellulose (CNCs) sont des nanoparticules à hauts aspects de forme qui comptent au rang des nouveaux « ors verts » de la transition écologique. Depuis la conception des premières usines pilotes au cours de la dernière décennie, ces nanomatériaux biosourcés et biodégradables sont produits à l'échelle industrielle (plus d'une tonne par jour) et suscitent de fortes attentes pour leurs propriétés en milieux aqueux : les nanocristaux se (re)dispersent aisément dans l'eau pour y former des suspensions colloïdales stables, des cristaux liquides, ou des hydrogels en fonction de leurs niveaux de concentration. Les CNCs peuvent notamment servir de rhéoépaississants ou d'émulsificateurs, et leurs suspensions aqueuses agir comme intermédiaires pour la production par évaporation de nanocomposites et de matériaux auto-assemblés.

Plus difficile, la dispersion des CNCs en milieux non-polaires (solvants et polymères) restreint en revanche leur champ d'applications et illustre la nécessité d'une approche plus fondamentale sur la question. La compréhension des mécanismes conduisant à la dispersion et à l'auto-organisation des CNCs est ainsi un paramètre clé dans le développement de nouvelles applications. Ces problématiques, identifiées par l'industrie, ont généré un effort de recherche pancanadien : soutenu par des fonds publics et impliquant huit universités, son objectif général est l'approfondissement des fondamentaux sur la cellulose nanocrystalline.

Réalisée dans ce cadre, cette thèse de doctorat a pour objectif de développer des outils permettant de comprendre et prédire le potentiel de dispersion et d'auto-organisation des CNCs en milieu non-aqueux (avec un accent sur les solvants). La démarche de résolution, de type cœur-coque, part du nanocrystal (structure et propriétés de surface), puis considère son environnement immédiat (interactions CNC/solvant, mécanismes de stabilisation colloïdale), et enfin la suspension dans son ensemble (auto-organisation, gélification). Afin de combler les lacunes qui existent dans la description de l'affinité chimique des CNCs et de leur potentiel d'interaction, nous avons déterminés les critères quantitatifs qu'un solvant doit remplir afin de pouvoir disperser les CNCs et permettre leur auto-organisation.

Basée sur la théorie des paramètres de solubilité de Hansen (HSP), cette dissertation démontre le caractère amphiphile des CNCs avec deux composantes : polaire majoritaire et non-polaire minoritaire. La composante polaire a un paramètre de solubilité  $\delta_T$  de 31.3 MPa<sup>1/2</sup> qui se décompose à hauteur de 34-38-28 % en termes d'interactions dispersives (D), dipole-dipole (P), et hydrogène (H, ce qui inclue les autres interactions acide/base de Lewis). Les surfaces non-polaires ont un  $\delta_T$  de 19.2 MPa<sup>1/2</sup> avec des fractions D-P-H de 61-17-22 %. Cette

caractérisation quantitative permet d'estimer l'affinité chimique des CNCs pour leur environnement via la distance HSP,  $R_a$ . Sa validité a été confirmée par des mesures de mouillabilité qui ont également permis de déterminer des équivalents en termes de paramètres de tension de surface. Les solvants interagissent avec les CNCs selon deux schémas distincts : ils peuvent dissocier les liaisons ioniques entre les particules et leurs contre-ions et/ou s'adsorber à la surface des nanocristaux. Ces interactions conduisent potentiellement à de la stabilisation électrostatique et/ou induite par solvation. Le potentiel de dispersion peut être prédit sur la base du niveau de stabilité colloïdale dont bénéficient les CNCs : quatre catégories de solvants ont été établies selon que s'appliquent 2, 1, ou aucuns mécanismes. Finalement, nous avons déterminé que même si la stabilisation électrostatique était le seul pré-requis pour l'auto-formation de structures chirales, c'est la combinaison des deux stabilisations (électrostatique et induite par la solvation) qui permet au milieu de bénéficier de propriétés équivalentes aux suspensions aqueuses de CNCs.

Les stabilisations électrostatique et induite par la solvation sont respectivement contrôlées par la constante diélectrique,  $\varepsilon$ , et la distance HSP,  $R_a$ . Des valeurs seuils ont pu être établies en termes de  $\varepsilon$  et  $R_a$ . Celles-ci s'appliquent indifféremment aux solvants purs et aux mélanges binaires. Bien que les milieux aqueux restent le choix le plus évident, nous suggérons que ces critères peuvent être directement appliqués pour sélectionner le meilleur solvant ou la meilleure combinaison de solvants afin de produire des suspensions finement dispersées, des gels, et/ou des matériaux optiquement actifs. Cela est pertinent pour la coulée par solvant de nanocomposites incluant des substances non-hydrosolubles, mais aussi pour des applications comme les peintures ou les cosmétiques qui impliquent des mélanges complexes.

## ABSTRACT

Cellulose nanocrystals (CNCs), often described as plants' building blocks, are biosourced and biodegradable rod-like nanomaterials whose production rate has been scaled up from a few kilograms to >1 ton/day within the last decade. They carry high expectations that arise from their properties in water: a solvent in which CNCs are readily dispersible and form stable isotropic colloidal suspensions at dilute levels, then liquid crystals and gels at higher concentrations. These aqueous suspensions are a platform towards a broad range of applications: CNCs may hence act as fillers in nanocomposites, as templating agents for self-assembled materials, as rheological modifiers, or as Pickering emulsifiers.

Their applicability has however been hindered by the difficulty encountered when dispersing these predominantly polar particles in non-polar solvents and matrices. This illustrates the need for protocols that improve dispersion and allow the transfer of CNC's useful properties to less polar media. Understanding of the mechanisms underlying this dispersion and the formation of CNC chiral self-assemblies is a key factor for broadening CNC's range of applications. These limitations, identified at the industrial level, have triggered a Canada-wide state-funded research effort involving 8 universities to further investigate the fundamentals of CNC properties.

Within this context, this Ph.D. aims at developing tools to understand and predict the dispersion and self-ordering properties of cellulose nanocrystals in non-aqueous media. The research problem was approached through a core-shell strategy: first quantify CNC's potential for interaction, then map its interactions with its surrounding environment (with a focus on solvents), and finally investigate how nanocrystals interact with each other throughout the media to form complex self-assemblies. Significant gaps were identified in the literature on the three matters, primarily due to the lack of quantitative determination of CNC chemical affinity. Through this process, we determined quantitative requirements, in terms of solvent parameters, for dispersion and self-ordering to occur.

Based on Hansen solubility parameter (HSP) theory, we verified CNCs to be amphiphilic particles with a predominant polar component. These polar moieties had a solubility parameter  $\delta_T$  of 31.3 MPa<sup>1/2</sup> that splits 34-38-28 % into dispersive (D), dipole-dipole (P), and hydrogen bonding (H) interactions, respectively. The less polar surface had a  $\delta_T$  of 19.2 MPa<sup>1/2</sup> that splits 61-17-22 % into D-P-H interactions. This quantitative characterization enables for an estimation of CNC/solvent chemical affinity through the HSP distance,  $R_a$ . This was supported by wettability measurements and the surface tensions of the CNC film surfaces were

determined. Solvents were found to have two main interactions with CNCs: dissociate the nanocrystal from its counter ions and/or adsorb on the nanocrystal surface. These provide CNCs with two potential paths towards colloidal stability: electrostatic and solvation-induced stabilization, respectively. CNC dispersibility could be entirely predicted by the nature of the mechanisms that applies in suspensions and four categories of solvents were established whether 2, 1, or no mechanism applies. Finally, we found that while electrostatic stabilization was the only prerequisite for chiral self-assemblies to form, a combination of solvation-induced and electrostatic stabilizations was needed to yield water-like levels of properties.

Electrostatic and solvation-induced stabilizations are controlled by the dielectric constant,  $\varepsilon$ , and the HSP distance,  $R_a$ , respectively. Criteria in terms of  $\varepsilon$  and  $R_a$  that apply to pure solvents and binary mixtures alike were established. While aqueous-based media remain the most obvious choice, we suggest that these criteria could readily be employed to select the best solvent or combination of solvents to produce finely dispersed suspensions, gels, and/or optically active materials. This is relevant for the casting of nanocomposites that include non-hydrosoluble chemicals, but also for applications such as paints and cosmetics where complex mixtures are involved.

## TABLE OF CONTENTS

DEDICATION . . . . .	iii
ACKNOWLEDGMENTS . . . . .	iv
RÉSUMÉ . . . . .	vii
ABSTRACT . . . . .	ix
TABLE OF CONTENTS . . . . .	xi
LIST OF TABLES . . . . .	xiv
LIST OF FIGURES . . . . .	xv
LISTS OF SYMBOLS AND ABBREVIATIONS . . . . .	xvii
CHAPTER 1 INTRODUCTION . . . . .	1
1.1 Background . . . . .	1
1.2 Field and scope of studies . . . . .	2
1.3 Outline of the dissertation . . . . .	3
CHAPTER 2 CRITICAL LITERATURE REVIEW . . . . .	4
2.1 Native arrangement of cellulose in plants . . . . .	4
2.1.1 Arrangement in plant cell wall . . . . .	4
2.1.2 Molecular structure . . . . .	6
2.1.3 Elementary microfibril models . . . . .	8
2.2 Cellulose nanocrystals . . . . .	10
2.2.1 Extraction processes . . . . .	10
2.2.2 Morphology . . . . .	11
2.2.3 Surface properties . . . . .	15
2.3 CNC/solvent interactions and stabilization mechanisms . . . . .	17
2.3.1 Ionic interactions and electrostatic stabilization . . . . .	17
2.3.2 Weak interactions: solvation-induced and steric stabilizations . . . . .	18
2.4 CNC behavior in suspensions . . . . .	22
2.4.1 Aqueous CNC suspensions . . . . .	22
2.4.2 Non-aqueous CNC suspensions . . . . .	24



2.4.3	Interfacial behaviors . . . . .	25
CHAPTER 3	RESEARCH OBJECTIVES . . . . .	27
3.1	Identification of the problem . . . . .	27
3.2	Research hypothesis . . . . .	27
3.3	Objectives . . . . .	28
3.3.1	Main objective (MO) . . . . .	28
3.3.2	Specific objectives (SO) . . . . .	28
CHAPTER 4	COHERENCE OF THE ARTICLES . . . . .	29
CHAPTER 5	ARTICLE 1: THE STRUCTURAL AMPHIPHILICITY OF CELLULOSE NANOCRYSTALS CHARACTERIZED FROM THEIR COHESION PARAMETERS . . . . .	33
5.1	Introduction . . . . .	33
5.2	Materials and methods . . . . .	36
5.2.1	Materials . . . . .	36
5.2.2	Sedimentation tests . . . . .	37
5.2.3	Thermodynamic approach - Hansen solubility parameters . . . . .	39
5.3	Results and discussion . . . . .	41
5.4	Concluding remarks . . . . .	47
5.5	Conflicts of interest . . . . .	48
5.6	Acknowledgments . . . . .	48
CHAPTER 6	ARTICLE 2: SELF-ASSEMBLY BEHAVIORS OF COLLOIDAL CELLULOSE NANOCRYSTALS: A TALE OF STABILIZATION MECHANISMS . . . . .	49
6.1	Introduction . . . . .	50
6.2	Materials and methods . . . . .	51
6.2.1	Materials . . . . .	51
6.2.2	Protocols . . . . .	53
6.3	Analysis of the stabilization mechanisms . . . . .	54
6.3.1	Electrostatic stabilization: $\varepsilon$ as a control parameter . . . . .	54
6.3.2	Solvation: $R_a$ as a control parameter . . . . .	55
6.3.3	A diagram for stability mechanisms . . . . .	56
6.4	Results and discussion . . . . .	58
6.4.1	Behavior of CNC suspensions upon solvent casting . . . . .	58
6.4.2	Insights on the competition between EISA and DISA . . . . .	68

6.4.3	Limitations and extrapolability . . . . .	69
6.5	Concluding remarks . . . . .	71
6.6	Conflicts of interest . . . . .	72
6.7	Acknowledgments . . . . .	72
CHAPTER 7 ARTICLE 3: ORIENTING CELLULOSE NANOCRYSTAL FUNCTION-		
	ALITIES TUNES THE WETTABILITY OF AIR/SAMPLE INTERFACES . . .	73
7.1	Introduction . . . . .	73
7.2	Experimental Section . . . . .	76
7.2.1	Cellulose nanocrystals . . . . .	76
7.2.2	CNC film preparation . . . . .	77
7.2.3	Contact angle measurements . . . . .	78
7.3	A model for the wettability of CNC films based on the orientation of their lattice plane . . . . .	79
7.3.1	Contact angles: a background . . . . .	79
7.3.2	Wettability of real chemically heterogeneous surfaces . . . . .	80
7.3.3	CNC surface tension parameters . . . . .	82
7.4	Results and discussion . . . . .	83
7.4.1	Wettability results . . . . .	83
7.4.2	Chemical composition of air/sample interfaces . . . . .	85
7.4.3	Speculative mechanism for CNC orientation at the air/water interface	87
7.5	Conclusions . . . . .	92
7.6	Acknowledgements . . . . .	93
7.7	Supporting Information description . . . . .	94
CHAPTER 8 GENERAL DISCUSSION . . . . .		95
CHAPTER 9 CONCLUSIONS AND RECOMMENDATIONS . . . . .		97
9.1	Conclusions . . . . .	97
9.2	Recommendations . . . . .	98
REFERENCES . . . . .		100
APPENDICES . . . . .		126

## LIST OF TABLES

Table 2.1	Plant-based CNCs cross-sectional shape measurements (CNC widths, $w_{\text{CNC}}$ , and heights, $h_{\text{CNC}}$ ). . . . .	13
Table 2.2	Hansen solubility parameters for cellulose and lignin . . . . .	21
Table 5.1	Cellulose nanocrystal surface properties according to the lattice plane displayed . . . . .	36
Table 6.1	Solvents and their main properties . . . . .	52
Table 7.1	Surface and interfacial tension parameters . . . . .	84
Table B.1	Properties of the solvent set at 25 °C . . . . .	133
Table B.2	Binary mixture properties at 25 °C . . . . .	134
Table B.3	Polymer Hansen Solubility Parameters at 25 °C . . . . .	135
Table C.1	Solvents and their properties . . . . .	147
Table C.2	Binary mixtures and their properties . . . . .	148
Table C.3	Summary of colloidal CNC behavior in standing suspensions and upon solvent-casting as a function of their stabilization mechanisms . . . .	149
Table D.1	Nomenclature for the Article 3 . . . . .	164
Table D.2	Parameters of the crystallographic analysis . . . . .	165
Table D.3	Influence of the surface tension coefficients of EG on $f^{\text{nps}}$ predictions (Eq. 7.7) . . . . .	165
Table D.4	Surface tension parameters for various cellulose $\text{I}_\beta$ nanocrystals' samples and surfaces as a function of the method of determination . . . .	166
Table D.5	ARCA results for spin-coated and oven-cast samples analyzed with EG and DIM . . . . .	167

# LIST OF FIGURES

Figure 2.1	Plant structure: from macro to nanocellulose . . . . .	5
Figure 2.2	Crystallographic unit cells for cellulose I . . . . .	7
Figure 2.3	Elementary microfibril models for cellulose $I_\beta$ . . . . .	9
Figure 2.4	Interparticular distance, $d_{\text{inter}}$ (measured from center to center), as a function of CNC concentration in water, $[\text{CNC}]$ . . . . .	23
Figure 4.1	Graphical abstract: Article 1 . . . . .	29
Figure 4.2	Graphical abstract: Article 2 . . . . .	30
Figure 4.3	Graphical abstract: Article 3 . . . . .	32
Figure 5.1	Anisotropy of cellulose . . . . .	35
Figure 5.2	HSP graph of wood-based sulfuric acid-hydrolyzed CNCs . . . . .	42
Figure 5.3	HSP graph of wood-based sulfuric acid hydrolyzed CNCs compared to some commodity polymers . . . . .	46
Figure 6.1	Expected stabilization mechanisms in CNC suspensions as a function of the dielectric constant of the solvent and of its chemical affinity for the CNC particles . . . . .	57
Figure 6.2	Stability against sedimentation of 16 CNC suspensions and their oven-casting in PTFE evaporating dishes as functions of the dielectric constant of the solvent and of its chemical affinity for the CNC particles . . . . .	60
Figure 6.3	Self-assembly in systems stabilized by a combination of solvation and electrostatic effects . . . . .	61
Figure 6.4	Effect of oven temperature and heat transfer on the casting of CNC suspensions in N,N-dimethylformamide (DMF) . . . . .	64
Figure 6.5	Solvent casting of CNC suspensions in binary mixtures of dimethylsulfoxide (DMSO), water (W), N-methylformamide (MF), or formamide (F), in N,N-dimethylformamide (DMF) . . . . .	66
Figure 7.1	Morphology and representation of cellulose $I_\beta$ nanocrystals . . . . .	76
Figure 7.2	ARCA results for spin-coated and oven-cast films and their predictions in terms of non-polar fraction for the air/sample interface . . . . .	86
Figure 7.3	Repeatably of CNC orientation during the spin-coating and oven-casting processes based on EG results . . . . .	88
Figure 7.4	Mechanism for CNC orientation at the air/sample interface . . . . .	89
Figure B.1	Sedimentation tests in the set of pure solvents . . . . .	131
Figure B.2	Sedimentation tests in the set of binary mixtures . . . . .	132

Figure C.1	Teas graph of the solvents employed in this study . . . . .	137
Figure C.2	Optical microscopy images of the PTFE evaporating dish . . . . .	138
Figure C.3	Dispersion tests of 16 CNC suspensions ( $10 \text{ mg}_{\text{CNC}}/\text{mL}_{\text{solvent}}$ ) as a function of the dielectric constant, $\epsilon$ , of the solvent and of its chemical affinity for the CNC particles, $R_a$ . . . . .	140
Figure C.4	Vial tests at $\sim 25^\circ\text{C}$ for CNC suspensions in water (W), N-methylformamide (MF), dimethylsulfoxide (DMSO), and formamide (F) at concentrations ranging from 10 to $100 \text{ mg}_{\text{CNC}}/\text{mL}_{\text{solvent}}$ . . . . .	143
Figure C.5	Effect of the evaporating dish, PTFE or Al, on the continuity of the thin film casted from some electrostatically-stabilized suspensions (DMF, EG, PC) . . . . .	145
Figure D.1	Length ( $L_{\text{CNC}}$ ) times diameter ( $D_{\text{CNC}}$ ) distribution of CNC bundles on TEM images based on an analysis with ImageJ . . . . .	153
Figure D.2	XRD spectra and cross-sectional shapes of CNCs within the spray-dried powder and the oven-cast films . . . . .	154
Figure D.3	Evolution of the drop parameters (volume, $V^{\text{drop}}$ , contact diameter, $D^{\text{drop}}$ , and dynamic contact angle, $\theta$ ) over the course of an ARCA experiment conducted with diiodomethane on an oven-cast film . . .	161

## LISTS OF SYMBOLS AND ABBREVIATIONS

Lists of symbols and abbreviations provided here-below are non-exhaustive.

### Symbols

#### Most common symbols and variables

$[X]$	Concentration in specie “X” ( $\text{mg mL}^{-1}$ , wt%, or vol%)
$\delta$	Hansen solubility parameter ( $\text{MPa}^{1/2}$ )
$\varepsilon$	Dielectric constant (dimensionless)
$\gamma$	Surface tension <sup>a</sup> ( $\text{mN m}^{-1}$ )
$\theta$	Contact angle ( $^{\circ}$ )
$\rho$	Density ( $\text{g cm}^{-3}$ )
$\eta$	Viscosity ( $\text{Pa s}$ )
$\Delta E$	Surface energy variations ( $\text{mJ m}^{-2}$ )
$D$	Diameter (m)
$E$	Molar energy ( $\text{J mol}^{-1}$ )
$f$	Surface fraction ( $0 \leq f \leq 1$ , dimensionless)
$H$	Contact angle hysteresis ( $=\theta_a - \theta_r$ , $^{\circ}$ )
$R_0$	HSP radius of solubility ( $\text{MPa}^{1/2}$ )
$R_a$	HSP distance ( $\text{MPa}^{1/2}$ )
$T$	Temperature (K)
$v$	Rate of progression over a surface ( $\text{m s}^{-1}$ )

---

#### List of common variables’ subscripts and superscripts

a	Advancing (in Chapter 7), applies to $\theta_a$
comp	Composite (in Chapter 7), applies to $\theta_{\text{comp}}$
l	liquid (in Chapter 7), applies to $\gamma^l$ , $\rho^l$ , $\eta^l$ , $v^l$
r	Receding (in Chapter 7), applies to $\theta_r$
D	Dispersive, applies to $\delta_D$ , $\gamma_D$ , $E_D$
H	Hydrogen-bonding, applies to $\delta_H$ , $E_H$
nps	non-polar surfaces (in Chapter 7), applies to $\delta^{\text{nps}}$ , $\gamma^{\text{nps}}$ , $\theta^{\text{nps}}$ , $f^{\text{nps}}$
p	Particle (in Chapter 6), applies to $\delta_p$
P	Polar, applies to $\delta_P$ , $\gamma_P$ , $E_P$
ps	polar surfaces (in Chapter 7), applies to $\delta^{\text{ps}}$ , $\gamma^{\text{ps}}$ , $\theta^{\text{ps}}$ , $f^{\text{ps}}$
s	solid (in Chapter 7), applies to $\gamma^s$

s	solvent (in Chapter 6), applies to $\eta_s$ , $\delta_s$
solv	solvent (in Chapter 5), applies to $\varepsilon_{\text{solv}}$ , $\eta_{\text{solv}}$ , $\rho_{\text{solv}}$
T	Total, applies to $\delta_T$ , $E_T$
W	Wenzel (in Chapter 7), applies to $\theta_W$
Y	Young (in Chapter 7), applies to $\theta_Y$

---

### Other symbols and variables

$\delta_a$ , $\delta_b$	Acidic and basic Karger partial solubility parameter ( $\text{MPa}^{1/2}$ )
$\Delta H$	Enthalpy variations (vaporization, dissociation, etc...) ( $\text{J mol}^{-1}$ )
$(a,b,c,\alpha,\beta,\gamma)$	Lattice parameters: dimensions (nm) and angles ( $^\circ$ ) of the crystal cell <sup>a</sup>
$A$	Area ( $\text{m}^2$ )
$\Pi$	Surface pressure ( $\text{mN m}^{-1}$ )
$CED$	Cohesive energy density (MPa)
$d$	d-spacing between lattice planes (nm)
$d_{\text{inter}}$	Interparticular distance in suspension (nm)
$E_{\text{others}}$	Contributions to $E_T$ , others than $E_D$ , $E_P$ , and $E_H$ ( $\text{J mol}^{-1}$ )
$FIT$	Fit function for the HSP sphere ( $0 \leq FIT \leq 1$ , best fit for $FIT=1$ )
$g$	Gravitational force constant ( $\sim 9.81 \text{ m s}^{-2}$ )
$h_{\text{CNC}}$	CNC height (nm)
$IC$	Cristallinity index
$k_B$	Boltzmann constant ( $\sim 1.381 \cdot 10^{-23} \text{ J K}^{-1}$ )
$K_{\text{eq}}$	Equilibrium constant
$L_{\text{CNC}}$	CNC length (nm)
$n_{\text{Sulf}}$	Number of sulfate groups per $\beta$ -D-anhydroglucose units
$N_{\text{Bo}}$	Bond number (dimensionless)
$N_{\text{CA}}$	Capillary number (dimensionless)
$r_{\text{surf}}$	Surface roughness coefficient (dimensionless)
$R$	Ideal gas constant ( $8.314 \text{ J mol}^{-1} \text{ K}^{-1}$ )
$R_q$	Standard deviation in terms of surface's height (m)
$RED$	Relative energy difference ( $=R_a/R_0$ )
$RST$	Relative sedimentation time ( $\text{m}^4\text{s}^2$ )
$t_{\text{sed}}$	Absolute sedimentation time (h)
$V_m$	Molar volume ( $\text{m}^3/\text{mol}$ )
$w_{\text{CNC}}$	CNC width (nm)

<sup>a</sup>  $\gamma$  usually describes the surface tension, with the exception of section 2.1.2 where it stands for an angle of the crystal unit.

## Abbreviations

(hkl)	Miller indices for the crystallographic lattice planes, $\{h; k; l\} \subset \mathbb{N}^3$
AFM	Atomic Force Microscopy
Al	Aluminum
ARCA	Advancing/receding contact angle
CA	Contact angle
CesA	Cellulose synthase: protein responsible for the extrusion of cellulose
CI	Counter-ion
CMF(s)	Cellulose microfibril(s)
CNC(s)	Cellulose nanocrystal(s)
CNF(s)	Cellulose nanofibril(s)
DIM	Diiodomethane
DISA	Destabilization-induced self-assembly
DMF	N,N-Dimethylformamide
DMSO	Dimethylsulfoxide
EDS, EDX	X-Ray energy dispersive spectroscopy
EG	Ethylene glycol
EISA	Evaporation-induced self-assembly
F	Formamide
HSP	Hansen solubility parameters
OC	Oven-cast
PC	Propylene carbonate
PE	Poly(ethylene)
PEG	Poly(ethylene glycol)
PLA	Poly(lactic acid)
PMMA	Poly(methyl methacrylate)
POM	Polarized optical microscopy
PTFE	Poly(tetrafluoroethylene)
PP	Poly(propylene)
PVOH	Poly(vinyl alcohol)
MF	N-methylformamide
NMR	Nuclear magnetic resonance spectroscopy
SANS	Small-angle neutron spectroscopy
SAXS	Small-angle X-ray spectroscopy
SC	Spin-coated



SI	Supplementary information
SEM	Scanning electron microscopy
TC	Terminal complex: assembly of CseA proteins
TEM	Transmission electron microscopy
w, W	Water
WANS	Wide-angle neutron spectroscopy
WAXS	Wide-angle X-ray spectroscopy
XRD	X-ray diffraction

## CHAPTER 1 INTRODUCTION

### 1.1 Background

The Canadian pulp and paper industry was developed from the end of the 19<sup>th</sup> century to meet the rapidly growing demand for newsprint in the United States of America [2]. Pulp production, mostly from softwoods, reached 1 Mt yr<sup>-1</sup> in the 1910s, 5 Mt yr<sup>-1</sup> in the 1940s, 10 Mt yr<sup>-1</sup> in the 1960s, 20 Mt yr<sup>-1</sup> in the 1970s and hit a maximum of nearly 25 Mt yr<sup>-1</sup> in the year 2000. Growth has been steady with only some momentary declines caused by the Great Recession in the thirties, the world wars, and the oil crisis in the seventies. Shifts in reading habits and the development of the digital economy from the beginning of the 21<sup>st</sup> century, coupled with the economic recession of 2007-2009 brought an end to this perpetual growth. Pulp production has steadily decreased since then, down to roughly 16 Mt yr<sup>-1</sup> in 2018 [3].

With its core activities in crisis, the sector is looking for new outlets through the development of advanced value-added wood-based biomaterials [4]. Nanocellulose, first described in the fifties [5] and long limited to lab-scale applications [6], received a renewed attention and a significant boost with the creation of the first large scale production units [7]. Nanocellulose is a generic term that encompasses both cellulose nanofibers (CNFs) and nanocrystals (CNCs). CNCs are rod-like nanoparticles that are obtained by eliminating the amorphous content of CNFs. In Canada they were first produced at large scale, respectively by Celluforce in Windsor (Québec, 1 t d<sup>-1</sup>) [8] and by Kruger Biomaterials in Trois-Rivières (Québec, 5 t d<sup>-1</sup>) [9], from technologies initially developed by FPInnovations (Pointe-Claire, Québec) [10, 4]. More recently, Blue Goose Biorefineries Inc. (Saskatoon, Saskatchewan) [11], InnoTech Alberta (Edmonton, Alberta) [12], and Anomera (Mississauga, Ontario) [13] have also emerged as CNC producers on the Canadian market [10, 14]. Their mechanical, optical, and rheological properties coupled with their light densities make CNCs interesting in various industries [6]. In 2017, its main sectoral markets in term of value were those of composites (30 %), of paints, films & coatings (15 %), and of pulp & papers (14 %) [6]. The global nanocellulose market is estimated at US\$ ~300 millions in 2020 and should reach US\$ ~780 millions by 2025 [15].

Nanomaterials come with distinct advantages over their larger counterparts: they have an improved specific surface area and a greater homogeneity that minimizes defects. For instance, going nano enables cellulose to reach a crystalline content up to 85-90 % [16], which results in a Young's modulus similar to steel in the chain direction [17]. Models predict a

value as high as 208 GPa [18], while experimental determination through Raman spectroscopy yields a value of 105 GPa for cotton-based CNCs [19]. With specific surface areas of  $\sim 400\text{--}500\text{ m}^2/\text{g}_{\text{CNC}}$  [20] and densities of  $\sim 1.5\text{--}1.6\text{ g cm}^{-3}$  [21, 22, 23, 17], a few weight percents of CNCs may significantly reinforce polymer matrices [24, 25].

However, benefiting from these enhanced features presupposes the ability to first reach a nanosize dispersion, and then to maintain it over a time lapse compatible with the life-time of the material. When produced through sulfuric acid hydrolysis, CNCs have negatively charged surfaces that provide them with long-term colloidal stability and self-ordering properties in water [7]. These native behavior in aqueous systems justify the current market for CNCs. CNC polar nature, however, prevents their good dispersion in non-polar media. This category includes most thermoplastic matrices such as polyolefins (polyethylene, polypropylene, ...). The melt processing of thermoplastic CNC nanocomposites is further made difficult by the low thermal stability of the nanocrystals [26]. CNCs polarity may be explained by the numerous -OH groups exposed at their surface. They may be functionalized [22] to increase the nanocrystals hydrophobicity and improve their dispersion in non-polar media [24, 7].

In line with these issues and in efforts to develop CNC and CNF industrial applications, FPInnovations addressed in February 2015 six challenges to the research community [27]:

1. Dispersion of cellulose nanocrystals in aqueous media [28].
2. Dispersion of cellulose nanocrystals in non-polar matrices [29].
3. Reinforcement potential of nanomaterials derived from wood fibre [30].
4. Characterization of nanomaterials derived from wood fibre [31].
5. Compatibilization of nanomaterials derived from wood fibre [32].
6. Thermal stability of nanomaterials derived from wood fibre [33].

This work was led in the context of the second challenge: the dispersion of CNCs in non-polar matrices [29].

## 1.2 Field and scope of studies

Our field of research encompasses the description of the second challenge [29]. The studies shall focus on cellulose nanocrystals provided by Celluforce and on their dispersion in both common solvents and thermoplastics. Solvents in which cellulose chains are dissolved rather than suspended are excluded. The objective fixed by the challenge is first to develop new approaches to characterize and/or measure the extent of the CNC dispersibility in these

media. Second, it is to develop a dispersibility index that could be used online or offline to estimate the dispersion state of CNCs in a solvent or a polymer matrix.

This dissertation does not pretend to bring a full solution to the challenge. Instead, it focuses on the CNC behavior in suspensions and aims at applying a new approach based on the Hansen solubility parameters (HSP) to characterize and quantify CNC chemical affinity for its environment. Chemical affinity is then correlated to the solvent’s ability to physically adsorb at CNC surfaces: significant solvent adsorption brings solvation-induced stabilization to the system. We demonstrate that it is the combination of solvation-induced and electrostatic stabilizations that provide CNCs with their colloidal stability and self-assembly potential in suspensions. It enables the prediction of CNC bulk behavior from quantitative solvent criteria, hence establishing a comprehensive mapping of CNC potential for dispersion and self-assembly in suspensions. Finally, the results are translated in terms of surface tension parameters through the Owens-Wendt-Rabel-Kaelble (OWRK) method, which are, in addition to HSP, the other widespread theory to quantify surface properties. Surface tension parameters apply to the description of the interfacial behavior such as wetting and adhesion. They were employed to prove a decade-old theory on CNC interfacial behavior: their potential to orient their functionalities to better stabilize an interface.

This work hence provides quantified characterization of CNC chemical affinity (using the 2 mainstream theories of surface characterization: Hansen solubility and OWRK surface tension parameters) before investigating its role on the dispersion, self-assembly, and interfacial behavior of the nanocrystals.

### 1.3 Outline of the dissertation

This dissertation attempts at establishing a comprehensive link between the molecular structure of the cellulose chains, the surface properties of the nanocrystals, and their behavior in suspensions. Chapter 2 reviews the literature in a bottom-up approach: cellulose native arrangement in plants, then CNC morphology and their surface properties, the interactions that can form between CNC surfaces and solvent molecules, and finally CNC behaviors in the bulk and at the interfaces of liquid systems. Chapter 3 exposes the research hypotheses and the objectives. Chapter 4 establishes the coherence of the various articles (Chapters 5 to 7) with the objectives of the thesis. Chapter 8 is a general discussion that analyzes the results in the wider perspective of the challenge on CNC dispersion. Finally, Chapter 9 summarizes the work, its originality, and provides recommendations for the completion of the challenge.

## CHAPTER 2 CRITICAL LITERATURE REVIEW

Understanding the nature of cellulose nanocrystals (CNCs) is a prerequisite to develop pertinent strategies and appropriate characterization tools to investigate their dispersion and self-assemblies in suspensions. We review in section 2.1 the hierarchy of cellulose in wood, the main industrial source for cellulosic fibers, and its molecular structure. Processes, especially sulfuric acid hydrolysis, through which cellulose nanocrystals are extracted, the morphology of the resulting particles, and their surface properties are described in section 2.2. We present in section 2.3 the physical and chemical interactions that can occur at CNC surfaces and their influence on CNC colloidal stability. Finally, we analyze in section 2.4 the behavior that have been reported for CNCs in terms of solvent dispersion, self-assembly, and interfacial adsorption. While the relationships between CNC structure and surface properties are well described, this chapter highlights the lack of experimental evidences that link surface properties to CNC behavior in suspensions. It is the purpose of this dissertation to provide the tools and the evidences that lead to an integrated framework.

### 2.1 Native arrangement of cellulose in plants

#### 2.1.1 Arrangement in plant cell wall

Cellulose is the most abundant biopolymers on earth as it can be extracted from plants, bacteria, fungi, or marine animals such as tunicates [7]. Industry, however, overwhelmingly relies on wood, which accounts for 93 % of its need in cellulosic fibers [34]. Although hardwoods have received some attention in South America, Europe, or Asia, softwoods are the primary wood source in North America. Softwoods are vascular plants: they possess a tubular network for the distribution of water and mineral salts throughout their organisms. This network is made of a continuous succession of adjacent tracheid cells whose rigidity is ensured by a 1  $\mu\text{m}$  to 10  $\mu\text{m}$ -thick cellulosic wall. A cellulosic fiber is the combination of a lumen, formed by the tracheid cells, and its surrounding wall (Figure 2.1). Neighboring fibers are separated by the middle lamella (ML) and provide softwoods with most of their structural support. Each fiber wall is subdivided into cellulose microfibrils (CMFs) arranged in a succession of concentric layers labeled from surface to core: the primary wall (P,  $\sim 0.1 \mu\text{m}$  thick) and the secondary wall, itself divided in an outer ( $S_1$ ,  $\sim 0.08\text{-}0.2 \mu\text{m}$ ), middle ( $S_2$ ,  $\sim 1\text{-}10 \mu\text{m}$ ), and inner ( $S_3$ ,  $\sim 0.1 \mu\text{m}$ ) layers [7]. It corresponds to a cross section of approximately  $10^9$  cellulose chains [35, 36], which are mostly oriented in the same direction than the fiber [37].

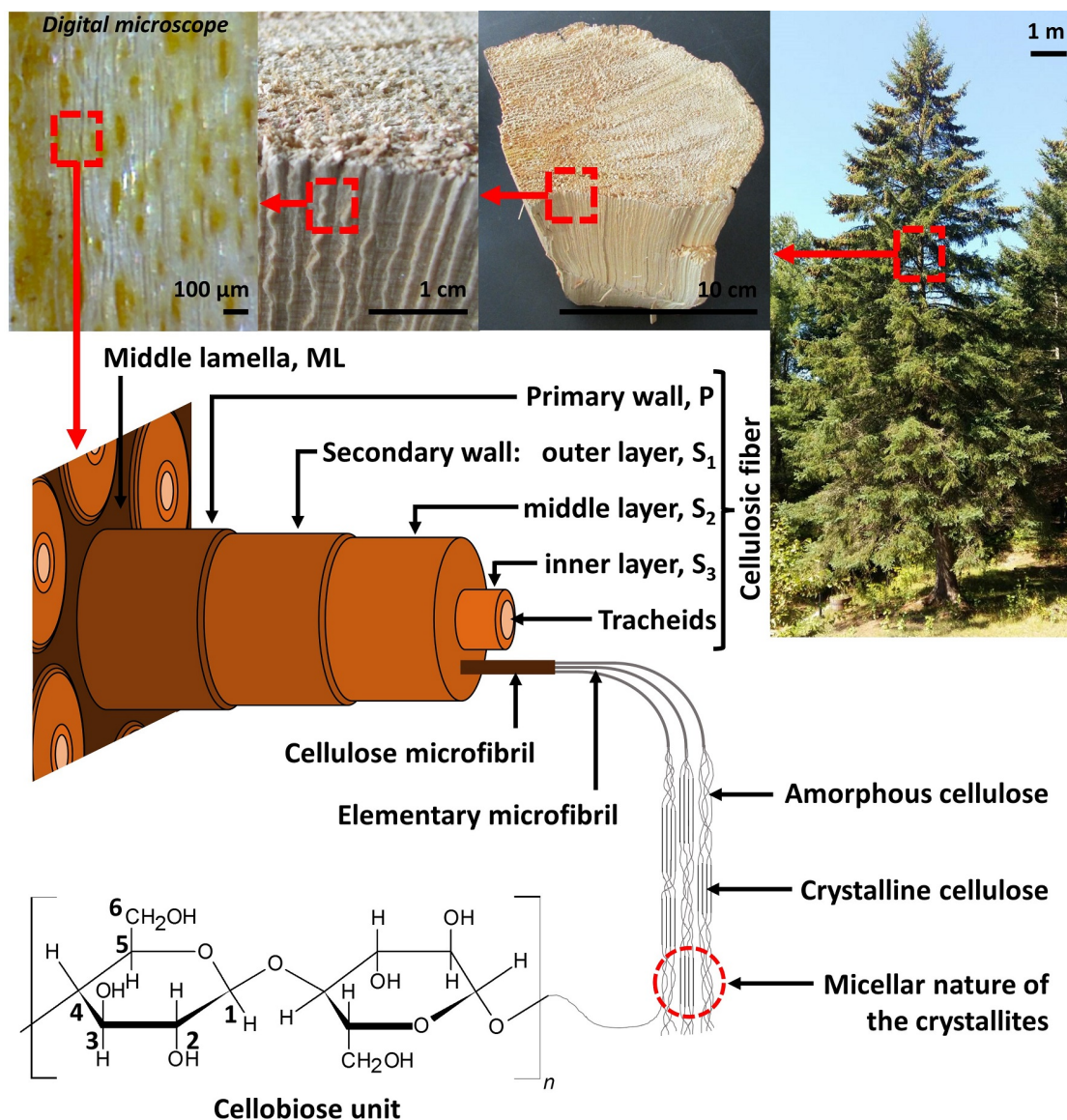


Figure 2.1 Plant structure: from macro to nanocellulose. Pictures are taken from a softwood. Adapted from Hamad [7].

Cellulose, whose chemical formula is  $[\text{C}_6\text{H}_{10}\text{O}_5]_n$  with  $n$  ranging from  $\sim 10,000$  to  $\sim 15,000$  depending on its source [7], coexists in wood cell walls with hemicellulose, lignin, and extractives [38]. Hemicellulose is a generic term to account for polysaccharides found in wood cells that are not cellulose, they are amorphous branched polymers with a low degree of polymerization (150-200) [7]. Lignin is a complex macromolecule made of phenyl propane-type groups forming a three-dimensional reticulated network [39]. Extractives comprise under a same denomination all the small constituents of wood, mostly resins and polyphenols, which are soluble in organic solvents [7].

The average orientation of the microfibrils and their chemical composition vary for each section of the tracheid cell wall. Lignin is more concentrated in the ML and the P than in the secondary walls while hemicellulose reaches its highest concentration in the S<sub>1</sub>. S<sub>2</sub>, which represents  $\sim 90$  % of the fiber mass, accounts for  $\sim 50$  % of the lignin and has the highest cellulose content [7]. It is also there that cellulose molecules are the most aligned with the fiber orientation. It is usually considered that cellulose represents the main structure of a fiber while hemicellulose acts as a binder between the microfibrils and lignin as a reinforcing agent due to its cross-linked nature [37].

CMFs are themselves divided into elementary cellulose microfibrils whose cross section is, in most plants, around  $10\text{-}15\text{ nm}^2$  large and contains roughly 36 cellulose chains [40, 23, 41]. This number of 36 reflects the structure of the terminal complexes (TCs) [40, 42] responsible through the cellulose synthase (CesA) proteins for the extrusion of cellulose in cell walls [41, 43, 44]. In plants, including softwoods, TCs are arranged in rosettes ( $\sim 24$  nm in diameter) containing 6 TC units each ( $\sim 8$  nm large) [40]. TCs are thought to be made, among others, of 6 CesA proteins and thus to extrude 6 adjacent cellulose chains [45, 23, 41]. Consequently, each rosette produces  $6 \times 6 = 36$  contiguous cellulose chains that assemble together to form an elementary microfibril [45, 23, 41]. The organization of the TCs, their shape, the number of CesA proteins per TC, and thus the number of cellulose chains per elementary microfibril vary depending on the organisms, aforementioned values were reported for plant-based CMFs [23, 46].

### 2.1.2 Molecular structure

In elementary microfibrils, cellulose chains are arranged in successions of crystalline and amorphous sections. The former are called “crystallites” or sometimes “micelles”. Indeed, from a microscopic point of view, individual or adjacent crystallites form, in microfibrils, micelle-like structures surrounded by amorphous cellulose, lignin, and hemicellulose (Figure 2.1) [7, 23]. Crystallites ensure the cohesion and the axial rigidity of the CMFs. Their dimensions vary utterly depending on the cellulose source but remain, in the case of plant cellulose, roughly in the range of 50 nm to 1  $\mu\text{m}$  for their length and 2 nm to 20 nm for their width —depending on the number of adjacent elementary CMFs involved in the crystalline regions— with aspect ratios up to 40 [47, 16, 48, 49, 50]. In bacteria [51] and tunicates [52], crystalline regions can be several micrometers long and have higher aspect ratios. The amorphous sections account for the normal flexibility of the microfibrils, thus enabling elementary CMFs entanglements to form.

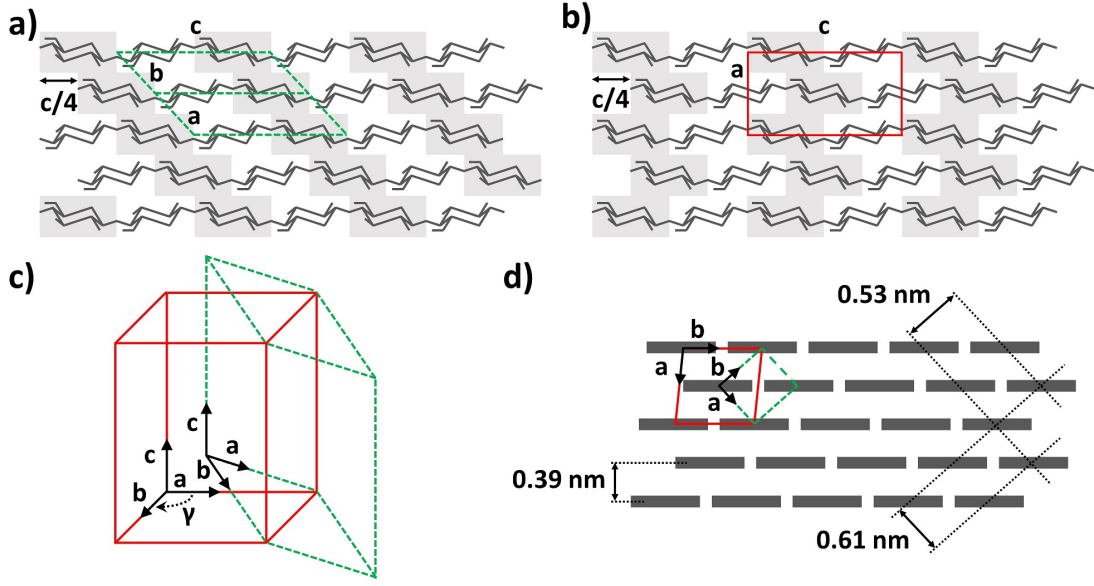


Figure 2.2 Crystallographic unit cells for cellulose I. (a) and (b) Cut view longitudinally to the cellulose chains axis and perpendicularly to the equatorial OH-O bonding plane for cellulose I<sub>α</sub> and I<sub>β</sub>, respectively. In the former, cellobiose units belonging to adjacent chains are arranged linearly with a constant relative displacement of  $c/4$  between two units, whereas they alternate in cellulose I<sub>β</sub> with a relative displacement switching between  $+c/4$  and  $-c/4$ . (c) Cellulose I<sub>α</sub> (dashed green line) and I<sub>β</sub> (solid red line) respective unit cells. (d) Cut view perpendicularly to the cellulose chain axis, each rectangle represents a cellulose chain, the distance between the main cross sectional lattice planes are represented. Adapted from Moon et al. [23], Sugiyama et al. [53], and Imai et al. [54].

Cellulose, or poly(anhydro- $\beta$ -1,4-glucopyranose), is a polymer of cellobiose (Figure 2.1), itself being a dimer of  $\beta$ -D-anhydroglucose units [7]. In the chain direction, cellulose cohesion is primarily ensured by covalent C-O-C bonds while OH-O hydrogen bonds play a role in the molecule's rigidity [55]. Molecular modeling indeed suggests that the OH groups of cellulose are all equatorial to the anhydroglucose rings and that strong OH-O hydrogen bonds can form in the equatorial plane only. In the perpendicular axial direction (top & bottom of the anhydroglucose rings), only weaker CH-O hydrogen bonds and van der Waals interactions can form. As a result of this asymmetry, cellulose chains form sheet-like structures parallel to the equatorial plane of the anhydroglucose rings [55, 21, 56, 57, 58]. This anisotropy of the cellulose chains structure translates into their elastic properties. Dri et al. computed the Young modulus of the structure alongside its 3 main directions [18]: the largest value, 208 GPa, was found in the cellulose chains direction while the perpendicular equatorial direction had a Young's modulus of 98 GPa. The lowest value, 19 GPa, was found in the axial direction into which the cellulose sheets stack up.



In natural cellulose, two main different intersheet hydrogen bonding patterns coexist: the corresponding allomorphs are labeled cellulose  $I_\alpha$  and  $I_\beta$  [21, 56, 17]. They are illustrated in Figure 2.2. Cellulose  $I_\alpha$  forms a crystallographic triclinic unit cell ( $a=0.672$  nm,  $b=0.596$  nm,  $c=1.040$  nm,  $\alpha=118.1^\circ$ ,  $\beta=114.8^\circ$ ,  $\gamma=80.4^\circ$ ) [56]. Cellulose  $I_\beta$ , on the reverse, forms a crystallographic monoclinic unit cell ( $a=0.778$  nm,  $b=0.820$  nm,  $c=1.038$  nm,  $\gamma=96.5^\circ$ ) [21]. In both cases,  $c$  corresponds to the chain direction. In cellulose  $I_\alpha$ , cellobiose units belonging to adjacent chains are arranged linearly between the different sheets with a constant relative displacement of  $c/4$  between each, whereas they alternate in cellulose  $I_\beta$  with a relative displacement switching between  $+c/4$  and  $-c/4$  [23, 54, 56, 53]. The lattice planes perpendicular to the chain direction of cellulose  $I_\alpha$  ((110), (010), (100)) and  $I_\beta$  ((200), (110), ( $1\bar{1}0$ )) are, however, almost identical in term of d-spacing with 0.39 nm, 0.53 nm, and 0.61 nm, respectively. These experimental crystallographic results are supported by molecular modeling [59].

Other thermodynamically more stable allomorphs, cellulose II, III, & IV, may be obtained through processing of cellulose I [23]. It has to be noted that cellulose II is a natural allomorph too as it is marginally present in some bacteria and algae [60]. Cellulose I is however the allomorph with the highest Young's modulus in the chain direction when both crystalline and amorphous sections are considered [23, 61].

### 2.1.3 Elementary microfibril models

With the elucidation of the molecular structure of crystalline cellulose, models were proposed to describe the arrangement of cellulose chains in elementary microfibrils. For land plant-sourced cellulose, these models consider 36 chains according to the biological observations made on the terminal complexes of plant cell walls [40, 23, 41]. Indeed, the pattern of rosettes including six TCs seems to have been conserved among all land plants (angiosperms, gymnosperms, ferns, mosses, liverworts) from an evolutionary point of view, and may even be found in some green algae [46]. Although the following models can also describe the formation of cellulose  $I_\alpha$ , we will focus on the description of the cellulose  $I_\beta$  synthesis, which is by far the most common allomorph in higher plants [62, 17].

The first detailed 36 chains model, illustrated in Figure 2.3 can be traced back to Brown [46]. Brown proposed that plant TCs produces 6 cellulose chains arranged linearly in mini-sheets along the ( $1\bar{1}0$ ) lattice plane of crystalline cellulose  $I_\beta$  and bonded thanks to van der Waals interactions. The sheets produced by the different TCs then assemble and crystallize thanks to the formation of OH-O hydrogen bonds along the (200) plane [46, 60, 63]. The resulting crystallite has a  $6\times 6$  rectangular cross sections with (110) and ( $1\bar{1}0$ ) surfaces [46, 23]. They

are respectively  $\sim 3.7$  nm-wide and  $\sim 4.3$  nm-height based on the crystallographic monoclinic unit cell dimensions determined by Nishiyama et al. [21].

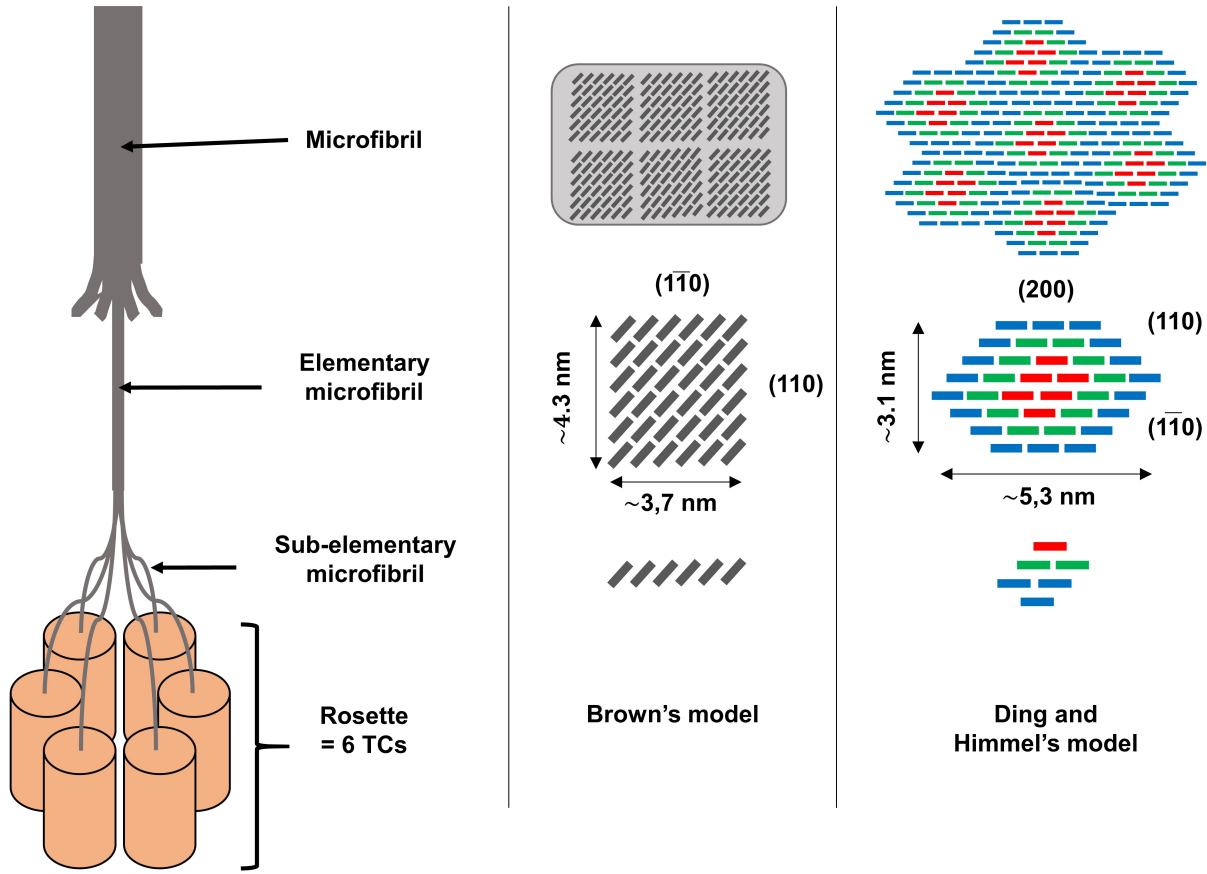


Figure 2.3 Elementary microfibril models for cellulose  $I_{\beta}$ . (left) Rosettes are made of 6 terminal complexes, each of which extrudes a sub-elementary microfibril made of 6 cellulose chains for a total of 36 chains per elementary microfibril. Sub-elements assemble to form an elementary microfibril, and then a microfibril wherein they may be separated by lignin or hemicellulose content. Each rectangle represents a cellulose chain viewed from the (a, b) crystallographic plane (Figure 2.2). (center) In Brown's model [46], sub-elementary microfibrils are mini-sheets of cellulose chains assembled by weak van der Waals interaction alongside the  $(1\bar{1}0)$  lattice plane, while elementary microfibrils have a rectangular  $\sim 3.7 \times 4.3$  nm<sup>2</sup> cross-section and expose mostly their (110) and  $(1\bar{1}0)$  planes at their surface. (right) In Ding and Himmel's model [41], sub-elements and elementary microfibrils have respectively a triangular and an hexagonal cross-section. Three kind of cellulose chains coexists, from core to skin: crystalline (red, 6 chains), subcrystalline (green, 12 chains), subcrystalline/non-crystalline (blue, 18 chains). Elementary microfibrils exposes 6 faces corresponding to their (110),  $(1\bar{1}0)$ , and (200) lattice plane for an overall cross section of  $\sim 5.3 \times 3.1$  nm<sup>2</sup>. Adapted from Brown [46], Ding and Himmel [41], and Moon et al. [23].

With the improvement of atomic force microscopy (AFM) techniques, Ding and Himmel [41] proposed a new model based on the direct AFM observation of untreated maize primary cell wall and on the hexagonal organization proposed by Doblin et al. [45] for CesA proteins within a TC. According to their model illustrated in Figure 2.3, each TC contains three kind of CesA proteins and extrudes a triangularly shaped sub-elementary fibril made of six chains: 1 crystalline (in red), 2 sub-crystalline (in green), and 3 sub-crystalline/non-crystalline (in blue). Sub-elementary fibrils produced by a same rosette then assemble in an hexagonal elementary microfibril made of three concentric layers: a crystalline core (6 chains), a sub-crystalline layer (12 chains), and an outer layer (18 chains), which can be either sub-crystalline or non-crystalline depending on the plant parts. This distinction between the 3 layers provides a reasonable explanation for the 2 nm-wide nanofibrils sometimes reported through TEM observations [42, 41]: they would correspond to elementary fibril whose outer layer was non-crystalline and was thus digested during the extraction process. In their model, the crystal size can vary between  $\sim 1.5 \times 3 \text{ nm}^2$  and  $\sim 3 \times 5 \text{ nm}^2$  for elementary fibrils possessing 18 or 36 crystalline chains respectively [41]. Ding et al. brought further evidences in favor of an hexagonally shaped elementary microfibril through AFM visualization [41, 64, 65]. The main surfaces correspond to the lattice planes (110), ( $1\bar{1}0$ ), and (200) [41, 66].

## 2.2 Cellulose nanocrystals

### 2.2.1 Extraction processes

Amorphous cellulose is more reactive than its crystalline counterpart and consequently degrades first upon treatment. The process to extract the crystallites from CMFs exploits this peculiarity: a strong acid hydrolysis (HCl, HBr,  $\text{H}_2\text{SO}_4$ , or  $\text{H}_3\text{PO}_4$ ) [67, 7, 68, 69, 70], or an oxidative treatment in one [22, 71, 72, 73] or two [74] steps digests the amorphous cellulose while preserving most of the crystalline parts. Lately, other strategies based on subcritical water hydrolysis [75] and ionic liquids [76, 77, 78, 79, 80, 81, 82] have emerged, but remain in their developing stages. Nanoparticles obtained through these processes are made of a few adjacent crystallites and are called cellulose nanocrystals (CNCs).

The choice of the mineral in the acid hydrolysis process has a key influence on the properties of the CNCs obtained [7]. A treatment of purified cellulose, either by mechanical disintegration or by HCl (2.5 M, 105 °C, 15 min) leads to particles whose lengths, measured as a function of the degree of polymerization, is leveled off: they are almost not reduced by further treatment [83]. The use of HBr, instead of HCl, produces similar results [69, 70]. When treated with  $\text{H}_2\text{SO}_4$  or  $\text{H}_3\text{PO}_4$ , sulfate or phosphate half-ester groups are introduced on the cellulose

backbone through an esterification of its OH groups [22, 7]. The negatively charged surface of the esterified CNCs brings electrostatic stability to their aqueous suspensions [84, 85]. They are colloidal at low concentrations and form chiral nematic or birefringent ordered structures at intermediate or high levels, respectively [85, 86, 87, 49]. These self-assembling properties are also observed in the solid phase: CNCs suspensions can be processed into solid films which keep these optical properties [88, 87] or have uniaxial orientation [89], while freeze and spray-drying yields respectively an aerogel [90, 16, 91] or a powder [91].

Oxidative treatments aim at extracting the CNCs from the CMFs bulk while introducing aldehydes or carboxylic acid functions on the cellulose backbone [22]. The most common process to obtain aldehydes is through periodate oxidation of the vicinal diols on carbons C<sub>2</sub> and C<sub>3</sub> (Figure 2.1) [72, 73, 92, 22], while carboxylic acids are obtained through TEMPO-mediated oxidation of the C<sub>6</sub> hydroxyl group [71, 22]. These oxidations are sometimes performed following an HCl acid hydrolysis for the sole sake of functionalizing the CNCs as aldehydes and carboxylic acid functions may serve as starting points for further modifications [17, 23, 22].

From the aforementioned techniques, sulfuric acid hydrolysis is at the same time the most common process for CNCs production —before hydrochloric acid hydrolysis— [17, 23, 22], the first historically [93, 94], and up to now the most scalable [7, 68]. Sulfated CNCs are cheaper and less toxic to produce than phosphated ones. In comparison with HCl-hydrolyzed particles, they possess tunable self-assembling properties and readily form stable colloidal suspensions in water thanks to their surface charges. They are also smaller, which translates in a higher degree of crystallinity and a higher specific surface area, and can be produced in higher yield [7]. They are however less thermally stable as sulfate groups favor their thermal decomposition through a dehydration reaction [51, 26]: the threshold for thermal degradation may hence decrease from  $\sim 250\text{--}300^\circ\text{C}$  for unsulfated CNCs to as low as  $180^\circ\text{C}$  for sulfated particles. It is also worth noting that the unmodified surface of HCl-hydrolyzed CNCs may be an asset in some specific applications (compatibilizer, stabilizer) or as a starting point for chemical functionalization.

### 2.2.2 Morphology

A challenge in characterizing CNC morphology is to draw a line between an individual nanocrystal and an agglomerate. There is no real definition of what a CNC is: they are alternatively described as rod-like particles, each made of a single crystallite, or as ribbon-like particles made of irreversibly 2-D aggregated crystallites (whose cross-sections hence are several times larger than thicker).

The shape of a crystallite is expected to match that of an elementary cellulose microfibril. Using Scherrer equation, it is possible to triangulate their cross-section from X-ray diffraction (XRD) data [95, 96, 97].  $^{13}\text{C}$  nuclear magnetic resonance ( $^{13}\text{C}$ -NMR) achieves the same outcome by differentiating the contribution between core and surface cellulose chains [97]. Cross-sections determined through these techniques are feedstock-dependent. Their shapes vary from near rectangles  $-(110)$  and  $(1\bar{1}0)$  surfaces only as in Brown’s model [46]–to hexagons  $-(110)$ ,  $(1\bar{1}0)$ , and  $(200)$  surfaces as in Ding and Himmel’s model [41]. These crystallites are typically made of up to  $\sim 70$ -90 cellulose chains (instead of the 36 predicted for an elementary cellulose microfibril). This inconsistency between crystallite dimensions predicted from the biological observation of plants’ terminal complexes and those measured in CNCs remains to be investigated. It is worth noting that some authors have proposed an octagonal shape for the crystallites with the presence of  $(010)$ ,  $(110)$ ,  $(1\bar{1}0)$ , and  $(200)$  surfaces [98]. This shape-hypothesis cannot be verified by XRD or  $^{13}\text{C}$ -NMR (see discussion and illustration in Appendices, section D.2).

Crystallite dimensions, determined by XRD or  $^{13}\text{C}$ -NMR, may then be compared to those of the CNC particles, estimated through transmission electron microscopy (TEM), AFM, or a combination of both. Table 2.1 summarizes the outcome of particle size measurements in studies where a special effort was provided to measure both the height,  $h_{\text{CNC}}$ , and the width,  $w_{\text{CNC}}$  of the nanocrystals. Results are classified by characterization method and by extraction protocol (acid nature and concentration,  $[\text{Acid}]$ , temperature,  $T$ , and duration,  $t$ ). Each entry is labeled from 1 to 16. While TEM is most commonly employed to measure CNC lengths and widths, it may also be used to determine their heights: a 3-dimensional object projects a shadow on its support if it is illuminated from the side. Correlating the size of the shadow with the angle of incidence of the electron beam provides with an estimate for the height of the object. This technique was first applied in 1953 by Mukherjee and Woods [5] to the characterization of particles obtained from the sulfuric acid hydrolysis of ramie, hemp, jute, and cotton fibers. From the shadow projected by the particles on the electron microscopy micrographs, Mukherjee and Woods determined that their width was roughly 4.5 times larger than their height (Table 2.1, entries 3 to 6). They hypothesized that these ribbon-like particles were made of  $\sim 4$ -5 layers of glucose residues but abstained from further considerations given the low reliability of their height measurements. Using the same approach, Vogel [99] and later Marchessault [100] obtained similar sizes for ramie sulfated CNCs (Table 2.1, lines 1 & 2) and drawn identical conclusions.

Table 2.1 Plant-based CNCs cross-sectional shape measurements (CNC widths,  $w_{\text{CNC}}$ , and heights,  $h_{\text{CNC}}$ ).

Treatment conditions				TEM		WAXS/WANS	SAXS/SANS		AFM		Ref.
Cellulose source	[Acid] wt%	$T$ °C	$t$ h	$w_{\text{CNC}}$ nm	$h_{\text{CNC}}$ nm	$h_{\text{CNC}}$ nm	$w_{\text{CNC}}$ nm	$h_{\text{CNC}}$ nm	$w_{\text{CNC}}$ nm	$h_{\text{CNC}}$ nm	
<i>H<sub>2</sub>SO<sub>4</sub> acid hydrolysis</i>											
1 ramie	11.4	20	6+10 <sup>a</sup>	8.0-10.0	3.0						[99]
2 ramie	48.8	40	24	15.0-16.0	4.0-5.0						[100]
3 ramie	48.7	20	216	15.5±2.0	3.5±0.4						[5]
4 jute	43.4	40	24	8.5±1.1	2.0±0.3						[5]
5 hemp	43.4	20	144	13.0±1.6	3.0±0.3						[5]
6 cotton	48.7	20	216	13.0±0.8	2.5±0.1						[5]
7 cotton	64	45	0.83						20.4±7.8 <sup>i</sup>	6.8±3.3 <sup>i</sup>	[101]
8 cotton	64	45	0.83						20±6 <sup>i</sup>	8.9±2.8 <sup>i</sup>	[102]
9 cotton	65	45	0.5	27±14		6 <sup>b</sup>	27 <sup>c</sup>	6.0		7.3±1.5	[96]
10 cotton	65	72	0.5	21±11			21 <sup>c</sup>	6.0			[96]
11 wood <sup>h</sup>	65	72	0.5	12±5		4.4 <sup>b</sup>	12 <sup>c</sup>	3.8			[96]
12 wood <sup>h</sup>	64	45	1			3.0±0.2 <sup>b</sup>	24.4	3.0 <sup>d</sup>		4.0±0.3	[103]
13 softwood				8.0±0.1						4.19±0.07	[20]
14 softwood				7.1±0.1						4.35±0.08	[20]
<i>HCl acid hydrolysis</i>											
15 softwood <sup>e</sup>	8.4	105	7			2.7±0.5 <sup>b</sup>	21.7	2.7 <sup>d</sup>		3.2±0.4	[103]
<i>TEMPO mediated oxidation</i>											
16 softwood <sup>f</sup>			24	8.2±3.4			12.7±5.5 <sup>g</sup>	3.2±2.2 <sup>g</sup>			[104]

<sup>a</sup> Acid hydrolysis was conducted in 2 steps between which the acid was removed and replaced by fresh sulfuric acid

<sup>b</sup> A cylinder model is used to determine the size of an elementary fibril

<sup>c</sup> Width value is taken from TEM measurement as an input in the model

<sup>d</sup> Height value is taken from WANS measurement as an input in the model

<sup>e</sup> Carboxymethylated cellulose nanofibers of a softwood pulp (60 % Norwegian spruce, 40 % Scottish pine)

<sup>f</sup> Maritime pine, particles obtained are not CNCs but short CNFs (length <1 µm)

<sup>g</sup> A simplified ribbon model enable a calculation without any input for  $w_{\text{CNC}}$  or  $h_{\text{CNC}}$

<sup>h</sup> Avicel

<sup>i</sup> An extensive calibration allows for the determination of both height and width through AFM

Nowadays, heights are typically measured from AFM measurements. Performed with a cantilever, AFM has a height resolution in the height of a few Angstroms but a planar resolution that is no better than the geometry of the tip (a few nanometers). With extensive calibration, it is possible to deconvolute the signal to account for the tip's geometry and achieve planar measurements with AFM. Hence, Urena et al. [101, 102] found cotton-based sulfuric acid-hydrolyzed CNCs to be 2 to 3 times larger than high through AFM-only measurements (Table 2.1, lines 7 & 8). In both cases, the particle height is coherent with that of a crystallite, but the width points towards an aggregation.

Using a wider array of methods, Elazzouzi-Hafraoui et al. [96] characterized the cross-section of CNCs obtained through the sulfuric acid hydrolysis of cotton. The size of a crystallite was estimated by applying a cylinder model on wide-angle X-ray scattering (WAXS) data. The diameter obtained (6 nm for cotton) was found to be similar to the CNC height measured through AFM ( $7.3 \pm 1.5$  nm) (Table 2.1, line 9). The cylinder model was no longer relevant once applied on small-angle X-ray scattering (SAXS) data, and Elazzouzi-Hafraoui et al. [96] thus applied a parallelepiped model in which the width was set according to the TEM results ( $27 \pm 14$  nm). They obtained a third measurement for the height, 6.0 nm, which was coherent with the ones measured thanks to WAXS and AFM analysis. They concluded that cotton-based CNCs were ribbon-like particles ( $\sim 140 \times 27 \times 6$  nm<sup>3</sup>) made of several 2-D aggregated crystallites. Similar results were obtained with cotton-based CNCs obtained through different acid hydrolysis conditions (Table 2.1, line 10) and with wood-based CNCs (line 11).

Other studies that employed combinations of techniques, including small-angle neutron spectroscopy (SANS) and wide-angle neutron spectroscopy (WANS), also reported ribbon-like particles [103, 20] (Table 2.1, line 12 to 14). Interestingly, wood-based CNCs obtained through alternative processes such as acid chloride hydrolysis [103] and TEMPO-mediated oxidation [104] have similar agglomeration patterns (Table 2.1, lines 15 & 16).

Hence, particles characterized in the aforementioned works are apparently constituted of rod-like crystallites that form 2-D ribbon-like aggregates. These aggregates are observed in aqueous suspensions through diffraction methods (SAXS/WAXS, SANS/WANS) and on CNCs deposited on supports through TEM/AFM. Widths and heights measured through TEM/AFM seem to be systematically some Angstroms larger than those obtained through diffraction. Beyond the precision of each technique, this difference may be attributed to the presence of a thin layer of amorphous or paracrystalline cellulose around the crystalline core chains [41]. Besides this deviation, AFM and TEM measurements seem to provide good approximates of CNC heights and widths, respectively [96, 20]. The width distribution observed through TEM for the ribbon-shaped CNCs deposited on a support corresponds quite

accurately to the size distribution observed in solution through cryo-TEM for a randomly oriented ribbon of similar dimensions [96] or through SAXS with a ribbon-like model [104]. Su et al. noted that TEM analyses may underestimate slightly the concentration in larger CNCs [104]. Abitbol et al. [105] reported the coexistence of individual and aggregated crystallites: by deconvoluting the width distribution observed in cryo-TEM, they found that their data may be representative of particles whose lateral size is close to the height measured through AFM and that are arranged in singlets ( $\sim 50$  % of the population), doublets ( $\sim 25$  %), or multiplets ( $\sim 25$  %) [105].

There are two main interpretations to these 2-D aggregates of crystallites. The first suggests that they could already be present in the untreated plant cell wall: upon sulfuric acid hydrolysis, these aggregates are then either preserved or broken to yield a polydispersity of 2-D crystallite aggregates [96]. These aggregates can be considered as irreversibly bonded (if crystallites could not be separated by the extraction process, then no further dispersion treatment can break them). Alternatively, CNCs could be made of single crystallites whose 2-D aggregation is spontaneous and reversible. Uhlig et al. [103] associated the tendency to form 2-D agglomerates to the amphiphilicity of CNC particles: the crystallites assemble their hydrophobic edges –corresponding to the lattice planes (200)– to minimize the overall interfacial tension. The positioning of these hydrophobic lattice planes at the nanocrystal surface justifies the 2-D pattern of CNC agglomeration.

### 2.2.3 Surface properties

#### Amphiphilicity of the nanocrystal

The amphiphilicity of CNC particles, mentioned in the previous section, arises from the anisotropy of cellulose chains within the nanocrystals [106]. Each lattice plane intersects the crystal cell with a different orientation, which results in various chemical compositions. Hence, while (200) lattice planes predominantly display C-H bonds, (110), ( $1\bar{1}0$ ), and (010) lattice planes are rich in hydroxyl groups. There is no experimental characterization for the surface properties of these lattice planes. Molecular modeling simulations attempt to fill this gap, both by predicting the strength of solvent-CNC surfaces interactions and their impact on the arrangement of solvent molecules and in the crystalline structure of the particles [23].

Modeling base on water, the most investigated solvent, demonstrated that the ( $1\bar{1}0$ ) and (110) lattice planes of cellulose  $I_\beta$  have roughly the same hydrophilicity (differences in water density and in water potential energies close to these surfaces are below 0.5 % [107]). Matthews et al. [108] reported similar results: on the (110) and ( $1\bar{1}0$ ) surfaces, cellulose structured the



surrounding solvent by influencing the bulk water hydrogen bonding pattern at a distance of up to 0.8 nm from the nanocrystal surface, corresponding to at least 3 layers of water molecules. Water structuring was slightly more pronounced on (010) surfaces. (200) surfaces were, however, found to be more hydrophobic in nature with a significantly different water molecule ordering than the three others lattice planes [108].

The hydrophobicity of (200) surfaces was investigated by simulating their wetting properties. Modeled water-drop hence have a contact angle of  $43^\circ$  and  $95^\circ$  with the (110) and (200) surfaces, respectively [109]. This amphiphilicity is also reflected in terms of modeled surface energies: (200) surfaces have a modeled surface energy that is  $\sim 40\%$  smaller than those of (110) and  $(1\bar{1}0)$  lattice planes [110]. No estimation was provided for (010) surfaces [110]. The affinity of (200) surface for mildly non-polar compounds is supported by molecular dynamic studies: benzophenone [111] and lignin [112, 113] were found to interact preferentially with (200) surfaces. In both cases, (110) and  $(1\bar{1}0)$  surfaces exhibited roughly equivalent properties [111, 112, 113].

### Degree of sulfatation

Besides their native amphiphilicity, the main surface feature of sulfuric acid hydrolyzed CNCs is the presence of sulfate half-ester groups,  $-\text{OSO}_3\text{H}$ . They result from the esterification of the hydroxyl groups displayed by (110),  $(1\bar{1}0)$ , and (010) surfaces. These OH groups are the most reactive functionalities on CNC surfaces [22]. The degree of surface sulfatation influences the behavior of CNCs in aqueous suspensions [47, 114], their thermal properties [51, 26] and their self-assemblies [90]. Indeed, while the proton of an hydroxyl group has little lability in water, sulfate half-ester groups are acidic. Sulfatation hence introduces negative charges on CNC surfaces whose influence may be modulated by exchanging the proton for another counter-ion, typically  $\text{Na}^+$ .

The sulfur content,  $S$  (wt%), may be characterized directly from an elemental analysis. The global sulfur content is commonly reported as a number of sulfate groups per  $\beta$ -D-anhydroglucose units,  $n_{\text{Sulf}}$ , based on the chemical formula  $\text{C}_6\text{H}_{10}\text{O}_5-(\text{SO}_3)_{n_{\text{Sulf}}}$  [16]:

$$S(\text{wt}\%) = 100 \frac{n_{\text{Sulf}} S}{6C + 10H + (5 + 3n_{\text{Sulf}})O + n_{\text{Sulf}} S} \quad (2.1)$$

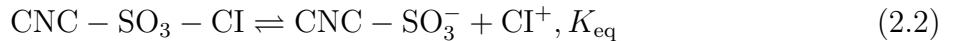
where  $C$ ,  $H$  and  $O$  are the weight fractions of the respective elements determined by elemental analysis. Experimentally,  $n_{\text{Sulf}}$  increases with the harshness of the sulfuric acid hydrolysis (duration, temperature, acid concentration) and may reach up to  $\sim 0.06$ - $0.07$  sulfate group per  $\beta$ -D-anhydroglucose unit [16].

## 2.3 CNC/solvent interactions and stabilization mechanisms

Excluding metal/ligand bonds, organic substrates may form three kinds of interactions with their environment: covalent, ionic, and weak (which includes van der Waals, hydrogen bonds, and other Lewis acid/base interactions). A molecule that binds with a substrate through a covalent or an ionic interaction is said to be chemically adsorbed over the substrate (chemisorption), while weak interactions lead to physical adsorption (physisorption). Covalent bonds are *a priori* non-reversible under ambient conditions: their formation through chemisorption hence alters the chemical nature of the nanocrystals, which is off-topic for this dissertation. The various functionalities susceptible to react with CNC surfaces were reviewed by Eyley et al. [22]: corresponding chemicals are to be excluded. Note that a traditional approach to review the influence of ionic and weak CNC/solvent interactions on the mechanisms at play in suspensions would have consisted in establishing the diagram of the interaction energy as a function of the interparticular distance based on the Derjaguin-Landau-Verwey-Overbeek (DLVO) theory [115]. While this course of action was considered, the fact that a relevant interaction such as solvation [116, 117, 118] remains poorly described by DLVO theory however prevents a complete resolution of the interaction energy. As a consequence, an empirical approach will hence be considered in this thesis, which is based on identifying the behavioral changes (described in section 2.4: sedimentation, gelation, nematic self-assembly, .), that CNC/solvent interactions can trigger within the system.

### 2.3.1 Ionic interactions and electrostatic stabilization

The only bonds that may be considered as ionic in CNCs are those between the sulfate groups and their counter-ions, CI. The dielectric constant,  $\epsilon$ , quantifies the ability of a solvent to dissociate the ionic bonds of its solutes [119]. Dissociation is reversible and controlled by the constant equilibrium,  $K_{eq}$ :



$$K_{eq} = \frac{[\text{CNC} - \text{SO}_3^-] [\text{CI}^+]}{[\text{CNC} - \text{SO}_3 - \text{CI}]} \quad (2.3)$$

where  $[X]$  is the concentration of the suspension in “X”. The rate of dissociation,  $K_{eq}$ , is directly proportional to the surface charge of the particles. It may be tuned by changing the nature of the counter-ions, the temperature, or the nature of the solvent [119]. Alternatively,

the equilibrium may be altered by varying the concentration in CNCs or by increasing the ionic strength of the suspension (addition of a salt to tune  $[CI^+]$ ). In suspensions, the surface charges, the dielectric constant, and the ionic strength are relevant for the electrostatic stabilization they provide to the system [120].

Dissociated counter-ions form a cloud around the nanoparticles, the electrostatic double layer, whose thickness and density increase with the dielectric constant and the surface charges. When two particles approach each other, their electrostatic double layers overlap first, which locally increase the concentration in counter-ions. It creates an osmotic force from the bulk liquid that promotes the dilution of the overlapped clouds and hence prevents particles from colliding: it is the electrostatic stabilization [120]. The strength of this osmotic force is a function of the gradient in counter-ions concentration between the clouds and the bulk of the media: increasing the ionic strength of the suspension reduces the efficiency of electrostatic stabilization [120]. Experimentally, the influence of ionic strength [84, 121] and dielectric constant [122] on the colloidal stability of CNC particles is well known. The nature of the counter-ions was also found to alter the CNC redispersibility [123].

### 2.3.2 Weak interactions: solvation-induced and steric stabilizations

#### Solubility parameters: quantifying weak interactions

Physisorption relates to the notion of chemical affinity, which is proportional to the magnitude of the weak interactions that can be formed between two substrates. Hildebrand was the first to propose a quantitative thermodynamic approach to describe the potential of a material for cohesion: it relied on a single parameter,  $\delta_T$  ( $\text{MPa}^{1/2}$ ) [124, 125].  $\delta_T$ , the Hildebrand cohesion or solubility parameter, is the square root of the cohesive energy density,  $CED$  ( $\text{MPa}$ ).  $CED$  is itself described as the fraction of the total molar cohesive energy between the substrate and its surrounding likewise pure medium,  $E_T$  ( $\text{J mol}^{-1}$ ), by the molar volume of the substrate,  $V_m$  ( $\text{m}^3/\text{mol}$ ). Experimentally and assuming an ideal gas behavior,  $E_T$  may be quantified by correcting the molar enthalpy of vaporization,  $\Delta H_{\text{vap}}$  ( $\text{J mol}^{-1}$ ), by a factor of  $RT$ , where  $R$  ( $\text{J mol}^{-1} \text{K}^{-1}$ ) is the ideal gas constant and  $T$  (K) is the temperature of the system:

$$\delta_T = \sqrt{CED} = \sqrt{\frac{E_T}{V_m}} = \sqrt{\frac{\Delta H_{\text{vap}} - RT}{V_m}} \quad (2.4)$$

Solubility theories lie on the historic principle that “like dissolves like”, which may be extended to “like seeks like” to include polymers and nanoparticles [126, 127]. The closer are the

solubility parameters of two substrates, the most likely they will dissolve, swell, or disperse, in each other. The use of a single parameter,  $\delta_T$ , was proved to be insufficient to predict many situations. Indeed, the total cohesive energy results from the additive contributions of the atomic non-polar/dispersive interactions,  $E_D$  ( $\text{J mol}^{-1}$ ), of the molecular permanent dipole-permanent dipole interactions,  $E_P$  ( $\text{J mol}^{-1}$ ), of the molecular hydrogen bonding interactions,  $E_H$  ( $\text{J mol}^{-1}$ ), and of every other interactions,  $E_{\text{others}}$  ( $\text{J mol}^{-1}$ ), which include ion-permanent and instantaneous dipoles interactions for instance [126, 127]. Hansen proposed that  $E_{\text{others}}$  may be neglected in most dispersion case studies and split  $\delta_T$  in 3 parameters:  $\delta_D$ ,  $\delta_P$ , and  $\delta_H$  (all in  $\text{MPa}^{1/2}$ ). They correspond to the remaining contributions to the total energy:  $E_D$ ,  $E_P$ , and  $E_H$ , respectively [126, 127].

$$E_T = E_D + E_P + E_H + E_{\text{others}} \approx E_D + E_P + E_H \quad (2.5)$$

$$\frac{E_T}{V_m} \approx \frac{E_D}{V_m} + \frac{E_P}{V_m} + \frac{E_H}{V_m} \quad (2.6)$$

$$\delta_T^2 \approx \delta_D^2 + \delta_P^2 + \delta_H^2 \quad (2.7)$$

The limitations of the Hansen solubility parameters (HSP) lie in this approximation, but also in the fact that sterical effects and molecular shapes are not taken into account in the theory. For instance, the model was found to poorly describe the solubility of strong acids and bases. Karger et al. [128] thus proposed to add a fourth parameter by splitting  $\delta_H$  into an acidic,  $\delta_a$  ( $\text{MPa}^{1/2}$ ), and a basic,  $\delta_b$  ( $\text{MPa}^{1/2}$ ) partial contributions.  $\delta_a$  and  $\delta_b$  reflect the ability of a molecule to participate in hydrogen bonds by providing or receiving protons, respectively.

$$\delta_H^2 = 2\delta_a\delta_b \quad (2.8)$$

However, Hansen solubility parameters accurately describe the behavior of numerous substrates while enabling an easy interpretation of the results in a 3-D graph [127]. Substrates are represented in this three dimensional solubility space by spheres whose centers are given by their HSP ( $\delta_D; \delta_P; \delta_H$ ) and whose radius,  $R_0$  ( $\text{MPa}^{1/2}$ ), reflects a threshold in their behavior (in terms of swelling, dispersion, or solubility). A same chemical may hence have several HSP radii depending on the behavior that is characterized (e.g., since it is usually easier to swell a polymer than to dissolve it, the  $R_0$  threshold for solubility will be smaller than that for swelling). The HSP distance between the substrate  $A$  and a solvent  $B$ ,  $R_a$  ( $\text{MPa}^{1/2}$ ), is calculated as the norm of the vector  $\overrightarrow{AB}$  in the solubility space:

$$R_a = \left[ 4(\delta_{D,A} - \delta_{D,B})^2 + (\delta_{P,A} - \delta_{P,B})^2 + (\delta_{H,A} - \delta_{H,B})^2 \right]^{1/2} \quad (2.9)$$

The factor 4 in front of  $\delta_D$  emphasizes the importance of dispersive interactions and is backed both by experimental results and by theoretical considerations [129, 127]. The relative energy difference (*RED*) is expressed as the fraction of  $R_a$  by the solubility radius,  $R_0$ :  $RED \leq 1$  means that *B* can dissolve, swell, or disperse *A* (depending whether  $R_0$  stands for a behavioral change in terms solubility, swelling, or dispersion).

$$RED = R_a/R_0 \quad (2.10)$$

### Hansen solubility parameters of cellulosic materials

Hansen solubility parameters have been used to characterize substrates such as polymers, pigments, (nano)fillers, and (nano)fibers [130, 127, 131]. To do so, the substrate to be characterized is tested in a range of solvents whose HSP are known and a qualitative mark, either “good” or “bad”, is attributed to each outcome. The ratio between the number of good (G) solvents, X, over the total (T) number of solvents tried, Y, is reported as  $G/T = X/Y$ . A solubility sphere ( $\delta_D; \delta_P; \delta_H; R_0$ ) is then fitted on the data. The quality of the fit, measured through a *FIT* function ( $0 \leq FIT \leq 1$ , best fit for  $FIT=1$ ), increases with the number of solvents probed. It is optimal if every good solvent is included in the sphere while any bad ones are excluded. A *FIT* slightly below 1 is desirable since it is a sign that the solubility sphere is well circumscribed [127].

Wood components—cellulose, hemicellulose, and lignin—have been investigated by Hansen and Björkman [132, 129] (results reproduced in Table 2.2). Amorphous cellulose HSP are thought to be close to those of dextran C. Lignin is less polar and hemicellulose is in between. simulations through group contributions suggest that hemicellulose possesses polar groups that preferentially bond with cellulose, and non-polar ones that are more likely to bond with lignin [129, 127].

The HSP coordinates of a polymer may, however, be affected if its chains assemble to form structures [129]. Cellulose, with organized crystalline regions, falls in this category. Natural swollen cotton cellulose fibers have lower Hansen solubility parameters than dextran C, which may be due to the organization of cellulose in microfibrils [133, 134, 129]. Indirect measurements through inverse gas chromatography also yield lower values for  $\delta_D$  and  $\delta_P$ , but seem to overestimate  $\delta_H$  in the case of cotton-based cellulose [135] and microcrystalline cellulose [136]. These two last data sets are less reliable since they are not based on solubility spheres fitting but on an interaction model [135, 136].

Table 2.2 Hansen solubility parameters for cellulose and lignin. Measurements relying on a direct sphere fitting (and for which a *FIT* value can be calculated) are deemed more reliable than those determined indirectly [129]. G/T refers to the ratio of good solvents over the total number of solvent probed.

Substrate	$\delta_T^a$	$\delta_D^a$	$\delta_P^a$	$\delta_H^a$	$R_0^a$	Reliability	<i>FIT</i>	G/T	Ref.
Dextran C <sup>b</sup>	37.5	24.3	19.9	22.5	17.4	High	0.999	5/50	[132, 129]
Chem. access. cellulose <sup>c</sup>	31.2	18.8	15.8	15.2	11.7	High	0.991	6/19	[134, 129]
Cellulose <sup>d</sup>	36.9	16.9	16.4	28.4		Tedious <sup>f</sup>	-	-/10	[135]
Microcrystalline cellulose <sup>e</sup>	39.3	19.4	12.7	31.3		Tedious <sup>f</sup>	-	-/14	[136]
Lignin	33.9	21.9	14.1	16.9	13.7	High	0.981	16/82	[132, 129]

<sup>a</sup> Expressed in  $\text{MPa}^{\frac{1}{2}}$ .

<sup>b</sup> Equivalent to amorphous cellulose.

<sup>c</sup> Chemically accessible cellulose, cotton-based.

<sup>d</sup> Cotton-based.

<sup>e</sup> Wood-based microcrystalline cellulose.

<sup>f</sup> Indirect fitting based on the Snyder/Karger-Hansen interaction model [135, 136].

Partial HSP characterization has already been achieved by Peng et al. [137] for freeze-dried and never-dried wood-based sulfuric acid-hydrolyzed CNCs. However, the little number of solvents probed —5 to 6—, as well as the methodology employed—which does not take into account the difference in densities between the solvents and the particles, nor the solvent viscosities to calculate the sedimentation time—, prevents any HSP calculations. Never-dried CNCs had a slightly better dispersibility than freeze-dried ones [137]. This was attributed to the drying/re-dispersion process since the degree of surface sulfatation is relatively similar with sulfur contents of 1 wt% and 0.96 wt% for never-dried and freeze-dried CNCs, respectively. Their results also demonstrated the pertinence of HSP characterization for surface modified CNCs. Significant differences were indeed observed in the case of hexanoyl, dodecanoyl, and oleoyl-grafted CNCs when compared with unmodified CNCs. Grafted CNCs exhibited a more pronounced hydrophobic behavior [137]. In the same research group, Yoo and Youngblood [138] conducted a similar study with limited HSP characterization (9 solvents) for CNCs grafted by fatty acids, biodiesel, or plant oils.

Hansen solubility parameters offer an efficient tool to characterize the chemical affinity of fillers, and recent partial HSP studies on cellulose nanocrystals [137, 139, 138, 140] and nanofibers [141, 142] confirm the growing interest and the potential of this method to assess CNC chemical affinity.

## Solvation-induced and steric stabilizations

At this point, it is worth remembering that CNCs are organic nanoparticles whose cohesion relies on weak interactions between cellulose chains [57]: hence, strong enough CNC/solvent physical interactions can compromise the structural integrity of the nanocrystal itself. In theory, it should be possible to distinguish between 4 levels of CNC/solvent interactions: no significant interactions; physisorption at the nanocrystal surfaces; swelling of the nanocrystals; dissolution of the nanocrystals.

Significant physisorption should lead to the formation of a dense, and eventually structured, layer of solvent molecules around the nanocrystals [116, 117, 118]. Such a steric barrier prevents particles from immediately agglomerating upon collision: solvent molecules need to desorb first, which results in an oscillatory force whose range is that of the layers thickness. This structural (or solvation) force provides particles with solvation-induced stabilization. It notoriously alters colloidal behaviors such as agglomeration [116, 117] and sedimentation, which justifies that chemical affinity can be characterized from sedimentation tests [127].

Swelling disturbs the arrangement of cellulose chains close to the surface: in practice, the small cross-section of CNCs (a few tens of cellulose chains) however means that any swelling will also alter the core structure of the nanocrystals. Experimentally, this may be used to recrystallize natural cellulose I nanocrystals into more stable cellulose allomorphs (II, III, or IV) [23]. Solvents with strong Lewis acid/base properties such as N-methylmorpholine, N-oxide, and ionic liquids are able to swell, and eventually solubilize cellulose [143]. This may also be achieved in water under harsh basic or acidic conditions [143]. Since our work focuses on solvents that disperse rather than swell or dissolve CNCs, strong acids and bases are to be excluded. Incidentally, these solvents are those that cannot be described properly by HSP theory: as per Karger et al. [128],  $\delta_H$  needs to be split to account for their exceptional acid/base potential (Equation 2.8). HSP theory should, however, apply to describe CNC interactions with common solvents.

## 2.4 CNC behavior in suspensions

### 2.4.1 Aqueous CNC suspensions

Sulfuric acid-hydrolyzed CNCs are produced as aqueous suspensions [7] whose colloidal stability enables for storage in the wet state [144], which makes water the most investigated solvent for CNC suspensions. Alternatively, the particles may be dried and the initial state of dispersion recovered by ultrasonication [91, 145]. The obvious interest of using water (instead of another solvent) for the development of cost-effective, scalable, green, and biologically-

compatible applications means that CNC behaviors in aqueous suspensions has been investigated since the early 90s [85].

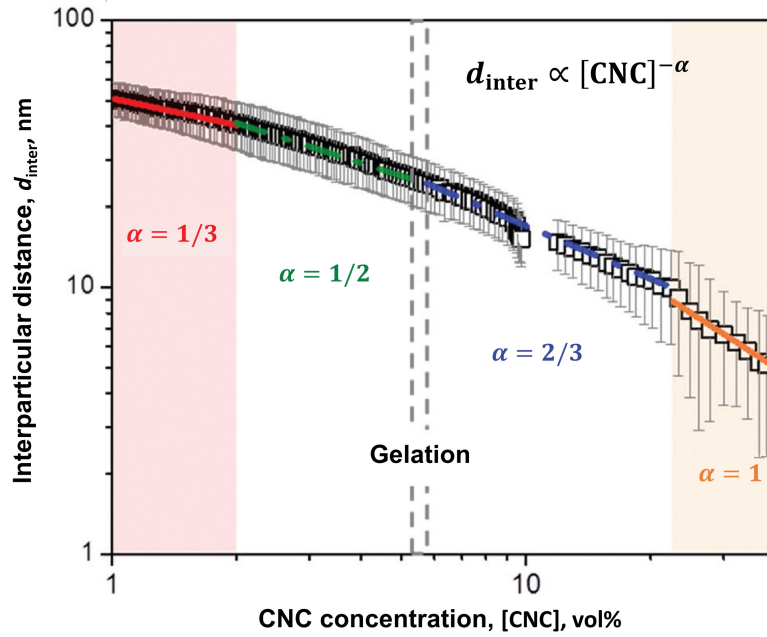


Figure 2.4 Interparticle distance,  $d_{\text{inter}}$  (measured from center to center), as a function of CNC concentration in water,  $[\text{CNC}]$ . Measurements were performed through SAXS during the evaporation of a levitating droplet of CNC aqueous suspension [146].  $d_{\text{inter}}$  varies with  $[\text{CNC}]$  following a power-law relationship,  $d_{\text{inter}} \propto [\text{CNC}]^{-\alpha}$ . The exponent,  $\alpha$ , is of  $1/3$  at low concentrations (red), then  $1/2$  (green),  $2/3$  (blue), and  $1$  (orange). All fittings have an adjusted R-square above 0.98. Gelation occurs from  $[\text{CNC}] \approx 6$  vol%. Adapted from reference [146] - Published by The Royal Society of Chemistry (Creative Commons Attribution 3.0 Unported License).

CNC behavior in water can be best described by following the evolution of the interparticle distance,  $d_{\text{inter}}$  (measured from center to center), as a function of CNC concentration,  $[\text{CNC}]$ :  $d_{\text{inter}} \propto [\text{CNC}]^{-\alpha}$  [146].  $[\text{CNC}]$  may be varied by slowly evaporating an initially dilute media. Figure 2.4 plots  $d_{\text{inter}} = f([\text{CNC}])$  as measured through SAXS by Liu et al. [146] during the evaporation of a levitating drop of CNC aqueous suspension. In an isotropic suspension,  $\alpha \approx 1/3$ : any deviation in  $\alpha$  reflects an anisotropy that underlines the presence of CNC-CNC interactions. At low  $[\text{CNC}]$ , and besides their tendency to form small 2-D agglomerates (see section 2.2.2), CNCs behave as colloidal particles in water:  $\alpha \approx 1/3$  [103, 146]. From  $\sim 2$  vol% (all thresholds mentioned in this section may vary with CNC aspect ratio [147, 148]),  $\alpha$  rises to  $\sim 1/2$ : it corresponds to a phase of nematic self-assembly [146]. CNCs form helical liquid crystals that provide the suspension with optical properties and a distinctive viscosity profile



[49]. From  $\sim 5\text{-}6\text{ vol\%}$ ,  $\alpha$  increases to  $\sim 2/3$  [146]: this threshold coincides with a gelation of the suspension [146]. The transition from a liquid to a gel, detectable in rheology [49], creates a yield stress that interrupts the nematic self-assembly. From  $\sim 20\text{ vol\%}$ ,  $\alpha$  reaches a plateau of  $\sim 1$  [146]: the compression becomes uniaxial.

The helical pitch size of CNC structures (formed between  $\sim 2$  and  $\sim 5\text{-}6\text{ vol\%}$ ) decreases upon drying [149, 150]: starting from a few micrometers, it typically reaches the visible spectrum in the dried state, which provides CNC materials with iridescent properties [7, 147]. The final pitch size is a function of CNC particle size, aggregation state, and temperature [151, 152, 147]. Annealing may tune the optical properties of the material [153].

#### 2.4.2 Non-aqueous CNC suspensions

By comparison with aqueous suspensions, the state of knowledge on non-aqueous CNC suspensions is embryonic. The aqueous pattern of stable colloidal suspensions, liquid crystals formation, and gelation, seems to be replicated for other polar and highly dielectric solvents such as N,N-dimethylformamide, N-methylformamide, and formamide [122]. Bruckner et al. [122] reported that the concentration threshold for gelation and the rate of helical self-ordering were correlated to the dielectric constant of the solvent.  $\varepsilon$  also alters the final pitch size and its dependency on concentration. CNC gels were also reported to form in dimethylsulfoxide [154].

Other solvents such as acetone [155, 156, 157], 1,4-dioxane [154], toluene [157, 158], or chloroform [155, 156] are frequently used to carry surface modification or to solvent cast nanocomposites. However, non-polar solvents do not provide CNCs with long term stability and settling appears to be complete over time [137]. Intermediate outcomes seem possible for solvents with strong H-bonding potentials such as ethanol [137]. Besides  $\varepsilon$ , the ability to form H-bonds (and other Lewis acid/base interactions) is thought to play an essential role in CNC self-ordering [159, 122].

While CNC behavior in non-aqueous media is scarcely described, it seems possible to gather some insights on self-assembly from other nanoparticles and especially from inorganic nanocrystals [160]. Inorganic rod-like nanocrystals behave as a function of their colloidal stability [160]: strongly stabilized particles may form 2-D nematic liquid crystals upon solvent evaporation (as for CNCs in aqueous suspensions [147]); poorly stabilized particles aggregate to form 3-D self-assemblies. Therefore, describing CNC/solvent interactions and their influence on stabilization mechanisms (see section 2.3) could lead to breakthroughs in both CNC dispersion and self-assembly.

### 2.4.3 Interfacial behaviors

Beside their self-assembling properties in the bulk of the suspensions, CNCs have also attracted attention for their potential to stabilize interfaces [161, 162]. In aqueous suspensions, and even in dilute conditions ( $\sim 0.001$  wt%), sulfuric acid-hydrolyzed CNCs have been reported to migrate to the air/water interface over a time scale of few hours [163]. The migration is limited by the diffusion of the particles towards the interface: increasing the bulk concentration accelerates the process. CNCs were found to adsorb at the interface as a discontinuous mono-layer with a contact angle  $< 90^\circ$  (most of the particle surface remain immersed in water). CNC density at the interface can be optimized through salt addition [164]: the screening effect probably weakens electrostatic stabilization, which reduces the average interparticular distance at the interface.

This behavior is also observed for CNC-stabilized oil-in-water Pickering emulsions [165, 98, 166]. Kalashnikova et al. [98] observed that decreasing the degree of surface sulfatation improves the stability of these emulsions. This can probably be related to a question of particle density at the oil/water interface: desulfating CNCs weakens the electrostatic stabilization, which in turns should increase CNC population at the interface and hence the stability of the emulsion. Particle density at the oil/water interface was also found to correlate with the oil/water interfacial tension,  $\gamma^{o/w}$  (whose value was tuned by altering the chemical nature of the oil). Analyzed by interfacial rheology, the normalized surface pressure is significant for  $\gamma^{o/w} \approx 50 \text{ mN m}^{-1}$ , but negligible for  $\gamma^{o/w} \approx 8 \text{ mN m}^{-1}$  [167].

It was proposed that the structural amphiphilicity of the nanocrystals plays a role at interfaces: CNCs are thought to orient their (200) surfaces towards the oil and their polar moieties towards water [98]. This is supported by SANS analysis that demonstrate CNCs to remain totally immersed within the aqueous phase upon adsorption at the oil/water interface [168]. This hypothesis, which still remains to be formally demonstrated, matters in order to calculate the variation in surface energy upon adsorption,  $\Delta E_{\text{ad}}$ , and hence the potential of an interface for stabilization. For a rod-like particle, whose surface is chemically homogeneous,  $\Delta E_{\text{ad}}$  may be calculated from  $\gamma^{o/w}$  and from the contact angle with which the particle is adsorbed at the oil/water (o/w) interface,  $\theta_{\text{ad}}^{o/w}$  [169].  $A$  is the change in o/w interfacial area caused by the particle adsorption.

$$\Delta E_{\text{ad}} = A\gamma^{o/w} (1 - |\cos\theta_{\text{ad}}^{o/w}|) \quad (2.11)$$

This expression is commonly employed in the literature for CNC stabilized interfaces [161, 167, 162]. However, if CNC amphiphilicity plays a role and can indeed orient their functional-

ities at interfaces, this means that CNCs should be considered as “Janus” particles (particles whose surface is composed of 2 or more distinct chemistries). The expression to calculate  $\Delta E_{\text{ad}}$  becomes more complex since it requires, in addition to  $\gamma^{o/w}$ , an estimation of both the particle surface composition and of the various interfacial tensions (polar surface/water, polar surface/oil, non-polar surface/water, and non-polar surface/oil) [170]. Improperly using equation 2.11 for Janus particles may result in significant deviations [170]. Estimating CNC surface tension parameters hence becomes a prerequisite to the accurate description of CNC interfacial behavior.

Alternatively,  $\Delta E_{\text{ad}}$  may be estimated from interfacial rheology measurements [171, 163]:

$$\Delta E_{\text{ad}} = \frac{\Pi A}{f_{\text{part}}} \quad (2.12)$$

where  $\Pi$  is the surface pressure (expressed in  $\text{mN m}^{-1}$  due to the fact that it is measured along the perimeter of a biconical disk or du Noüy ring geometry positioned at the interface of interest) and  $f_{\text{part}}$  (dimensionless) the surface fraction covered by adsorbed particles at the interface.  $\Delta E_{\text{ad}}$  was estimated at  $\sim 5 \times 10^3 k_{\text{B}}T$  for CNCs at the air/water interface, where  $k_{\text{B}}$  is the Boltzmann constant (and  $k_{\text{B}}T$  an estimation of the thermal energy available to the system) [162, 163]. Note that  $\Pi$  is only measurable through interfacial rheology at macroscopic interfaces and that equation 2.12 is of no use for microemulsions, for instance.

## CHAPTER 3 RESEARCH OBJECTIVES

### 3.1 Identification of the problem

Cellulose chains assemble in anisotropic sheet-like crystalline structures, crystallites, whose size is a function of their feedstock. Crystallite surfaces oriented alongside the (010), (110), or (1 $\bar{1}$ 0) lattice planes are expected to be hydrophilic, while those oriented alongside the (200) surfaces are modeled as hydrophobic. Two models, Brown's [46] and Ding & Himmel's [41], are in competition to describe crystallite cross-sections. Both predict the exposition of (110) and (1 $\bar{1}$ 0) surfaces, which have similar wetting properties according to molecular dynamic simulations, but only Ding & Himmel's model predicts the display of a hydrophobic (200) surface [41].

Extracting the crystallites through sulfuric acid hydrolysis, the most scalable process, yields cellulose nanocrystals whose surface is partially sulfated [16, 7]. These nanoparticles are made of individual or 2-D aggregated crystallites. Besides chemical reactions and swelling/dissolution, solvents may form two kind of interactions with CNC surfaces: dissociate the ionic bond between CNC sulfate groups and their counter-ions, and physically adsorb. These may provide CNCs with colloidal stability through electrostatic and solvation-induced stabilizations, respectively. In systems where particles bear a constant charge and whose ionic strengths are kept constant, electrostatic stabilization mostly relies on the dielectric constant of the solvent. It is a well understood phenomenon and CNCs were reported to form stable colloidal suspensions in highly dielectric solvents such as water, formamide, and N-methylformamide [122]. However, the role of physical adsorption on the CNC behavior in suspensions remains to be formally investigated. It would first involve the mapping and the quantification of CNC chemical affinity, and then the description of its influence in suspensions. Besides bulk behavior, characterizing CNC surface properties may lead to breakthroughs in the description and prediction of CNC-stabilized interfaces.

### 3.2 Research hypothesis

This dissertation hypothesizes that CNC potential for colloidal dispersion and self-ordering may be entirely predicted from solvent properties. The adequate characterization of CNC/solvents interactions (ionic dissociation and physisorption) is, however, a prerequisite. This requires appropriate theoretical frameworks: while the dielectric constant is the main parameter for ionic dissociation [119], the Hansen solubility parameter (HSP) theory may be

used to describe the physisorption of solvent molecules over CNC surfaces [127]. It should then be possible to associate variations in term of chemical affinity and dielectric constants to changes in CNC behaviors. HSP characterization is thought to be sensitive enough to characterize the structural amphiphilicity of the nanoparticles, which is expected to influence the aggregation patterns in the water bulk [103] and the orientation of the particles at interfaces [161].

### **3.3 Objectives**

#### **3.3.1 Main objective (MO)**

Develop a tool that predicts CNC potential for dispersion and self-assembly based on solvent parameters only.

#### **3.3.2 Specific objectives (SO)**

- SO 1** Determine the amphiphilic nature of cellulose nanocrystals and map their chemical affinity through HSP theory.
- SO 2** Correlate the CNC behavior in suspensions (dispersion and self-assembly) to solvent parameters only.
- SO 3** Demonstrate the role of the CNC amphiphilicity on the stabilization of interfaces.

## CHAPTER 4 COHERENCE OF THE ARTICLES

The task to describe the CNC behavior in suspensions, any suspensions, seems tedious at first sight. Excluding solvents that swell/dissolve CNCs or react with their surface circumscribes the scope of the work, but still leaves thousands of chemical and an almost infinite number of mixtures. The study may, however, be scaled down to a few tens of representative solvents only: HSP theory indeed represents chemical affinity as a continuous 3-D space and each solvent as a dot in this space. A solvent set is representative if it adequately samples the 3-D space: increasing the number of probed solvents only refines the mesh size and the precision of the HSP characterization. Besides their differences in terms of chemical affinities, these solvents have physical properties that can range over 2 orders of magnitude (in terms of viscosities and dielectric constants for instance), which reflects on CNC behaviors in suspension. Characterization techniques that involve a prerequisite (e.g., in terms of colloidal stability such as dynamic light scattering or rheology) cannot be employed over the full range of suspensions, which means that this dissertation often relies on qualitative data (pictures, microscopy) to yield quantitative results. This procedure is actually a standard in HSP characterization [127, 131]: the precision that is lost by using qualitative data can be retrieved by refining the mesh size in the areas of interest. Note that in the specific case of sedimentation tests, it would have been possible to retrieve quantitative data by the mean of a turbimeter and to fasten the process by using analytical centrifugation [172].

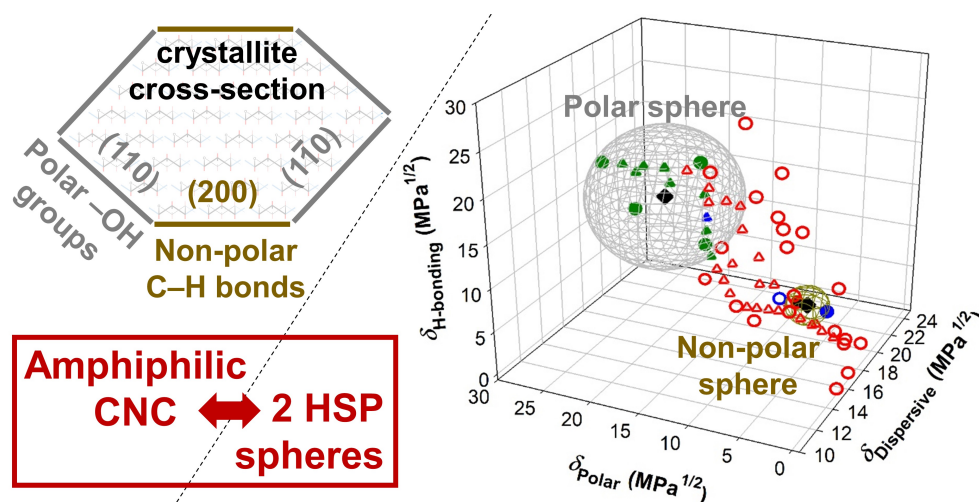


Figure 4.1 Graphical abstract of Article 1: *The structural amphiphilicity of cellulose nanocrystals characterized from their cohesion parameters* (Chapter 5). The amphiphilicity of CNC structure (left) translates into two distinct HSP spheres (right).

The first article [106] (Chapter 5), whose graphical abstract is displayed in Figure 4.1, probes the qualitative behavior of CNCs in 27 pure solvents (at  $10 \text{ mg}_{\text{CNC}}/\text{mL}_{\text{solvent}}$  and room temperature, plotted as circles). The paper distinguishes 3 main categories of solvents: CNCs either preserve their colloidal stability over time (clear suspensions, green symbols), aggregate without sedimentation (cloudy suspensions, blue symbols), or aggregate and sediment (clear suspensions with deposits at the bottom of the vial, red symbols). 32 additional binary mixtures (plotted as triangles in Figure 4.1) were used to refine the mesh size. Plotted in the 3-D HSP space, these 59 media highlight two areas of dispersibility in the polar and mildly non-polar regions of the graph. The corresponding HSP spheres were attributed to the influence of the polar (in grey) and non-polar (in yellow) surfaces of CNCs, respectively, and enabled for a quantitative characterization of CNC chemical affinity. This answers the first specific objective (“Determine the amphiphilic nature of cellulose nanocrystals and map their chemical affinity through HSP theory”).

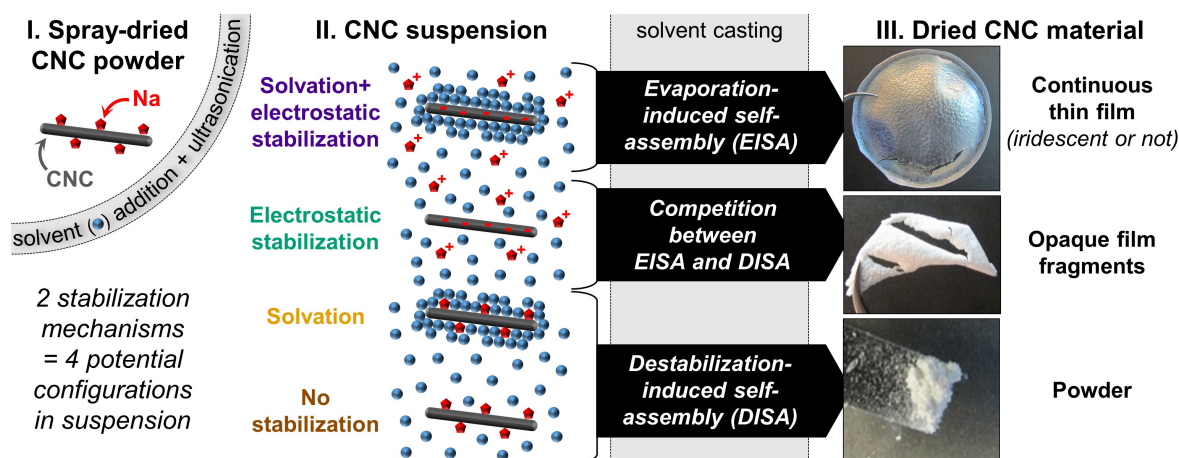


Figure 4.2 Graphical abstract of Article 2: *Self-assembly behaviors of colloidal cellulose nanocrystals: A tale of stabilization mechanisms* (Chapter 6). Upon dispersion in a solvent, CNCs may experience two different stabilization mechanisms: solvation-induced and electrostatic stabilizations. It corresponds to 4 combinations in suspensions, which lead to various outcomes upon solvent-casting: while strongly stabilized systems yield continuous thin films through EISA, lowly stabilized suspensions produce powders of agglomerates through DISA. Opaque film fragments are produced in systems where EISA and DISA are in competition.

The second article [173] (Chapter 6), whose graphical abstract is displayed in Figure 4.2, revisits the dispersion results of the first paper and analyzes the outcome of solvent casting in a set of 16 solvents and 23 binary mixtures. It focuses on CNC/solvent interactions (ionic dissociation of the Na<sup>+</sup> counter-ions –plotted as red pentagons–, and physical adsorption of solvent molecules –plotted as blue circles) and on their influences on CNC (plotted as grey rods) stabilization mechanisms in suspensions. Two stabilization mechanisms were found to

apply in suspensions: solvation-induced and electrostatic stabilizations, for which quantitative thresholds were established in terms of HSP distance,  $R_a$  (Equation 2.9), and dielectric constant,  $\epsilon$ , respectively. They lead to four potential scenarios: no stabilization (in brown on Figure 4.2), solvation-induced stabilization only (in yellow), electrostatic stabilization only (in green), or a combination of electrostatic and solvation-induced stabilizations (in purple). Strong levels of stabilizations (e.g., combination of electrostatic and solvation-induced stabilizations) lead to helical self-assembly during solvent-casting following a mechanism of evaporation-induced self-assembly (EISA). Aqueous CNC suspensions belong to this category. However, the lack of sufficient colloidal stability (e.g., solvation-induced stabilization only) leads to destabilization-induced self-assembly (DISA): a bulk aggregation process that yields either a powder or a glass-like gel. Intermediate levels of colloidal stability (e.g., electrostatic stabilization only) lead to a competition between EISA and DISA, which typically yields discontinuous opaque films. By categorizing the outcome of solvent-casting from solvent-parameters only ( $R_a$ ,  $\epsilon$ ), this article answers the second specific objective (“Correlate the CNC behavior in suspensions (dispersion and self-assembly) to solvent parameters only”).

At this stage, the overall influence of chemical affinity ( $R_a$ ) on the bulk behavior of CNCs is elucidated: significant physical adsorption prevents CNC sedimentation, which makes it a pre-requisite to colloidal stability. Physical adsorption alone is, however, not sufficient to trigger CNC helical self-assembly. It is coherent with SAXS analysis in aqueous suspensions, which demonstrates that the onset of self-assembly occurs for an interparticular distance of  $\sim 40$  nm [146], a range that is incompatible with solvation-induced stabilization. Electrostatic stabilization hence appears to be the dominant factor for EISA, which justifies that partial film formation is possible even in the lack of any solvation-induced self-assembly.

The last article (Chapter 7), whose graphical abstract is displayed in Figure 4.3, investigates the role of chemical affinity at air/water interfaces. It demonstrates the hypothesis that CNCs can orient their functionalities (polar in blue, or non-polar in yellow) at interfaces [98, 168] and proves its effect on the wettability of the films casted from these suspensions. Ethylene glycol contact angle ( $\theta^{\text{EG}}$ ) variations of up to  $\sim 30^\circ$  can be measured as a function of the solvent-casting protocol: while oven-cast films are amphiphilic, spin-coating leads to purely polar films (Figure 4.3). This article provides estimates for the surface tension parameters of both polar and non-polar surfaces of CNCs and demonstrate the role of CNC amphiphilicity on the stabilization of interfaces, which respectively completes SO1 and answers SO3 (“Demonstrate the role of the CNC amphiphilicity on the stabilization of interfaces”). It is worth considering that the level of amphiphilicity displayed by the films are expected to be influenced by the cross-sectional shape and hence the feedstock of the CNCs.



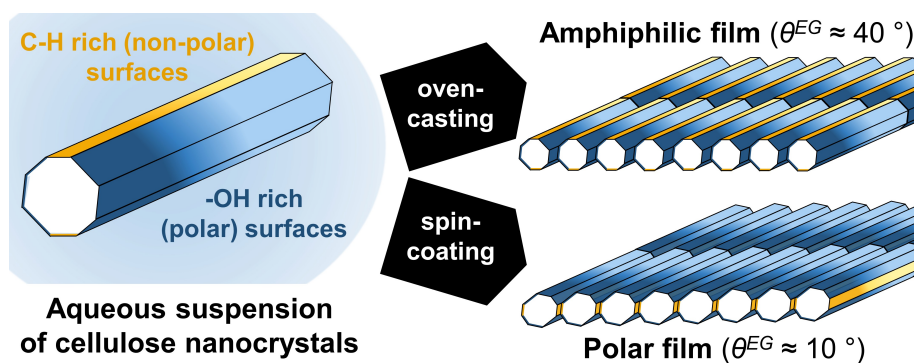


Figure 4.3 Graphical abstract of Article 3: *Orienting cellulose nanocrystal functionalities tunes the wettability of air/samples interfaces* (Chapter 7). The protocol influences CNC orientation at the air/sample interface and hence the wettability of the solvent-cast thin films.

Figures 4.1 and 4.3 plot hexagonal and octagonal cross-sections, respectively. A structural characterization of the CNCs used in this dissertation could not determine which cross-sectional shape was the most appropriate (see Appendix, section D.2). Since the exact cross-sectional shape of CNC particles remains debated (see Section 2.2.2), the shapes employed in Articles 1 and 3 reflect those employed in their respective literature: hexagonal as per Ding et al. [41, 64, 65] for Article 1, and octagonal as per Capron and co-workers [98, 161, 174] for Article 3. The potential influence of cross-sectional shape over our results is discussed in Article 3.

Besides the three articles presented here-above and discussed in this dissertation, this project contributed to 6 other publications (one of which was awarded), 12 oral presentations (one of which as invited speaker, 3 awards), and 6 poster presentations (2 awards). A list of the contributions and awards is provided in Appendix A.

## CHAPTER 5 ARTICLE 1: THE STRUCTURAL AMPHIPHILICITY OF CELLULOSE NANOCRYSTALS CHARACTERIZED FROM THEIR COHESION PARAMETERS

Charles Bruel, Jason R. Tavares, Pierre J. Carreau, and Marie-Claude Heuzey. The structural amphiphilicity of cellulose nanocrystals characterized from their cohesion parameters. *Carbohydrate Polymers*, 205 (2019) 184-191.

### Abstract

Cellulose nanocrystals (CNCs), usually considered as isotropically polar nanoparticles, are sheet-like crystalline assemblies of cellulose chains. Here, we link the anisotropy of the CNC structure to an amphiphilic behavior in suspension. The Hansen solubility parameters (HSP:  $\delta_D$ ;  $\delta_P$ ;  $\delta_H$ ) of wood-based  $H_2SO_4$ -hydrolyzed CNCs were measured from sedimentation tests in a wide set of 59 solvents and binary mixtures. Two sets of cohesion parameters corresponding to a polar surface  $(18.1; 20.4; 15.3) \pm (0.5; 0.5; 0.4) \text{ MPa}^{1/2}$  and to a mildly non-polar one  $(17.4; 4.8; 6.5) \pm (0.3; 0.5; 0.6) \text{ MPa}^{1/2}$  were determined, with respective solubility radii of 7.8 and 2.1  $\text{MPa}^{1/2}$ . The polar sphere is thought to correspond to the (110)&(1 $\bar{1}$ 0) surfaces of cellulose  $I_\beta$  nanocrystals, while the smaller non-polar sphere is coherent with the exposure of (200) surfaces. The HSP graph provides new insights on the amphiphilic nature of CNCs and a mapping of their chemical affinity for solvents and polymer matrices.

**Keyword:** cellulose nanocrystals; surface properties; structure-property relationships; chemical affinity; amphiphilicity; Hansen solubility parameters.

### 5.1 Introduction

D-glucopyranose polymerization produces, through a dehydration, polysaccharides such as starch, glycogen, dextran, and cellulose [175, 176]. In (1,4)-linked macromolecules, anhydroglucose rings are locked in a chair conformation where all their hydrophilic hydroxyl groups are in equatorial position while all their more hydrophobic C-H bonds are axial. For  $\alpha$ -(1,4)-linked polysaccharides, such as dextrans, it results in an apolar behavior in solution [175], a feature famously exploited in cyclodextrins whose structure forms a cavity rich in C-H bonds that may be used to encapsulate hydrophobic chemicals [177], including for delivery in living organisms [178].

Although being insoluble in water, amorphous cellulose, a  $\beta$ -(1,4)-linked polymer of anhydroglucopyranose (Fig. 5.1.a&b), does not display such a marked apolarity in solution [143, 175]. Its structural anisotropy, and its resulting amphiphilicity [143], are however reflected in the crystalline networks cellulose chains form in living organisms such as plants, fungi, algae, bacteria, or tunicates [23, 7]. From the various allomorphs [23, 175], cellulose  $I_\alpha$  [56] and  $I_\beta$  [21] are the only ones that may be found naturally in land plants [23]. They both reproduce on the nanocrystal level the anisotropy of their monomeric unit. Indeed, cellulose chains assemble in sheets, parallel to the equatorial planes of the anhydroglucose rings, which then stack up to form multilayer crystalline structures, crystallites (Fig. 5.1.c) [57, 66]. Intra and intersheet cohesions are respectively insured by interchain OH-O hydrogen bonds and by weaker interchain CH-O and van der Waals interactions [57, 179]. The formation of these van der Waals interactions is thought to be the initial step through which cellulose chains crystallize [180].

Hydrolysing cellulosic feedstocks in acidic conditions, usually with sulfuric acid, digests their amorphous and non-cellulosic contents while mostly preserving their crystalline parts [175, 23, 7]. Under harsh enough conditions, the treatment yields highly crystalline cellulose-made particles, cellulose nanocrystals (CNCs). They are hypothesized to be made of several adjacent crystallites [103, 64, 65] assembled with a right-handed chirality [181]. Introduction of sulfate half-ester groups at CNC surface during the hydrolysis provides them with an electrostatic stabilization upon suspension in water and with interesting self-organization properties [182, 7].

CNCs, especially sulfated ones, are usually described as polar particles, which stems from the difficulty encountered to disperse them in non-polar solvents and polymer matrices [7]. Although arising from experimental observations, this description is at odd with the amphiphilic behavior that can be expected from CNC anisotropic structure. Analysis of wide (WAXS) and small angle X-ray scattering (SAXS) [96, 97] as well as high resolution atomic force microscopy (AFM) (Ding et al., [41, 64, 65]) indeed suggests that up to three kinds of lateral surfaces are displayed by the nanocrystals extracted from cellulose  $I_\beta$  sources (Fig. 5.1.c), by far the most common allomorph in higher plants –wood included [62, 17]. Within the crystalline unit, they correspond respectively to the lattice planes (110), (1 $\bar{1}$ 0), and (200) [41, 46]. The latter, parallel to the sheets plane, displays mostly C-H bonds, while the two former intersect the plane of the sheets and thus display hydroxyl groups (Fig. 5.1.c). Molecular dynamic simulations suggests that (110) and (1 $\bar{1}$ 0) surfaces have similar hydrophilicity [107, 108] and surface energies [110], while (200) surfaces are expected to be more hydrophobic, with higher water contact angle [109] and lower surface energies [110] (Table 5.1).

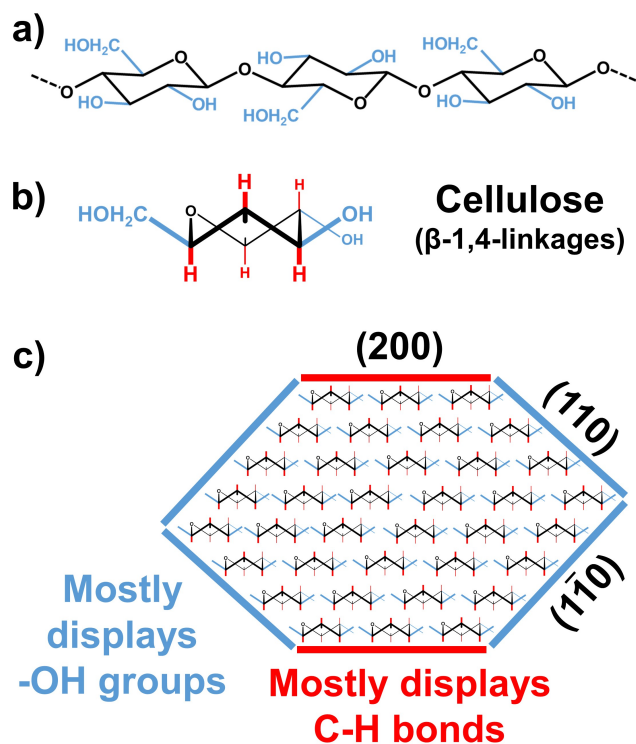


Figure 5.1 Anisotropy of cellulose. (a) Cellulose, a  $\beta$ -(1,4)-linked polymer of anhydroglucopyranose [176], has its monomeric units locked in a conformation where all their hydroxyl substituents (in blue) are in equatorial position while their C-H bonds (in red) are axial as exemplified in a profile view (b). (c) The structure of cellulose  $I_\beta$  crystallite reflects this anisotropy as cellulose chains are arranged in sheets held together by OH-O hydrogen bonds, which then stack-up through the formation of CH-O H-bonds and van der Waals interactions [57, 66]. Based on Ding and Himmel's model [41], the resulting crystallite displays up to three kind of surfaces corresponding to the lattice planes (110), ( $1\bar{1}0$ ), and (200) of its crystalline unit. The latter displays mostly C-H bonds, while the two former are rich in hydroxyl groups.

Chemically, a proof that CNCs display hydroxyl groups rich surfaces –which would correspond to the (110) and ( $1\bar{1}0$ ) lattice planes– may be provided easily by attempting to functionalize them [22]. Furthermore ( $1\bar{1}0$ ) lattice planes have already been observed by atomic force microscopy on cellulose  $I_\beta$  samples [183]. The detection of unreactive C-H bonds rich surfaces –which would correspond to the (200) lattice plane– is, however, harder to achieve. The main clue is that the display of (200) lattice planes by CNCs should result in a certain level of amphiphilicity, as experimentally confirmed : stable suspensions of CNCs in chloroform have been reported [155, 156]. This mildly non-polar solvent may also form inclusions in cellulose I fibers [184]. It is worth noting that not every work reports a good dispersion in chloroform [138, 185] and it remains to be seen whether this divergence has to be attributed to differences

Table 5.1 Cellulose nanocrystal surface properties according to the lattice plane displayed.  $\delta_T$  is the total solubility parameter.  $\delta_D$ ,  $\delta_P$ , and  $\delta_H$  are its decomposition in term of dispersive, polar, and hydrogen bonding components, respectively [127].  $R_0$  is the HSP radius.

Lattice plane		(110)	(1 $\bar{1}$ 0)	(200)
Surface energy <sup>a</sup>	mN m <sup>-1</sup>	155	155	92
Water contact angle <sup>b</sup>	°	43	-	95
$\delta_T$	MPa <sup>1/2</sup>	31.3±1.4		19.2±2.7
$\delta_D$	MPa <sup>1/2</sup>	18.1±0.5		17.4±0.3
$\delta_P$	MPa <sup>1/2</sup>	20.4±0.5		4.8±0.5
$\delta_H$	MPa <sup>1/2</sup>	15.3±0.4		6.5±0.6
$R_0$	MPa <sup>1/2</sup>	7.8		2.1

<sup>a</sup> Modeled values as calculated by Yamane et al. [110].

<sup>b</sup> Modeled values as calculated by Mazeau and Rivet [109].

in feedstock, hydrolysis conditions, or protocol of dispersion, such as the intensity of the ultrasonication for instance. Other hydrophobic interactions of cellulose include those with cellulases [186, 64] and congo red [187, 188, 189] whose aromatic parts are both thought to adsorb primarily on the (200) surfaces.

Although these preliminary results point toward a chemical influence of (200) surfaces for some CNC suspensions, thus conforming WAXS, SAXS, and AFM observations, none of them really isolate their potential contribution from the stronger influence of the (110) and (1 $\bar{1}$ 0) surfaces.

In this work, we apply a thermodynamic approach based on the Hansen solubility parameters (HSP) and on sedimentation tests using 59 solvents and binary mixtures, to isolate experimentally the influence of the hydrophobic (200) surfaces from the predominant one of the more hydrophilic (110) and (1 $\bar{1}$ 0) surfaces (as reported in Table 5.1). These investigations result into a mapping of CNC affinity for common solvents and polymers. The identification of an amphiphilic behavior for the nanocrystals establishes a direct link between their structure and their surface properties.

## 5.2 Materials and methods

### 5.2.1 Materials

CNCs, provided by Cellulforce (Montreal, QC, Canada) as a spray-dried powder, were obtained from Kraft wood pulp by a sulfuric acid hydrolysis treatment followed by a neutralization with sodium hydroxide (NaOH). Previous work from our team on CNCs from the same batch demonstrated that these particles are in average  $\sim 165$  nm long and  $\sim 13$  nm wide with

a sulfur content equivalent of 3.4 sulfate half ester ( $\text{O}-\text{SO}_3\text{H}$ ) per 100 anhydroglucose units [145]. The X-ray diffractogram is typical of  $\text{I}_\beta$  cellulose [96, 97] and the crystallinity index was found to be of 81 %.

To obtain the dimensions of the CNCs the following procedure was applied [145]. A drop of a sonicated water suspension of CNCs, diluted at  $10 \mu\text{g}_{\text{CNCs}} \text{ mL}_{\text{water}}^{-1}$ , was deposited on a copper TEM grid covered by a 5 to 6 nm-thick layer of pure carbon. Average dimensions, with standard deviations in the range of  $\pm 10\%$ , were obtained from measurements of over 100 particles performed on transmission electronic microscopy (TEM) micrographs obtained at 200 kV with a bright field imaging Jeol JEM 2100F [145]. The sulfur content was measured from X-Ray energy dispersive spectroscopy (EDX) analysis performed on the CNC spray-dried powder with a Tabletop Hitachi TM3030+ scanning electron microscope. Scanning of three samples on different locations, for a total of ten scans, yielded a sulfur over carbon (S/C) atomic ratio of 0.0057 with a standard deviation of  $\pm 0.0005$  [145]. The oxygen over carbon (O/C) atomic ratio was of  $0.79 \pm 0.02$ , very close to the theoretical value of 0.83 for cellulose, and is indicative of a high level of purity for the nanocrystals [190]. The CNC crystallinity was measured through X-ray diffraction (XRD) with a X'pert instrument (Philips) operating with  $\text{Cu K}\alpha$  radiations (wavelength of 0.1542 nm generated at 50 kV with a current of 40 mA). Scan type was continuous with an angle  $2\theta$  varying from  $5.01^\circ$  to  $49.99^\circ$  with steps of  $0.02^\circ$  and a scan time of 1 s per step. The crystallinity index,  $IC$ , was measured as  $IC = 1 - I_{\text{AM}}/I_{200}$ , according to Segal's empirical method [191].  $I_{\text{AM}}$  and  $I_{200}$  are the intensities of the amorphous peak ( $2\theta = 18.85^\circ$ ) and of the peak corresponding to the (200) lattice planes ( $2\theta = 23.01^\circ$ ), respectively.

Organic solvents employed were purchased from commercial suppliers at high purity grade (purity  $> 99\%$ , see Table B.1). The only exceptions are ethanol, used in its denatured form (purity of  $\sim 95\%$ ), and d-limonene (purity of  $\sim 96\%$ ), as higher purity grades of d-limonene are generally not available commercially. Distilled water was employed. Binary mixtures were prepared by mixing pure solvents. Densities and viscosities of solvents and mixtures at  $25^\circ\text{C}$  were obtained by averaging experimental values reported in the specialized literature (Tables B.1&B.2).

### 5.2.2 Sedimentation tests

**Protocol:** 10 mL of the different solvents and binary mixtures were added to 0.1 g of CNCs in a glass vials of radius 2.1 cm. An ultrasonic probe (Cole-Parmer) operating at a frequency of 20 kHz with a CV334 converter and a tapered microtip was used to disperse the CNCs. The treatment had a power of  $\sim 25$  W and was applied with a pulse cycle ON-OFF of 5 s–2 s for a

total energy of  $10,000 \text{ J g}_{\text{CNCs}}^{-1}$ . Previous experimentation demonstrated that such a treatment do not result into desulfation of the CNCs [145]. The vials were placed in an ice bath to avoid any overheating during the ultrasonication. CNC suspensions ( $10 \text{ mg}_{\text{CNCs}} \text{ mL}_{\text{solvent}}^{-1}$ ) were then allowed to rest at  $25^\circ\text{C}$  for a relative sedimentation time,  $RST = 1.18 \times 10^{11} \text{ s}^2\text{m}^{-2}$ . Calculated with Eq. 5.1 [127], it corresponds for instance to an absolute sedimentation time,  $t_{\text{sed}}$ , of 12.1 h in acetone, 48.0 h in water, or 1140 h in ethylene glycol (Tables B.1&B.2). Once the time of sedimentation had elapsed, three kinds of qualitative behaviors were observed for CNC sedimentation. Graded on a scale from best, 2, to worst, 0, they correspond respectively to: 2- a suspension without formation of any sediment (as shown in Fig. 5.2.a for DMSO), 1- a turbid suspension in which a sediment is formed (dichloromethane), and 0- all remaining cases in which a sediment is formed and the suspension is clear enough for text to be read through (toluene). The only exception to the aforementioned protocol is the sedimentation in triethanolamine, which was interrupted after a  $RST$  of  $1.18 \times 10^{10} \text{ s}^2\text{m}^{-2}$  (10% of the standard  $RST$ ). Due to the very high viscosity of triethanolamine, it corresponds to a time of sedimentation  $t_{\text{sed}}$  of 4100 h. Its behavior is clearly that of a 0-grade solvent (Fig. B.1).

$$t_{\text{sed}} = RST \frac{\eta_{\text{solv}}}{\rho_{\text{CNCs}} - \rho_{\text{solv}}} \quad (5.1)$$

***RST* calibration:** Sulfating CNCs provides them with surface charges, generating electrostatic stabilization. It is a kinetic effect: the thermodynamically favored outcome of a colloidal suspension is the coagulation of the particles [120]. For electrostatic stabilization to manifest, there has to be dissociation between the negatively charged CNCs and their counter-ions, an outcome favored in solvents whose dielectric constants,  $\epsilon_{\text{solv}}$ , are high [120]. HSP characterization is a thermodynamic approach and a  $RST$  of  $1.18 \times 10^{11} \text{ s}^2\text{m}^{-2}$  was selected following a calibration aimed at minimizing the influence of such kinetic effects on the sedimentation results.

At low  $RST$ , sedimentation results were strongly correlated with the dielectric constants of the solvents (Table B.1). Quickly, a discrimination however appeared among highly dielectric solvents and, at a  $RST$  of  $5.9 \times 10^{10} \text{ s}^2\text{m}^{-2}$ , we were already able to hint “good” solvents from “poor” ones independently of their dielectric constant. At  $RST = 1.18 \times 10^{11} \text{ s}^2\text{m}^{-2}$ , results were no longer correlated with the dielectric constants. Highly dielectric solvents like methanol ( $\epsilon_{\text{solv}}=33.0$ ), ethylene glycol (41.4), DMF (38.3), or propylene carbonate (66.1) received the grade 0, while DMSO (47.2) or ethanolamine (31.9) were at 2. The state of sedimentation at  $RST = 1.18 \times 10^{11} \text{ s}^2\text{m}^{-2}$  was found to be meta-stable as increasing the  $RST$  beyond  $1.18 \times 10^{11} \text{ s}^2\text{m}^{-2}$  no longer affects the results. Vials were kept for months and

in volatile media such as chloroform and dichloromethane, the solvent was fully evaporated before any significant change in the suspension turbidity could be observed. It does not mean that the electrostatic stabilizing effect is no longer felt at  $RST = 1.18 \times 10^{11} \text{ s}^2\text{m}^{-2}$ , but that electrostatic stabilization alone is no longer sufficient to prevent sedimentation at this point. For particles to remain in suspension at high  $RST$ , and whatever the level of electrostatic stabilization, there has to be a certain level of chemical affinity. It is this chemical affinity that the HSP analysis seeks to capture.

### 5.2.3 Thermodynamic approach - Hansen solubility parameters

**Background:** Initially developed to address the issue of the dispersibility of the various components of paints, solubility -or cohesion- parameters theory aims at quantifying the cohesive energy density (taken equal to  $\delta_T^2$ , MPa) between a chemical and its neighboring media [124, 125, 127]. Hansen proposed to split the total cohesion parameter,  $\delta_T$ , into its three main components resulting from the London dispersion forces ( $\delta_D$ ), the dipole-dipole interactions ( $\delta_P$ ), and hydrogen bonding interactions ( $\delta_H$ ) [192, 193, 126, 127]. The linearity of the decomposition in terms of energies means that  $\delta_T$  square may then be written as the sum of the squared HSP (Eq. 5.2). In the HSP theory, every chemical may be represented by a triplet ( $\delta_D$ ,  $\delta_P$ ,  $\delta_H$ ), and then be plotted in a 3 dimensional graph [127]. HSP values of solvents may be determined directly experimentally or estimated by group contribution methods and are now tabulated, alongside those of many commodity polymers [126, 127, 131]. Gardebjer et al. [194] used one of these group contribution methods to estimate the HSP of cellulose's repeating unit, cellobiose. They computed a value of  $(\delta_D, \delta_P, \delta_H) = (16.3; 16.2; 20.7) \text{ MPa}^{1/2}$  and assumed it to be the HSP values of CNCs [194]. Although it provided a quick and easy estimate, the method is unsatisfactory as it does not take into account the fact that polymer HSP are almost systematically greater than those of their repeating units, nor the fact that crystallinity may greatly affect HSP values [127, 131]. Unknown HSP may be determined more accurately through an indirect approach. Affinity tests between the material and various solvents are conducted with the idea that, “like seeking like”, the stronger are the interactions the shorter is the distance,  $R_a$  ( $\text{MPa}^{1/2}$ , Eq. 5.3), between their respective Hansen solubility parameters [127]. “Good” solvents, where the “goodness” may be assigned quantitatively (e.g. maximum solubility) or qualitatively (e.g. suspension turbidity or swelling behavior), thus describe a sphere of radius  $R_0$  ( $\text{MPa}^{1/2}$ ), whose center corresponds to the unknown's HSP [127]. The set of solvents may be completed by mixtures [195]. Their HSP ( $\delta_{D,\text{mix}}$ ;  $\delta_{P,\text{mix}}$ ;  $\delta_{H,\text{mix}}$ ) can be calculated through Eq. 5.4 [127], in which ( $\delta_{D,i}$ ;  $\delta_{P,i}$ ;  $\delta_{H,i}$ ) are the HSP values of the constituent  $i$  and  $\Phi_i$  its volume fraction;  $n$  is the total number of solvents in the mixture.



$$\delta_T^2 = \delta_D^2 + \delta_P^2 + \delta_H^2 \quad (5.2)$$

$$R_a^2 = 4(\delta_{D,1} - \delta_{D,2})^2 + (\delta_{P,1} - \delta_{P,2})^2 + (\delta_{H,1} - \delta_{H,2})^2 \quad (5.3)$$

$$\delta_{D,\text{mix}} = \sum_{i=1}^n \Phi_i \delta_{D,i} ; \delta_{P,\text{mix}} = \sum_{i=1}^n \Phi_i \delta_{P,i} ; \delta_{H,\text{mix}} = \sum_{i=1}^n \Phi_i \delta_{H,i} \quad (5.4)$$

Our set of solvents was selected based on their position in the HSP graph to maximize the coverage and based on the uncertainty of the solvents' HSP coordinates. Indeed, the precision of the coordinates determined indirectly through the fitting of a HSP sphere is limited by that of the solvents that are employed to perform the characterization. Historically, HSP coordinates were determined experimentally for a set of 90 common solvents, from which group contribution models have been derived [127]. Nowadays, and based on these group contribution methods, HSP of thousands of solvents have been calculated [127, 131]. When we selected our 27 pure solvents, we aimed at picking them from the list of the 90 experimentally confirmed solvents. Exceptions to the list are ethyl benzoate, heptane, d-limonene, triethanolamine, and water. Water, with its three sets of HSP, is a special case [127]). Heptane, being purely dispersive, has a low uncertainty (uncertainty arises mostly from the calculation of the polar and hydrogen-bonding components:  $\delta_P$  and  $\delta_H$ , respectively) [131]. Ethyl benzoate, d-limonene, and triethanolamine HSP values have been calculated, rather than empirically determined, inducing a greater uncertainty. They were nonetheless selected for their interesting position in the HSP graph.

**HSP analysis:** HSP analysis was performed with the software HSPiP [131]. HSP values of pure solvents, binary mixtures, and polymers, were extracted from the HSPiP database [131] and are respectively provided in Tables B.1, B.2, and B.3.

For the sphere fitting, we considered both grade 1 and grade 2-solvents (and mixtures) to be “good” and grade 0-ones to be “poor”. The algorithm of the software maximizes the function *FIT* described below (Eq. 5.6) [127, 131]. The ideal result is a sphere of center  $(\delta_{D,s} ; \delta_{P,s} ; \delta_{H,s})$  and of radius  $R_0$  that contains all the “good” solvents and mixtures while excluding any “poor” ones. A solvent/mixture is located in the sphere if its distance to the sphere's center,  $R_a$  (Eq. 2), is smaller than or equal to  $R_0$ . It corresponds to a reduced energy difference  $RED \leq 1$  (Eq. 5.5).

$$RED = R_a/R_0 \quad (5.5)$$

The quality of the fitting may be assessed through the *FIT* value and through the uncertainty on the  $(\delta_{D,s}; \delta_{P,s}; \delta_{H,s})$  coordinates [127, 131]. *FIT* (Eq. 5.6) is a desirability function [127] that provides information about the quality of the fit on the  $m$  solvents tested : indeed, a “poor” solvent/mixture located inside a sphere ( $RED \leq 1$ ) or a “good” one located outside ( $RED > 1$ ) induces a penalty on the *FIT* coefficient. The better the fit, the closest *FIT* will be from 1.0 ( $FIT \leq 1.0$ ). The uncertainty “ $\pm(\Delta\delta_{D,s}; \Delta\delta_{P,s}; \Delta\delta_{H,s})$ ” provides information on the tightness of the HSP sphere core’s position. Values in the range of  $\pm 0.25$ - $0.50 \text{ MPa}^{1/2}$  are indicative of a very good fit and of a tight core, while a poor fit will result in uncertainties in the range of  $\pm 1 \text{ MPa}^{1/2}$  [131]. It is possible to have a tight core for two parameters and a loose one for the last, meaning that there is a lack of data points in that direction [131]. It has to be noted that fitting a sphere on less than 4-5 good solvents necessarily leads to an uncertainty that may not be reflected in the *FIT* value nor in the “ $\pm(\Delta\delta_{D,s}; \Delta\delta_{P,s}; \Delta\delta_{H,s})$ ”. The existence of an uncertainty means that results obtained in running several times the algorithm on the same data differ slightly. Results reported here are those corresponding to the highest *FIT* value and the lowest uncertainty over at least 10 runs of the fitting algorithm. The values were overall very stable between the different fits with variations in the range of 0.001 for *FIT* and of  $\sim 0.05 \text{ MPa}^{1/2}$  for the different uncertainties: “ $\pm(\Delta\delta_{D,s}; \Delta\delta_{P,s}; \Delta\delta_{H,s})$ ”.

$$FIT = \left( \prod_{i=1}^m A_i \right)^{1/m}$$

For “good” solvents inside a sphere :  $A_i = 1$

For “poor” solvents outside a sphere :  $A_i = 1$

For “good” solvents outside a sphere :  $A_i = e^{+(R_0 - R_a)}$

For “poor” solvents inside a sphere :  $A_i = e^{+(R_a - R_0)}$

(5.6)

### 5.3 Results and discussion

Considering both grade 2 and 1 as “good” solvents, two distinct regions of preferential dispersibility may clearly be distinguished. The first is in the polar region of the graph (high  $\delta_P$  and  $\delta_H$ , Fig. 5.2.c) and contains all of the grade 2 solvents: dimethylsulfoxide (DMSO), formamide, water, and ethanolamine. The area delimited by these solvents is bordered by 0-grade ones like triethanolamine, propylene carbonate, N,N-dimethylformamide, or acetone. A second distinct region may then be distinguished in the mildly non-polar region (intermediate  $\delta_P$  and  $\delta_H$ ) where chloroform and dichloromethane are classified as grade 1 and stand

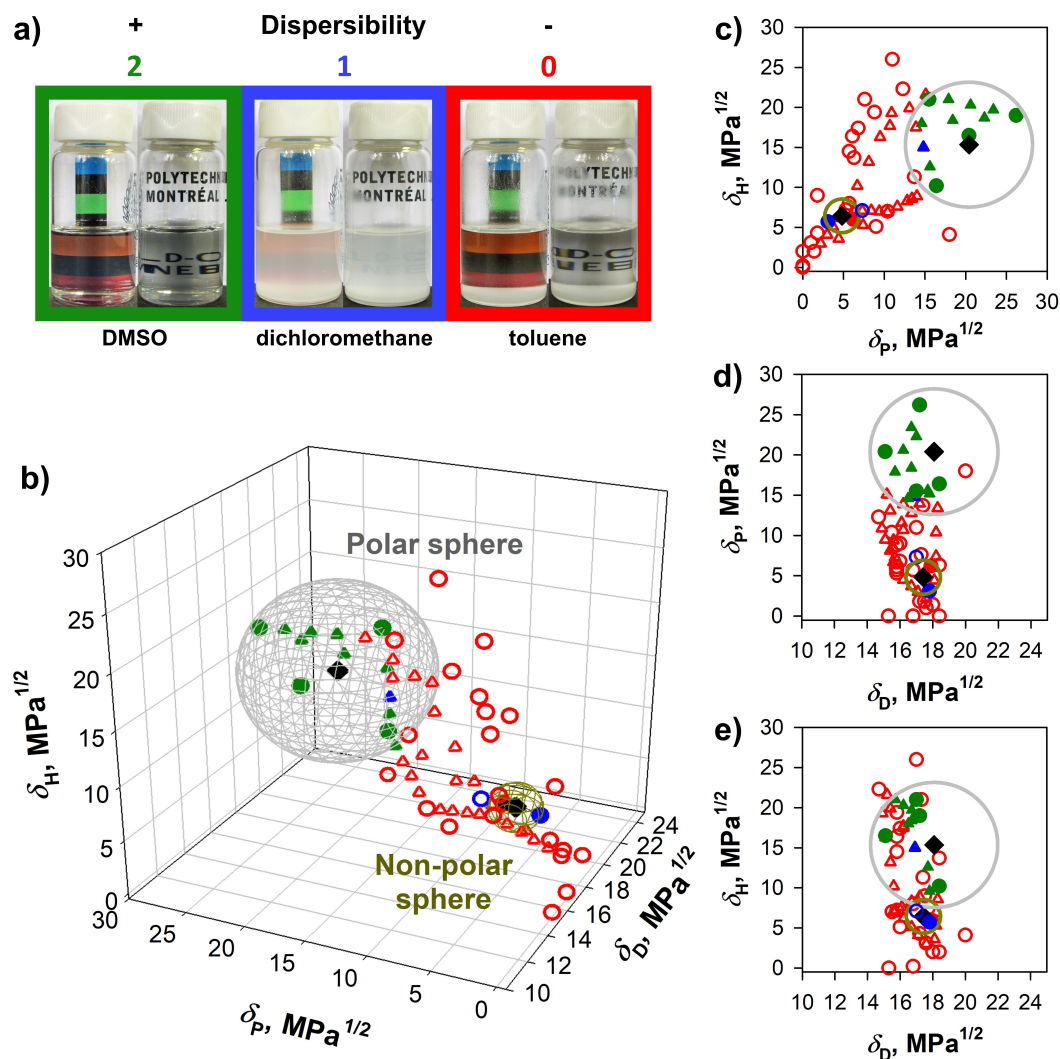


Figure 5.2 HSP graph of wood-based sulfuric acid-hydrolyzed CNCs. **(a)** CNC scale of dispersibility. Three different grades were attributed to the CNC state of dispersion, from best to worst: 2-in green-No sediment at the bottom of the vial, 1-in blue-Presence of a sediment, the suspension is too turbid to be able to read a text through, 0-in red-Presence of a sediment, the suspension is less turbid/clear. Pure solvents are represented by circles, binary mixtures by triangles, sphere centers by black diamonds. Two different spheres may be plotted : a large polar sphere ( $\delta_D; \delta_P; \delta_H$ ) = (18.1; 20.4; 15.3)  $\pm$  (0.5; 0.5; 0.4)  $\text{MPa}^{1/2}$  and another smaller sphere in the mildly non-polar region ( $\delta_D; \delta_P; \delta_H$ ) = (17.4; 4.8; 6.5)  $\pm$  (0.3; 0.5; 0.6)  $\text{MPa}^{1/2}$ . Symbols located inside a sphere are full and symbols outside are empty. The HSP graph is represented in a 3-dimensional view **(b)**, and in 2-dimensional views alongside the planes  $\delta_H$ - $\delta_P$  **(c)**,  $\delta_P$ - $\delta_D$  **(d)**, and  $\delta_H$ - $\delta_D$  **(e)**.

alone surrounded by poor solvents. This behavior, with two distinct regions, is expected in the HSP theory for amphiphilic species such as particles or block copolymers for instances [127]. In this configuration, two HSP spheres, which correspond to the different affinities of the chemical, may be drawn.

For a better HSP fit, sedimentation tests were performed for binary mixtures of DMSO + acetone, toluene, and methanol, and binary mixtures of formamide + methanol and 1-propanol. Results obtained with binary mixtures validate our scale of dispersibility as the “goodness” of a grade 2 solvent like DMSO decreases to grade 1 once 40 vol% of methanol, a grade 0 solvent, is added and then to 0 beyond 60 vol% (Fig. B.2.b&e). DMSO is known to be one of the best solvent for CNCs dispersion as it enables strong gel formation upon heating [154].

Using HSPiP (Hansen Solubility Parameters in Practice) software [131], it was possible to obtain a well defined sphere ( $FIT = 1.0$ , see Eq. 5.6) of radius  $R_{0,P}=7.8\text{MPa}^{1/2}$  in the polar region. It includes 13 good solvents and mixtures while excluding any poor ones. Its center’s coordinates ( $\delta_D$ ;  $\delta_P$ ;  $\delta_H$ ) are  $(18.1; 20.4; 15.3) \pm (0.5; 0.5; 0.4) \text{MPa}^{1/2}$  for a  $\delta_T$  of  $31.3 \pm 1.6 \text{MPa}^{1/2}$ . Having defined with precision what stands clearly for the dominant affinity of CNCs, the case of chloroform and dichloromethane may be addressed. These results are concordant with reports by Yu et al. of stable suspensions of sulfuric acid hydrolyzed CNCs in chloroform [155, 156]. A fitting in this area of the graph yields a  $FIT$  of 0.974 with a sphere of radius  $R_{0,P}=2.1\text{MPa}^{1/2}$  and centered about  $(\delta_D; \delta_P; \delta_H) = (17.4; 4.8; 6.5) \pm (0.3; 0.5; 0.6) \text{MPa}^{1/2}$ . It corresponds to a  $\delta_T$  of  $19.2 \pm 2.7 \text{MPa}^{1/2}$ . Here, the  $FIT$  value is lowered by ethyl benzoate, which is a 0-grade solvent despite having HSP close to that of dichloromethane and chloroform. It is not clear whether it highlights a limitation of the HSP method itself –as we know that conformation effects for instance are not accounted for in HSP theory– or a limitation of the HSP group contribution models. Ethyl benzoate is indeed among the few solvents we employed whose HSP were calculated without any experimental confirmation [127]. It may thus be that the  $FIT$  value is only lowered by imprecise solvent coordinates: ethyl benzoate while being plotted as inside of the non-polar sphere (Fig. 2) may actually be out of it. From the 90 solvents experimentally proofed by Hansen and co-workers [193, 192, 126], and aside from chloroform and dichloromethane, none is located in the area of interest, meaning that this issue cannot be settled easily with the current experimental method. Fitted using only two good solvents, the position of the non-polar sphere thus has to be considered with caution. It however provides the first experimental estimates of CNC hydrophobic surface HSP.

The polar sphere is considered to correspond to the HSP of the hydroxyl rich (110) and ( $1\bar{1}0$ ) surfaces. Computer simulations indeed predicts that (110) and ( $1\bar{1}0$ ) surfaces have similar surface energies [110] and hydrophilicity [107, 108], which means that they are expected to be represented by a single HSP sphere (Table 5.1). Meanwhile, the mildly non-polar sphere is attributed to the display of (200) surfaces by the nanocrystals. Their lower simulated surface energy [110] and higher modeled water contact angle [109] are indeed expected to result into a distinct HSP sphere.

The contrast between the better fit and wider radius of the polar sphere and the lesser ones of the non-polar sphere is coherent with the fact that sulfuric acid hydrolyzed CNCs have been reported to exhibit experimentally a predominant polar and hydrophilic behavior. HSP of the polar sphere are furthermore very close to those obtained for the chemical accessibility of cellulose :  $(\delta_D; \delta_P; \delta_H) = (19.09; 15.77; 15.29) \pm (0.15; 0.25; 0.30) \text{ MPa}^{1/2}$  [129, 134, 133]. These are calculated from the ability of different solvents to swell cotton-based  $I_\alpha$  cellulose pulp. Swelling increases the active surface area of the pulp by increasing hydroxyl group accessibility, the amount of which is quantified chemically through a thallation of the -OH functions [133]. The only significant deviation lies in  $\delta_P$ , the polar component, that is increased by  $+4.6 \text{ MPa}^{1/2}$  from the chemical accessibility of cellulose HSP to our polar sphere's results. Slight variations in  $\delta_D$  and  $\delta_H$ , coupled to a sharp increase in  $\delta_P$  are coherent with the effect of surface sulfatation based on the predictions of HSP group contributions [196]. The  $\delta_P$  increase for CNCs with respect to the cotton-based pulp is thus attributed to the introduction of sulfate groups on the hydroxyl groups of the nanocrystal surfaces during the sulfuric acid hydrolysis [16, 7]. Part of this variation is also probably imputable to the difference in wettability between  $I_\alpha$  and  $I_\beta$  hydroxyl-rich surfaces, although simulations predict very similar surface energies with  $154 \text{ mN m}^{-1}$  and  $155 \text{ mN m}^{-1}$ , respectively [110].

It is worth noting that this shift of  $+4.6 \text{ MPa}^{1/2}$  in  $\delta_P$  reduces the HSP distance of CNCs with water from  $\sim 9.3 \text{ MPa}^{1/2}$  to  $\sim 6.1 \text{ MPa}^{1/2}$ , which may be able to partly explain the increased affinity of sulfated CNCs for water. As contact angles have usually been found experimentally to be positively correlated with HSP distance [127], this finding is also coherent with the water contact angle value obtained by simulation by Mazeau and Rivet [109]. The  $43^\circ$  of the (110) surface corresponds to a HSP distance of  $\sim 6.1 \text{ MPa}^{1/2}$ , while the  $95^\circ$  of the (200) surface corresponds, based on our results, to a HSP distance of  $\sim 19.1 \text{ MPa}^{1/2}$ .

From our knowledge of the CNC structure, it is thus possible to assign each of the spheres to a lattice plane, which enables us for the first time to estimate the amphiphilicity of wood-based sulfated CNCs. Our results also highlight the limitations of group contribution methods to estimate cellulose nanocrystal HSP. Given that they do not take into account

conformation effects, computations by Gardebjer et al. [194] were not able to predict a second non-polar sphere for CNCs. If we compare their results to those of our polar sphere, they also underestimated  $\delta_D$  and  $\delta_P$  by  $1.7 \text{ MPa}^{1/2}$  and  $4.2 \text{ MPa}^{1/2}$ , respectively, which is not unexpected when HSP of a polymer are compared to those of its repeating unit [127]. The hydrogen bonding component,  $\delta_H$ , was however overestimated by  $5.4 \text{ MPa}^{1/2}$  [194]. It may probably be attributed to the incapacity of group contribution method to predict the formation of intramolecular interactions. Hydrogen bonds are indeed known to play a role in cellulose crystalline networks [57, 55] and the involvement of cellulose's -OH groups in intramolecular H-bonds may thus reduce their ability to form H-bonds with the surrounding media.

The amphiphilicity of cellulose chains has recently been advanced as a key-factor to explain the low solubility of cellulose chains in polar solvents [143]. This parameter was not considered by Hansen and Björkman [129] when they worked on wood ultrastructure and cellulose affinity. While Fig. 5.2 provides experimental evidence for this amphiphilicity, we believe that due to the high dependency of HSP with conformation effects, such as those induced by crystallinity [127, 131], any extrapolation from crystalline to amorphous cellulose has to be considered with great caution. Our interest in HSP instead lies in their ability to represent in a same graph –thus enabling comparisons– chemicals of very different scales, from solvents to polymers, (nano)particles, and macro-scale surfaces. Determining HSP of cellulose nanocrystals, based on their behavior in a set of solvents, may thus provide information about their affinity for polymer matrices. HSP of some common polymer matrices, such as poly(vinyl alcohol) (PVOH), poly(lactic acid) (PLA), poly(ethylene glycol) (PEG), poly(methyl methacrylate) (PMMA), poly(ethylene) (PE), and poly(propylene) (PP), are available [131] and are plotted in the Fig. 5.3. It is worth pointing out that the HSP values of polymers are notably functions of their molecular weight and degree of crystallinity [127, 131] and the parameters employed here are average values as provided in the HSPiP polymer dataset [131]. These polymers may be split into 3 groups based on their HSP: I-in the polar sphere (PVOH), II-in between the spheres (PEG, PLA, PMMA) and III-in the non-polar region (PE and PP). CNC-polymer affinity is not the only factor at play for CNC dispersion in polymer matrices.

The protocol employed (melt mixing or solvent casting) has, for instance, a major influence [197, 198]. Assuming that the quality of CNC dispersion in the solvent is important for solvent casting, then other parameters such as the "goodness" of the solvent (Fig. 5.2), the initial state of CNCs [145, 137] –the use of never-dried, freeze-dried, or spray-dried–, and the protocol employed for the dispersion –such as ultrasonication conditions [199]– are also relevant. Keeping these points in mind, it is striking how these polymer-categories (I, II, and

III), based solely on HSP, match with the experimental quality reported for the dispersion of sulfuric acid-hydrolyzed CNCs in the aforementioned matrices: PVOH has been reported to be one of the best matrices for CNC dispersion both in solvent casting and melt mixing [7], which is coherent with it being in the dominant polar sphere of CNCs. A good dispersion of CNCs is also achievable in PLA [200, 197, 198], PEG [199, 201, 202, 203, 204], and PMMA [205] through a solvent casting. Direct melt mixing may however remain difficult for this group II-polymers as in the case of PLA [206, 207, 208, 198].

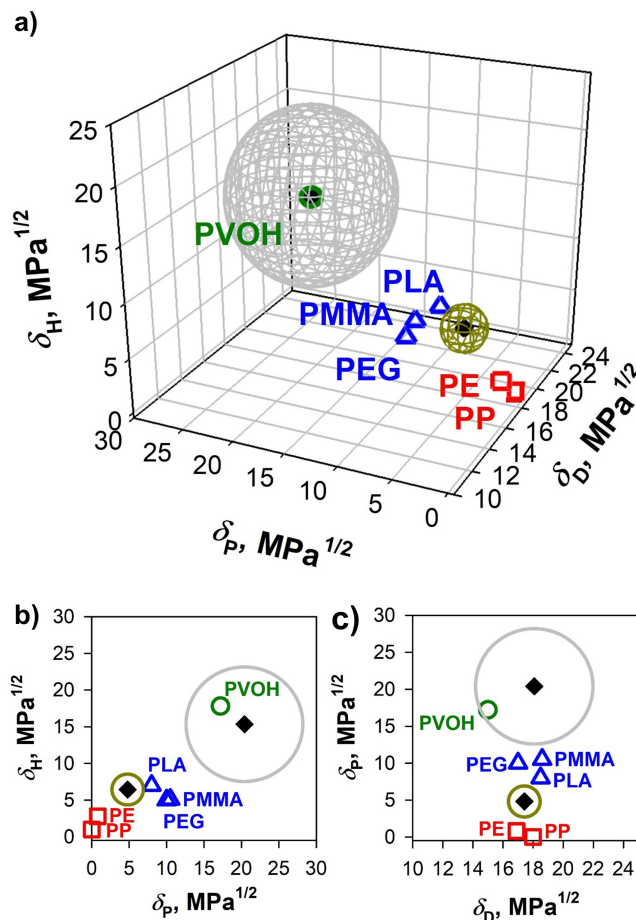


Figure 5.3 HSP graph of wood-based sulfuric acid hydrolyzed CNCs (see Fig. 5.2) compared to some commodity polymers. These polymers may be split into 3 groups based on their HSP [131]: I-green circles-in the polar sphere for poly(vinyl alcohol) (PVOH); II-blue triangles-in between the spheres for poly(lactic acid) (PLA), poly(ethylene glycol) (PEG), and poly(methyl methacrylate) (PMMA); and III-red squares-in the non-polar region for poly(ethylene) (PE), and poly(propylene) (PP). Categories I, II, and III match, from best to worst, with experimental reports for the dispersibility of CNCs in these matrices. The HSP graph is represented in a 3-dimensional view (a), and in 2-dimensional views alongside the planes  $\delta_H$ - $\delta_P$  (b), and  $\delta_P$ - $\delta_D$  (c).

Dhar et al. [208] demonstrated that the sulfatation of CNC surfaces lessens their dispersibility in PLA matrices, which is consistent with our HSP results: the shift of  $\sim +4.6 \text{ MPa}^{1/2}$  in the  $\delta_P$  of the polar sphere between sulfated CNCs and chemically accessible cellulose increases the distance between the PLA matrices and the (110) and (1 $\bar{1}$ 0) surfaces' sphere from  $\sim 11.4$  to  $\sim 15.0 \text{ MPa}^{1/2}$ . Based on the HSP theory, the absence of any adsorption of PEG on CNC surfaces [199, 209] is also coherent with this polymer being out of any sphere, adsorption being only expected for compounds of very similar HSP [130]. Modification of the nanocrystal OH groups, which is expected to result in a shift of the corresponding surfaces HSP sphere [137, 138], may significantly improve the CNC dispersion and the reinforcing effect in group II-matrices [206, 205, 200, 207]. It is likely that a systematic HSP characterization of the modified CNCs would have concluded that any chemical modification that improves the CNC dispersion in a matrix also reduces the HSP distance between the polar sphere and this matrix, as in the case of Peng et al. [139]. In group III-matrices such as PP [210, 211] and PE [212, 213], nanoscale dispersion in melt compounding seems to be impossible without the use of a compatibilizer. While unmodified nanocrystals have an interfacial tension with PP more than fourfold that with PLA, surface modification may, here again, shift the relative affinity of CNCs and make dispersion more favorable in PP with a slightly lower interfacial tension [211]. Probably due to the low solubility of these polymers in common solvents [127], no experimental data are available for the solvent casting of these PP and PE nanocomposites.

#### 5.4 Concluding remarks

In conclusion, we linked CNC dispersibility in a large set of solvents and binary mixtures to the anisotropy of the nanocrystal structure. Wood-based sulfuric acid-hydrolyzed CNCs were found to be predominantly polar particles with a main HSP sphere of radius  $7.8 \text{ MPa}^{1/2}$  and of center  $(\delta_D ; \delta_P ; \delta_H) = (18.1; 20.4; 15.3) \pm (0.5; 0.5; 0.4) \text{ MPa}^{1/2}$ . This main behavior is thought to reflect the influence of their hydroxyl-rich (110) and (1 $\bar{1}$ 0) surfaces and is coherent with their behavior described in the literature. While predicted years ago through simulations and expected based on cross-sectional structure analysis of the nanocrystals through X-ray scattering and AFM techniques, this study is the first to experimentally confirm the contribution of hydrophobic surfaces to the behavior of CNCs in suspensions. We provide an approximation of their chemical influence through the determination of their Hansen solubility parameters (HSP). Although refinements are still necessary, as based only on two good solvents, the non-polar sphere location is estimated in the range of  $(17.4; 4.8; 6.5) \pm (0.3; 0.5; 0.6) \text{ MPa}^{1/2}$  with a radius of  $2.1 \text{ MPa}^{1/2}$ . This position, relatively to that of the polar sphere, is coherent with results from computer simulations for the display of (200)



lattice planes by the CNC particles. Further work is required to determine the influence of the feedstock, of the hydrolysis conditions, and of the dispersion protocol on the display of an amphiphilic behavior by CNCs.

HSP graphs are a useful tool to predict the CNC dispersion in polymer matrices and allow us a better understanding of results already published in the literature. Such characterization could be carried out on functionalized particles to understand the effect of the chemical modification on the surface properties of the nanocrystals [138, 137] and on their dispersibility [139] in non-polar media.

### **5.5 Conflicts of interest**

There are no conflicts to declare

### **5.6 Acknowledgments**

The authors acknowledge the financial contributions of FPIInnovations (Pointe-Claire, QC, Canada), of PRIMA Québec (grant number FPI NCC RD001), and of the National Science and Engineering Research Council (NSERC, grant number RDCPJ 490786-15). The Fond de Recherche du Québec - Nature et Technologies (FRQNT) kindly provided C. Bruel with a scholarship (number 208324). Celluforce (Montréal, QC, Canada) is also gratefully acknowledged for providing the cellulose nanocrystals. The authors would like to thank Dr. W. Y. Hamad, from FPIInnovations, for his contribution in reviewing this work. We are grateful to Dr. Q. Beuguel for his contribution to the TEM and EDX analyses. Finally, Mr. J.-P. Masse is acknowledged for his help with the XRD analysis.

## CHAPTER 6 ARTICLE 2: SELF-ASSEMBLY BEHAVIORS OF COLLOIDAL CELLULOSE NANOCRYSTALS: A TALE OF STABILIZATION MECHANISMS

Charles Bruel, Tom S. Davies, Pierre J. Carreau, Jason R. Tavares, and Marie-Claude Heuzey. Self-assembly behaviors of colloidal cellulose nanocrystals: A tale of stabilization mechanisms. *Journal of Colloid and Interface Science*, 574 (2020) 399-409.

### Abstract

**Hypothesis:** In solvent casting, colloidal nanocrystal self-assembly patterns are controlled by a mix of cohesive and repulsive interactions that promote destabilization-induced self-assembly (DISA) or evaporation-induced self-assembly (EISA). Tuning the strength and nature of the stabilization mechanisms may allow repulsive interactions to govern self-assembly during the casting of colloidal cellulose nanocrystal (CNC) suspensions.

**Experiments:** We propose a tool to classify the level of electrostatic and solvation-induced stabilizations based on two solvent parameters only: dielectric constant,  $\varepsilon$ , and chemical affinity for CNCs, in terms of Hansen Solubility Parameters,  $R_a$ . These criteria are applied to study CNC self-assembly in solvent casting experiments in various media and binary mixtures.

**Findings:** In solvent casting of suspensions stabilized through a combination of electrostatic and solvation effects the primarily governing mechanism is EISA, which leads to the formation of chiral nematic domains and optically active thin films. In electrostatically-stabilized suspensions, EISA and DISA are in competition and casting may yield anything from a continuous film to a powder. In other suspensions, DISA prevails and evaporation yields a powder of CNC agglomerates. By classifying media according to their stabilization mechanisms, this work establishes that the behavior of CNC suspensions in solvent casting may be predicted from solvent parameters only.

**Keyword:** cellulose nanocrystal suspensions; self-assembly; colloidal stability; evaporation; destabilization; solvent casting.

## 6.1 Introduction

Self-assembly of colloidal nanocrystals has the potential of yielding highly ordered superlattices and networks with unique electronic, optical, and electromagnetic properties [160]. In the case of hard-core particles, the self-assembly process is governed by a mix of attractive weak forces (e.g., van der Waals, electrostatic, or H-bonding) and repulsive hard particle interactions, such as excluded volume [160]. Stabilization mechanisms create long-range repulsive interactions between nanoparticles that prevent the system from immediately agglomerating, thus favoring the formation of complex self-assemblies [160, 120].

For stabilized suspensions (in which repulsive interactions are dominant), the two main mechanisms for self-ordering are evaporation-induced self-assembly (EISA) and destabilization-induced self-assembly (DISA). EISA is a 2-D mechanism for self-ordering that is governed by repulsive interactions upon the unidimensional volume contraction of the suspension, typically between an air/liquid interface and a support [160]: it usually yields a thin film. DISA is a 3-D mechanism that occurs in the bulk of the suspension when a slow decrease in the stabilization mechanisms' efficiency shifts the balance in favor of cohesive interactions. This leads to the nucleation of agglomerates, which may or may not be able to ultimately coalesce into a single structure [160], and usually yields a powder of nanocrystals or a single larger 3-D structure (e.g., a gel or a dendrite).

While stabilization mechanisms play a critical role in the self-assembly of colloidal nanocrystals [160], this topic has been largely ignored for non-aqueous suspensions of cellulose nanocrystals (CNCs).

Herein, we propose an experimental case study of the influence of electrostatic and solvation-induced stabilizations, two of the main stabilization mechanisms [116], on the self-ordering of CNC suspensions upon evaporation. Our initial postulate is that EISA is expected to compete with DISA in these systems: the more stable the initial colloidal system is, the more likely that self-ordering will be governed by EISA. The last main route to stability, steric stabilization, is not considered since it usually requires particles to have a rough, soft, and weakly adhering surface [116, 160], which is not the case for uncoated nanocrystals such as CNCs.

CNCs are organic rod-like nanoparticles [23] that may be extracted from biomass with morphological characteristics nearly as controlled as those of their inorganic counterparts. CNCs obtained through the sulfuric acid hydrolysis of biomass and neutralized by the addition of NaOH have well-known self-ordering properties upon solvent casting in water [7]. The extraction process introduces sulfate half-ester groups on their surface, yielding charged par-

ticles that are subject to electrostatic stabilization in highly dielectric solvents, such as water [16]. Water also has a high chemical affinity for CNCs and has been modeled to adsorb on CNC surfaces, forming a layer several molecules thick [107, 108]. Therefore, CNCs likely undergo combination of electrostatic and solvation-induced stabilizations in water, which act as a strong deterrent from DISA. In these conditions, evaporation is expected to be governed by hard-particle interactions and cause the formation of a crystalline superstructure following a four step mechanism: isotropic, then nematic, smectic, and finally crystalline [214]. While several steps have indeed been reported upon drying of a CNC aqueous suspension [146], EISA stops at the nematic stage, where destabilization (gelation) occurs. However, it remains debated whether CNCs undergoing EISA would be able to form smectic phases, should gelation not occur, due to their rather large particle size distribution [147]. The helicoidal structures formed at the nematic stage yields, in the dried state, a chiral structure whose pitch size is in the range of visible wavelengths, thus providing optical properties to the solvent-cast thin films [147].

Building upon our previous work on the cohesive parameters of CNCs [106, 215, 216, 217], we propose a way to classify the nature of the stabilization mechanisms occurring in suspensions based on solvent parameters only. By switching the initial suspending solvent from water to one of 15 other solvents (or binary mixtures thereof), we tune the dielectric constant of the media and the chemical affinity of the CNCs for their environment. This probes the spectrum of electrostatic and solvation-induced stabilizations, demonstrating the preponderant role played by these mechanisms in EISA and in hindering DISA. Interestingly, their influence may be assessed by visual characterization and tabletop rheology only. The outcome of the solvent casting may then be predicted from the qualitative behavior of the initial suspensions. Hence, we develop a predictive tool for the efficiency of EISA based colloidal stability in initial CNC suspensions. Employing tabulated solvent properties, the tool is transposable to over 10,000 solvents (and their binary mixtures), thus providing a mapping of CNCs' potential for EISA. Finally, our work suggests that the tools developed to analyze and predict the self-assemblies of inorganic nanocrystals may advantageously be exploited to describe the behavior of organic particles like CNCs.

## 6.2 Materials and methods

### 6.2.1 Materials

The cellulose nanocrystals were provided by Celluforce, Montreal, QC, Canada. Produced from the sulfuric acid hydrolysis of kraft wood pulp followed by neutralization with sodium

hydroxide, these CNCs have dimensions, as measured by transmission electron microscopy, of  $\sim 165$  nm for their length and  $\sim 13$  nm for their width [145] with a crystalline level of 81 % [106], calculated according to Segal’s empirical method [191].

Elemental analysis, through X-Ray energy dispersive spectroscopy (EDS), demonstrated that these CNCs have a sulfur content of  $\sim 3.4$  sulfate half esters ( $\text{O}-\text{SO}_3\text{H}$ ) per 100 anhydroglucose units [145]. The oxygen over carbon (O/C) atomic ratio that theoretically stands at 0.83 for cellulose [190] was measured to be  $0.79 \pm 0.02$  [145], which suggests a higher level of purity for the nanocrystals.

Aqueous suspensions were prepared using distilled water. The 15 organic solvents employed in this study were purchased from commercial suppliers at high purity grade (typically  $>99\%$ , see Table C.1). They were selected based on Hansen Solubility Parameter (HSP) theory [127] to provide a representative sample of solvents based on intermolecular forces (see section on “solvent selection” in supplementary information). Binary mixtures were prepared by mixing

Table 6.1 Solvents and their main properties. “Rkg” stands for solvents’ ranking in term of dielectric constants,  $\epsilon$  (highest to lowest), and “Abbr.” for the abbreviations with which the solvents are referred to throughout the work. Otherwise mentioned,  $\epsilon$  values are provided at  $20^\circ\text{C}$ . The Hansen solubility parameter (HSP) distance to CNCs,  $R_a$ , was calculated at  $25^\circ\text{C}$  using Eq. 6.2. References for the data are provided in the extended version of this table presented in supplementary information (Table C.1).

Solvent set			Parameters	
Rkg	Abbr.	Solvent	$\epsilon$	$R_a$ ( $\text{MPa}^{1/2}$ )
13	$\text{CCl}_3$	chloroform	4.8	19.8
11	DCM	dichloromethane	$8.9^a$	15.6
6	DMF	N,N-dimethylformamide	38.3	7.9
5	DMSO	dimethylsulfoxide	47.2	6.5
15	Dx	1,4-dioxane	2.2	19.7
12	EA	ethyl acetate	6.1	17.7
7	EG	ethylene glycol	41.4	14.4
2	F	formamide	111	7.1
16	Hep	heptane	1.9	26.1
8	MeOH	methanol	33.0	17.1
10	MEK	methyl ethyl ketone	18.6	15.9
1	MF	N-methylformamide	191	2.2
9	PrOH	1-propanol	20.8	14.4
4	PC	propylene carbonate	66.1	12.1
14	Tol	toluene	$2.4^a$	23.2
3	W	water	80.1	6.1

<sup>a</sup>  $\epsilon$  are provided at  $25^\circ\text{C}$  and  $23^\circ\text{C}$  for DCM and PC, respectively.

the pure solvents at the desired composition. Solvents' abbreviations and most relevant properties to this work are provided in Table 6.1. Extended solvent properties and binary mixture properties are tabulated in supplementary information (Tables C.1&C.2).

### 6.2.2 Protocols

The suspensions were all prepared by pouring the solvent on top of the spray-dried particles in glass vials (radius of 2.1 cm). Dispersion was achieved through a strong ultrasonic treatment following a protocol that was proved, in water, to break CNC spray-dried agglomerates without leading to any measurable desulfation [145, 199]. Using an ultrasonic probe (Cole-Parmer) operating with a CV334 converter and a tapered microtip, the treatment was performed at  $\sim 25$  W (frequency of 20 kHz). The signal was pulsated (ON/OFF cycles of 5 s/2 s) and the vials were put in an ice bath during ultrasonication in order to avoid any overheating. A total energy dose of  $10,000 \text{ J g}_{\text{CNCs}}^{-1}$  was provided to the system as per Beuguel et al. [145, 199] - guidelines for a 2.1 cm vial.

The suspensions were then transferred to an evaporating dish, either made of polytetrafluoroethylene (PTFE) or of aluminum (Al) before being placed in the oven (OV-11, MBI Lab Equipment, QC, Canada). The PTFE dishes had a radius of 63 mm and a height of 10 mm, while the Al dishes had a radius of 51 mm and a height of 17 mm. Both were purchased from Fisher Scientific (Canada). The discrepancy in radii between the PTFE and Al dishes, which translates into a surface area ratio of  $\sim 1.5$  ( $63^2/51^2 \approx 1.5$ ), was accounted for by normalizing the initial height of liquid in the dishes. Solvent casting experiments were thus performed by pouring 15 or 10 mL of the suspensions in the PTFE or Al dishes, respectively. These suspensions were prepared by adding the desired amount of solvent (or binary mixture) over 0.45 or 0.30 g of spray-dried CNC powder in order to reach a concentration of  $30 \text{ mg}_{\text{CNC}}/\text{mL}_{\text{solvent}}$ . It corresponds to a volume fraction of  $\sim 1.9 \text{ vol}\%$  at which we can expect CNC suspensions to be fully isotropic [122].

Vials for gelation tests were prepared by pouring 10 mL of solvent over the desired quantity of spray-dried CNC powder, from 0.10 to 1.0 g, corresponding to concentrations ranging from 10 to  $100 \text{ mg}_{\text{CNC}}/\text{mL}_{\text{solvent}}$ . It corresponds to the range over which gelation has been reported in the literature [122].

For solvent casting experiments, the suspensions were in evaporating dishes and were placed in a pre-heated oven within 5 min of ultrasonication. The oven was operated under a flux of air at near atmospheric pressure (typically at  $\sim 0.9$  bar) to avoid any leaks. The substrate was left to dry for 72 h unless the solvent had a boiling point over  $180^\circ\text{C}$ , in which case additional time was provided for a complete evaporation (see extended protocols in SI).

Further experimental details as well as characterization protocols for optical and electron scanning microscopy are provided in supplementary information.

### 6.3 Analysis of the stabilization mechanisms

In order to compare the influence of the stabilization mechanisms with the outcome of solvent casting experiments, we need to control and characterize the mechanisms. Two may apply to unmodified sulfuric acid-hydrolyzed CNCs: electrostatic and solvation-induced stabilizations. Building on theoretical concepts and empirical evidences, the following sections explain how we were able to describe these mechanisms using only the dielectric constant,  $\varepsilon$ , and the chemical affinity,  $R_a$ , calculated from Hansen solubility parameters. Control was then asserted by changing the chemical nature of the solvent to screen different combinations of  $\varepsilon$  and  $R_a$ .

#### 6.3.1 Electrostatic stabilization: $\varepsilon$ as a control parameter

Upon dispersion in a solvent, ionic bonds may dissociate to yield an anion and a cation; the level of dissociation as well as the average distance between the counter-charged electrolytes are functions of the dielectric constant of the media [119]. In the case of sulfuric acid-hydrolyzed sodium-neutralized CNCs (Fig. 6.1.a), dissociation yields polyanionic nanocrystals and  $\text{Na}^+$  counter-ions [7]. These counter-ions form a cloud around the nanocrystals: the electrostatic double-layer [119]. When two nanocrystals approach each other on a collision course, e.g. under the influence of Brownian-motion, their electrostatic double-layers overlap first. The overlapping volume experiences a brutal increase in counter-ion concentration, which induces an osmotic pressure from the surrounding solvent to dilute this area, thus altering the trajectory of the CNCs and eventually preventing them from colliding [120].

The efficiency of this mechanism depends on the thickness of the double layer (controlled by the dielectric constant,  $\varepsilon$ ), on the concentration of counter ions in the double layer (linked to the surface charge of the nanoparticles and to the level of dissociation, also controlled by  $\varepsilon$ ), on the average concentration of counter ions in the solvent (controlled by the overall concentration in nanoparticles and by the ionic strength) [119]. All these parameters are also functions of the nature of the counter-ions (valence, electronegativity, etc.). Experimentally, CNC suspensions have hence been reported to be more stable for the following cases: in highly dielectric media [122], if the CNC surface charge is increased [47, 114], at low concentrations [47, 49], in the absence of added salts [84, 121]; and the counter-ions have been reported to have a significant effect on the redispersibility [123].

To simplify the analysis, the parameters related to the CNCs were kept constant in the present investigation. The study was done on a single batch of CNCs (dimensions, surface charge and density assumed as constant), with a sodium counter-ion,  $\text{Na}^+$ , a consistent initial concentration of  $30 \text{ mg}_{\text{CNC}}/\text{mL}_{\text{solvent}}$ , and without the addition of any extra salt.

Parameters such as temperature,  $T$ , and viscosity of the media,  $\eta_s$ , also appear in the equations that govern electrostatic stabilization [119].  $T$  was thus kept constant unless otherwise mentioned. This leaves  $\varepsilon$  and  $\eta_s$ , which vary concomitantly as the nature of the solvent changes. While most common solvents have a viscosity in the range of  $\sim 1 \text{ mPa}\cdot\text{s}$ , their dielectric constant ranges over two orders of magnitude from  $\sim 1$  to  $\sim 100$  (Table C.1).  $\varepsilon$  is thus expected to be most significant as confirmed by van der Hoeven and Lyklema [119] and was chosen as our control parameter in analyzing the influence of the electrostatic stabilization on the dispersion state. In their theoretical-empirical work on electrostatic stabilization in non-aqueous solvents, van der Hoeven and Lyklema [119] indeed found that particles dispersed in a system whose dielectric constant,  $\varepsilon$ , was above 11 may experience a water-like level of electrostatic stabilization. Intermediate values,  $5 < \varepsilon < 11$ , led to a potential stabilization but in conditions (addition of extra salts) that are not met in our study, while lower values ( $\varepsilon < 5$ ) prevent any form of electrostatic stabilization.

### 6.3.2 Solvation: $R_a$ as a control parameter

The adsorption of solvent molecules into structured layers on the surface of particles creates a sterical barrier that stabilize the system and prevents its immediate coagulation [116, 117, 118]. The collision between nanoparticles, by disturbing solvent molecules' arrangement, results in an oscillatory force whose characteristic range is that of the layers thickness. This structural or solvation (in water, hydration) force has been reported to enable rod-like nanoparticles to self-assemble into nematic and smectic structures [116, 117].

For CNC aqueous suspensions, models suggest that water molecules form a  $\sim 1\text{-}2 \text{ nm}$ -thick cage structure around the nanocrystal [107, 108]. The lack of parameters to measure and compare the adsorption of solvent molecules on CNC surfaces (Fig. 6.1.b) is likely the reason why the role of solvent adsorption is rarely discussed in the literature. Knowing that CNCs are rich in hydroxyl groups, it was proposed that solvents having a high potential for H-bond formation and more generally for Lewis acid/base interactions were favorable for CNC self-ordering [159, 122]. These articles however fell short of mentioning the structural force. Focusing on the sole potential of the solvent does not account for the specific interactions that may form between the solvent and the CNCs or represent an effective measurement of solvent adsorption on CNC surfaces.



We suggest that the failure to correctly account for the chemical affinity between the CNCs and their surrounding media, and for the solvation effect induced by this chemical affinity, is the primary reason why the understanding on the non-aqueous dispersion and self-ordering of unmodified CNCs has remained challenging. HSP theory [126] is an effective tool to measure chemical affinity: each chemical is described by 3 parameters  $\delta_D$ ,  $\delta_P$ , and  $\delta_H$ , which respectively accounts for its potential to form dispersive, dipole-dipole, and hydrogen bonding (& other Lewis) interactions [127]. Solvent parameters at 25 °C,  $\{\delta_{D,s}; \delta_{P,s}; \delta_{H,s}\}$ , are tabulated [127, 131]. Polymer and nanoparticle parameters,  $\{\delta_{D,p}; \delta_{P,p}; \delta_{H,p}\}$ , may be determined indirectly through any test of chemical affinity: e.g., swelling, sedimentation, or inverse gas chromatography [127]. The chemical affinity between them may then be expressed as a HSP distance [127],  $R_a$  (Eq. 6.1).

In a recent work, we characterized the main affinity of our CNC particles based on sedimentation tests to be  $\{\delta_{D,CNC}; \delta_{P,CNC}; \delta_{H,CNC}\} = \{18.1; 20.4; 15.3\} \pm \{0.5; 0.5; 0.4\} \text{ MPa}^{1/2}$  [106]. Inserting these values in Eq. 6.1 yields to a numerical expression for the chemical affinity of solvents for our CNCs (Eq. 6.2).

$$R_a = \left[ 4(\delta_{D,s} - \delta_{D,p})^2 + (\delta_{P,s} - \delta_{P,p})^2 + (\delta_{H,s} - \delta_{H,p})^2 \right]^{1/2} \quad (6.1)$$

$$R_a = \left[ 4(\delta_{D,s} - 18.1)^2 + (\delta_{P,s} - 20.4)^2 + (\delta_{H,s} - 15.3)^2 \right]^{1/2} \quad (6.2)$$

The threshold for long-term stability against sedimentation,  $R_0$ , was found to be  $R_a \leq R_0 = 7.8 \text{ MPa}^{1/2}$  and to be uncorrelated with the dielectric constant of the solvent, and thus with electrostatic stability. Resistance to sedimentation being a sign of significant solvent adsorption in suspension [127], we selected  $R_a$  as a control parameter to analyze the influence of solvation on the dispersion and use  $R_0 = 7.8 \text{ MPa}^{1/2}$  as an expected threshold for behavioral changes.

### 6.3.3 A diagram for stability mechanisms

The parameters  $\varepsilon$  and  $R_a$  (Eq. 6.2) were thus identified as controls for the electrostatic ( $\varepsilon > 11$ ) and solvation-induced ( $R_a \leq 7.8 \text{ MPa}^{1/2}$ ) stabilizations, respectively. Knowing that each dispersing media has a unique set of  $\{\varepsilon; R_a\}$  coordinates, , we may construct a 2-dimensional graph to explain the different stabilization mechanisms (Fig. 6.1.c). The different schemes of the figure aim to represent the average state of CNC particles (grey rods) in suspension: the counter-ions,  $\text{Na}^+$  (red pentagons), get dissociated from the sulfate groups as the dielectric constant increases (Fig. 6.1.a); and the solvent molecules (blue dots) are more adsorbed on CNC surfaces as  $R_a$  decreases and the chemical affinity improves (Fig. 6.1.b). Threshold values of  $\varepsilon \approx 11$  and  $R_a \approx 7.8 \text{ MPa}^{1/2}$  are therefore expected for reaching a water-like level

of electrostatic stabilization through counter-ion dissociation [119], and of solvation-induced stabilization through a significant level of solvent molecules' adsorption on CNC polar surfaces [106] (Fig. 6.1.c):

- $\{\varepsilon < 11; R_a > 7.8 \text{ MPa}^{1/2}\}$  No stabilization: poor solvent/CNC chemical affinity in a poorly dielectric environment.
- $\{\varepsilon > 11; R_a > 7.8 \text{ MPa}^{1/2}\}$  Electrostatic stabilization: poor solvent/CNC chemical affinity in a highly dielectric environment.
- $\{\varepsilon < 11; R_a < 7.8 \text{ MPa}^{1/2}\}$  Solvation-induced stabilization: good solvent/CNC chemical affinity in a poorly dielectric environment.
- $\{\varepsilon > 11; R_a < 7.8 \text{ MPa}^{1/2}\}$  Solvation-induced and electrostatic stabilizations: good solvent/CNC chemical affinity in a highly dielectric environment.

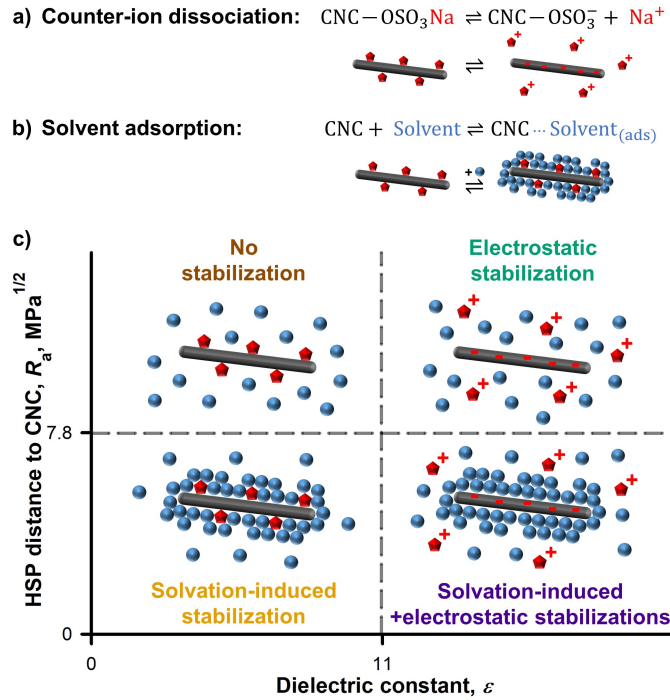


Figure 6.1 Expected stabilization mechanisms in CNC suspensions as a function of the dielectric constant,  $\varepsilon$ , of the solvent and of its chemical affinity for the CNC particles (grey rods),  $R_a$ . They respectively govern the counter-ion dissociation of  $\text{Na}^+$  (red pentagons) with the half-ester sulfate groups **(a)** and solvent (blue dots) adsorption over CNC surfaces **(b)**. Four kind of stabilization mechanisms may hence be predicted from the various sets of  $\{\varepsilon; R_a\}$  coordinates **(c)**: no stabilization; electrostatic stabilization; solvation-induced stabilization; and a combination of solvation-induced and electrostatic stabilizations.

Note that given the high polarity of the hydroxyl group-rich CNC surface, no solvent can have both a high affinity for these surfaces and be poorly dielectric. CNCs, however, are amphiphilic particles and solvents such as chloroform and dichloromethane were suggested to display some level of chemical affinity for the less-polar surfaces of CNCs [106]. These surfaces have a different set of HSP coordinates where Eq. 6.2 is no longer applicable [106]. In practice, it means that the bottom-left quarter of the Fig. 6.1  $\{\varepsilon < 11; R_a < 7.8 \text{ MPa}^{1/2}\}$  is empty as no solvent matches these criteria, but that CNC suspensions in dichloromethane and chloroform, while occupying the top-left quarter  $\{\varepsilon < 11; R_a > 7.8 \text{ MPa}^{1/2}\}$  of the graph, are expected to benefit from some solvation-induced stabilization due to their chemical affinity for the non-polar surfaces of CNC particles.

The pertinence of an approach based on stabilization mechanisms to predict the long-term behavior of CNC suspensions in standing vials is discussed in supplementary information. This involves the reinterpretation of some previously published results [106] in the light of the classification proposed in Fig. 6.1.c.

## 6.4 Results and discussion

### 6.4.1 Behavior of CNC suspensions upon solvent casting

The outcome of solvent casting at 60 °C in PTFE dishes is plotted in Fig. 6.2: it ranges from a powder to a continuous thin film. Symbols account for the position of the solvents in the  $\varepsilon$ - $R_a$  graph. Their shape is a function of CNC behavior in suspensions (determined from our previous work [106], see discussion in SI): suspensions that are stable against sedimentation are plotted as filled circles, and those that sediment over time as empty diamonds. The color code refers to the expected nature of the stabilization mechanism (see Fig. 6.1): solvation and electrostatic (purple), electrostatic only (sea green), solvation only (yellow), none (brown). Fig. 6.2 highlights the pertinence of an approach based on stabilization mechanisms to categorize the results. The best outcomes, continuous and transparent thin films, are obtained from suspensions stabilized by a combination of solvation and electrostatic stabilization, whereas a lack of any stabilization leads to a powder. Some intermediate outcomes are obtained for suspensions stabilized electrostatically only. In the following sections, results are analyzed category by category. The robustness of our approach is then probed by using binary mixtures to explore the transition from electrostatic stabilization only to a combination of solvation and electrostatic stabilizations.

## Combined influence of solvation-induced and electrostatic stabilizations

Fig. 6.3 displays results for the four solvents of our set in which CNCs are stabilized by a combination of solvation-induced and electrostatic stabilizations: water (W), N-methylformamide (MF), dimethylsulfoxide (DMSO), and formamide (F). In this figure, the rheological state of CNC suspensions, fluid or gelified, is determined at  $30 \text{ mg}_{\text{CNC}}/\text{mL}_{\text{solvent}}$  through tabletop rheology in the absence of any evaporation. It is then compared with digital, optical microscopy, and electron microscopy images of the thin films casted from these suspensions at  $60^\circ\text{C}$  in PTFE dishes.

Casting of CNC aqueous suspensions yielded the outcome reported in the literature [7]: transparent and continuous thin films (Figs. 6.2&6.3.b). Other films casted from likewise suspensions, co-stabilized by solvation and electrostatic effects, had the same macroscopic appearance. Polarized optical microscopy (POM, Figs. 6.3.c&d) revealed that they all display some sort of iridescence except the formamide-cast film which had large non-iridescent areas. Observations under unpolarized light (Figs. 6.3.e&f), highlight that films casted from water and MF suspensions have a highly structured iridescence, while those obtained from formamide and DMSO suspensions do not. These films instead have, imprinted on their bottom-side (Fig. 6.3.f), the spiral pattern displayed on the top-side of the PTFE evaporating dishes (see SI): the ductility required for the imprinting to occur suggests an earlier gelation in DMSO and formamide upon solvent casting, which leads to a glassy system [147].

In order to assess whether suspensions in DMSO and formamide are indeed more prone to gelation than those in MF or water, we performed tabletop rheology experiments [218], where gel formation is assessed by inclining vials and measuring the deviation between the air/media interface and the horizontal plane (fluids being expected to stabilize with a horizontal interface). The first set of experiments involved suspensions with increasing concentrations stored for 24 h at  $\sim 25^\circ\text{C}$ : a gel formed from  $70 \text{ mg}_{\text{CNC}}/\text{mL}_{\text{solvent}}$  in water and MF, and from  $50 \text{ mg}_{\text{CNC}}/\text{mL}_{\text{solvent}}$  in DMSO and formamide (Fig. C.4). It is worth noting that suspensions at  $30 \text{ mg}_{\text{CNC}}/\text{mL}_{\text{solvent}}$ , the initial concentration for the solvent casting experiments, remained liquid in all circumstances (Fig. 6.3.a). In the second set of experiments, vials at  $30 \text{ mg}_{\text{CNC}}/\text{mL}_{\text{solvent}}$  were either kept for 5 months at  $\sim 25^\circ\text{C}$ , in which case strong gels formed in formamide and DMSO; or at  $60^\circ\text{C}$  for 24 h, in which case a weak gel formed in formamide only. Other suspensions remained fluid (Fig. 6.3.a).

Qualitatively, these tests confirm that suspensions in formamide and DMSO are more likely to form a gel than those in water or MF. The suspensions in formamide may form gels from  $30 \text{ mg}_{\text{CNC}}/\text{mL}_{\text{solvent}}$  after 24 h at  $60^\circ\text{C}$  and this is coherent with the lack of detectable optical properties for the films casted from these suspensions (Figs. 6.3.c&d). Indeed, if DISA-

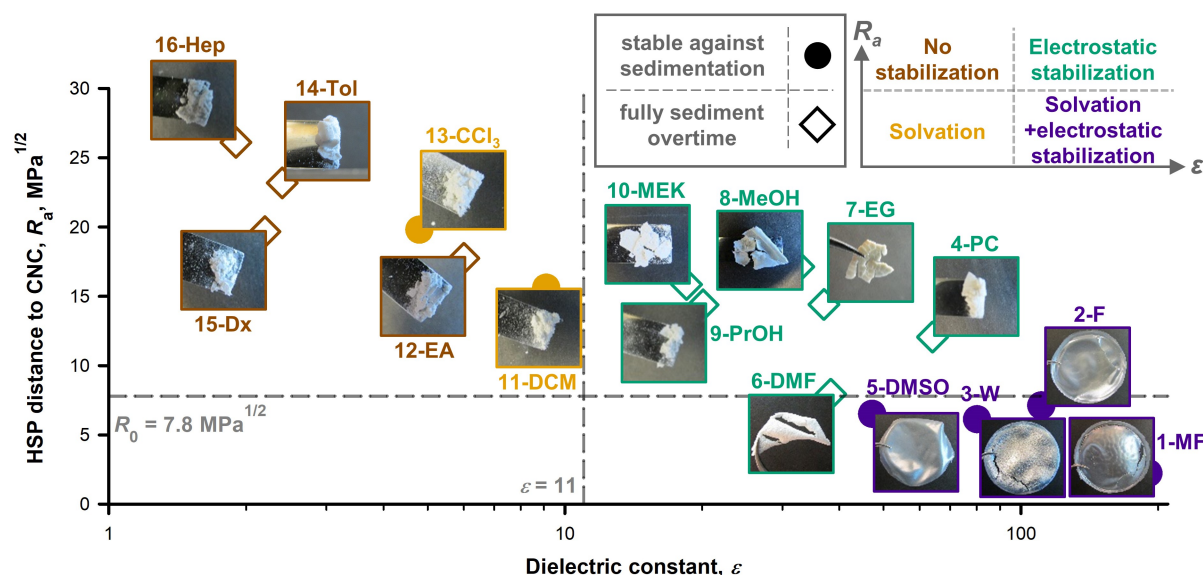


Figure 6.2 Stability against sedimentation of 16 CNC suspensions and their oven-casting in PTFE evaporating dishes as functions of the dielectric constant,  $\epsilon$ , of the solvent and of its chemical affinity for the CNC particles,  $R_a$ . The inset in the figure illustrates the different stability zones as presented in Fig. 6.1. Suspensions stabilized by a combination of solvation and electrostatic effects displayed water-like levels of EISA. Electrostatically-stabilized suspensions displayed a form of EISA with the recovery of CNC film fragments in most circumstances. Other suspensions yielded a powder upon casting as no obvious EISA could be observed. Full-size images are provided in Fig. 6.3.b (for MF, F, W, DMSO), in Fig. 6.3.c (DMF), and in Fig. C.4 (PC and EG). All chemical abbreviations are defined in Table 6.1.

induced gelation occurs within 24h in formamide, it will inhibit the EISA process before it even begins (evaporation of formamide lasts over  $\sim 13$  days at  $60^\circ\text{C}$ ). If chiral nematic domains cannot form upon evaporation, no iridescence should be observed. The lack of any immediate DISA in DMSO, water, and MF, however means that some EISA is expected to occur in these suspensions, which is supported by the optical activity detectable through POM (Figs. 6.3.c&d). A more elaborate discussion on gelation, in which we further analyze our tabletop rheology results in the light of those presented in the literature, is conducted in supplementary information.

In the case of suspensions stabilized by a combination of solvation and electrostatic effects, the competition thus seems to be between chiral nematic domain formation (EISA) and early gelation (DISA), which lead to the formation of iridescent or “glass-like” structures, respectively. If the kinetics of gelation are slow with respect to those for self-ordering, then chiral nematic domains will form, while if gelation is too fast, evaporation will yield a glassy

system. We did not push the rheological characterization of the suspensions or the analysis of the films' optical properties further since systems in which CNCs form stable colloidal suspensions have already been thoroughly investigated in the literature [147, 150].

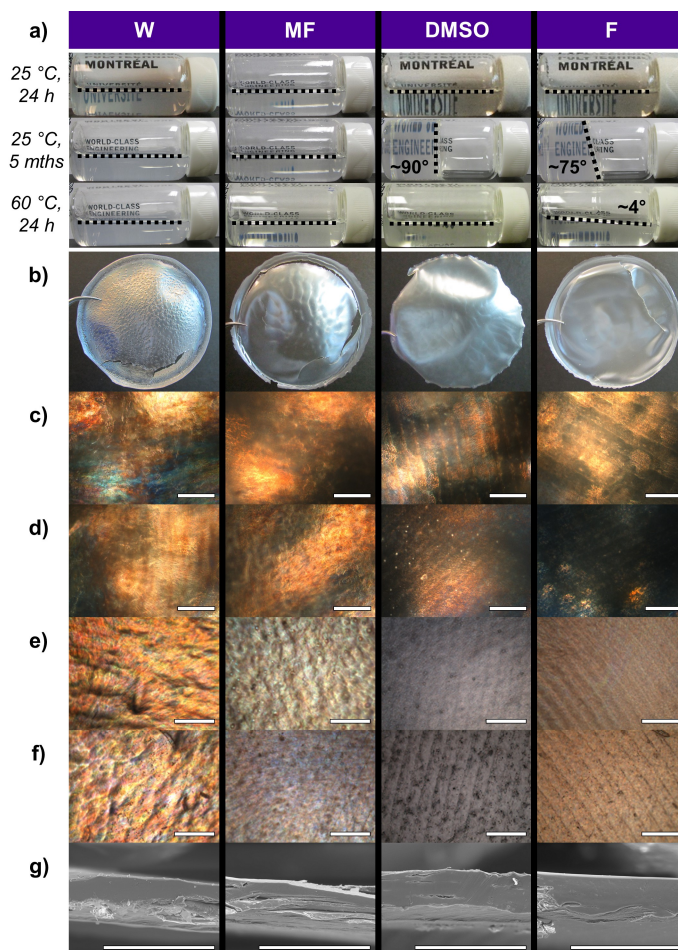


Figure 6.3 Self-assembly in systems stabilized by a combination of solvation and electrostatic effects, corresponding to CNC suspensions in water (W), N-methylformamide (MF), dimethylsulfoxide (DMSO), and formamide (F). Gelation tests at a concentration of  $30 \text{ mg}_{\text{CNC}}/\text{mL}_{\text{solvent}}$ , a temperature of 25 or 60 °C, and a period of 24 h or 5 months (a). The air/media interface is highlighted by a dotted line on the images, its angle with the horizontal plane is specified when it deviates from zero. Digital image (b) and optical microscopy (c-f) of films casted at 60 °C from various CNC suspensions in PTFE evaporating dishes. Micrographs in transmission through aligned polarizers (c) and cross-polarizers (d) where a white light is polarized twice in the same direction, or in opposite directions, respectively; micrographs in reflection, using an unpolarized white light, of the top (e) and bottom (f) sides of the thin films, respectively exposed to the air or the PTFE interface during evaporation. Scanning electron microscopy of a thin film cross-section (g): the top and bottom sides of the film correspond to the upper and lower parts of the micrograph, respectively.

## Electrostatic-only stabilization

Solvent casting of electrostatically-stabilized CNC suspensions yielded mixed results illustrated in Fig. 6.2: some samples gave nothing more than powders (MEK, PrOH, PC) while others formed film fragments (MeOH, DMF, EG) that were eventually resistant enough to be held by tweezers (DMF, EG). Here, we define a film fragment as a part of a white opaque film: the cohesion between the different fragments that constitute the film seems to be lost upon total solvent evaporation in a process akin to the formation of “mudcracks” upon drying of mud sediments [219]. They are common defects in nanocrystal self-assemblies: solvent evaporation creates voids in imperfectly assembled systems whose anisotropic propagation causes cracks [160, 220].

In these suspensions, while the dielectric constant is high enough to expect the particles to be charged and undergo electrostatic stabilization, sedimentation occurs and is completed over a time span ranging from a few hours to a few days [106]. Sedimentation is promoted by DISA: in these media, destabilization seems to lead to the formation of agglomerates instead of a gel as in suspensions that are further stabilized by solvation. We suggest that the lack of an adsorbed solvent on the CNC surfaces favors coagulation and the formation of dense assemblies over longer range interactions. Due to their larger size, agglomerates sediment faster and are recovered after evaporation as a powder. A competition thus takes place between EISA and DISA: solvents in which evaporation (and its induced chiral nematic domain formation) is fast compared to destabilization (and its induced sedimentation) are expected to yield films (or film fragments). In the reverse situation, particles are expected to agglomerate and to sediment too quickly for any EISA to occur. Solvent casting experiments during which EISA is competitive compared to DISA should thus be made of a mix of ordered domains and agglomerates. In those where DISA outmatches EISA, a powder of agglomerates is expected.

Examining data of Fig. 6.2, casting in PC ( $\epsilon \approx 64$ ) yielded a powder because the sedimentation rate (full sedimentation within a few hours) is faster than evaporation (full evaporation within  $\sim 14$  days at  $60^\circ\text{C}$ ): in these conditions, all CNCs have been destabilized before any evaporation may occur. In the cases of MEK and PrOH, evaporation (within  $\sim 1$  h) is faster than sedimentation (within 2 days), so sedimentation should not be an issue. The rate at which evaporation occurs, however, seems to be too fast compared to the rate at which chiral nematic domains are formed. Due to their relatively low dielectric constants [122], MEK ( $\epsilon \approx 18.5$ ) and PrOH ( $\epsilon \approx 20$ ) suspensions would need days to self-order into nematic domains. This configuration is slightly reminiscent of what may happen during the spray-drying of CNC aqueous suspensions, where a rapid evaporation leads to the formation of

non-iridescent CNC agglomerates [211]. MeOH suspensions have a similar ratio of evaporation/sedimentation rate as MEK and PrOH ones, but their higher dielectric constant ( $\epsilon \approx 33$ ) is enough for small film fragments to form. These fragments were, however, mechanically too weak to be handled. In DMF ( $\epsilon \approx 38$ ), the time for full sedimentation is in line with that for evaporation ( $\sim 2$  days) and the solvent casting yielded small interconnected film fragments. In EG ( $\epsilon \approx 37$ ), sedimentation is slowed by the high viscosity of the solvent and full sedimentation happens within  $\sim 10$  days, which is also in line with the  $\sim 9$  days required to fully evaporate the solvent: casting yielded small interconnected film fragments as for DMF. In both case, the fragments were mechanically strong enough to be handled with tweezers (Fig. 6.2).

While temperature increases the frequency of collisions between particles and their average velocity, it is known to be a deterrent for DISA [160]: increasing the thermal energy available in the media favors particle-particle interaction breakdown and redispersion, while balancing gravitational potential energy. In a solvent such as DMF, EISA is already competitive with DISA based on our current protocol (evaporation at  $60^\circ\text{C}$ ); hence, it should be possible to promote EISA by improving the heat transfer within the evaporating dish (by switching its material from PTFE to aluminum). Conversely, applying a temperature ramp to the oven (instead of an immediate step-like temperature increase from  $25$  to  $60^\circ\text{C}$ ) should favor DISA. Indeed, the poorest results were obtained for films casted with a temperature ramp in a PTFE dish and the best for films casted with a step-like temperature increase in an Al dish (Fig. 6.4). Increasing the temperature to  $80^\circ\text{C}$  (step-like temperature profile) in the PTFE dish further increased the continuity of the thin films to a level close to that observed at  $60^\circ\text{C}$  in aluminum.

Optical microscopy analysis highlights a bilayer structure for the films with a top transparent layer and an opaque and cracked bottom layer. The cracks may be seen by transparency through the top layer: their width is obviously larger on the bottom side than at the interlayer border. The luminosity of the light source during the optical microscopy was kept constant between the various samples (Figs. 6.4.a-e) and a greater continuity in the film thus appears to be correlated with a stronger ability to reflect the light (and with a lighter micrograph). The most continuous films were rigid enough to enable cross-sectional imaging by SEM. The competition between sedimentation and self-ordering was clearly visible as the bottom layer was made of CNC agglomerates held together by the top self-ordered layer. For the sake of comparison, a cross-sectional analysis of the films obtained by solvent casting in water, DMSO, MF, and formamide was also performed (Fig. 6.3.g). These are single layered films whose structure is similar to that of the top layer observed on the DMF-cast films (Fig. 6.3.d), thus confirming that the top layer is the one formed upon EISA. Our micrographs of the self-



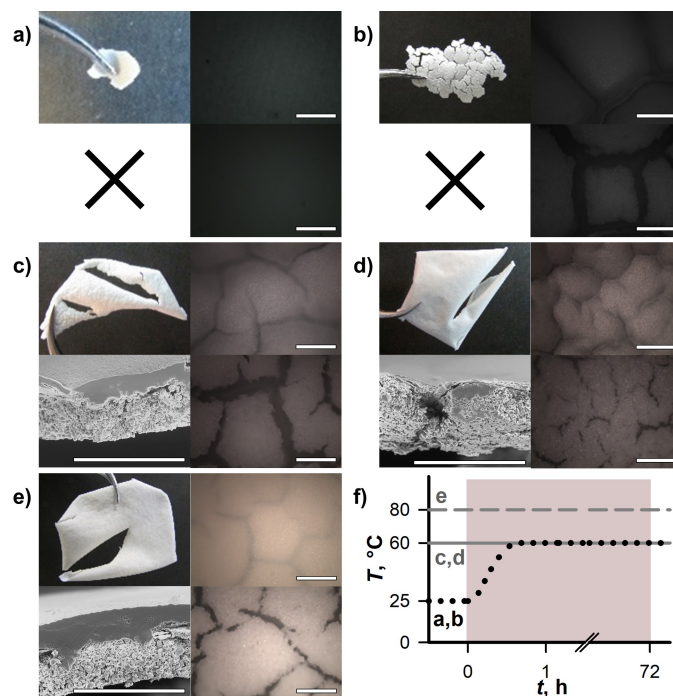


Figure 6.4 Effect of oven temperature and heat transfer on the casting of CNC suspensions in N,N-dimethylformamide (DMF). Casting was either performed in a PTFE (**a,c&e**) or in an Al dish (**b&d**). Temperature profile in the oven over time (**f**): the time span during which the sample was in the oven is highlighted in grey. The suspensions were either introduced in an oven at 25 °C that was heated to 60 °C at an average rate of  $\sim 1\text{ }^{\circ}\text{C min}^{-1}$  (**a&b**) or pre-heated directly at 60 °C (**c&d**) or 80 °C (**e**). In each configuration, the figure displays 4 micrographs (all scale bars represent 250  $\mu\text{m}$ ): a digital image (top left), optical micrographs in reflection of the top (top right) and bottom (bottom right) sides of the films (or fragments thereof), which were respectively exposed to the interface with air or with the dish, and a scanning electron microscopy micrograph of its cross-section in which the upper and lower parts respectively correspond to the top and bottom sides of the films (or fragments thereof). The fragments were sometimes too fragile to perform a cross-section (**a&b**). The intensity of the light source was kept constant between the various samples (**a-f**).

ordered layer are similar to what has been published elsewhere for the casting of aqueous CNC suspensions [123, 221, 222]: the pitch lines, whose dimensions are expected to be in the range of  $\sim 0.2$  to  $1\text{ }\mu\text{m}$ , could not however be detected with our instrument (micrographs had dimensions of  $40 \times 55\text{ }\mu\text{m}^2$  at the highest resolution we could probe).

It is worth noting that some exploratory tests were performed under vacuum (at a pressure of  $\sim 0.6$  bar instead of  $\sim 0.9$  bar for the results presented in Fig. 6.4), but that they were not conclusive. Our interpretation is that while both vacuum and temperature have the potential to increase the evaporation rate, only temperature is able to meaningfully shift the balance between attractive and repulsive interactions by increasing the thermal energy available.

## In the absence of electrostatic stabilization

Suspensions lacking electrostatic stabilization mechanism did not show any self-ordering upon solvent casting, yielding instead a powder of CNC agglomerates. These suspensions present a low dielectric constant which provides little incentive for helicoidal self-ordering [122]. For non-stabilized CNC suspensions, this promotes almost immediate agglomeration, and therefore sedimentation. In contrast to suspensions where solvation, and its induced structural force, is coupled with an electrostatic repulsion, the adsorbed solvent layer present in suspensions only stabilized by the solvation effect does not prevent agglomeration from occurring (suspensions are cloudy, see Fig. C.3). This suggests that the repulsion experienced at short distance between particles is not sufficient for the assumption of hard particle interactions to apply. Thus, neither solvation only stabilized nor non-stabilized CNC suspensions provide any operation window for EISA to occur. The presence of surface charges is, however, not supposed to be a prerequisite for the EISA of nanorods into chiral nematic domains [160]. Colloidal nanocrystals that are more efficiently stabilized, i.e. sterically, by the grafting of polymer chains or the addition of voluminous surfactants instead of relying on solvent adsorption, are expected to be able to self-order upon evaporation as well [160].

Although irrelevant for our study on the EISA potential of unmodified CNCs, it is worth noting that other investigators indeed witnessed chiral nematic domain formation in a low-polarity solvent such as cyclohexane by modifying CNCs with an anionic surfactant [223, 224] or in a polar aprotic solvent such as DMF [225] by grafting side polymer chains to the nanocrystals. In a solvent like DMSO, for instance, grafting alkyl chains on CNCs allows to switch from the combination of electrostatic and solvation-induced stabilization mechanisms described in this work to a steric stabilization. It does not prevent structure formation, but it dramatically alters the viscosity of the system, its temperature dependence, and the concentration threshold at which the structure is formed [154]. Modifying CNC surfaces thus seems a promising way to promote their self-ordering potential in poorly dielectric solvents. However, further work is needed to characterize the structure of the chiral nematic domains formed by these surface-modified CNCs and understand how they differ from the ones formed by  $\text{H}_2\text{SO}_4$ -hydrolyzed CNCs stabilized by a combination of electrostatic and solvation effects. It shows that, as already demonstrated for inorganic nanocrystals [160], the EISA of colloidal CNCs is not just a matter of charges, but more broadly a matter of tuning the overall balance of stabilizing and destabilizing interactions to promote hard-particle interactions and to inhibit DISA.

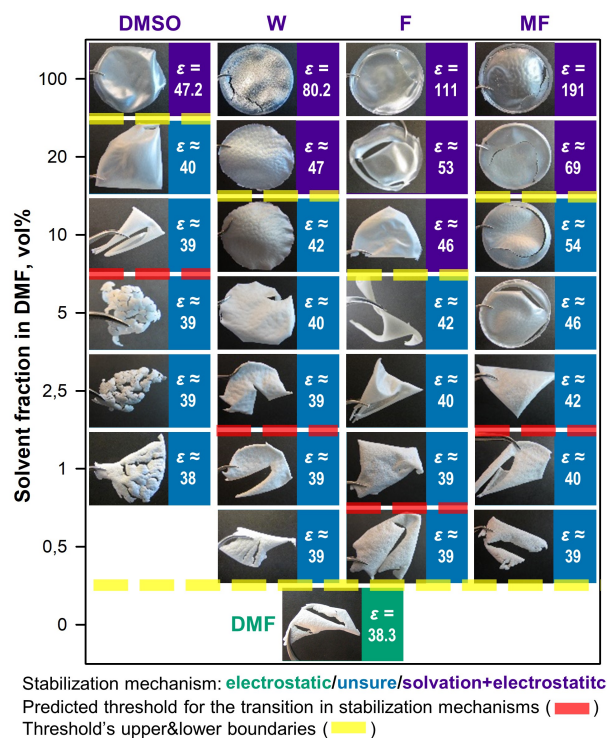


Figure 6.5 Solvent casting (60 °C, PTFE dishes) of CNC suspensions in binary mixtures of dimethylsulfoxide (DMSO), water (W), N-methylformamide (MF), or formamide (F), in N,N-dimethylformamide (DMF). The appearance of the casted film is shown as function of the volume percent (vol%) of added solvent in DMF. The dielectric constants,  $\epsilon$ , are linear extrapolations based on the composition of the mixture. Based on our predictive tool (Eq. 6.2), the systems are expected to be initially electrostatically-stabilized with or without the combination of a solvation effect. There is, however, a rather large uncertainty on the threshold at which the system should benefit from a sufficient solvation effect: it translates into an upper and a lower boundary for the predicted threshold. Predicted values for the threshold (red dotted lines) and their upper boundaries (yellow dotted lines) are of 6-50 vol%, 2-15 vol%, 2-15 vol%, and 0.9-7.0 vol% for DMSO, water, MF, and formamide, respectively. The lower boundaries (longest dotted line, also in yellow) tend towards zero for all these mixtures. Binary mixtures' properties are summarized in Table C.2.

## Casting of CNC suspensions in binary mixtures

Industrially relevant systems often involve complex solvent mixtures or the presence of various additives. The study of CNC dispersibility and casting potential in binary mixtures is thus essential as a first step toward the extrapolation of our results to more complex systems. In our case, binary mixtures come with a further opportunity: the possibility to probe the frontier between the electrostatic only and the combination of solvation-induced and electrostatic stabilization regimes.

In HSP theory, a mixture's potential for interactions  $\{\delta_{D,\text{mix}}; \delta_{P,\text{mix}}; \delta_{H,\text{mix}}\}$  may be described as the volume barycenter of its constituents' parameter  $\{\delta_{D,i}; \delta_{P,i}; \delta_{H,i}\}$  and calculated through Eq. 6.3, in which  $\Phi_i$  is the volume fraction of the constituent “ $i$ ” in the mixture [127].

$$\delta_{D,\text{mix}} = \sum_{i=1}^n \Phi_i \delta_{D,i} ; \delta_{P,\text{mix}} = \sum_{i=1}^n \Phi_i \delta_{P,i} ; \delta_{H,\text{mix}} = \sum_{i=1}^n \Phi_i \delta_{H,i} \quad (6.3)$$

Based on sedimentation tests [106], we assumed  $R_a \leq R_0 = 7.8 \text{ MPa}^{1/2}$  to be the threshold for the solvation-induced stabilization of CNC suspensions (Eq. 6.2). DMF is a relatively poor solvent for our CNCs as it is just short of this criteria ( $R_{a,\text{DMF}} = 7.9 \text{ MPa}^{1/2}$ ). Mixing DMF with good solvents such as water, DMSO, MF, and formamide, yields mixtures whose HSP match the criterion,  $R_0$ , for a stable suspension, and allows for a comparison between the experimental casting results and the predictions by HSP theory. DMF is perfectly miscible with DMSO, W, F, and MF, and does not form any azeotrope upon mixing with these solvents. Based on Eq. 6.2, the combination of an electrostatic with a solvation-induced stabilization may be predicted from  $\sim 0.9$  (formamide),  $\sim 2$  (MF),  $\sim 2$  (water), and  $\sim 6$  vol% (DMSO) of added solvent in DMF. These values need to be considered carefully. Indeed, while the uncertainty on the HSP coordinates of CNCs is relatively narrow with  $\{\delta_{D,\text{CNC}}; \delta_{P,\text{CNC}}; \delta_{H,\text{CNC}}\} = \{18.1; 20.4; 15.3\} \pm \{0.5; 0.5; 0.4\} \text{ MPa}^{1/2}$  and those predictions are thus relatively accurate for pure solvents, it is no longer true for their binary mixtures. There, a low uncertainty on the HSP coordinates may translate in a rather large uncertainty on the volume fractions if the HSP distance (Eq. 6.1) between the mixture's constituents is small. The upper boundaries for the threshold at which solvation becomes significant is as high as 7.0 (formamide), 15 (MF), 15 (water), and 50 vol% (DMSO) in DMF, while all the lower boundaries tend towards 0 vol%. The transition from a discontinuous to a continuous and transparent thin film occurred below the upper threshold values (Fig. 6.5), which is a sign that DISA-induced sedimentation is no longer the limiting factor. However, the exact location of the frontier is blurry and we suggest that, beyond the average chemical affinity, it is the ability of the solvent to structure itself around CNCs in a thick and stable adsorbed layer that is affected. Furthermore, the composition of the media is evolving over time: a mixture that initially contains 10 vol% of water in DMF will, for instance, see its water content decreases upon evaporation as water has a lower boiling point than DMF. An evolving composition, by perturbing the media, is known to promote DISA [160] by potentially lowering the chemical affinity and perturbing the stabilization mechanisms. This has recently been exploited to favor the 3-D printing of CNC gels: the initially good solvent is exchanged for a poorer one by diffusion, thus triggering DISA and the solidification of the printed structure [226].

Fig. 6.5 shows how the continuity of film obtained by solvent casting (60 °C, PTFE dishes) and its optical transparency are progressively improved by the addition of a given volume percent of good solvent (W, MF, DMSO, or F) to a CNC suspension in DMF (0 vol% = pure DMF, 100 vol% = no DMF). The predicted value for the threshold between an electrostatically-stabilized suspension benefiting or not from a solvation effect is marked by a red dotted line, its upper and lower boundaries by yellow dotted lines. A non-linear scale was chosen for the volume fractions to be investigated (0.5, 1, 2.5, 5, 10, and 20 vol%) to account for the fact that there is roughly an order of magnitude between the predicted threshold and its upper boundary. Films casted from suspensions that are known to benefit from the solvation effect (in purple), because their composition is outside the uncertainty interval, are fully transparent and continuous (akin to those presented in Fig. 6.3.b). Suspensions in which the exact nature of the stabilization mechanism is uncertain (in blue) however yield anything between a continuous film and fragments thereof.

Generally speaking, our approach seems to apply to binary mixtures within the limits of its predicted uncertainty, which arose from the determination of HSP coordinates [106]. The barycenter nature of Eq. 6.3 means that this uncertainty decreases as the chemical distance,  $R_a$  (Eq. 6.1), between the two components of the mixture increases. The tool has a workable uncertainty (of  $\sim 6$  vol%) for a mixture made of solvents such as formamide and DMF ( $R_a = 14.7 \text{ MPa}^{1/2}$ ) but that increases to over 40 vol% for closely related chemicals such as DMSO and DMF ( $R_a = 3.5 \text{ MPa}^{1/2}$ ).

#### 6.4.2 Insights on the competition between EISA and DISA

An analogy between self-assembly mechanisms described for inorganic colloidal nanocrystals and CNC-solvent suspensions suggests that CNC self-ordering in chiral nematic domains is prompted during evaporation by hard particle interactions such as excluded volume [160, 214]. For hard particle interactions to govern the self-assembly, it is assumed that particles repel each other at short distances (instead of agglomerating). This assumption is made possible by the action of stabilization mechanisms that provide a deterrent to agglomeration [227, 160, 214]. During evaporation, the formation of chiral nematic domains should thus be possible provided the hard particle hypothesis applies. For unmodified CNCs, these conditions are met at low concentrations in suspensions stabilized by a combination of electrostatic and solvation effects ( $\varepsilon > 11$ ;  $R_a < 7.8 \text{ MPa}^{1/2}$ ). Upon evaporation, and as the concentration increases, electrostatic stabilization fades progressively and there is a concentration threshold above which attractive particle-particle interactions become strong enough to cause gelation and kinetic arrest to the system. Besides the increase in concentration, other phenomena

such as desulfation [228] or salt addition [229], may also weaken electrostatic stabilization to trigger agglomeration or gelation. Overall, circumstances in which attractive interparticle interactions cannot be mitigated during evaporation lead to DISA with the formation of 3-D self-assemblies (gels or agglomerates) [160]. Circumstances in which they may be mitigated long enough upon evaporation lead to EISA with the formation of 2-D self-assemblies (mono or polycrystalline thin-films). This phenomenon occurs when a crowded suspension (sufficiently concentrated) experiences a unidirectional volume compression [160], as is the case between the air/solvent interface and the support upon evaporation.

In suspensions stabilized only by electrostatic effects ( $\varepsilon > 11$ ;  $R_a > 7.8 \text{ MPa}^{1/2}$ ), DISA occurs even in the absence of evaporation and simultaneously leads to the formation of agglomerates and sedimentation. In these conditions, solvent casting becomes a race between DISA and EISA, with EISA attempting nematic self-assembly while DISA inhibits it by promoting CNC bulk agglomeration and sedimentation. As expected from the literature, our results show that increasing the temperature or the heat transfer within the media promotes EISA over DISA. The competition between EISA and DISA results in a bilayer film with the top-side controlled by EISA (continuous & transparent) and a bottom side by DISA (made of CNC agglomerates, see Fig. 6.4)

In suspensions only stabilized by the solvation effect or lacking stabilization mechanisms ( $\varepsilon < 11$ ), attractive interactions are predominant: DISA overcomes EISA and chiral nematic domains cannot form. Instead, solvent casting yields a powder of CNC agglomerates. This result is likely to be only valid for suspensions of unmodified CNCs in which steric stabilization does not occur. The literature indeed suggests that sterically-stabilized CNCs (e.g., by polymer chain grafting or by using surfactants) may form chiral nematic domains even in the least polar solvents [223, 224, 225].

Therefore, the behavior of colloidal CNCs in standing suspension and upon solvent casting may be categorized as a function of the stabilization mechanisms that apply on CNCs, which themselves are functions of the solvent parameters. Table C.3 offers a summary of our analysis' grid and of our findings.

### 6.4.3 Limitations and extrapolability

The main limitation to our work lies in the fact that we studied a single-kind of CNCs to focus on solvent parameters. The influence of particle parameters such as the biomass feedstock, aspect ratio, counter-ion, degree of sulfatation, purity, or crystallinity, thus remain to be investigated. It is striking for instance that Cheung et al. [123] reported their CNCs to be fully stable in DMF while ours were not. Based on our criteria, full stability means

that their CNCs benefited from a combination of electrostatic stabilization and solvation in DMF and it is thus coherent that they were able to cast iridescent thin films from these suspensions. We suggest that the degree of sulfatation (unreported in their work) may be responsible since a lower sulfur content should be able to shift CNC chemical affinity toward DMF and thus to promote DMF adsorption on CNC surfaces [106]. Further characterization is, however, necessary to fully understand why some authors report their sodium-neutralized sulfuric acid-hydrolyzed CNCs to be stable in DMF, while others do not. The same goes for a solvent such as chloroform in which some investigators, including ourselves, report CNC stability against sedimentation [106, 215, 155, 156] while others do not [138, 185].

Those willing to use our work to predict the behavior of their unmodified CNCs upon solvent casting may thus want to perform quick vial tests similar to those presented in supplementary information (Fig. C.3). The behavior of the suspensions, assessed from naked eye over a couple of days (stability against sedimentation and cloudiness, see Table C.3), should provide a clear understanding as to whether or not DISA is occurring in suspension, thus enabling a prediction as to whether solvent casting will yield a satisfying outcome or not.

Other limitations involve the fact that HSP values are tabulated at 25 °C, while we used them over temperatures ranging from 25 °C to 80 °C. Predictions remain quite valid, since HSP vary with temperature as a function of the thermal dilatation coefficient and that a variation of up to 50 °C is not sufficient to significantly affect them [127, 131]. However, we do not recommend using Eq. 6.2 at much higher temperatures. Similarly, the threshold of  $\varepsilon \approx 11$  was proposed by van der Hoeven and Lyklema [119] for suspensions at room temperature. We do not know how temperature deviations affect this threshold.

Overall we believe our findings to be valid for Na-neutralized sulfuric acid-hydrolyzed CNCs with characteristics close to ours at temperature spanning around 25 to  $\sim 60$ -80 °C. We suggest that they may be extrapolated to other kinds of sulfuric acid-hydrolyzed CNCs based on vial tests assessed by a simple visual observation of what is going on in the suspension (DISA: agglomeration, sedimentation, and/or gelation). Further work would, however, be needed before confidently generalizing our approach to CNCs with distinctly different properties.

## 6.5 Concluding remarks

This work stems from the hypothesis that, as described for inorganic colloidal nanocrystals [160], the outcome of CNC solvent casting is decided by the nature of the stabilization mechanisms that prevail in suspensions. A stable suspension may indeed validate the assumption that the CNC behavior is governed by hard-core repulsion [227], which predicts the formation of chiral nematic domains as the concentration in nanorods increases [214].

In the first part of this article, we proposed a tool to classify CNC colloidal suspensions in terms of their stabilization mechanisms (none, solvation-induced, electrostatic, or solvation-induced and electrostatic) based on two solvent parameters only: the dielectric constant,  $\epsilon$ , and the chemical affinity of the solvent for CNC surfaces,  $R_a$ . In the latter part, we demonstrated how these parameters are effective in predicting the behavior of CNC suspensions upon dispersion and solvent casting. Among standing suspensions, those stabilized by a combination of electrostatic and solvation effects are the only ones not to experience DISA at low concentrations. During evaporation, EISA promotes sufficient self-ordering for a continuous and transparent (and eventually iridescent) thin film to be cast. In electrostatically-stabilized only suspensions where EISA competes with DISA, solvent casting may yield anything between a powder (DISA dominates) and a fully continuous thin film (EISA dominates). For unmodified CNCs and in the absence of electrostatic stabilization, agglomeration (DISA) is favored and solvent casting yields a powder.

While previous investigations used quantitative analysis to optimize the outcome of solvent casting in a narrow set of solvents, usually selected among the few best (such as water, formamide, N-methylformamide, N,N-dimethylformamide, or dimethylsulfoxide) [122, 123, 154], this work is the first to feature an extensive characterization that covers, based on HSP theory, the full spectrum of available chemistries. The broad range of behavior we had to assess compelled us to rely on qualitative analysis to draw a line between the best solvents, in which only EISA is possible, and the others in which DISA is competitive. Our results, formulated in terms of solvent requirements ( $\epsilon$ ;  $R_a$ ), establish categories that are transposable to a dataset of over 10,000 solvents and all of their mixtures [131]. In binary mixtures, users should carefully calculate uncertainties as they may become unworkable for closely related chemicals.

Beyond providing insights on what occurs with suspensions, perspectives for this work include the prediction of DISA upon solvent mixing (or solvent exchange), with applications in 3-D printing [226] and aerogels production [230], and of EISA upon solvent casting of CNC nanocomposites and chirally templated materials [147]. Previous research has suggested that



the ability to form helicoidal networks upon solvent casting of colloidal CNCs was correlated to the ability to do so in the presence of a third party (typically a polymer) [123, 231]. Working with colloidal CNCs in a polymer suspension was even found to improve the solvent casting as the polymer increases the viscosity of the media [231]. Interpreted to the light of this work, solvent casting is improved because polymer chains, while having little effect on the evaporation rate of the solvent, reduce the frequency of particle-particle collisions and the sedimentation rate by increasing the overall viscosity of the media. EISA is thus promoted over DISA. Surface modification, by providing CNCs with steric stabilization, may also generalize the production of optically active materials to systems casted in non-polar solvents as is the case for inorganic colloidal nanocrystals [160].

## 6.6 Conflicts of interest

There are no conflicts to declare.

## 6.7 Acknowledgments

The spray-dried nanocrystals employed in this study were kindly provided by Celluforce (Montreal, QC, Canada). The authors would like to acknowledge FPIInnovations (Pointe-Claire, QC, Canada), PRIMA Québec (grant number FPI NCC RD001), the National Science and Engineering Research Council (NSERC, grant number RDCPJ 490786-15), and the Research Center for High Performance Polymer and Composite Systems (CREPEC) for their financial contribution to this work. The Fonds de Recherche du Québec - Nature et Technologies (FRQNT) and Polytechnique Montreal kindly provided C. Bruel (number 208324) and T.S. Davies, respectively, with scholarships. The authors are grateful to Dr. W. Y. Hamad, from FPIInnovations, who kindly contributed to reviewing this work. Mr. W. Raphael and Mr. M. Gauthier are acknowledged for their assistance in acquiring the data, and especially for their contribution to the SEM imaging.

## CHAPTER 7 ARTICLE 3: ORIENTING CELLULOSE NANOCRYSTAL FUNCTIONALITIES TUNES THE WETTABILITY OF AIR/SAMPLE INTERFACES

Charles Bruel, Salomé Queffeuilou, Pierre J. Carreau, Jason R. Tavares, and Marie-Claude Heuzey. Orienting cellulose nanocrystal functionalities tunes the wettability of air/samples interfaces. Submitted to *Langmuir* on 2020/06/17.

### Abstract

Cellulose nanocrystal (CNC)-based materials display apparently erratic wetting behaviors with contact angle (CA) variations as large as  $30^\circ$  from sample to sample. This work hypothesizes that it is the orientation of CNC amphiphilic functionalities at the interface with air that causes the variability in CA. By exploiting relationships with Hansen solubility parameters theory, a set of surface tension parameters is proposed for both the polar and the non-polar surfaces of cellulose  $I_\beta$  nanocrystals. These coefficients elucidate the wettability of CNC materials by establishing a correlation between the wetting properties of the air/sample interface and its chemical composition in terms of non-polar moieties. Advancing/receding CA experiments suggest that while spin-coating CNC suspensions yields purely polar films, oven-casting them produces amphiphilic surfaces. We proposed a mechanism where the state of dispersion (individual or agglomerated) in which CNCs reach the air/water interface during casting is the determining factor: while individual nanocrystals find it more stable to orient their non-polar surfaces toward the interface, the aspect ratio of CNC agglomerates favors an orientation of their polar surfaces. This represents the first compelling evidence of CNC orientation at an interface and can be applied to Pickering emulsions, nanocomposites, and to the production of CNC materials with tuned wettability.

**Keyword:** cellulose nanocrystals; thin film wettability; interface; surface tension; surface energy.

### 7.1 Introduction

Cellulose nanocrystals (CNCs) are biosourced rod-like nanoparticles whose high aspect ratio and mechanical properties may find applications in multiphase and interfacial systems such as nanocomposites, Pickering emulsions, and membranes [232, 174, 17, 23]. This potential is

avored by the amphiphilic nature of cellulose  $I_\beta$  allomorph, whose surfaces display alternating polar and non-polar regions around their circumferences: this means that a simple rotation around their axis may change the nature of the functionalities exposed by these nanocrystals [161, 174]. Polar surfaces are hydroxyl rich and usually negatively charged due to the presence of sulfate half-ester groups introduced during the sulfuric acid hydrolysis production step (the most common approach for large-scale production). Non-polar surfaces display C-H bonds and are described as being thinner than their polar counterparts [106, 98].

Investigating the orientation and the adhesion of CNCs at various interfaces is crucial to predict the stabilizing effect they may bring to multiphase systems. As a measure of a material's cohesive interactions, surface tension,  $\gamma$ , is the main predictor for the work of adhesion between a substrate and its environment. Attempts to estimate CNC surface tension were essentially conducted through contact angle measurements [233, 207, 234], but also through gas chromatography [235] and computer simulations [110]. Experimental approaches carried over large quantities of material usually yield surface tensions values that average the behavior of CNCs and cannot distinguish polar from non-polar surfaces. While computer simulations may overcome this problem, their results cannot be verified experimentally and surface tensions tend to be suspiciously high, with up to  $155 \text{ mN m}^{-1}$  being reported [110]. This is to be compared with  $\sim 20$  to  $50 \text{ mN m}^{-1}$  for commodity polymers [236]. Overestimation may arise from the hypotheses that must be formulated for the simulations to converge. Mazeau and Rivet [109] had, for instance, to hypothesize that CNC surfaces are flat and  $\sim 10 \text{ nm}$ -wide (nearly twice the diameter of a nanocrystal) in order to study their wetting behavior.

Here, we propose an alternate approach that combines modeling, to discriminate between the amphiphilic surfaces of the nanocrystals, with experimental validation. The model, which does not require any computer simulations, relies on two recent empirical investigations: the first determined the Hansen solubility parameters (HSP) of CNC polar and non-polar surfaces [106]; the other established the first correlations between Hansen solubility and surface tension parameters for solids [237]. The method provides estimates for the surface tension parameters of CNC surfaces that rely on empirical evidences only.

Experimental validation requires the production of macroscopic surfaces with a controlled orientation of the nanocrystals. There, our approach relies on the wetting behavior of CNC thin films: the water contact angle was measured to be as low as  $\sim 10^\circ$  on films prepared from spin-coated suspensions [233] and as high as  $\sim 45^\circ$  on films prepared by compressing CNC pellets [207]. Oven-cast films have intermediate water contact angle values [233, 207]. The influence of the casting protocol, when discussed, is sometimes attributed to differences

in surface roughness between the films [207]. This interpretation does not, however, hold up to scrutiny: ranking the films by roughness, spin-coated films are expected to be the smoothest, then oven-cast films, and finally those prepared from the compression of pellets. Based on Wenzel's equation for hydrophilic materials in the homogeneous wetting regime [238, 106], spin-coated films should hence have the highest water contact angle –the opposite is observed. Dankovich and Gray [233] noted that thicker CNC films (obtained through oven-casting) resulted in higher water contact angle values than thinner films (obtained through spin-coating). Their argumentation revolved around the thickness of the films and their potential for swelling [140]. While significant swelling of CNC films has indeed been reported with polar liquids,[140] this does not explain why large variations are also observed with a non-polar liquid such as diiodomethane.

Instead, our interpretation is that the variations observed in contact angles values capture a reorientation of the amphiphilic moieties of CNC particles at the air/sample interface as a function of the casting protocol. A similar argument is formulated to justify the stability provided by CNC particles at the interface of oil/water Pickering emulsions [98, 166, 168]. There, CNCs are thought to orient their non-polar surfaces toward the oil and their polar surfaces toward water. If such a mechanism is possible in micro-emulsions, it should also occur at the air/water interface of aqueous CNC suspensions and be reflected by the wettability of the films cast from these suspensions. Bertsch et al. [163] indeed demonstrated that a significant CNC migration towards the air/water interface, measurable through interfacial rheology, may occur over time for colloidal CNCs. What is left to determine is which surfaces these nanoparticles adsorb from at the interface. Our hypothesis is thus that the casting protocol, whether it is slow or fast, steady or turbulent, has the potential to influence the migration and the orientation of CNC particles at the interface with air. This interface may then be investigated with liquids, whose wetting behaviors reflect the composition of the sample surface down to the molecular-scale.

Hence, this work first produces estimates for the surface tension parameters of CNC amphiphilic surfaces. These coefficients are used to predict how modeled surfaces, with various ratios of non-polar over polar functionalities, would behave upon wetting. The predictions are then compared with experimental results obtained on thin films that were either oven-cast (slow and steady process), or spin-coated (fast and turbulent process). This yields an estimation of the surface fractions in non-polar moieties on both kinds of films. Using two probe liquids, ethylene glycol (EG) and diiodomethane (DIM), it is possible to validate our approach. These liquids were selected in order to minimize kinetic effects such as swelling (water was found unsuitable to yield high quality contact angle data on CNC materials). Our approach establishes that CNCs should be considered as amphiphilic particles that can

orient their functionalities at air/sample interfaces and that this orientation process can influence macroscale properties such as surface wettability. A mechanism is proposed to describe the influence of the casting protocol on the composition of the interface. It may apply to the production of CNC materials with tuned wetting behaviors. Finally, by providing the first experimentally-validated estimates for the surface tension parameters of CNC polar and non-polar surfaces, this work opens the field to quantitative predictions of CNC behavior in suspensions and multiphase systems such as Pickering emulsions and polymer blends.

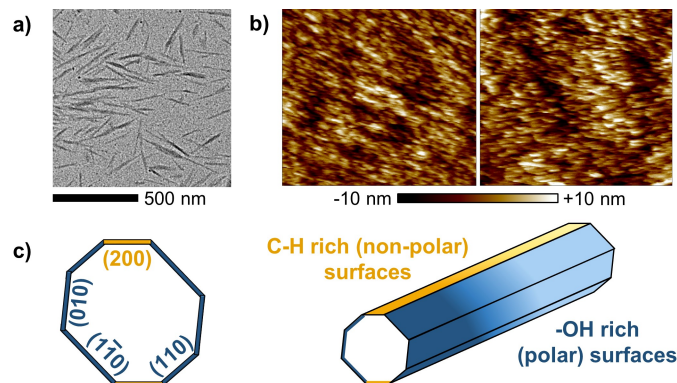


Figure 7.1 Morphology and representation of cellulose  $I_\beta$  nanocrystals. (a) TEM image of individual and agglomerated CNCs. (b) AFM height images of spin-coated (left) and oven-cast (right) CNCs. Micrographs are  $2\mu\text{m}$  wide and were flattened (by a second-order polynomial) in order to remove their mesoscale roughness. (c) On the left is the cross-section of a cellulose  $I_\beta$  nanocrystal: polar surfaces  $-(010)$ ,  $(110)$ , and  $(1\bar{1}0)$  lattice planes—are plotted in blue, and non-polar ones  $-(200)$  lattice planes—are in yellow. On the right is a scheme of the octogonally-shape nanocrystal: its lateral surfaces are constituted of polar and non-polar stripes.

## 7.2 Experimental Section

### 7.2.1 Cellulose nanocrystals

Cellulose nanocrystals were provided by Celluforce (Montreal, QC, Canada) as a spray-dried powder. They were produced through the sulfuric acid hydrolysis of a bleached softwood kraft pulp followed by neutralization with sodium hydroxide. Since morphology has been reported to play a major role in the behavior of CNC particles at interfaces [161], a detailed structural characterization of the particles is performed in supplementary information (SI). It includes transmission electron microscopy (TEM), elemental analysis, Zeta-potential, and X-ray-diffraction (XRD). Fig. 7.1.a is a TEM image of the rod-like nanocrystals that shows a mix of individual and agglomerated particles. It was obtained by drying a dilute suspension of

nanocrystals over a TEM grid. Nanocrystals are  $\sim 7\text{-}8\text{ nm}$  wide and  $\sim 105\text{-}120\text{ nm}$  long based on these analyses (see details and protocols in SI). Fig. 7.1.b are atomic force microscopy (AFM) height images of CNCs that were either spin-coated (left) or oven-cast (right). The micrographs are  $2\text{ }\mu\text{m}$  wide and were flattened (by a second-order polynomial) in order to remove their mesoscale roughness: they highlight the parallel alignment of CNC particles at the air/sample interface.

For graphical purposes, this work considers CNCs to have an octagonally-shaped cross-section as per Kalashnikova et al. [98] (Fig. 7.1.c). The validity of this hypothesis is discussed in SI and supported by the deconvolution of the XRD spectra and their analysis using Scherrer's equation [95, 96, 97]. Neglecting the extremities of the rod, a cellulose  $I_\beta$  nanocrystal exposes up to four different kinds of lateral surfaces, each corresponding to a lattice plane: (010), (110), ( $1\bar{1}0$ ), and (200) [161]. While (200) surfaces primarily display C-H bonds, the three others are rich in hydroxyl groups and have roughly equivalent chemistries [108, 110, 106]. They will be referred as non-polar and polar surfaces throughout this work and be represented in yellow and blue, respectively. Hence, CNCs display a majority of polar surfaces that are combined with some non-polar ones. This is coherent with their behavior in suspensions where CNCs display a predominantly polar behavior doubled by a non-polar component [106, 215].

### 7.2.2 CNC film preparation

Spray-dried CNCs were dispersed in water at a concentration of  $30\text{ mg}_{\text{CNC}}/\text{mL}$  using an ultrasonic probe (Cole-Parmer), which operated with a CV334 converter and a tapered microtip. The suspensions were prepared adding  $15\text{ mL}$  of water atop  $0.45\text{ g}$  of CNCs in a glass vial ( $2.1\text{ cm}$  of radius). As per Beuguel et al. [145], an energy of  $4.5\text{ kJ}$  ( $10\text{ kJ/g}_{\text{CNC}}$ ) was then provided to the system at a frequency of  $20\text{ kHz}$  and a power of  $\sim 30\text{ W}$  using ON-OFF pulses ( $5\text{ s-}2\text{ s}$ ) and an ice bath to avoid any overheating. Since our CNCs do not form significant structuring below  $\sim 40\text{ mg}_{\text{CNC}}/\text{mL}$  [145], the resulting suspensions are expected to be isotropic. The suspensions were either poured in a polystyrene Petri dish ( $10\text{ cm}$  of diameter) and placed in an oven (OV-11, MBI Lab Equipment) at  $60^\circ\text{C}$  and near atmospheric pressure ( $\sim 0.9\text{ bar}$ ) for  $24\text{ h}$ , or used for spin-coating. In the latter, a few  $\text{mL}$  of suspension were placed at the center of a polished n-type Si wafer ( $15\text{ cm}$  of diameter), that was spun at  $500\text{ rpm}$  (revolutions per minute) for  $20\text{ s}$  in a spin-coater (Brewer Science CEE-200). Immediately after, the spun-discs were deposited on a hot plate ( $60^\circ\text{C}$ ) for a few minutes. Drying, evidenced by the apparition of iridescent patterns, occurred within a few seconds. This process, from liquid deposition to iridescent patterns formation was typically shorter than  $2\text{ min}$ .

While the oven-cast (OC) films were free-standing (thickness of  $\sim 40\text{ }\mu\text{m}$ ) and could be analyzed as such, the spin-coated (SC) layer ( $\sim 1\text{ }\mu\text{m}$  thick) was stuck on the support. Hence, analyses of SC thin films were carried on the layer still deposited atop the Si wafer. Those requiring a minimal thickness for the sample, such as XRD and elemental analysis, were only performed on the OC films.

### 7.2.3 Contact angle measurements

Contact angle measurements were performed at room temperature ( $\sim 23^\circ\text{C}$ ) on a OCA20 tensiometer (DataPhysics Instruments GmbH) operating with a high-resolution CCD camera and a motorized syringe (0.50 mm of outer diameter). Ethylene glycol (EG) and diiodomethane (DIM) were used as probe liquids. Through pendant drop experiments, their surface tensions were found to be within  $1\text{ mN m}^{-1}$  ( $\sim 2\%$ ) of their theoretical values ( $48\text{ mN m}^{-1}$  for EG, and  $50.8\text{ mN m}^{-1}$  for DIM). From casting to testing, thin films were stored with covers in a ventilated environment. Prior to analyses, their surfaces were subjected to a cleaning with compressed air in order to desorb any potential contaminant and remove humidity traces. Cleaning was achieved with a compressed air gun operating at  $\sim 2\text{ bar}$  for  $\sim 1\text{ min}$ .

In a typical static sessile drop experiment, a droplet of  $3\text{ }\mu\text{L}$  is grown at the tip of the syringe, far from the sample, at a rate of  $0.5\text{ }\mu\text{L s}^{-1}$ . It is then deposited on the substrate and the measurement is taken after 5 s based on the video footage.

For advancing/receding contact angle (ARCA) experiments, the tip of the needle was first cleaned with the probe liquid, dried, then placed at  $\sim 0.5\text{ mm}$  from the substrate. A volume of  $4\text{ }\mu\text{L}$  (DIM as probe liquid) or  $5\text{ }\mu\text{L}$  (EG) was then injected at a rate of  $0.1\text{ }\mu\text{L s}^{-1}$ . The discrepancy between DIM and EG in terms of injected volumes arises from their differences in terms of dewetting behaviors: a lower receding CA value (as with EG) requires to grow a larger drop in order to witness any receding. Once the injection was completed, and after a delay of at least 5 s (typically  $\sim 10\text{ s}$ ), the liquid was withdrawn from the substrate at the same rate ( $0.1\text{ }\mu\text{L s}^{-1}$ ). The drop remained roughly axisymmetric during the whole process.

ARCA measurements were obtained based on video footages. The baseline and the shape of the drop were fitted automatically as a function of the light contrast between the drop, the substrate, and the background. The contact angle was then determined using the Young-Laplace equation. A manual fitting was performed for each test to confirm the validity of the automatically-derived measurements. Measurements were performed during the period where the base diameter of the drop,  $D^{\text{drop}}$ , was greater than 3 mm (6 times the needle's diameter) in order to minimize the influence of the needle over the shape of the droplet [239].

The ratio between the hydrodynamic forces and the surface tension of the liquid,  $\gamma^l$ , is defined as the capillary number,  $N_{Ca}$  (Eq. D.4). The ratio between the gravitational forces and  $\gamma^l$  is defined as the Bond number,  $N_{Bo}$  (Eq. D.5). In our experiments, the surface tension largely dominated the force balance by 2 to 3 orders of magnitude (see SI, section “Capillary and Bond numbers”). In terms of importance, it is followed by gravitational forces ( $N_{Bo} \approx 10^{-2}$ - $10^{-3}$ ) and then viscous forces ( $N_{Ca} \approx 10^{-5}$ - $10^{-6}$ ). Hence, the protocol described here-above makes it possible to model ARCA results based on surface tension-related considerations only. Furthermore and according to Strobel and Lyons [240],  $N_{Ca} < 10^{-5}$  generally ensures that the CA measured at the moving three-phase boundary is equal to that measured just after it stops, i.e. that it corresponds to a thermodynamic state. Overall, this condition was verified during our experiments. A nomenclature of the symbols employed throughout this work is provided in Table D.1.

### 7.3 A model for the wettability of CNC films based on the orientation of their lattice plane

#### 7.3.1 Contact angles: a background

A liquid droplet sitting on a surface has a three-phase boundary between the liquid, the solid, and the air, that is characterized by its contact angle (CA) [241]. Ideal substrates are expected to be flat, rigid, chemically homogeneous, and unperturbed by the chemical interactions they may form with the liquid [242]. There, the Young contact angle,  $\theta_Y$ , is the single CA that may form at rest: it is a thermodynamic equilibrium that may be met independently of the sample’s or the drop’s history [241]. According to Young’s equation,  $\theta_Y$  is a function of the surface tensions of the solid,  $\gamma^s$ , of the liquid,  $\gamma^l$ , and of the interfacial tension between the liquid and the solid,  $\gamma^{s/l}$  [241]:

$$\gamma^s = \gamma^{s/l} + \gamma^l \cos(\theta_Y) \quad (7.1)$$

On real substrates, deviations from ideality create hysteresis, defined as a difference between the wetting and dewetting behaviors. Irregularities impede the progression of the liquid upon wetting, and prevent its receding upon dewetting [241]. In a dynamic experiment, the highest CA value is thus measured in advancing conditions: the advancing contact angle,  $\theta_a$ ; and the lowest CA in receding conditions: the receding contact angle,  $\theta_r$ . The contact angle hysteresis,  $H$ , is defined as  $H = \theta_a - \theta_r$  ( $H \geq 0^\circ$ ).  $H$  is a direct measure of a sample’s deviation from ideality [241].



There are two kinds of hysteresis: kinetic and thermodynamic [241, 242, 240]. Kinetic hysteresis arises from physical and chemical interactions occurring at the interfaces [242]. It includes: swelling, chemical reactions, and reorientation of the functional groups at the liquid/solid interface; evaporation at the air/liquid interface; adsorption of contaminants or vapor molecules at the air/solid interface; or the diffusion of liquid throughout the sample. Thermodynamic hysteresis is caused by surface heterogeneities in terms of roughness or chemistry [242]. In practice, near ideal substrates have an hysteresis in the range of 1-2°, and  $H$  commonly reaches  $\sim 10^\circ$  for real substrates [241, 242, 240]. It may be as high as 50-60° in some circumstances [243].

In this work, kinetic and roughness-induced hystereses were minimized, respectively by appropriately identifying the most suited probe liquids (SI: section “Minimization of kinetic hysteresis”) and by producing films whose surface roughness is in the range of a single nanocrystal diameter (SI: section “Thermodynamic hysteresis”). This leaves chemical heterogeneity as the main source of hysteresis.

### 7.3.2 Wettability of real chemically heterogeneous surfaces

Assuming an expression for the interfacial tension between the liquid and the solid,  $\gamma^{s/l}$ , it is possible to measure the theoretical Young contact angle from  $\gamma^s$  and  $\gamma^l$ , only. Several models were proposed for  $\gamma^{s/l}$ , the most employed being the Owens-Wendt-Rabel-Kaelble (OWRK) model. It splits the total surface tension,  $\gamma$ , into a dispersive,  $\gamma_D$ , and a polar component,  $\gamma_P$  (Eq. 7.2).  $\gamma_P$  accounts both for dipole-dipole and Lewis acid/base (including H-bonding) interactions.

$$\gamma = \gamma_D + \gamma_P \quad (7.2)$$

The OWRK model expresses the total interfacial tension  $\gamma^{s/l}$  as a geometric mean that considers  $\gamma^s$  and  $\gamma^l$  components:

$$\begin{aligned} \gamma^{s/l} &= \gamma_D^{s/l} + \gamma_P^{s/l} \\ &= \left( \sqrt{\gamma_D^s} - \sqrt{\gamma_D^l} \right)^2 + \left( \sqrt{\gamma_P^s} - \sqrt{\gamma_P^l} \right)^2 \\ &= \gamma^s + \gamma^l - 2 \left( \sqrt{\gamma_D^s \gamma_D^l} + \sqrt{\gamma_P^s \gamma_P^l} \right) \end{aligned} \quad (7.3)$$

Note that a good compatibility between the materials results in a low interfacial tension. It is null ( $\gamma^{s/l}=0$ ) if the components of the liquid match those of the solid. Combining Eqs. 7.1&7.3 yields:

$$\cos(\theta_Y) = \frac{2}{\gamma^l} \left( \sqrt{\gamma_D^s \gamma_D^l} + \sqrt{\gamma_P^s \gamma_P^l} \right) - 1 \quad (7.4)$$

This equation is only valid if  $\gamma^s < \gamma^l + \gamma^{s/l}$ , which, in practice, remains the case as long as the surface tension of the liquid is high enough. Otherwise, the liquid totally wets the surface, thus forming a zero-contact angle. Van Oss et al. [244] proposed a threshold of  $\gamma^l \gtrsim 44 \text{ mN m}^{-1}$  above which probe liquids should be suitable for the analysis of most common surfaces.

Surface roughness may shift the value of  $\theta_Y$ , and an apparent Young's ("Wenzel") contact angle,  $\theta_W$ , is measured instead [238, 241]. In the homogeneous wetting regime, this may be accounted for by the Wenzel equation, in which  $r_{\text{surf}}$ , dimensionless, is defined as the surface area of the sample divided by its projected surface area ( $r_{\text{surf}}=1$  for a perfectly smooth surface):

$$\cos(\theta_W) = r_{\text{surf}} \cos(\theta_Y) \quad (7.5)$$

$r_{\text{surf}}$  stood at  $1 < r_{\text{surf}} \leq 1.02$  for all our samples due to their relative flatness (see SI). Our modeling hence assumes that  $\cos(\theta_W) \approx \cos(\theta_Y)$ .

Chemical heterogeneity may be accounted for using a generalized Cassie-Baxter equation [245]. CNCs are amphiphilic particles, on which the liquid is expected to form a Young's contact angle equal to  $\theta_Y^{\text{ps}}$  with polar surfaces ("ps") that have a higher surface energy, and equal to  $\theta_Y^{\text{nps}}$  with non-polar surfaces ("nps") that have a lower surface energy ( $\theta_Y^{\text{nps}} > \theta_Y^{\text{ps}}$ ). On a substrate composed by a mix of these polar and non-polar surfaces, with respective surface fractions of  $f^{\text{ps}}$  and  $f^{\text{nps}}$  (with  $f^{\text{ps}}=1-f^{\text{nps}}$ ), a composite contact angle,  $\theta_{\text{comp}}$ , is measured [245]:

$$\cos(\theta_{\text{comp}}) = f^{\text{nps}} \cos(\theta_Y^{\text{nps}}) + (1 - f^{\text{nps}}) \cos(\theta_Y^{\text{ps}}) \quad (7.6)$$

Combining Eq. 7.6 with Eq. 7.4 applied to polar and non-polar surfaces yields:

$$\cos(\theta_{\text{comp}}) = \frac{2}{\gamma^l} \left[ f^{\text{nps}} \left( \sqrt{\gamma_D^{\text{nps}} \gamma_D^l} + \sqrt{\gamma_P^{\text{nps}} \gamma_P^l} \right) + (1 - f^{\text{nps}}) \left( \sqrt{\gamma_D^{\text{ps}} \gamma_D^l} + \sqrt{\gamma_P^{\text{ps}} \gamma_P^l} \right) \right] - 1 \quad (7.7)$$

### 7.3.3 CNC surface tension parameters

Eq. 7.7 relates the predicted contact angle formed by the liquid over the sample,  $\theta_{\text{comp}}$ , to its composition,  $f^{\text{nps}}$ . It assumes that the surface tension components of the solid ( $\gamma_{\text{D}}^{\text{nps}}$ ,  $\gamma_{\text{P}}^{\text{nps}}$ ,  $\gamma_{\text{D}}^{\text{ps}}$ , and  $\gamma_{\text{P}}^{\text{ps}}$ ) can be estimated. This was achieved by exploiting the empirical correlations between surface tension and Hansen solubility parameters (HSP). The HSP of CNCs were determined in a previous work [106]. HSP represent a set of three parameters:  $\delta_{\text{D}}$ ,  $\delta_{\text{P}}$ , and  $\delta_{\text{H}}$ , which account for the potential of the surface in terms of dispersive, polar (dipole-dipole), and hydrogen-bonding (and other Lewis acid/base) interactions, respectively [127]. They are expressed as the square-root of an energy density (in  $\text{MPa}^{1/2}$ ). The polar surfaces of CNCs had estimated HSP of  $\{\delta_{\text{D}}^{\text{ps}}; \delta_{\text{P}}^{\text{ps}}; \delta_{\text{H}}^{\text{ps}}\} = \{18.1; 20.4; 15.3\} \pm \{0.5; 0.5; 0.4\} \text{ MPa}^{1/2}$ , while the non-polar surfaces were estimated at:  $\{\delta_{\text{D}}^{\text{nps}}; \delta_{\text{P}}^{\text{nps}}; \delta_{\text{H}}^{\text{nps}}\} = \{17.4; 4.8; 6.5\} \pm \{0.3; 0.5; 0.6\} \text{ MPa}^{1/2}$  [106]. Together, they constitute the total (or “Hildebrand”) solubility parameter,  $\delta_{\text{T}}$  (Eq. 7.8), that accounts for the potential of cohesion between a substrate and its environment.

$$\delta_{\text{T}} = \left( \delta_{\text{D}}^2 + \delta_{\text{P}}^2 + \delta_{\text{H}}^2 \right)^{1/2} \quad (7.8)$$

HSP are by definition closely related to surface tension since they both relate to the amount of interactions that a material may form with its environment. Hence, it should be possible to express the surface tension as a function of HSP. While previous models also relied on molar volume [246, 247, 248, 131], Jia and Shi [249] recently proposed a direct correlation between  $\gamma_{\text{D}}$  and  $\delta_{\text{D}}$  that was applicable to liquids and polymers. Yu and Hou [237] generalized these models to the various components of surface tension. Four empirical equations were proposed,  $\gamma = f(\delta_{\text{T}})$  (Eq. 7.9);  $\gamma = f(\delta_{\text{D}}, \delta_{\text{P}}, \delta_{\text{H}})$  (Eq. 7.10);  $\gamma_{\text{D}} = f(\delta_{\text{D}})$  (Eq. 7.11); and  $\gamma_{\text{P}} = f(\delta_{\text{P}}, \delta_{\text{H}})$  (Eq. 7.12). Two further correlations explored in their work,  $\gamma_{\text{P}} = f(\delta_{\text{P}})$  and  $\gamma_{\text{P}} = f(\delta_{\text{H}})$ , are not considered here: these correlations have systematic deviations at high  $\gamma_{\text{P}}$  values (over- or underestimations). It is consistent with the fact that  $\gamma_{\text{P}}$  accounts for all non-dispersive interactions, i.e for polar and Lewis acid/base interactions. It should thus be predicted from both  $\delta_{\text{P}}$  and  $\delta_{\text{H}}$  as in Eq. 7.12.

$$\gamma = 1.88 \delta_{\text{T}}^{0.94} \quad (7.9)$$

$$\gamma = 0.12 [\delta_{\text{D}} + 0.25 (\delta_{\text{P}} + \delta_{\text{H}})]^{1.86} \quad (7.10)$$

$$\gamma_D = 0.035\delta_D^{2.34} \quad (7.11)$$

$$\gamma_P = 4.30 \times 10^{-2} (\delta_P + \delta_H)^{1.75} \quad (7.12)$$

Eq. 7.9 gives estimates that are slightly smaller than those provided by Eq. 7.10. Considered together, they provide a lower and an upper bound for CNC surface tensions with  $\gamma^{ps}$  and  $\gamma^{nps}$  ranging from  $\sim 47.8$  to  $55.2 \text{ mN m}^{-1}$  and from  $\sim 30.3$  to  $32.2 \text{ mN m}^{-1}$ , respectively. Through Eqs. 7.11&7.12, it is possible to estimate the dispersive and polar components and check that their sum fall within these ranges. Uncertainties reported here are those that arise from HSP. For the polar surfaces, the sum of  $\gamma_D^{ps}$  ( $30.7 \pm 2.0 \text{ mN m}^{-1}$ ) and  $\gamma_P^{ps}$  ( $22.4 \pm 1.0 \text{ mN m}^{-1}$ ) yields a  $\gamma^{ps}$  of  $53.1 \pm 3.0 \text{ mN m}^{-1}$ . For the non-polar surfaces, it was  $\gamma_D^{nps} = 28.0 \pm 1.1 \text{ mN m}^{-1}$  and  $\gamma_P^{nps} = 3.0 \pm 0.5 \text{ mN m}^{-1}$  for a sum of  $\gamma^{nps} = 31.0 \pm 1.6 \text{ mN m}^{-1}$ . These surface tension values, summarized in Table 7.1, fall within the ranges calculated through Eqs. 7.11&7.12 and are considered in the rest of this work.

Despite being more conservative than those published previously (Table D.4), these estimates are in line with what can be expected from a polymeric material ( $\sim 20 \text{ mN m}^{-1}$  to  $50 \text{ mN m}^{-1}$  for commodity polymers [236]). Historically, characterizing surface tension has been challenging for cellulose rich materials [233]. Wood, itself, is commonly measured in a range as large as  $\sim 40$  to  $90 \text{ mN m}^{-1}$  [250]. Besides variations in the samples' composition, issues in contact angle measurements arise from the potential porosity, swelling behaviors, and anisotropic roughness of the material. These are all susceptible to lower the contact angle values measured at the interface between the sample and the liquid, which leads to an overestimation of the solid apparent surface tension. Since previous CA studies all relied on water as a probe liquid and that water interacts strongly with CNCs [140, 106, 173], our interpretation is that these works [233, 207] overestimated the surface tension of CNCs.

## 7.4 Results and discussion

### 7.4.1 Wettability results

The various phases of an ARCA experiments and the process through which they were analyzed are presented in SI (section “ARCA experiments and analyses”). To account for the local nature of a drop-based measurement (analysis of few  $\text{mm}^2$  only), each film was analyzed on at least three locations and at least three films were produced for each condition. It represents a minimum of 9 repetitions per experimental condition (excepted  $\theta_r^{EG}$ , which is

Table 7.1 Surface and interfacial tension parameters (expressed in  $\text{mN m}^{-1}$ ). Our approach distinguishes between polar and non-polar surfaces for the parameters of cellulose  $\text{I}_\beta$  nanocrystals (see Fig. 7.1). References for the surface tension of liquids are provided in SI. “Abbr.” stands for the abbreviation through which the substrates are referred to within the text.

Substrate	Abbr.	Surface tension parameters			Interfacial tensions <sup>a,b</sup>		
		$\gamma$	$\gamma_D$	$\gamma_P$	ps	nps	w
Polar surfaces	ps	$53.1 \pm 3.0^c$	$30.7 \pm 2.0^c$	$22.4 \pm 1.0^c$	0	-	-
Non-polar surfaces	nps	$31.0 \pm 1.6^c$	$28.0 \pm 1.1^c$	$3.0 \pm 0.5^c$	$\sim 9.0$	0	-
Water	w	72.8	21.8	51.0	$\sim 6.4$	$\sim 29.6$	0
Hexadecane	h	27.0	$\sim 27.0$	$\sim 0.0$	$\sim 22.5$	$\sim 3.0$	$\sim 51.3$
Ethylene glycol	EG	48.0	22.6	25.4	$\sim 0.6$	$\sim 11.2$	-
Diiodomethane	DIM	50.8	48.5	2.3	$\sim 12.3$	$\sim 2.8$	-

<sup>a</sup> The interfacial tension with air is assumed to be equal to the surface tension  $\gamma$ .

<sup>b</sup> Estimated based on the Owens-Wendt-Rabel-Kaelble (OWRK) model (Eq. 7.3).

<sup>c</sup>  $\gamma = \gamma_D + \gamma_P$ , with  $\gamma_D$  and  $\gamma_P$  calculated from Eqs. 7.11&7.12, respectively. Uncertainties reflect those on the HSP values.

based on 3 repetitions only). Uncertainties reported in the text and error bars plotted on the graphs are standard deviations. A full breakdown of the results and their statistical analysis, including 95% confidence intervals, is provided in Table D.5.

Figs. 7.2.a&c plot the wettability results obtained with DIM (in purple) and EG (in green) on spin-coated and oven-cast films, respectively. ARCA measurements on OC films yielded  $\theta_a$  (empty triangles up) and  $\theta_r$  (empty triangles down) values of  $41.0 \pm 4.3^\circ$  and  $15.0 \pm 1.8^\circ$  with EG. It was  $46.1 \pm 1.2^\circ$  and  $16.7 \pm 1.3^\circ$  with DIM. These imply significant hysteresis,  $H$ , of  $\sim 26^\circ$  and  $\sim 30^\circ$ , respectively.

On the SC films, contact angles values dropped to  $\theta_a = 10.2 \pm 0.6^\circ$  and  $\theta_r = 0^\circ$  (no receding) with EG. The lack of any receding prevents an accurate determination of the hysteresis, which may only be said to be smaller than  $\sim 10^\circ$ . Note that no significant variations were observed by increasing the drying time of the spin-coated films from a few minutes to 24 h (same conditions as the oven-cast films). With DIM,  $\theta_a$  and  $\theta_r$  were measured at  $34.8 \pm 3.4^\circ$  and  $11.6 \pm 1.8^\circ$ , corresponding to an hysteresis of  $\sim 23^\circ$ . It was a concern that the spin-coated layer could be too thin to prevent the substrate from affecting the measurement, especially for EG, which seems to swell the film ( $\theta_r = 0^\circ$ ). However, preliminary tests performed on bare Si wafers yielded EG advancing contact angles that were greater than those measured on the spin-coated films ( $14.1 \pm 0.5^\circ$  instead of  $10.2 \pm 0.6^\circ$ ). Furthermore, CA measurements performed on films spun at 4000 rpm (and thus thinner than those prepared at 500 rpm) yielded results that were not statistically different ( $11.2 \pm 0.5^\circ$  instead of  $10.2 \pm 0.6^\circ$ ). Hence, we do not believe the substrate to influence the measurements: the abrupt lowering in CA

values observed with EG between oven-cast and spin-coated films may be attributed to a variation at the surface of the CNC coating rather than to an influence of the thickness or of the substrate.

Since kinetic hysteresis and surface roughness were preemptively minimized, the concordant variation in CA hysteresis between the samples for both EG and DIM can be attributed to the surface chemistry of the films: spin-coated films are chemically more homogeneous than oven-cast ones. The fact that this decrease in  $H$  is driven by a drop of the advancing contact angle values suggests that spin-coated films have a higher apparent surface energy. Thus, spin-coating a CNC suspension, instead of oven-casting it, leads to an impoverishment of air/sample interfaces in non-polar moieties. Furthermore, the lack of any receding with EG points to a very good interface between the SC film and the probe liquid. Since EG has interfacial tensions (Eq. 7.3) of  $\sim 0.6 \text{ mN m}^{-1}$  and  $\sim 11.2 \text{ mN m}^{-1}$  with the polar and non-polar surfaces of CNCs, respectively, this lack of receding is coherent with the surface being rich in polar moieties.

#### 7.4.2 Chemical composition of air/sample interfaces

The most likely interpretation from wettability results is that oven-cast films are richer in (200) surfaces than spin-coated substrates, which translates into a greater chemical homogeneity for the latter. This interpretation may be confronted with the projections derived from Eq. 7.7 by plotting  $\theta_{\text{comp}}$  as a function of the surface fraction in non-polar surfaces,  $f^{\text{nps}}$  (Fig. 7.2.b). Considering the smoothness of CNC thin films and their propensity for kinetic phenomena such as swelling, the advancing contact angle is likely to be the most representative estimate of the composite contact angle  $\theta_{\text{comp}}$  in the generalized Cassie-Baxter equation (Eq. 7.7). Furthermore, advancing contact angles are the most representative CA to detect non-polar moieties [240, 251]. This is because low surface tension areas tend to prevent the liquid from advancing, which reflects on  $\theta_{\text{a}}$  values.

Projecting the advancing contact angle values on our model (hypothesis  $\theta_{\text{a}} \approx \theta_{\text{comp}}$ ) returns an estimate of  $f^{\text{nps}}$ . This projection is highlighted on Fig. 7.2 by the dashed lines that cross from Fig. 7.2.a to 7.2.b, and from 7.2.c to 7.2.b, respectively.  $f^{\text{nps}}$  estimates, whether determined from EG or DIM advancing contact angle values, are consistent: they are in the range of  $\sim 0.42$ - $0.44$  and  $\sim 0$ - $0.03$  for oven-cast and spin-coated films, respectively. These ranges may be extended to  $\sim 0.34$ - $0.50$  and  $\sim 0$ - $0.06$  once the standard deviations on  $\theta_{\text{a}}$  values are considered. It is consistent with our previous findings: spin-coated films are poorer in non-polar surfaces and chemically more homogeneous than oven-cast substrates.

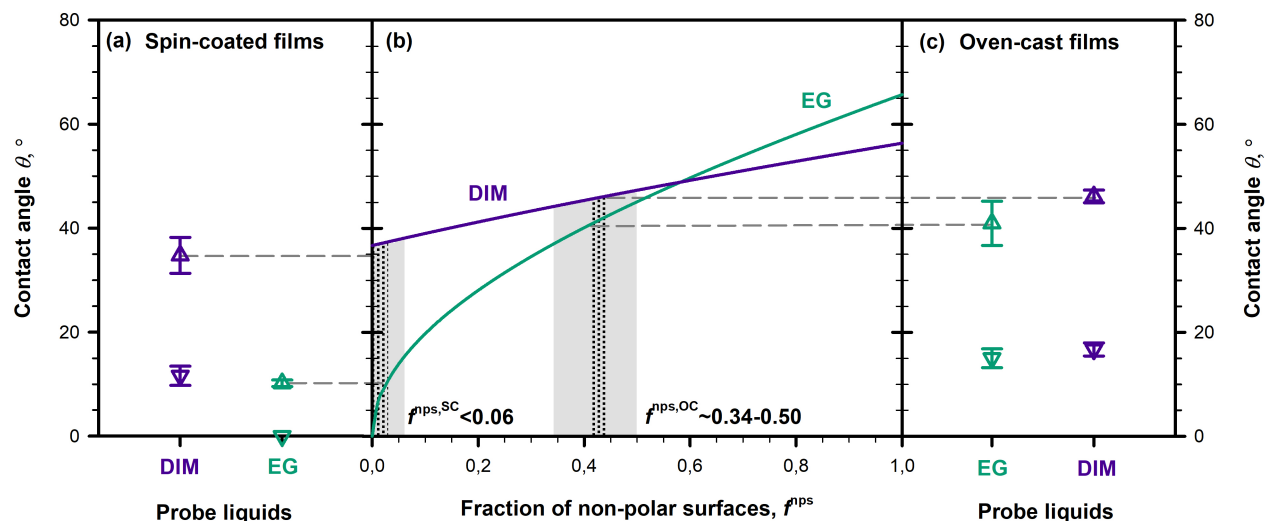


Figure 7.2 ARCA results for spin-coated (a) and oven-cast (c) films and their predictions in terms of non-polar fraction,  $f^{nps}$ , for the air/sample interface (b). EG and DIM results are plotted in green and purple, respectively. Average  $\theta_a$  values are represented by empty triangles up and  $\theta_r$  values by empty triangles down. In (b), filled lines are the plots of  $\theta_a$  as a function of  $f^{nps}$  (Eq. 7.7) for EG and DIM. The projection of  $\theta_a$  values (grey dashed lines) over these plots provides estimates for the samples' surface content in non polar surfaces. The consistency observed between the  $f^{nps}$  predictions derived from EG and DIM (with  $\sim 0.02$ - $0.03$  between both predictions, highlighted by the dotted areas) confirms the validity of CNC surface tension parameters. Error bars in (a)&c are standard deviations. Their influence on the determination of  $f^{nps}$  is highlighted by the grey areas in (b).

An analysis of the standard deviations highlights that reproducibility is better through spin-coating than through oven-casting. The large uncertainty observed on  $f^{nps}$  (0.34 to 0.50) for oven-cast films actually arises from film-to-film variations. This is highlighted in Fig 7.3.a, where EG advancing contact angle values measured for each film are plotted as a function of the model predictions for  $f^{nps}$ . EG was chosen for its greater sensitivity to the orientation of CNCs. Average  $\theta_a$  values for spin-coated and oven-cast films are represented by green triangles (as in Fig. 7.2).  $\theta_a$  values for each film are plotted in black (SC films) or brown (OC films). The figure's inset is a zoom to help the visualization of the spin-coated results. There are little deviations from sample to sample and spin-coating seems to repeatably yield thin films whose  $f^{nps}$  are in the range of 0.02-0.03 (based on EG results). For oven-cast films, uncertainties on  $f^{nps}$  are within  $\pm 0.03$ , which suggests that surface heterogeneities are well dispersed across the sample. However, each film is statistically different from the other.

To investigate further the reproducibility of the oven-casting process, 7 new OC films were prepared and investigated through static sessile drop measurements. In our case, static sessile drop measurements fell within  $\sim 1^\circ$  of the advancing contact angle values, meaning that they constitute an effective way to quickly probe a larger amount of samples. Fig 7.3.b plot the distribution of 30 sessile drop CA and confirms the low repeatability of the oven-casting process: CA values spread over nearly 4 decades from  $\sim 12^\circ$  to  $\sim 50^\circ$ . CA measurements at the bottom of the distribution (pointed by the red arrow) were measured on different locations of a same film that apparently failed to orient its non-polar fonctionnalités toward the air/sample interface. Hence, over the 10 oven-cast films we analyzed (3 through ARCA and 7 through sessile drop measurements), 9 managed to orient at different extents their non-polar functionalities to the air interface and produced EG contact angles ranging from  $\sim 30$  to  $\sim 50^\circ$ . The last film produced CA values ranging from  $\sim 12$  to  $\sim 16^\circ$ , which is close to what can be measured on spin-coated films ( $\theta_a = 10.2 \pm 0.6^\circ$ ). Sessile drop measurements performed on the same films with DIM (Fig 7.3.c) show a lesser variability from film to film, which underlines the greater sensitivity of EG to non-polar surface orientation. The red arrow in Fig 7.3.c points towards the results that were gathered from the film already highlighted in Fig 7.3.b.

#### 7.4.3 Speculative mechanism for CNC orientation at the air/water interface

Based on Eq. 7.3, water has interfacial tensions of  $\gamma^{\text{ps/w}} = 6.4 \text{ mN m}^{-1}$  and  $\gamma^{\text{nps/w}} = 29.6 \text{ mN m}^{-1}$  with the polar and non-polar surfaces of CNCs, respectively (Table 7.1). To understand what may happen in suspensions, it is possible to calculate the energy variations that result from the various options available to the nanocrystal. Fig. 7.4 plots these various paths, which involve migration to the air/water interface and/or agglomeration, and propose a mechanisms for CNC orientation at the air/sample interface. In the case of interfacial migration, a scenario in which the nanocrystal remains fully immersed in water (with the exception of the adsorbed surfaced) was considered: the influence of CNC normal positioning at the air/water interface over the energy variation was found to be secondary and was hence neglected. The exact normal positioning of CNCs at interfaces remains to be computed: experimentally, the nanocrystals were reported to be mostly immersed in water at air/water interfaces [163] and fully immersed in water at oil/water interfaces [168]. Energy calculations were done by amalgamating surface tensions with surface energies, which equates to neglecting the heat generated by the process [241]. Energy variations due to ionic bond dissociation (occurring on the sulfate half-ester groups of CNCs) are also neglected. While CNC negative charges may have an effect on the kinetics of the processes described here-below (because of electrostatic stabilization for instance), energy variations associated with these charges are small in front of



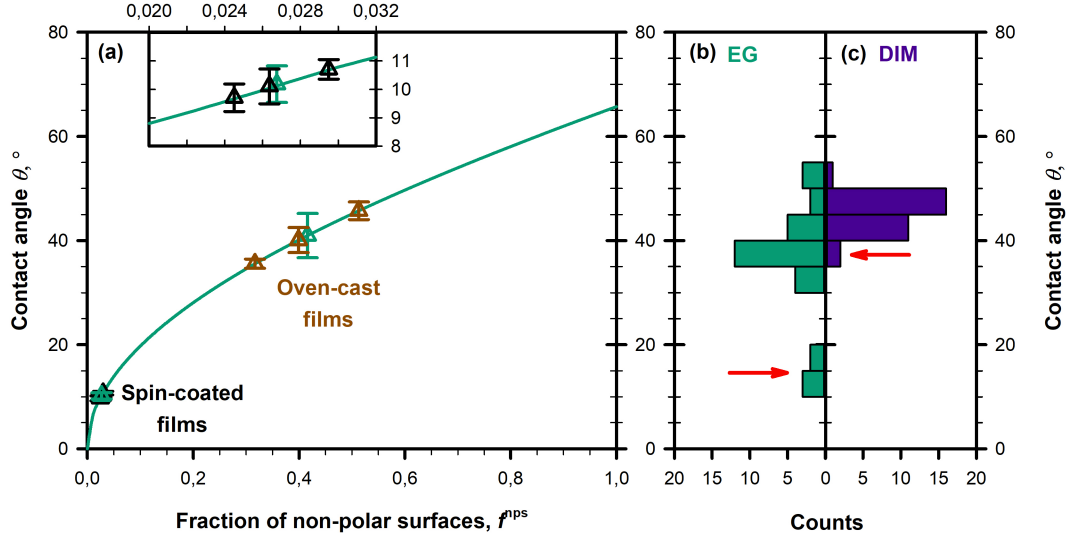


Figure 7.3 Repeatably of CNC orientation during the spin-coating and oven-casting processes based on EG results (a). The green line and the green triangles up are the plots for Eq. 7.7 and for the average advancing CA values (see Fig. 7.2). The black and brown triangles up represent the advancing CA values measured for each of the spin-coated and oven-cast films, respectively. The insert is a zoom of the spin-coated results for greater readability. Error bars are standard deviations. Sessile drop measurements taken on 7 additional oven-cast films with EG (b) and DIM (c). The results pointed by the red arrows are from a single data set, taken on a film that apparently failed to orient its non-polar functionalities at the air/sample interface to the same extent as the 6 other samples.

interfacial phenomena and should not affect the thermodynamics of the system (justification provided in SI). It is worth underlining that beyond energy calculations, the mechanism hypothesized in this section yet remains to be supported by experimental evidences.

When an individual CNC (Fig. 7.4.a) migrates from the water bulk towards the air/water interface, it removes an air/water and a water/solid interface and creates an air/solid one. The surface energy difference may thus be calculated as  $\Delta E \approx \gamma^{\text{nps}} - \gamma^{\text{nps/w}} - \gamma^{\text{w}} \approx -71 \text{ mJ m}^{-2}$  if a non-polar surface adsorbs at the air/water interface, and as  $\Delta E \approx -26 \text{ mJ m}^{-2}$  if it is a polar surface. Therefore, the air/water interface is better stabilized by the adsorption of a non-polar surface (Fig. 7.4.d). This assumes that the surface areas in terms of polar and non-polar moieties are comparable, which is roughly the case for the sidewalls of an individual nanocrystal.

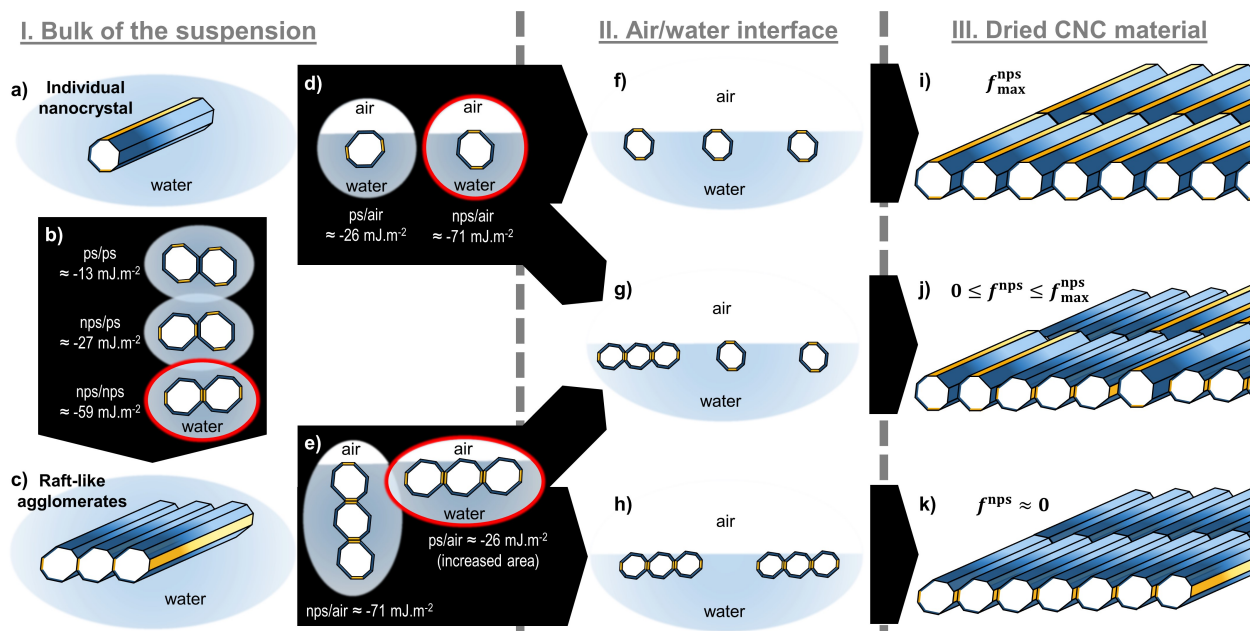


Figure 7.4 Mechanism for CNC orientation at the air/sample interface. Assuming CNCs are initially well dispersed (a), they may either migrate to the air/water interface as individual nanocrystals or first agglomerate in the water bulk. Upon agglomeration (b), CNCs preferentially assemble their non-polar surfaces to form raft-like structures (c). Upon migration towards the air/water interface, individual CNCs orient their non-polar surfaces towards the air (d). 2-D agglomerates may, however, prefer to orient their polar surfaces if their cross-sectional aspect ratio is large enough (e). Depending on the state of CNC dispersion within the water bulk, the air/water interface may be populated by individual nanocrystals only (f), by a mix of individual and agglomerated particles (g), or by agglomerated CNCs only (h). Upon casting, these result into thin films whose surface is either amphiphilic (i)&(j) or purely polar (k). The fraction of non-polar surfaces that a film can expose should reach a maximum of  $f_{\text{max}}^{\text{nps}}$  in (i), whose amplitude is a function of the nanocrystals' geometry, and a minimum of  $\sim 0$  in (k).

Instead of migrating towards the air/water interface, CNCs could agglomerate (Fig. 7.4.b): matching two polar surfaces together yields an energy variation of  $\sim -13 \text{ mJ m}^{-2}$ , it decreases to  $\sim -27 \text{ mJ m}^{-2}$  for a polar surface agglomerated with a non polar one, and to  $\sim -59 \text{ mJ m}^{-2}$  for two non-polar surfaces together. In aqueous suspensions, CNCs hence find it more favorable to agglomerate by matching their non-polar surfaces together. Repeating the process yields raft-like structures assembled by their (200) surfaces (Fig. 7.4.c). Similar 2-D aggregates were reported by Uhlig et al. [103] for aqueous suspensions of sulfuric acid-hydrolyzed CNCs. This trend is probably favored by the combination of solvation-induced and electrostatic stabilizations experienced by CNC polar surfaces in water [173]. Other works have

suggested that it was hydrogen bonding networks that were responsible for the strong cohesion of CNC agglomerates [91]. Our calculations show that in water, at least, dispersive interactions between the (200) surfaces of CNCs particles are those that require the highest energy to be broken. This is because water molecules can form H-bonds of their own with the hydroxyl groups of CNCs, which minimizes the relative importance of these bonds from a thermodynamic point of view ( $\gamma^{w/ps} \approx 6.4 \text{ mN m}^{-1}$ ).

The formation of 2-D self-assemblies change the aspect ratio of the nano-objects that can migrate towards the interface: if they are wide enough, it may become advantageous to orient their polar moieties towards the air/water interface (Fig. 7.4.e). Indeed, while the area in (200) surfaces remain constant, a raft made of 3 nanocrystals may for instance triple the area in polar surfaces that can be exposed at the interface with air. Based on our calculations, the raft needs to be roughly 3 times larger than thicker in order for polar surfaces to adsorb preferentially at the air/water interface: this could correspond to as little as 2 to 4 nanocrystals depending on their exact cross-section and positioning at the interface. This threshold of aggregation is likely reached in suspension: Uhlig et al. [103] reported 2-D CNC agglomerates that were up to 8 times larger than thicker.

From these calculations, it is possible to propose a mechanism for CNC orientation at the air/water interface: in circumstances where CNCs can migrate to the interface prior to agglomerating, the individual nanocrystals (7.4.a) orient their non-polar surface towards air (7.4.f). The film that results from this process is amphiphilic, with stripes of non-polar and polar surfaces (7.4.i) and  $f^{nps}$  reaches its maximum,  $f_{\text{max}}^{nps}$ . However, in circumstances where bulk agglomeration is competitive, CNC may first form raft-like assemblies (Fig. 7.4.b). Upon migration to the interface, these 2-D structures orient their polar surfaces towards the air (Fig. 7.4.h), which leads to purely polar surfaces upon drying (Fig. 7.4.h,  $f^{nps} \approx 0$ ). If it only takes  $\sim 2$ -4 nanocrystals to form agglomerates that preferentially orient their polar surfaces at the air/water interface, then slight variations in the initial state of CNC aqueous dispersion (caused by the efficiency of the ultrasonication process for instance) can cause fluctuations to the level of amphiphilicity displayed by the films. This is illustrated in Fig. 7.4.g where the air/water interface is populated by a mix of individual and agglomerated CNCs, which leads to an intermediate content in terms of non-polar surfaces for the film (Fig. 7.4.k,  $0 \leq f^{nps} \leq f_{\text{max}}^{nps}$ ). Note that the representations made in Figs. 7.4.i-k is coherent with the level of CNC alignment that is observed in AFM analyses (Fig. 7.1.b).

A process such as spin-coating, in which a significant centrifugal force is applied to the system over a short period of time, likely destabilizes the suspension and favors CNC agglomeration. Spin coating has indeed been reported to favor local concentration increases [252] (which may

in turn favor particle/particle agglomeration). It would explain that SC films experimentally display a polar behavior ( $f^{\text{nps}} < 0.06$ ) with a small standard deviation: if the suspension is subjected to a treatment that cause CNC agglomeration, it is possible to repeatably produce a scenario where only agglomerates make it to the interface as in Fig. 7.4.k. It is worth noting that the shear forces generated by the process may also contribute to orient the 2-D CNC assemblies.

However, a slow and steady process such as oven-casting is likely to preserve CNC dispersion long enough for individual CNCs to reach the interface, which would explain the amphiphilic behavior displayed by OC films. The impossibilities to completely prevent CNC agglomeration in suspension and to control the ratio between individual and agglomerated CNCs that reach the interface may be responsible for the large standard deviations observed on OC films: it is harder to repeatably produce and maintain an individual dispersion of CNCs than to repeatably cause their agglomeration. In practice, while it should theoretically be possible to reach  $f_{\text{max}}^{\text{nps}}$  (Fig. 7.4.i), a small fraction of the interface will be made of CNC agglomerates, which lowers  $f^{\text{nps}}$  (Fig. 7.4.j). The least polar film we could produce through oven-casting had a  $f^{\text{nps}}$  of  $\sim 0.55$  (Fig. 7.3.a), but there is no way to verify whether this really corresponds to  $f_{\text{max}}^{\text{nps}}$  or to the maximum that we could reach given our current protocol.

Based on Fig. 7.4.i,  $f_{\text{max}}^{\text{nps}}$  should be a function of the nanocrystal cross-sectional shape. However, CNC shape cannot be totally resolved through XRD due to the lack of peak for (010) surfaces (see SI) and  $\sim 0.55$  is currently the best estimate we can provide for our CNCs. Since the CNC dimensions and the cross-sectional shape are a function of their feedstocks [98, 96, 97], it should be possible to tune  $f_{\text{max}}^{\text{nps}}$  by working with other kind of nanocrystals.

Calculations led here-above may confirm quantitatively whether CNCs find it favorable to orient their (200) surfaces towards the oil at the interface of oil in water Pickering emulsions [98, 166, 168]. Note that aggregation state was also found to play a role on the interfacial stability of these emulsions. [168, 161]. Kalashnikova et al. [98, 166] produced CNC stabilized hexadecane in water emulsions. Hexadecane has an interfacial tension of  $51.2 \text{ mN m}^{-1}$  with water,  $22.5 \text{ mN m}^{-1}$  with CNC polar surfaces, and  $3.0 \text{ mN m}^{-1}$  with CNC non-polar surfaces (Table 7.1). Thus, hexadecane is nearly a perfect match for the (200) surfaces of CNCs: its adsorption from the water bulk to the oil/water interface leads to an energy variation of  $\sim -78 \text{ mJ m}^{-2}$  ( $-35 \text{ mJ m}^{-2}$  for a polar surface). This provides a quantitative backing to the series of articles by Kalashnikova and co-workers [165, 98, 166], which have been cornerstones in the field of CNC stabilized micro-emulsions.

Another interesting result is the comparison between the theoretical energy required to disperse an agglomerate of CNCs in water and the experimental input that needs to be provided to the system in order to do so. A  $\sim 7\text{-}8\text{ nm}$  wide,  $\sim 105\text{-}120\text{ nm}$  long nanocrystal has a specific surface area of  $\sim 350\text{ m}^2/\text{g}_{\text{CNC}}$  (assuming a density of  $\sim 1.6\text{ g/cm}^3$ ). Since breaking CNC-CNC interactions in water requires from  $\sim 13$  to  $\sim 59\text{ mJ m}^{-2}$ , dispersing a densely packed agglomerate of CNCs will require  $\sim 5$  to  $\sim 20\text{ J/g}_{\text{CNC}}$  from a thermodynamic point of view. Experimentally, Beck et al. [91] reported satisfactory dispersion from  $950\text{ J/g}_{\text{CNC}}$  for spray- and air-dried CNCs at concentrations of 2.8 wt% ( $\sim 1.8\text{ vol\%}$ ). Beuguel et al. [145] mentioned  $10\,000\text{ J/g}_{\text{CNC}}$  as a safer threshold for 1 to 5 wt% ( $\sim 0.6\text{-}3.1\text{ vol\%}$ ) CNC suspensions. Hence, the ultrasonication process has an energy efficiency (energy provided to the system over energy required to disperse CNCs) that lies in the range of  $\sim 0.1\text{-}1\%$  for dilute CNC suspensions. This seems plausible since it falls within one order of magnitude of CNC volume fraction ( $\sim 0.6\text{-}3.1\text{ vol\%}$ ).

## 7.5 Conclusions

This work proposes the first compelling evidence of CNC orientation at an interface. It provides experimental backing to nearly a decade of research during which this hypothesis has been used to justify the stability brought by CNCs to oil-in-water Pickering emulsions. This was achieved by investigating the influence of the casting protocol on the wettability of CNC thin films. It remained an open-ended question with contact angle variations of up to  $30^\circ$  being reported from sample to sample without convincing explanations. Here, we demonstrate that such variations could be explained by considering the amphiphilicity of the nanocrystals. Liquids are sensitive to molecular-scale heterogeneities and cellulose crystalline surfaces, whose dimensions are nano, are large enough to influence wetting behaviors.

Based on thermodynamic calculation, a mechanism for CNC orientation at interface is proposed: while individual nanocrystals have an energy incentive to orient their non-polar surfaces to the air interface, CNC agglomerates preferentially expose their polar moieties. This is because CNCs form 2-D assemblies upon agglomeration. Previously reported by Uhlig et al. [103], these raft-like structures find it more stable to orient their largest surfaces, which happen to be polar, towards air. Hence, in a slow and steady protocol such as oven-casting during which CNC dispersion is preserved over a long period of time, CNC may migrate as near-individual particles to the interface, which ultimately yields an amphiphilic film. In a spin-coating protocol, however, CNC suspensions are subject to an important centrifugal force that may favor local increases in particle concentration and thus their agglomeration: a polar film is produced. It is worth noting that this mechanism for CNC orientation at in-

terfaces remains to be properly demonstrated: experimentally, this manuscript only demonstrates that oven-cast films displayed an estimated 0.34-0.50 fraction of non-polar moieties while spin-coated samples stood below 0.06. Reproducibility was lower for the production of amphiphilic films from oven-casting: probably due to its high dependency to the level of initial CNC dispersion. We suggest that working with never-dried CNCs instead of spray-dried particles could improve the repeatability of the process: it would remove the variability introduced during the step of ultrasound-assisted redispersion.

Based on the OWRK model, these calculations on energies and surface composition were made possible via the estimation of CNC surface tension parameters for both the polar and the non-polar surfaces of the nanocrystals:  $\gamma^{ps}=53.1\pm3.0\text{ mN m}^{-1}$  ( $\gamma_D^{ps}=30.7\pm2.0\text{ mN m}^{-1}$ ,  $\gamma_P^{ps}=22.4\pm1.0\text{ mN m}^{-1}$ ), and  $\gamma^{nps}=31.0\pm1.6\text{ mN m}^{-1}$  ( $\gamma_D^{nps}=28.0\pm1.1\text{ mN m}^{-1}$ ,  $\gamma_P^{nps}=3.0\pm0.5\text{ mN m}^{-1}$ ). They were obtained by exploiting the empirical correlations that exist between surface tension and Hansen solubility parameters. These coefficients enable for quantitative predictions regarding the behavior of CNC particles at interfaces. Hence, the plausibility of CNC adsorption at the oil/water interface could be confirmed: their (200) surfaces are a good match for stabilizing the interface of an hexadecane in water emulsion [98, 166]. It was also possible to estimate the energy required to disperse a densely packed agglomerate of CNCs in water: it is in the range of  $\sim 5$  to  $\sim 20\text{ J/g}_{\text{CNCs}}$ . This provides an element of comparison and an horizon for the redispersion of CNCs [91, 145]: the energy optimization of these protocols is crucial to make them industrially relevant [253]. Other applications involve the prediction of CNC behavior in polymer blends and the production of CNC materials with tuned wettability.

## 7.6 Acknowledgements

The authors acknowledge FPIinnovations (Pointe-Claire, QC, Canada), PRIMA Québec (grant number FPI NCC RD001), and the National Science and Engineering Research Council (NSERC, grant number RDCPJ 490786-15) for their financial contribution. They are grateful to Cellulforce (Montréal, QC, Canada) for kindly providing the cellulose nanocrystals. C. Bruel acknowledge the Fond de Recherche du Québec - Nature et Technologies (FRQNT) for providing him with a scholarship (number 208324). The authors thank Dr. W. Y. Hamad, from FPIinnovations, for his contribution in reviewing this work; MM. T. Darlow and T.S. Davies for their contribution to the contact angle measurements; Mr. J.-P. Masse for his help with the XRD analyses; Mrs. P. Moraille for assisting the AFM acquisition; and finally MM. W. Raphael and M. Gauthier for their helpful recommendations and assistance.

## 7.7 Supporting Information description

Supporting Information (SI) provide: a nomenclature for the symbols and abbreviations; a morphological characterization (dimensions, sulfur content, purity, crystallinity) of the CNCs; a list of the precautions that were taken for the wettability model (Eq. 7.7) to apply; the description of a typical ARCA experiment and the detailed methodology with which the data was analyzed; a film by film breakdown of the ARCA results and their statistical analysis.

## CHAPTER 8 GENERAL DISCUSSION

The research challenge set an objective in terms of CNC dispersion in non-polar media (solvents and polymer matrices) [29]. Working with unmodified sulfuric acid-hydrolyzed CNCs, it was clear from the start that it would be impossible to reach a nanoscale dispersion in the least polar medias (e.g., cyclohexane or toluene). It was hence decided to determine the threshold of polarity from which they may be dispersed. An alternate course of action could have been to functionalize CNC surfaces and to study the dispersion of hydrophobized particles. While this latter approach was initially considered, it had some obvious flaws: developing a reliable and effective method of surface modification is a research objective in itself, which shifts the focus of the thesis away from dispersion; introducing a step of surface modification negates the advantage of working with a commercially available material, which narrows the scope, the reproducibility, and the impact of the study; finally, such an approach would infringe upon the 5<sup>th</sup> research challenge (“Compatibilization of nanomaterials derived from wood fibre”, see Chapter 1). Therefore and *stricto sensu*, this thesis did not achieve a non-polar dispersion of CNCs. However, it determined the prerequisites that a solvent must meet in order to disperse CNCs. This applies to solvent-casting protocols and highlights the potential of some polar aprotic solvents, such as DMF and DMSO, for the dispersion of CNCs in mildly non-polar polymer matrices (such as PLA, PEG, or PMMA) [106, 123].

While frequently mentioned, nanocomposites were not directly investigated in this dissertation. This is because studying chemical affinity, a thermodynamic concept, requires the system to reach an equilibrium state. In suspensions, a pseudo-equilibrium is reached over a time scale that ranges from a few seconds to several months (Table B.1), which is compatible with a Ph.D. project. The high viscosity of polymer matrices, their crystallinity, and their potential for entanglement may, however, prevent nanoparticles from reaching an equilibrium, at least at room temperature. Furthermore, polymer chains are polydisperse, which alters their chemical affinity: polymer HSP are a function of their molecular weights [127, 131]. It was hence necessary to first focus on solvent suspensions in order to characterize CNC thermodynamic properties, both in terms of Hansen solubility and surface tension parameters, after which it becomes possible to study more complex systems such as nanocomposites.

The fact that kinetics of agglomeration are slower in nanocomposites may actually be the key to achieve CNC dispersion in non-polar polymer matrices: if it is possible to trap the nanoparticles in a dispersed state within the polymer matrix, the level of dispersion should be preserved independently of the thermodynamics. This should remain true so far that



the kinetics of agglomeration remain slow enough (which implies, for instance, to avoid any heating of the matrix). Experimentally, several strategies were proposed to achieve this kind of kinetic trapping: the first, mentioned here-above, is to use a solvent as an intermediate [106, 123]. If the solvent can both preserve the dispersion of the nanoparticles and dissolve the polymer chains, solvent-casting may yield finely dispersed composites [199, 197, 198] and even cause the formation of helical structures within the matrix [123, 254]. Other protocols relying on co-precipitation were also proposed [255]. Alternatively, it is possible to favor CNC dispersion by dedensifying the initial aggregates of CNC particles: this is either achieved by freeze-drying CNCs to form an aerogel, or by using a masterbatch approach [25].

As a summary, this project developed tools that make possible to estimate CNC interactions with their environment, both in terms of chemical affinity (HSP distance and interfacial tension) and ionic dissociation (dielectric constant). In systems whose kinetics are fast, such as solvent suspensions, the thermodynamic state is accessible and a direct prediction of CNC level of dispersion can be achieved. In systems whose kinetics are slower, such as nanocomposites, these tools may be used to estimate whether a direct dispersion may be attempted or if an indirect approach is required to kinetically trap CNCs within the matrix (when the thermodynamics are too unfavorable). It is worth noting that under the principle of “like seeks likes”, the thermodynamics of dispersion cannot be strictly favorable: at best, they are roughly even. This remains true as long as complementary interactions are neglected (see Karger acid/base parameters [128], equation 2.8, and the motives for the exclusion of strong acid and bases from the scope of the study in section 2.3.2). If thermodynamic predictions are too unfavorable, it is also possible to alter them: either by using a compatibilizer or by modifying the surface of the nanocrystals.

The research challenge sets no objectives in terms of self-assembling properties and interfacial behaviors. These aspects were nonetheless investigated for their potential in probing the validity of our characterizations: pushing the analysis one step further is a mean to confirm our interpretations. Hence, establishing a comprehensive link between stabilization mechanisms and self-assembly behaviors (Chapter 6) validated the quantitative thresholds in terms of HSP distance ( $R_a < 7.8 \text{ MPa}^{1/2}$ ) and dielectric constant ( $\epsilon > 15$ ) for CNC dispersibility. Furthermore, proving the orientability of CNC functionalities at air/sample interfaces through wettability tests (Chapter 7) validated our surface tension estimates and supported our interpretation regarding the non-polar sphere of CNCs (Chapter 5): determined using 2 good solvents only (chloroform and dichloromethane), its location is in doubt and requires further confirmation. The degree of coherence between the wettability model predictions and the contact angle results provides experimental backing to the first article (Chapter 5).

## CHAPTER 9 CONCLUSIONS AND RECOMMENDATIONS

### 9.1 Conclusions

This dissertation explores the role of chemical affinity on the behavior of colloidal cellulose nanocrystals. It is based on the research hypothesis that the CNC potential for dispersion can be entirely predicted by quantifying the interactions between the media and the nanoparticles. There are two main CNC/solvent interactions: physical adsorption and ionic dissociation. Chemical adsorption, which involves the formation of new covalent bonds at CNC surfaces, is not considered. Neither are swelling and dissolution, which may occur with solvents whose potential for Lewis acid/base interactions is too strong.

The potential for ionic dissociation, which is related to electrostatic stabilization, is easily predicted from the dielectric constant of the media: for  $\epsilon \gtrsim 11$ , a medium benefits from aqueous-like levels of ionic dissociation [119]. CNC potential for physical adsorption used, however, to be poorly described. Thermodynamic tools, in terms of Hansen solubility and surface tension parameters theories, did exist but a comprehensive characterization remained to be performed. Therefore, this work first measured the HSP of both the polar and non-polar surfaces of cellulose nanocrystals. This is a direct characterization of the solvents' potential to adsorb at CNC surfaces, which means that the HSP radius ( $R_0=7.8 \text{ MPa}^{1/2}$ ) determined in Article 1 (Chapter 5) could directly be related to the threshold at which CNCs start benefiting from significant solvation-induced stabilization (Article 2, Chapter 6).

Hence, we established distinct thresholds in terms of solvent properties from which CNCs start benefiting from electrostatic and/or solvation-induced stabilizations. It makes it possible to categorize solvents from the level of colloidal stability they can bring to CNC particles in suspensions, and hence to predict CNC dispersibility. Colloidally stable particles have been reported to behave like hard particles and hard cylinders are known to form helical self-assemblies upon evaporation (Chapter 6). By extrapolating these principles to CNCs, we were able to predict their potential for helical self-assembly from their level of colloidal stability and hence from our solvent thresholds in terms of  $\epsilon$  and  $R_a$ . Interestingly, these criteria were found to apply for both pure solvents and binary mixtures.

Article 3 (Chapter 7) translated the HSP in terms of surface tension parameters, which enabled calculations related to adhesion and wettability behaviors. It also confirmed the amphiphilicity of the nanocrystals by demonstrating their orientability at air/sample interfaces. This was achieved by investigating one of the conundrum of CNC materials: the influence

of the preparation method on their wettability. The study also confirmed the pertinence of some recent hypotheses: CNC tendency to form 2-D raft like agglomerates in suspensions and their potential to stabilize oil-in-water Pickering emulsions.

As a conclusion, this work focused on CNC interactions with liquids: in suspension, during solvent-casting, or through wettability tests. These resulted in a mapping of CNC chemical affinity. Physical adsorption, or the lack thereof, was directly correlated to CNC potential for dispersion and self-assembly in the bulk, and to their orientation at interfaces. These concepts could not be probed in nanocomposites whose dispersion states are as much governed by kinetic and steric effects than they are by thermodynamics. Literature however suggests that solvent-casting a nanocomposites enables for an individual dispersion of CNCs within a polymer matrix [199, 197, 198] and for their self-assembly in helical patterns [123, 254]. Some of the understanding gathered on CNC colloidal behaviors may hence directly be applied to the preparation of nanocomposites through solvent-casting. A generalization of our results to CNC dispersion in polymer matrices is, however, out of reach for the time being.

## 9.2 Recommendations

The limitations of this work are summarized in Article 2 (Section 6.4.3) and mostly revolve around the little emphasis that was given to CNC characteristics: since a single kind of nanoparticles was investigated, parameters such as feedstock, cross-sectional shape, aspect ratio, degree of sulfatation, and nature of the counter-ion were not explored. The first recommendation is hence to revisit some of the results presented here-above with different kind of CNCs. An efficient way to do so could be to target litigious solvents, such as N,N-dimethylformamide and chloroform, that are sometimes reported as good, and sometimes reported as poor for CNC dispersion. This work hypothesized that the cross-sectional shape and the sulfur content were respectively responsible for CNC behaviors in chloroform (whether (200) surfaces are large enough to enable significant solvent adsorption) and DMF (sulfatation tunes the HSP of CNC polar surfaces). It would also be pertinent to confirm the influence of cross-sectional shape on the wettability of the oven cast films (Chapter 7).

Another aspect discussed in Chapter 4 is the qualitative nature of the analysis in terms of sedimentation state, gelation, and self-assembly. Since CNC behaviors can now be predicted from the parameters of the solvent, it should be possible to study each category separately, hence limiting the range of potential behaviors Bruckner et al. [122] were hence able to quantify the kinetics of CNC self-ordering by limiting the scope of the study to solvents in which CNCs benefit from electrostatic and solvation-induced stabilizations. Similar studies, focused for instance on the balance between EISA and DISA upon solvent-casting, could be

led on suspensions only stabilized by electrostatic effects.

In fact, we suggest that the greatest potential for direct applications lies with DISA mechanisms: while unstable suspensions form powder-like agglomerates, those that are initially stable before getting destabilized may be used to produce aerogels [230] and 3-D printed structures [226]. Investigating the various paths to destabilization (salt addition, solvent exchange, desulfation, concentration increase) will probably lead to novel industrially relevant applications as is the case for inorganic nanocrystals [160]. Note that since the diagram presented in Figure 6.1 applies to binary mixtures, it can predict the efficiency of solvent exchange strategies.

Regarding the challenge on CNC dispersion in polymer matrices, it is clear that solvent-related methods are not relevant from an industrial perspective unless they come with advanced properties such as iridescence or barrier properties. Mechanical reinforcement in itself is probably not valuable enough to justify the use of non-aqueous solvents. Working with solvent-cast nanocomposites, the recommendation is hence to stick to systems rich enough in CNCs to display these optical properties ( $\gtrsim 60$ -70 wt% of CNCs in the case of CNC/PEG nanocomposites for instance [254]). In a research-oriented mindset, solvent-casting could, however, be used to produce composites with optimized dispersion that can serve as a reference to gauge the efficiency of solvent-free approaches. This is assuming that solvent traces can be removed to avoid any plasticizing effect.

More generally, this work adds to the consensus (stated in the research challenge) that CNCs are too polar to be directly dispersed in non-polar matrices and that compatibilization is necessary to do so. However, what it does is clarifying the meaning of polar and non-polar by enabling a quantification of the chemical distance (in terms of HSP theory) between CNCs and the polymer matrix,  $R_a$ . The last recommendation is hence to use this tool to estimate the gain that can be achieved through compatibilization, which is: meaningless at low  $R_a$ ; useful but avoidable for intermediate  $R_a$  (in the case of PLA composites for instance where compatibilization yields good results [25] but where alternative strategies relying on the initial density of CNC agglomerates can be applied [256]); and unavoidable at high  $R_a$ . A quick calculation of  $R_a$  can hence serve as a justification for a step of compatibilization, which has an obvious interest to draw long-term research plans and/or fill grant applications. What constitutes a “low”, an “intermediate”, and a “high”  $R_a$  remains to be defined. Based on Table B.3 and on the HSP radius of CNCs ( $R_0=7.8\text{ MPa}^{1/2}$ ), it may nonetheless be estimated that  $R_a \approx R_0$  (e.g., PVOH) is low, that  $R_a \approx 2R_0$  (e.g., PEG, PLA, and PMMA) is intermediate, and that  $R_a \approx 3R_0$  (e.g., PE and PP) is high. Further investigations are required to probe these thresholds.

## REFERENCES

- [1] M.D. Abramoff, P.J. Magalhaes, and S.J. Ram. Image Processing with ImageJ. *Bio-photonics International*, 11:36–42, 2004.
- [2] B. E. C. Bogdanski. The rise and fall of the Canadian pulp and paper sector. *Forest. Chron.*, 90:785–793, 2014.
- [3] Natural Resources Canada. Natural Resources Canada – forest resources – statistical data, 2020. <https://cfs.nrcan.gc.ca/statsprofile>, accessed on 2020/06/26.
- [4] H. Charreau, M. L. Foresti, and A. Vázquez. Nanocellulose patents trends: a comprehensive review on patents on cellulose nanocrystals, microfibrillated and bacterial cellulose. *Recent Pat. Nanotechnol.*, 7:56–80, 2013.
- [5] S. M. Mukherjee and H. J. Woods. X-Ray and electron microscope studies of the degradation of cellulose by sulphuric acid. *Biochim. Biophys. Acta*, 10:499–511, 1953.
- [6] A. Dufresne. La nanocellulose, le nouvel “or vert”? *Techniques de l’Ingénieur*, Janvier-Février:46–47, 2017.
- [7] W. Y. Hamad. *Cellulose Nanocrystals Properties, Production and Applications*. Wiley, Chichester, U. K., 2017.
- [8] CelluForce. CelluForce-Manufacturing-Process, 2020. <http://www.celluforce.com>, accessed on 2020/05/23.
- [9] Kruger Biomaterials. THE PRODUCT, 2020. <http://biomaterials.kruger.com>, accessed on 2020/05/23.
- [10] J. Miller. 2015- December-Nanocellulose. State of the industry, December 2015. <http://www.tappinano.org/media/1114/cellulose-nanomaterials-production-state-of-the-industry-dec-2015.pdf>, accessed on 2020/06/18.
- [11] Blue Goose Biorefineries Inc. Product – bgb ultra<sup>tm</sup>, 2020. <https://bluegoosebiorefineries.com/product/>, accessed on 2020/06/18.
- [12] InnoTech Alberta. Cellulose nanocrystals (cnc) pilot plant, 2020. <https://innotechalberta.ca/research-facilities/cellulose-nanocrystals-cnc-pilot-plant/>, accessed on 2020/06/18.
- [13] Anomera. Anomera – about, 2020. <https://www.anomera.ca/>, accessed on 2020/07/09.
- [14] J. Miller. 2018- Summer- Cellulose Nanomaterials Production Update, December 2018. <https://www.tappinano.org/media/1266/2018-cellulose-nanomaterials-production-update.pdf>, accessed on 2020/06/18.

- [15] marketsandmarkets.com. Nanocellulose market by type (mfc & nfc, cnc/ncc, and others), application (pulp&paper, composites, biomedical & pharmaceutical, electronics & sensors, and others), region (europe, north america, apac, and rest of world) - global forecast to 2025. Technical report, April 2020. [http://www.marketsandmarkets.com/Market-Reports/nanocellulose-market-56392090.html?gclid=EAIaIQobChMI5o-d1Y\\_71gIVRh-GCh0j5wkHEAAYASAAEgJZyfD\\_BwE](http://www.marketsandmarkets.com/Market-Reports/nanocellulose-market-56392090.html?gclid=EAIaIQobChMI5o-d1Y_71gIVRh-GCh0j5wkHEAAYASAAEgJZyfD_BwE), accessed on 2020/06/18.
- [16] W. Y. Hamad and T. Q. Hu. Structure-process-yield interrelation in nanocrystalline cellulose extraction. *Can. J. Chem. Eng.*, 88:392–402, 2010.
- [17] Y. Habibi, L. A. Lucia, and O. J. Rojas. Cellulose Nanocrystals: Chemistry, Self-Assembly, and Applications. *Chem. Rev.*, 110:3479–3500, 2010.
- [18] F. L. Dri, L. G. Hector Jr., R. J. Moon, and P. D. Zavattieri. Anisotropy of the elastic properties of crystalline cellulose  $I_\beta$  from first principles density functional theory with Van der Waals interactions. *Cellulose*, 20:2703–2718, 2013.
- [19] R. Rusli and S. J. Eichhorn. Determination of the stiffness of cellulose nanowhiskers and the fiber-matrix interface in a nanocomposite using Raman spectroscopy. *Appl. Phys. Lett.*, 93:033111, 2008.
- [20] A. Brinkmann, M. Chen, M. Couillard, Z. J. Jakubek, T. Leng, and L. J. Johnston. Correlating Cellulose Nanocrystal Particle Size and Surface Area. *Langmuir*, 32:6105–6114, 2016.
- [21] Y. Nishiyama, P. Langan, and H. Chanzy. Crystal Structure and Hydrogen-Bonding System in Cellulose  $I_\beta$  from Synchrotron X-ray and Neutron Fiber Diffraction. *J. Am. Chem. Soc.*, 124:9074–9082, 2002.
- [22] S. Eyley and W. Thielemans. Surface modification of cellulose nanocrystals. *Nanoscale*, 6:7764–7779, 2014.
- [23] R. J. Moon, A. Martini, J. Nairn, J. Simonsen, and J. Youngblood. Cellulose nanomaterials review: structure, properties and nanocomposites. *Chem. Soc. Rev.*, 40:3941–3994, 2011.
- [24] M. Mariano, N. El Kissi, and A. Dufresne. Cellulose Nanocrystals and Related Nanocomposites: Review of some Properties and Challenges. *J. Polym. Sci. Pol. Phys.*, 52:791–806, 2014.
- [25] E. Vatansever, D. Arslan, and M. Nofar. Polylactide cellulose-based nanocomposites. *Int. J. Biol. Macromol.*, 137:912–938, 2019.
- [26] N. Wang, E. Ding, and R. Cheng. Thermal degradation behaviors of spherical cellulose nanocrystals with sulfate groups. *Carbohydr. Polym.*, 40:115–124, 2007.

- [27] NovaCentris. LIST OF ALL THE CHALLENGES, 2020.  
<http://www.novacentris.com/nc/en/list-of-challenges-to-be-solved>, accessed on 2020/07/06.
- [28] NovaCentris. Dispersion of cellulose nanocrystals in aqueous media, 2015.  
[http://www.novacentris.com/nc/en/fiche.php?todo=dl\\_defi&lang=en&def\\_id=1021163](http://www.novacentris.com/nc/en/fiche.php?todo=dl_defi&lang=en&def_id=1021163), accessed on 2020/07/06.
- [29] NovaCentris. Dispersion of cellulose nanocrystals in non-polar matrices, 2015.  
[http://www.novacentris.com/nc/en/fiche.php?todo=dl\\_defi&lang=en&def\\_id=1021164](http://www.novacentris.com/nc/en/fiche.php?todo=dl_defi&lang=en&def_id=1021164), accessed on 2020/07/06.
- [30] NovaCentris. Reinforcement potential of nanomaterials derived from wood fibre, 2015.  
[http://www.novacentris.com/nc/en/fiche.php?todo=dl\\_defi&lang=en&def\\_id=1021165](http://www.novacentris.com/nc/en/fiche.php?todo=dl_defi&lang=en&def_id=1021165), accessed on 2020/07/06.
- [31] NovaCentris. Characterization of nanomaterials derived from wood fibre, 2015.  
[http://www.novacentris.com/nc/en/fiche.php?todo=dl\\_defi&lang=en&def\\_id=1021166](http://www.novacentris.com/nc/en/fiche.php?todo=dl_defi&lang=en&def_id=1021166), accessed on 2020/07/06.
- [32] NovaCentris. Compatibilization of nanomaterials derived from wood fibre, 2015.  
[http://www.novacentris.com/nc/en/fiche.php?todo=dl\\_defi&lang=en&def\\_id=1021167](http://www.novacentris.com/nc/en/fiche.php?todo=dl_defi&lang=en&def_id=1021167), accessed on 2020/07/06.
- [33] NovaCentris. Thermal stability of nanomaterials derived from wood fibre, 2015.  
[http://www.novacentris.com/nc/en/fiche.php?todo=dl\\_defi&lang=en&def\\_id=1021168](http://www.novacentris.com/nc/en/fiche.php?todo=dl_defi&lang=en&def_id=1021168), accessed on 2020/07/06.
- [34] G. A. Smook. *Handbook for Pulp and Paper Technologists*. TAPPI & CPPA Publications, Atlanta, GA, U. S. A., 1982.
- [35] A. Frey-Wyssling. The fine structure of cellulose microfibrils. *Science*, 119:80–82, 1954.
- [36] A. Frey-Wyssling and K. Mühlethaler. *Ultrastructure Plant Cytology*, page 34–40. Elsevier, New York, NY, U. S. A., 1965.
- [37] R. E. Mark. *Cell Wall Mechanics of Tracheids*. Yale University Press, New Haven, CT, U. S. A., 1967.
- [38] D. Fengel and G. Wegener. *Wood: Chemistry, Ultrastructure, Reactions*. Walter de Gruyter, Berlin, Germany, 1984.
- [39] R. H. Marchessault. *Chimie et biochimie de la lignine, de la cellulose et des hémicelluloses; actes du symposium international de Grenoble*. Impr. Réunies de Chambéry, Chambéry, France, 1964.

- [40] W. Herth. Arrays of plasma-membrane “rosettes” involved in cellulose microfibril formation of *Spirogyra*. *Planta*, 159:347–356, 1983.
- [41] S.-Y. Ding and M. E. Himmel. The Maize Primary Cell Wall Microfibril: A New Model Derived from Direct Visualization. *J. Agric. Food Chem.*, 54:597–606, 2006.
- [42] M. A. Ha, D. C. Apperley, B. W. Evans, I. M. Huxham, W. G. Jardine, R. J. Viëtor, D. Reis, B. Vian, and M. C. Jarvis. Fine structure in cellulose microfibrils: NMR evidence from onion and quince. *Plant J.*, 16:183–190, 1998.
- [43] T. Arioli, L. Peng, A. S. Betzner, J. Burn, W. Wittke, W. Herth, C. Camilleri, H. Höfte, J. Plazinski, R. Birch, A. Cork, J. Glover, J. Redmond, and R. E. Williamson. Molecular analysis of cellulose biosynthesis in arabidopsis. *Science*, 279:717–720, 1998.
- [44] S. Kimura, W. Laosinchai, T. Itoh, X. Cui, C. R. Linder, and R. M. Brown Jr. Immunogold labeling of rosette terminal cellulose-synthesizing complexes in the vascular plant *vigna angularis*. *Plant Cell.*, 11:2075–2086, 1999.
- [45] M. S. Doblin, I. Kurek, D. Jacob-Wilk, and D. P. Delmer. Cellulose Biosynthesis in Plants: from Genes to Rosettes. *Plant Cell Physiol.*, 43:1407–1420, 2002.
- [46] R. M. Brown Jr. The biosynthesis of cellulose. *J. Macromol. Sci., Part A: Pure Appl. Chem.*, A33:1345–1373, 1996.
- [47] X. M. Dong, J.-F. Revol, and D. G. Gray. Effect of microcrystallite preparation conditions on the formation of colloid crystals of cellulose. *Cellulose*, 5:19–32, 1998.
- [48] M. M. de Sousa Lima and R. Borsali. Rodlike Cellulose Microcrystals: Structure, Properties, and Applications. *Macromol. Rapid Comm.*, 25:771–787, 2004.
- [49] S. Shafiei-Sabet, W. Y. Hamad, and S. G. Hatzikiriakos. Rheology of Nanocrystalline Cellulose Aqueous Suspensions. *Langmuir*, 28:17124–17133, 2012.
- [50] M.-C. Li, Q. Wu, K. Song, S. Lee, Y. Qing, and Y. Wu. Cellulose Nanoparticles: Structure-Morphology-Rheology Relationships. *ACS Sustainable Chem. Eng.*, 3:821–832, 2015.
- [51] M. Roman and W. T. Winter. Effect of Sulfate Groups From Sulfuric Acid Hydrolysis on the Thermal Degradation Behavior of Bacterial Cellulose. *Biomacromolecules*, 5:1671–1677, 2004.
- [52] V. Favier, H. Chanzy, and J. Y. Cavaille. Polymer Nanocomposites Reinforced by Cellulose Whiskers. *Macromolecules*, 28:6365–6367, 1995.
- [53] J. Sugiyama, R. Vuong, and H. Chanzy. Electron diffraction study on the two crystalline phases occurring in native cellulose from an algal cell wall. *Macromolecules*, 24:4168–4175, 1991.



- [54] T. Imai, J. L. Putaux, and J. Sugiyama. Geometric Phase Analysis of Lattice Images from Algal Cellulose Microfibrils. *Polymer*, 44:1871–1879, 2003.
- [55] C. Djahedi, M. Bergenstr hle Wohlert, L. A. Berglund, and J. Wohlert. Role of hydrogen bonding in cellulose deformation-the leverage effect analyzed by molecular modeling. *Cellulose*, 23:2315–2323, 2016.
- [56] Y. Nishiyama, J. Sugiyama, H. Chanzy, and P. Langan. Crystal Structure and Hydrogen Bonding System in Cellulose I $_{\alpha}$  from Synchrotron X-ray and Neutron Fiber Diffraction. *J. Am. Chem. Soc.*, 125:14300–14306, 2003.
- [57] M. Jarvis. Cellulose stacks up. *Nature*, 426:611–612, 2003.
- [58] Y. Nishiyama. Structure and properties of the cellulose microfibril. *J. Wood Sci.*, 55:241–249, 2009.
- [59] R. J. Vi tor, K. Mazeau, M. Lakin, and S. P rez. A priori crystal structure prediction of native celluloses. *Biopolymer*, 54:342–354, 2000.
- [60] R. M. Brown Jr. Cellulose Structure and Biosynthesis: What is in store for the 21st century? *J. Polym. Sci. A1*, 42:487–495, 2004.
- [61] A. Ishikawa, T. Okano, and J. Sugiyama. Fine structure and tensile properties of ramie fibres in the crystalline form of cellulose I, II, III $_I$  and IV $_I$ . *Polymer*, 38:463–468, 1997.
- [62] R. H. Atalla and D. L. Vanderhart. The role of solid state  $^{13}\text{C}$  NMR spectroscopy in studies of the nature of native celluloses. *Solid State Nucl. Magn. Reson.*, 15:1–19, 1999.
- [63] I. M. Saxena and R. M. Brown Jr. Cellulose Biosynthesis: Current Views and Evolving Concepts. *Ann. Bot.*, 96:9–21, 2005.
- [64] S.-Y. Ding, Y.-S. Liu, Y. Zeng, M. E. Himmel, J. O. Baker, and E. A. Bayer. How Does Plant Cell Wall Nanoscale Architecture Correlate with Enzymatic Digestibility? *Science*, 338:1055–1060, 2012.
- [65] S.-Y. Ding, S. Zhao, and Y. Zeng. Size, shape, and arrangement of native cellulose fibrils in maize cell walls. *Cellulose*, 21:863–871, 2014.
- [66] Q. Li and S. Renneckar. Supramolecular Structure Characterization of Molecularly Thin Cellulose I Nanoparticles. *Biomacromolecules*, 12:650–659, 2011.
- [67] S. Camarero Espinosa, T. Kuhnt, E. J. Foster, and C. Weder. Isolation of Thermally Stable Cellulose Nanocrystals by Phosphoric Acid Hydrolysis. *Biomacromolecules*, 14:1223–1230, 2013.
- [68] R. S. Reiner and A. W. Rudie. *Production and applications of Cellulose nanomaterials*, chapter Process scale-up of cellulose nanocrystal production to 25 kg per batch at the

- forest products laboratory, pages 21–24. TAPPI Press, Peachtree Corners, Chichester, U. K., 2013.
- [69] I. Filpponen and D. S. Argyropoulos. Regular Linking of Cellulose Nanocrystals via Click Chemistry: Synthesis and Formation of Cellulose Nanoplatelet Gels. *Biomacromolecules*, 11:1060–1066, 2010.
  - [70] H. Sadeghifar, I. Filpponen, S. P. Clarke, D. F. Brougham, and D. S. Argyropoulos. Production of cellulose nanocrystals using hydrobromic acid and click reactions on their surface. *J. Mater. Sci.*, 46:7344–7355, 2011.
  - [71] J. Araki, M. Wada, and S. Kuga. Steric Stabilization of a Cellulose Microcrystal Suspension by Poly(ethylene glycol) Grafting. *Langmuir*, 17:21–27, 2001.
  - [72] D. Chen and T. G. M. van de Ven. Morphological changes of sterically stabilized nanocrystalline cellulose after periodate oxidation. *Cellulose*, 23:1051–1059, 2016.
  - [73] H. Yang, D. Chen, and T. G. M. van de Ven. Preparation and characterization of sterically stabilized nanocrystalline cellulose obtained by periodate oxidation of cellulose fibers. *Cellulose*, 22:1743–1752, 2015.
  - [74] H. Yang, M. N. Alam, and T. G. M. van de Ven. Highly charged nanocrystalline cellulose and dicarboxylated cellulose from periodate and chlorite oxidized cellulose fibers. *Cellulose*, 20:1865–1875, 2013.
  - [75] L. P. Novo, J. Bras, A. García, N. Belgacem, and A. A. S. Curvelo. Subcritical Water: A Method for Green Production of Cellulose Nanocrystals. *ACS Sustain. Chem. Eng.*, 3:2839–2846, 2015.
  - [76] J. Lazko, T. Sénéchal, A. Bouchut, Y. Paint, L. Dangreau, A. Fradet, M. Tessier, J. M. Raquez, and P. Dubois. Acid-free extraction of cellulose type I nanocrystals using Brønsted acid-type ionic liquids. *Nanocomposites*, 2:65–75, 2016.
  - [77] J. Mao, B. Heck, G. Reiter, and M.-P. Laborie. Cellulose nanocrystals’ production in near theoretical yields by 1-butyl-3-methylimidazolium hydrogen sulfate ([Bmim]HSO<sub>4</sub>) – mediated hydrolysis. *Carbohydr. Polym.*, 117:443–451, 2015.
  - [78] J. Mao, A. Osorio-Madrado, and M.-P. Laborie. Preparation of cellulose I nanowhiskers with a mildly acidic aqueous ionic liquid: Reaction efficiency and whiskers attributes. *Cellulose*, 20:1829–1840, 2013.
  - [79] J. Lazko, T. Sénéchal, N. Landercy, L. Dangreau, J. M. Raquez, and P. Dubois. Well defined thermostable cellulose nanocrystals via two-step ionic liquid swelling-hydrolysis extraction. *Cellulose*, 21:4195–4207, 2014.
  - [80] X. Y. Tan, S. B. Abd Hamid, and C. W. Lai. Preparation of high crystallinity cellulose nanocrystals (cncs) by ionic liquid solvolysis. *Biomass Bioenergy*, 81:584–591, 2015.

- [81] S. Zhang, V. Lemaire, A. Féret, H. Lefebvre, M. Tessier, and A. Fradet. Synthesis of linear and hyperbranched polyesters in Brønsted acid ionic liquids. *Polymer Chemistry*, 4:1538–1545, 2013.
- [82] Z. Man, N. Muhammad, A. Sarwono, M. Bustam, M. Vignesh Kumar, and S. Rafiq. Preparation of Cellulose Nanocrystals Using an Ionic Liquid. *J. Polym. Environ.*, 19:726–731, 2011.
- [83] O. A. Battista, S. Coppick, J. A. Howsmon, F. F. Morehead, and W. A. Sisson. Level-off degree of polymerization—relation to polyphase structure of cellulose fibers. *Ind. Eng. Chem.*, 48:333–335, 1956.
- [84] X. M. Dong, T. Kimura, J.-F. Revol, and D. G. Gray. Effects of Ionic Strength on the Isotropic-Chiral Nematic Phase Transition of Suspensions of Cellulose Crystallites. *Langmuir*, 12:2076–2082, 1996.
- [85] J.-F. Revol, H. Bradford, J. Giasson, R. H. Marchessault, and D. G. Gray. Helicoidal Self-Ordering of Cellulose Microfibrils in Aqueous Suspensions. *Int. J. Biol. Macromol.*, 14:170–172, 1992.
- [86] R. H. Marchessault, F. F. Morehead, and N. M. Walter. Liquid crystal systems from fibrillar polysaccharides. *Nature*, 184:632–633, 1959.
- [87] J.-F. Revol, L. Godbout, and D. G. Gray. Solid self-assembled films of cellulose with chiral nematic order and optically variable properties. *J. Pulp Pap. Sci.*, 24:146–149, 1998.
- [88] J.-F. Revol, L. Godbout, and D. G. Gray. Solidified liquid crystals of cellulose with optically variable properties, 1997. US Patent 5,629,055.
- [89] Y. Nishiyama, S. Kuga, M. Wada, and T. Okano. Cellulose Microcrystal Film of High Uniaxial Orientation. *Macromolecules*, 30:6395–6397, 1997.
- [90] J. Han, C. Zhou, Y. Wu, F. Liu, and Q. Wu. Self-Assembling Behavior of Cellulose Nanoparticles during Freeze-Drying: Effect of Suspension Concentration, Particle Size, Crystal Structure, and Surface Charge. *Biomacromolecules*, 14:1529–1540, 2013.
- [91] S. Beck, J. Bouchard, and R. Berry. Dispersibility in Water of Dried Nanocrystalline Cellulose. *Biomacromolecules*, 13:1486–1494, 2012.
- [92] S. Perez and D. Samain. Structure and Engineering of Celluloses. *Adv. Carbohydr. Chem. Biochem.*, 64:25–116, 2010.
- [93] B. G. Rånby. Aqueous colloidal solutions of cellulose micelles. *Acta Chem. Scand.*, 40:649–650, 1949.

- [94] B. G. Rånby. The colloidal properties of cellulose micelles. *Discuss. Faraday Soc.*, 11:158–164, 1951.
- [95] P. Scherrer. Bestimmung der Größe und der inneren Struktur von Kolloidteilchen mittels Röntgenstrahlen. *Nachrichten von der Gesellschaft der Wissenschaften zu Göttingen, Mathematisch-Physikalische Klasse*, 2:98, 1918.
- [96] S. Elazzouzi-Hafraoui, Y. Nishiyama, J.-L. Putaux, L. Heux, F. Dubreuil, and C. Rochas. The shape and size distribution of crystalline nanoparticles prepared by acid hydrolysis of native cellulose. *Biomacromolecules*, 9:57–65, 2008.
- [97] G. Sèbe, F. Ham-Pichavant, E. Ibarboure, A. L. C. Koffi, and P. Tingaut. Supramolecular Structure Characterization of Cellulose II Nanowhiskers Produced by Acid Hydrolysis of Cellulose I Substrates. *Biomacromolecules*, 13:570–578, 2012.
- [98] I. Kalashnikova, H. Bizot, B. Cathala, and I. Capron. Modulation of Cellulose Nanocrystals Amphiphilic Properties to Stabilize Oil/Water Interface. *Biomacromolecules*, 13:267–275, 2012.
- [99] A. Vogel. *Zur Feinstruktur von Ramie*. PhD thesis, E. T. H. Zurich, 1953.
- [100] R. H. Marchessault, F. F. Morehead, and M. J. Koch. Some hydrodynamic properties of neutral suspensions of cellulose crystallites as related to size and shape. *J. Coll. Sci. Imp. U. Tok.*, 16:327–344, 1961.
- [101] E. E. Urena-Benavides, P. J. Brown Jr., and C. L. Kitchens. Effect of Jet Stretch and Particle Load on Cellulose Nanocrystal-Alginate Nanocomposite Fibers. *Langmuir*, 26:14263–14270, 2010.
- [102] E. E. Urena-Benavides, G. Ao, V. A. Davis, and C. L. Kitchens. Rheology and Phase Behavior of Lyotropic Cellulose Nanocrystal Suspensions. *Macromolecules*, 44:8990–8998, 2011.
- [103] M. Uhlig, A. Fall, S. Wellert, M. Lehmann, S. Prévost, L. Wågberg, R. von Klitzing, and G. Nyström. Two-dimensional aggregation and semidilute ordering in cellulose nanocrystals. *Langmuir*, 32:442–450, 2016.
- [104] Y. Su, C. Burger, B. S. Hsiao, and B. Chu. Characterization of TEMPO-oxidized cellulose nanofibers in aqueous suspension by small-angle X-ray scattering. *J. Appl. Crystallogr.*, 47:788–798, 2014.
- [105] T. Abitbol, E. Kloser, and D. G. Gray. Estimation of the surface sulfur content of cellulose nanocrystals prepared by sulfuric acid hydrolysis. *Cellulose*, 20:785–794, 2013.
- [106] C. Bruel, J. R. Tavares, P. J. Carreau, and M.-C. Heuzey. The structural amphiphilicity of cellulose nanocrystals characterized from their cohesion parameters. *Carbohydr. Polym.*, 205:184–191, 2019.

- [107] A. P. Heiner, L. Kuutti, and O. Teleman. Comparison of the interface between water and four surfaces of native crystalline cellulose by molecular dynamics simulations. *Carbohydr. Res.*, 306:205–220, 1998.
- [108] J. F. Matthews, C. E. Skopec, P. E. Mason, P. Zuccato, R. W. Torget, J. Sugiyama H. E. Himmel, and J. W. Brady. Computer simulation studies of microcrystalline cellulose I $\beta$ . *Carbohydr. Res.*, 341:138–152, 2006.
- [109] K. Mazeau and A. Rivet. Wetting the (110) and (100) Surfaces of I $\beta$  Cellulose Studied by Molecular Dynamics. *Biomacromolecules*, 9:1352–1354, 2008.
- [110] C. Yamane, T. Aoyagi, M. Ago, K. Sato, K. Okajima, and T. Takahashi. Two different surface properties of regenerated cellulose due to structural anisotropy. *Polym. J.*, 38:819–826, 2006.
- [111] K. Mazeau and C. Vergelati. Atomistic Modeling of the Adsorption of Benzophenone onto Cellulosic Surfaces. *Langmuir*, 18:1919–1927, 2002.
- [112] S. Besombes and K. Mazeau. The cellulose/lignin assembly assessed by molecular modeling. Part 1: adsorption of a threo guaiacyl  $\beta$ -o-4 dimer onto a I $\beta$  cellulose whisker. *Plant Physiol. Bioch.*, 43:299–308, 2005.
- [113] S. Besombes and K. Mazeau. The cellulose/lignin assembly assessed by molecular modeling. Part 2: seeking for evidence of organization of lignin molecules at the interface with cellulose. *Plant Physiol. Bioch.*, 43:277–286, 2005.
- [114] S. Shafiei-Sabet, W. Y. Hamad, and S. G. Hatzikiriakos. Influence of degree of sulfation on the rheology of cellulose nanocrystal suspensions. *Rheol. Acta*, 52:741–751, 2013.
- [115] J. N. Israelachvili. *Intermolecular and Surface Forces*. Academic Press, 2011.
- [116] Y. Min, M. Akbulut, K. Kristiansen, Y. Golan, and J. Israelachvili. The role of inter-particle and external forces in nanoparticle assembly. *Nat. Mater.*, 7:527–538, 2008.
- [117] K. Kocavar and I. Musevic. Structural forces near phase transitions of liquid crystals. *Chem. Phys. Chem.*, 4:1049–1056, 2003.
- [118] J. Israelachvili and D. Gourdon. Putting liquids under molecular-scale confinement. *Science*, 292:867–868, 2001.
- [119] Ph. C. van der Hoeven and J. Lyklema. Electrostatic Stabilization in Non-Aqueous Media. *Adv. Colloid Interface Sci.*, 42:205–277, 1992.
- [120] B. Kronberg, K. Holmberg, and B. Lindman. *Surface Chemistry of Surfactants and Polymers*, chapter Colloidal Stability. John Wiley & Sons, Ltd., Chichester, U. K., 1st edition edition, 2014.

- [121] S. Shafiei-Sabet, W. Y. Hamad, and S. G. Hatzikiriakos. Ionic Strength Effects on the Microstructure and Shear Rheology of Cellulose Nanocrystals Suspensions. *Cellulose*, 21:3347–3359, 2014.
- [122] J. R. Bruckner, A. Kuhnhold, C. Honorato-Rios, T. Schilling, and J. P. F. Lagerwall. Enhancing Self-Assembly in Cellulose Nanocrystal Suspensions Using High-Permittivity Solvents. *Langmuir*, 32:9854–9862, 2016.
- [123] C. C. Y. Cheung, M. Giese, J. A. Kelly, W. Y. Hamad, and M. J. MacLachlan. Iridescent Chiral Nematic Cellulose Nanocrystal/Polymer Composites Assembled in Organic Solvents. *ACS Macro Lett.*, 2:1016–1020, 2013.
- [124] J. Hildebrand and R. L. Scott. *The Solubility of Nonelectrolytes*. Reinhold, New York, NY, U. S. A., 3rd edition, 1950.
- [125] J. Hildebrand and R. L. Scott. *Regular Solutions*. Prentice-Hall, Englewood Cliffs, NJ, U. S. A., 1962.
- [126] C. M. Hansen. *The Three Dimensional Solubility Parameter and Solvent Diffusion Coefficient, Their Importance in Surface Coating Formulation*. PhD thesis, Technical University of Denmark, Copenhagen, Denmark, 1967.
- [127] C. M. Hansen. *Hansen Solubility Parameters A User’s Handbook*. CRC Press, Boca Raton, FL, U. S. A., 2007.
- [128] B. L. Karger, L. R. Snyder, and C. Eon. An expanded solubility parameter treatment for classification and use of chromatographic solvents and adsorbents. Parameters for dispersion, dipole and hydrogen bonding interactions. *J. Chromatogr.*, 125:71–88, 1976.
- [129] C. M. Hansen and A. Björkman. The Ultrastructure of Wood from a Solubility Parameter Point of View. *Holzforschung*, 52:335–344, 1998.
- [130] C. M. Hansen. Cohesion parameters for surfaces, pigments and fillers. *Surf. Coat. Int.*, 80:386–391, 1997.
- [131] S. J. Abbott, C. M. Hansen, and H. Yamamoto. Hansen solubility parameters in practice software, ebook, datasets, 2018. url: <http://www.hansen-solubility.com>, accessed on 2020/01/16.
- [132] C. M. Hansen. The universality of the solubility parameter. *Ind. Eng. Chem. Prod. Res. Dev.*, 8:2–11, 1969.
- [133] P. S. Minhas and A. A. Robertson. Accessibility of Cellulose by the Thallous Ethylate Method-Application to the Measurement of Cellulose Liquid Interactions 1. *Textile Res. J.*, 37:400–408, 1967.

- [134] A. Larsson and W. E. Johns. Acid-base interactions between cellulose/lignocellulose and organic molecules. *J. Adhesion*, 25:121–131, 1988.
- [135] H. L. Lee and P. Luner. The Solubility Parameter of Cellulose and Alkylketene Dimer (AKD) Determined by Inverse Gas Chromatography. *J. Wood Chem. Technol.*, 11:247–261, 1991.
- [136] N. Huu-Phuoc, H. Nam-Tran, M. Buchmann, and U. W. Kesselring. The Solubility Parameter of Cellulose and Alkylketene Dimer (AKD) Determined by Inverse Gas Chromatography. *Int. J. Pharm.*, 34:217–223, 1987.
- [137] S. X. Peng, H. Chang, S. Kumar, R. J. Moon, and J. P. Youngblood. A comparative guide to controlled hydrophobization of cellulose nanocrystals via surface esterification. *Cellulose*, 23:1825–1846, 2016.
- [138] Y. Yoo and J. P. Youngblood. Green One-Pot Synthesis of Surface Hydrophobized Cellulose Nanocrystals in Aqueous Medium. *ACS Sustainable Chem. Eng.*, 4:3927–3938, 2016.
- [139] S. X. Peng, S. Shrestha, Y. Yoo, and J. P. Youngblood. Enhanced dispersion and properties of a two-component epoxy nanocomposite using surface modified cellulose nanocrystals. *Polymer*, 112:359–368, 2017.
- [140] M. S. Reid, M. Villalobos, and E. D. Cranston. Cellulose Nanocrystal Interactions Probed by Thin Film Swelling to Predict Dispersibility. *Nanoscale*, 8:12247–12257, 2016.
- [141] J. Gu and Y.-L. Hsieh. Surface and Structure Characteristics, Self-Assembling, and Solvent Compatibility of Holocellulose Nanofibrils. *ACS Appl. Mater. Interfaces*, 7:4192–4201, 2015.
- [142] S. El barkany, A. El idrissi, C. Zannagui, F. Tabaght, A. Maaroufi, M. Abou-Salama, and H. Amhamdi. Homogeneous Grafting of New Amido Groups onto Hydroxyethyl Cellulose Acetate Microfibrils: Solubility Study. *Mor. J. Chem.*, 4:743–758, 2016.
- [143] B. Medronho, A. Romano, M. G. Miguel, L. Stigsson, and B. Lindman. Rationalizing cellulose (in)solubility: reviewing basic physicochemical aspects and role of hydrophobic interactions. *Cellulose*, 19:581–587, 2012.
- [144] S. Beck and J. Bouchard. Effect of storage conditions on cellulose nanocrystal stability. *Tappi J.*, 13:9–17, 2014.
- [145] Q. Beuguel, J. R. Tavares, P. J. Carreau, and M.-C. Heuzey. Ultrasonication of spray- and freeze-dried cellulose nanocrystals in water. *J. Colloid Interface Sci.*, 516:23–33, 2018.

- [146] Y. Liu, M. Agthe, M. Salajková, K. Gordeyeva, V. Guccini, A. Fall, G. Salazar-Alvarez, C. Schütz, and L. Bergström. Assembly of cellulose nanocrystals in a levitating drop probed by time-resolved small angle X-ray scattering. *Nanoscale*, 10:18113–18118, 2018.
- [147] J. P. F. Lagerwall, C. Schütz, M. Salajkova, J. Noh, J. H. Park, G. Scalia, and L. Bergström. Cellulose Nanocrystal-Based Materials: From Liquid Crystal Self-Assembly and Glass Formation to Multifunctional Thin Films. *NPG Asia Mater.*, 6:e80, 2014.
- [148] Y. Liu, C. Schütz, G. Salazar-Alvarez, and L. Bergström. Assembly, gelation, and helicoidal consolidation of nanocellulose dispersions. *Langmuir*, 35:3600–3606, 2019.
- [149] X. Mu and D. G. Gray. Formation of chiral nematic films from cellulose nanocrystal suspensions is a two-stage process. *Langmuir*, 30:9256–9260, 2014.
- [150] D. G. Gray. Recent advances in chiral nematic structure and iridescent color of cellulose nanocrystal films. *Nanomaterials*, 6:213–221, 2016.
- [151] S. Beck, J. Bouchard, and R. Berry. Controlling the Reflection Wavelength of Iridescent Solid Films of Nanocrystalline Cellulose. *Biomacromolecules*, 12:167–172, 2012.
- [152] S. Beck, J. Bouchard, G. Chauve, and R. Berry. Controlled production of patterns in iridescent solid films of cellulose nanocrystals. *Cellulose*, 20:1401–1411, 2013.
- [153] A. Tran, W. Y. Hamad, and M. J. MacLachlan. Tactoid Annealing Improves Order in Self-Assembled Cellulose Nanocrystal Films with Chiral Nematic Structures. *Langmuir*, 34:646–652, 2018.
- [154] H. Sojoudiasli, M.-C. Heuzey, P. J. Carreau, and B. Riedl. Rheological behavior of suspensions of modified and unmodified cellulose nanocrystals in dimethyl sulfoxide. *Rheol. Acta*, 56:673–682, 2017.
- [155] H. Yu and Z. Qin. Effect of Cellulose nanocrystal on Crystallization Behavior of Poly(3-hydroxybutyrate-co-3-hydroxyvalerate). *Adv. Mat. Res.*, 430-432:20–23, 2012.
- [156] H.-Y. Yu, Z.-Y. Qin, Y.-N. Liu, L. Chen, N. Liu, and Z. Zhou. Simultaneous improvement of mechanical properties and thermal stability of bacterial polyester by cellulose nanocrystals. *Carbohydr. Polym.*, 89:971–978, 2012.
- [157] C. Zhou, Q. Wu, and Q. Zhang. Dynamic rheology studies of in situ polymerization process of polyacrylamide-cellulose nanocrystal composite hydrogels. *Colloid. Polym. Sci.*, 289:244–255, 2011.
- [158] J. Yang, C.-R. Han, J.-F. Duan, M.-G. Ma, X.-M. Zhang, F. Xu, and R.-C. Sun. Synthesis and characterization of mechanically flexible and tough cellulose nanocrystals-polyacrylamide nanocomposite hydrogels. *Cellulose*, 20:227–237, 2013.



- [159] H. Okura, M. Wada, and T. Serizawa. Dispersibility of HCL Treated Cellulose Nanocrystals with Water-Dispersible Properties in Organic Solvents. *Chem. Lett.*, 43:601–603, 2014.
- [160] M. A. Boles, M. Engel, and D. V. Talapin. Self-Assembly of Colloidal Nanocrystals: From Intricate Structures to Functional Materials. *Chem. Rev.*, 116:11220–11289, 2016.
- [161] I. Capron, O.J. Rojas, and R. Bordes. Behavior of nanocelluloses at interfaces. *Curr. Opin. Colloid Interface Sci.*, 29:83–95, 2017.
- [162] P. Bertsch and P. Fischer. Adsorption and interfacial structure of nanocelluloses at fluid interfaces. *Adv. Colloid Interface Sci.*, 276:102089, 2020.
- [163] P. Bertsch, M. Diener, J. Adamcik, N. Scheuble, T. Geue, R. Mezzenga, and P. Fischer. Adsorption and Interfacial Layer Structure of Unmodified Nanocrystalline Cellulose at Air/Water Interfaces. *Langmuir*, 34:15195–15202, 2018.
- [164] P. Bertsch and P. Fischer. Interfacial rheology of charged anisotropic cellulose nanocrystals at the air-water interface. *Langmuir*, 35:7937–7943, 2019.
- [165] I. Kalashnikova, H. Bizot, B. Cathala, and I. Capron. New Pickering emulsions stabilized by bacterial cellulose nanocrystals. *Langmuir*, 27:7471–7479, 2011.
- [166] I. Kalashnikova, H. Bizot, P. Bertoncini, B. Cathala, and I. Capron. Cellulosic nanorods of various aspect ratios for oil in water Pickering emulsions. *Soft Matter*, 9:952–959, 2013.
- [167] J. Bergfreund, Q. Sun, P. Fischer, and P. Bertsch. Adsorption of charged anisotropic nanoparticles at oil–water interfaces. *Nanoscale Adv.*, 1:4308–4312, 2019.
- [168] F. Cherhal, F. Cousin, and I. Capron. Structural Description of the Interface of Pickering Emulsions Stabilized by Cellulose Nanocrystals. *Biomacromolecules*, 17:496–502, 2016.
- [169] B. P. Binks and T. S. Horozov. *Colloidal particles at liquid interfaces*. Cambridge University Press, Cambridge, U. K., 2006.
- [170] B. P. Binks and P. D. I. Fletcher. Particles adsorbed at the oil-water interface: A theoretical comparison between spheres of uniform wettability and “janus” particles. *Langmuir*, 17:4708–4710, 2001.
- [171] K. Du, E. Glogowski, T. Emrick, T. P. Russell, and A. D. Dinsmore. Adsorption energy of nano- and microparticles at liquid-liquid interfaces. *Langmuir*, 26:12518–12522, 2010.
- [172] S. Süß, T. Sobisch, W. Peukert, D. Lerche, and D. Segets. Determination of hansen parameters for particles: A standardized routine based on analytical centrifugation. *Adv. Powder Technol.*, 29:1550–1561, 2018.

- [173] C. Bruel, T. S. Davies, J. R. Tavares, P. J. Carreau, and M.-C. Heuzey. Self-assembly behaviors of colloidal cellulose nanocrystals: A tale of stabilization mechanisms. *J. Colloid Interface Sci.*, 574:399–409, 2020.
- [174] C. Moreau, A. Villares, I. Capron, and B. Cathala. Tuning supramolecular interactions of cellulose nanocrystals to design innovative functional materials. *Ind. Crop. Prod.*, 93:96–107, 2016.
- [175] A. Dufresne. *Nanocellulose. From Nature to High Performance Tailored Materials*. Walter de Gruyter GmbH, Berlin/Boston, 2nd edition edition, 2017.
- [176] A. D. French. Glucose, not cellobiose, is the repeating unit of cellulose and why that is important. *Cellulose*, 24:4605–4609, 2017.
- [177] H. M. C. Marques. A review on cyclodextrin encapsulation of essential oils and volatiles. *Flavour Frag. J.*, 25:313–326, 2010.
- [178] K. Chaturvedi, K. Ganguly, A. R. Kulkarni, V. H. Kulkarni, M. N. Nadagouda, W. E. Rudzinski, and T. M. Aminabhavi. Cyclodextrin-based siRNA delivery nanocarriers: a state-of-the-art review. *Expert Opin. Drug Del.*, 8:1455–1468, 2011.
- [179] Y. Nishiyama. Molecular interactions in nanocellulose assembly. *Phil. Trans. R. Soc. A.*, 376:20170047, 2017.
- [180] S. K. Cousins and R. M. Brown Jr. Cellulose I microfibril assembly: computational molecular mechanics energy analysis favours bonding by van der Waals forces as the initial step in crystallization. *Polymer*, 36:3885–3888, 1995.
- [181] I. Usov, G. Nyström, J. Adamcik, S. Handschin, C. Schütz, A. Fall, L. Bergström, and R. Mezzenga. Understanding nanocellulose chirality and structure–properties relationship at the single fibril level. *Nat. Commun.*, 6:7564, 2015.
- [182] D. Liu, X. Chen, Y. Yue, M. Chen, and Q. Wu. Structure and rheology of nanocrystalline cellulose. *Carbohydr. Polym.*, 84:316–322, 2011.
- [183] L. Kuutti, J. Peltonen, J. Pere, and O. Teleman. Identification and surface structure of crystalline cellulose studied by atomic force microscopy. *J. Microsc.-Oxford*, 178:1–6, 1995.
- [184] R. H. Wade and J. J. Creely. Structure and Stability of Chloroform-Included Cotton Cellulose1. *Text. Res. J.*, 44:941–945, 1974.
- [185] L. Petersson, I. Kvien, and K. Oksman. Structure and thermal properties of poly(lactic acid)/cellulose whiskers nanocomposite materials. *Compos. Sci. Technol.*, 67:2535–2544, 2007.

- [186] M. E. Himmel, S. Y. Ding, D. K. Johnson, W. S. Adney, M. R. Nimlos, J. W. Brady, and T. D. Foust. Biomass recalcitrance: engineering plants and enzymes for biofuels production. *Science*, 315:804–807, 2007.
- [187] K. Mazeau and M. Wyszomirski. Modelling of Congo red adsorption on the hydrophobic surface of cellulose using molecular dynamics. *Cellulose*, 19:1495–1506, 2012.
- [188] K. M. Conley, M. A. Whitehead, and T. G. M. van de Ven. Probing the structural chirality of crystalline cellulose with induced circular dichroism. *Cellulose*, 24:479–486, 2017.
- [189] K. M. Conley, L. Godbout, M. A. Whitehead, and T. G. M. van de Ven. Reversing the structural chirality of cellulosic nanomaterials. *Cellulose*, 24:5455–5462, 2017.
- [190] G. Siqueira, J. Bras, and A. Dufresne. New Process of Chemical Grafting of Cellulose Nanoparticles with a Long Chain Isocyanate. *Langmuir*, 26:402–411, 2010.
- [191] L. Segal, J. J. Creely, A. E. Martin, Jr., and C. M. Conrad. An Empirical Method for Estimating the Degree of Crystallinity of Native Cellulose Using the X-Ray Diffractometer. *Text. Res. J.*, 29:786–794, 1959.
- [192] C. M. Hansen. The Three Dimensional Solubility Parameter - Key to Paint Component Affinities I. - Solvents, Plasticizers, Polymers, and Resins. *J. Paint Techn.*, 39:104–117, 1967.
- [193] C. M. Hansen and K. Skaarup. The Three Dimensional Solubility Parameter - Key to Paint Component Affinities III. - Independent Calculation of the Parameter Components. *J. Paint Techn.*, 39:511–514, 1967.
- [194] S. Gardebjer, M. Andersson, J. Engström, P. Restorp, M. Persson, and A. Larsson. Using Hansen solubility parameters to predict the dispersion of nano-particles in polymeric films. *Polym. Chem.*, 7:1756–1764, 2016.
- [195] F. Machui, S. Langner, X. Zhu, S. Abbott, and C. J. Brabec. Determination of the P3HT:PCBM solubility parameters via a binary solvent gradient method: Impact of solubility on the photovoltaic performance. *Sol. Energ. Mat. Sol. C.*, 100:138–146, 2012.
- [196] E. Stefanis and C. Panayiotou. Prediction of Hansen Solubility Parameters with a New Group-Contribution Method. *Int. J. Thermophys.*, 29:568–585, 2008.
- [197] D. Bagheriasl, P. J. Carreau, B. Riedl, C. Dubois, and W. Y. Hamad. Shear rheology of polylactide (PLA)–cellulose nanocrystal (CNC) nanocomposites. *Cellulose*, 23:1885–1897, 2016.

- [198] D. Bagheriasl, F. Safdari, P. J. Carreau, C. Dubois, and B. Riedl. Development of cellulose nanocrystal-reinforced polylactide: A comparative study on different preparation methods. *Polym. Compos.*, 40:E342–E349, 2019.
- [199] Q. Beuguel, J. R. Tavares, P. J. Carreau, and M.-C. Heuzey. Rheological behavior of cellulose nanocrystal suspensions in polyethylene glycol. *J. Rheol.*, 62:607–618, 2018.
- [200] C. Zhang, M. R. Salick, T. M. Cordie, T. Ellingham, Y. Dan, and L.-S. Turng. Incorporation of poly(ethylene glycol) grafted cellulose nanocrystals in poly(lactic acid) electrospun nanocomposite fibers as potential scaffolds for bone tissue engineering. *Mater. Sci. Eng. C Mater. Biol. Appl.*, 49:463–471, 2015.
- [201] K. Yao, Q. Meng, V. Bulone, and Q. Zhou. Flexible and Responsive Chiral Nematic Cellulose Nanocrystal/Poly(ethylene glycol) Composite Films with Uniform and Tunable Structural Color. *Adv. Mater.*, 29:1701323, 2017.
- [202] C. Zhou, R. Chu, R. Wu, and Q. Wu. Electrospun polyethylene oxide/cellulose nanocrystal composite nanofibrous mats with homogeneous and heterogeneous microstructures. *Biomacromolecules*, 12:2617–2625, 2011.
- [203] X. Xu, F. Liu, L. Jiang, J. Y. Zhu, D. Haagenson, and D. P. Wiesenborn. Cellulose Nanocrystals vs. Cellulose Nanofibrils: A Comparative Study on Their Microstructures and Effects as Polymer Reinforcing Agents. *ACS Appl. Mater. Inter.*, 5:2999–3009, 2013.
- [204] X. Xu, H. Wang, L. Jiang, X. Wang, S. A. Payne, J. Y. Zhu, and R. Li. Comparison between Cellulose Nanocrystal and Cellulose Nanofibril Reinforced Poly(ethylene oxide) Nanofibers and Their Novel Shish-Kebab-Like Crystalline Structures. *Macromolecules*, 47:3409–3416, 2014.
- [205] Y. Yin, X. Tian, X. Jiang, H. Wang, and W. Gao. Modification of cellulose nanocrystal via SI-ATRP of styrene and the mechanism of its reinforcement of polymethylmethacrylate. *Carbohydr. Polym.*, 142:206–212, 2016.
- [206] J.-M. Raquez, Y. Habibi, M. Murariu, and P. Dubois. Polylactide (PLA)-based nanocomposites. *Prog. Polym. Sci.*, 38:1504–1542, 2013.
- [207] V. Khoshkava and M. R. R. Kamal. Effect of Surface Energy on Dispersion and Mechanical Properties of Polymer/Nanocrystalline Cellulose Nanocomposites. *Biomacromolecules*, 14:3155–3163, 2013.
- [208] P. Dhar, S. M. Bhasney, A. Kumar, and V. Katiyar. Acid functionalized cellulose nanocrystals and its effect on mechanical, thermal, crystallization and surfaces properties of poly (lactic acid) bionanocomposites films: A comprehensive study. *Polymer*, 101:75–92, 2016.

- [209] M. S. Reid, M. Villalobos, and E. D. Cranston. The role of hydrogen bonding in non-ionic polymer adsorption to cellulose nanocrystals and silica colloids. *Curr. Opin. Colloid In.*, 29:76–82, 2017.
- [210] D. Bagheriasl, P. J. Carreau, C. Dubois, and B. Riedl. Properties of polypropylene and polypropylene/poly(ethylene-co-vinyl alcohol) blend/CNC nanocomposites. *Compos. Sci. Technol.*, 117:357–363, 2015.
- [211] V. Khoshkava and M. R. R. Kamal. Effect of drying conditions on cellulose nanocrystal (cnc) agglomerate porosity and dispersibility in polymer nanocomposites. *Powder Technol.*, 261:288–298, 2014.
- [212] A. E. Lewandowska and S. J. Eichhorn. Raman imaging as a tool for assessing the degree of mixing and the interface between polyethylene and cellulose nanocrystals. *IOP Conf. Ser. Mater. Sci. Eng.*, 139:012030, 2016.
- [213] N. H. Inai, A. E. Lewandowska, O. R. Ghita, and S. J. Eichhorn. Interfaces in polyethylene oxide modified cellulose nanocrystal - polyethylene matrix composites. *Compos. Sci. Technol.*, 154:128–135, 2018.
- [214] P. Bolhuis and D. Frenkel. Tracing the Phase Boundaries of Hard Spherocylinders. *J. Chem. Phys.*, 106:667–687, 1997.
- [215] C. Bruel, Q. Beuguel, J. R. Tavares, P. J. Carreau, and M.-C. Heuzey. Apparent structural hydrophobicity of cellulose nanocrystals. *J-FOR*, 7:13–23, 2018.
- [216] C. Bruel, J. R. Tavares, P. J. Carreau, and M.-C. Heuzey. Impact of colloidal stability on cellulose nanocrystals self-ordering in thin films. *TechConnect Briefs*, 1:61–64, 2019.
- [217] Q. Beuguel, D. Bagheriasl, C. Bruel, J. R. Tavares, P. J. Carreau, and M.-C. Heuzey. Comportement rhéologique à l’état fondu de nanocomposites à base de nanocristaux de cellulose (cncs). *Rhéologie*, 34:10–16, 2018.
- [218] S. R. Raghavan and B. H. Cipriano. *Molecular gels*, chapter Gel formation: phase diagrams using tabletop rheology and calorimetry, pages 241–252. Springer, Dordrecht, Netherlands, 2006.
- [219] E. Santanach Carreras, F. Chabert, D. E. Dunstan, and G. V. Franks. Avoiding “mud” cracks during drying of thin films from aqueous colloidal suspensions. *J. Colloid Interface Sci.*, 313:160–168, 2007.
- [220] M. P. Pileni. Supracrystals of Inorganic Nanocrystals: An Open Challenge for New Physical Properties. *Acc. Chem. Res.*, 41:1799–1809, 2008.
- [221] D. Liu, S. Wang, Z. Ma, D. Tian, M. Gu, and F. Lin. Structure–color mechanism of iridescent cellulose nanocrystal films. *RSC Adv.*, 4:39322–39331, 2014.

- [222] A. Gümrah Dumanli, H. M. van der Kooij, G. Kamita, E. Reisner, J. J. Baumberg, U. Steiner, and S. Vignolini. Digital Color in Cellulose Nanocrystal Films. *ACS Appl. Mater. Interfaces*, 6:12302–12306, 2014.
- [223] L. Heux, G. Chauve, and C. Bonini. Nonflocculating and Chiral-Nematic Self-ordering of Cellulose Microcrystals Suspensions in Nonpolar Solvents. *Langmuir*, 16:8210–8212, 2000.
- [224] S. Elazzouzi-Hafraoui, J.-L. Putaux, and L. Heux. Self-assembling and Chiral Nematic Properties of Organophilic Cellulose Nanocrystals. *J. Phys. Chem. B*, 49:11069–11075, 2009.
- [225] J. Yi, Q. Xu, X. Zhang, and H. Zhang. Chiral-nematic self-ordering of rodlike cellulose nanocrystals grafted with poly(styrene) in both thermotropic and lyotropic states. *Polymer*, 49:4406–4412, 2008.
- [226] M. K. Hausmann, G. Siqueira, R. Libanori, D. Kokkinis, A. Neels, T. Zimmermann, and A. R. Studart. Complex-Shaped Cellulose Composites Made by Wet Densification of 3D Printed Scaffolds. *Adv. Funct. Mater.*, page 1904127, 2019.
- [227] G. Bryant, S. R. Williams, L. Qian, I. K. Snook, E. Perez, and F. Pincet. How hard is a colloidal “hard-sphere” interaction? *Phys. Rev. E*, 66:060501, 2002.
- [228] L. Lewis, M. Derakhshandeh, S. G. Hatzikiriakos, W. Y. Hamad, and M. J. MacLachlan. Hydrothermal Gelation of Aqueous Cellulose Nanocrystal Suspensions. *Biomacromolecules*, 17:2747–2754, 2016.
- [229] A. A. Moud, M. Arjmand, J. Liu, Y. Yang, A. Sanati-Nezhad, and S. H. Hejazi. Cellulose nanocrystal structure in the presence of salts. *Cellulose*, 26:9387–9401, 2019.
- [230] L. Heath and W. Thielemans. Cellulose nanowhisker aerogels. *Green Chem.*, 12:1448–1453, 2010.
- [231] L. S. Blachechen, J. P. de Mesquita, E. L. de Paula, F. V. Pereira, and D. F. S. Petri. Interplay of colloidal stability of cellulose nanocrystals and their dispersibility in cellulose acetate butyrate matrix. *Cellulose*, 20:1329–1342, 2013.
- [232] J. Tang, J. Sisler, N. Grishkewich, and K. C. Tam. Functionalization of cellulose nanocrystals for advanced applications. *J. Colloid Interf. Sci.*, 494:397–409, 2017.
- [233] T.A. Dankovich and D.G. Gray. Contact Angle Measurements on Smooth Nanocrystalline Cellulose (I) Thin Films. *J. Adhes. Sci. Technol.*, 25:699–708, 2011.
- [234] T. Javanbakht, W. Raphael, and J. R. Tavares. Physicochemical properties of cellulose nanocrystals treated by photo-initiated chemical vapour deposition (PICVD). *Can. J. Chem. Eng.*, 94:1135–1139, 2016.

- [235] Y. Peng, D.J. Gardner, Y. Han, Z. Cai, and M.A. Tshabalala. Influence of drying method on the surface energy of cellulose nanofibrils determined by inverse gas chromatography. *J. Colloid Interface Sci.*, 405:85–95, 2013.
- [236] D.K. Owens and R.C. Wendt. Estimation of the surface free energy of polymers. *J. Appl. Polym. Sci.*, 13:1741–1747, 1969.
- [237] W. Yu and W. Hou. Correlations of surface free energy and solubility parameters for solid substances. *J. Colloid Interface Sci.*, 544:8–13, 2019.
- [238] R. N. Wenzel. Resistance of solid surfaces to wetting by water. *Industrial & Engineering Chemistry Research*, 28:988–994, 1936.
- [239] R.P. Woodward. Contact angle measurements using the drop shape method, 2018.
- [240] M. Strobel and C. S. Lyons. An essay on contact angle measurements. *Plasma Process. Polym.*, 8:8–13, 2011.
- [241] C. Bruel, S. Queffellou, T. Darlow, N. Virgilio, J. R. Tavares, and G. S. Patience. Experimental Methods in Chemical Engineering: Contact Angles. *Can. J. Chem. Eng.*, 97:832–842, 2019.
- [242] R. G. Good. Contact angle, wetting, and adhesion: a critical review. *J. Adhes. Sci. Technol.*, 6:1269–1302, 1992.
- [243] R. G. Good, N. R. Srivatsa, M. Islam, H. T. L. Huang, and C. J. Van Oss. Theory of the acid-base hydrogen bonding interactions, contact angles, and the hysteresis of wetting: application to coal and graphite surfaces. *J. Adhes. Sci. Technol.*, 4:607–617, 1990.
- [244] C. J. van Oss, R. J. Good, and R. J. Busscher. Estimation of the polar surface tension parameters of glycerol and formamide, for use in contact angle measurements on polar solids. *J. Dispers. Sci. Technol.*, 11:75–81, 1990.
- [245] M. Nosonovsky. On the range of applicability of the wenzel and cassie equations. *Langmuir*, 23:9919–9920, 2007.
- [246] A. Beerbower. Surface free energy: a new relationship to bulk energies. *J. Colloid Interface Sci.*, 36:126–132, 1971.
- [247] D. M. Koenhen and C. A. Smolders. The determination of solubility parameters of solvents and polymers by means of correlations with other physical quantities. *J. Appl. Polym. Sci.*, 19:1161–1179, 1975.
- [248] I. Vavrch. On the determination of the factor between cohesive energy density and surface tension. *J. Colloid Interface Sci.*, 63:600–601, 1978.

- [249] L. Jia and B. Shi. A New Equation between Surface Tensions and Solubility Parameters without Molar Volume Parameters Simultaneously Fitting Polymers and Solvents. *J. Macromol. Sci. B*, 50:1042–1046, 2011.
- [250] M. de Meijer, S. Haemers, W. Cobben, and H. Militz. Surface Energy Determinations of Wood: Comparison of Methods and Wood Species. *Langmuir*, 16:9352–9359, 2000.
- [251] R. Di Mundo and F. Palumbo. Comments regarding an essay on contact angle measurements. *Plasma Processes and Polymers*, 8:14–18, 2011.
- [252] Y. Zhao and J. S. Marshall. Spin coating of a colloidal suspension. *Phys. Fluids*, 20:043302, 2008.
- [253] K. Nelson and D. Turpin. Advancing commercialization of nanocellulose: Critical challenges workshop report, 2020. <https://doi.org/10.13140/RG.2.2.33789.59363>.
- [254] M. Gu, C. Jiang, D. Liu, N. Prempeh, and I. I. Smalyukh. Cellulose nanocrystal/poly(ethylene glycol) composite as an iridescent coating on polymer substrates: Structure-color and interface adhesion. *ACS Appl. Mater. Interfaces*, 8:2565–32573, 2016.
- [255] J. C. Natterodt, A. Shirole, J. Sapkota, J. O. Zoppe, and C. Weder. Polymer nanocomposites with cellulose nanocrystals made by co-precipitation. *J. Appl. Polym. Sci.*, 135:45648, 2018.
- [256] M. R. Kamal and V. Khoshkava. Effect of cellulose nanocrystals (cnc) on rheological and mechanical properties and crystallization behavior of pla/cnc nanocomposites. *Carbohydrate Polymers*, 123:105–114, 2015.
- [257] P. J. Petrino and Y. H. Gaston-Bonhomme and J. L. E. Chevalier. Viscosity and Density of Binary Liquid Mixtures of Hydrocarbons, Esters, Ketones, and Normal Chloroalkanes. *J. Chem. Eng. Data*, 40:136–140, 1995.
- [258] V. K. Syal, S. Chauhan, and U. Kumari. Ultrasonic velocity of binary mixtures of acetone and dioxane with dimethylsulphoxide as one component. *IJPAP*, 43:844–848, 2005.
- [259] I. C. Wei and R. L. Rowley. Binary liquid mixture viscosities and densities. *J. Chem. Eng. Data*, 29:332–335, 1984.
- [260] M. I. Aralaguppi, T. M. Aminabhavi, S. B. Harogoppad, and R. H. Balundgi. Thermodynamic interactions in binary mixtures of dimethyl sulfoxide with benzene, toluene, 1,3-dimethylbenzene, 1,3,5-trimethylbenzene, and methoxybenzene from 298.15 to 308.15 K. *J. Chem. Eng. Data*, 37:298–303, 1992.



- [261] N. V. Sastry, R. R. Thakor, and M. C. Patel. Excess molar volumes, viscosity deviations, excess isentropic compressibilities and deviations in relative permittivities of (alkyl acetates (methyl, ethyl, butyl and isoamyl) + n-hexane, + benzene, + toluene, + (o-, m-, p-) xylenes, + (chloro-, bromo-, nitro-) benzene at temperatures from 298.15 to 313.15 K. *J. Mol. Liq.*, 144:13–22, 2009.
- [262] J. L. E. Chevalier and P. J. Petrino and Y. H. Gaston-Bonhomme. Viscosity and Density of Some Aliphatic, Cyclic, and Aromatic Hydrocarbons Binary Liquid Mixtures. *J. Chem. Eng. Data*, 35:206–212, 1990.
- [263] J. N. Nayak, M. I. Aralaguppi, and T. M. Aminabhavi. Density, Viscosity, Refractive Index, and Speed of Sound in the Binary Mixtures of Ethyl Chloroacetate + Cyclohexanone, + Chlorobenzene, + Bromobenzene, or + Benzyl alcohol at (298.15, 303.15, and 308.15) K. *J. Chem. Eng. Data*, 48:628–631, 2003.
- [264] P. S. Nikam and S. J. Kharat. Densities and Viscosities of Binary Mixtures of N,N-Dimethylformamide with Benzyl Alcohol and Acetophenone at (298.15, 303.15, 308.15, and 313.15) K. *J. Chem. Eng. Data*, 48:1291–1295, 2003.
- [265] K. Z. Yu, H. Gao, H. Wang, and L. Chen. Densities, Viscosities, and Refractive Properties of the Binary Mixtures of the Amino Acid Ionic Liquid (bmim) (Ala) with Methanol or Benzylalcohol at  $T = (298.15 \text{ to } 313.15) \text{ K}$ . *J. Chem. Eng. Data*, 56:2877–2883, 2011.
- [266] M. N. Sovilj. Kinematic Viscosities of Binary and Ternary Liquid Mixtures Involving Chloroform, 2-Propanol, and 2-Butanol at Several Temperatures. *J. Chem. Eng. Data*, 40:1058–1061, 1995.
- [267] B. González, Á. Domínguez, and J. Tojo. Dynamic viscosities of 2-butanol with alkanes ( $C_8$ ,  $C_{10}$ , and  $C_{12}$ ) at several temperatures. *J. Chem. Thermodyn.*, 36:267–275, 2004.
- [268] H. Iloukhani and M. Almasi. Densities, viscosities, excess molar volumes, and refractive indices of acetonitrile and 2-alkanols binary mixtures at different temperatures: Experimental results and application of the Prigogine-Flory-Patterson theory. *Thermochim. Acta*, 495:139–148, 2009.
- [269] N. C. Exarchos and M. Tasioula-Margari I. N. Demetropoulos. Viscosities and Densities of Dilute Solutions of Glycerol Trioleate + Octane, + p-Xylene, + Toluene, and + Chloroform. *J. Chem. Eng. Data*, 40:567–571, 1995.
- [270] I. Gascón, A. M. Mainar, F. M. Royo, and J. S. Urieta. Experimental Viscosities and Viscosity Predictions of the Ternary Mixture (Cyclohexane + 1,3-Dioxolane + 2-Butanol) at 298.15 and 313.15 K. *J. Chem. Eng. Data*, 45:751–755, 2000.

- [271] T. M. Aminabhavi and K. Banerjee. Density, Viscosity, Refractive Index, and Speed of Sound in Binary Mixtures of Dimethyl Carbonate with Methanol, Chloroform, Carbon Tetrachloride, Cyclohexane, and Dichloromethane in the Temperature Interval (298.15–308.15) K. *J. Chem. Eng. Data*, 43:1096–1101, 1998.
- [272] J. Wang, Y. Tian, Y. Zhao, and K. Zhuo. A volumetric and viscosity study for the mixtures of 1-n-butyl-3-methylimidazolium tetrafluoroborate ionic liquid with acetonitrile, dichloromethane, 2-butanone and N, N – dimethylformamide. *Green Chem.*, 5:618–622, 2003.
- [273] N. G. Tsierkezos. Cyclic Voltammetric Studies of Ferrocene in Nonaqueous Solvents in the Temperature Range from 248.15 to 298.15 K. *J. Solution Chem.*, 36:289–302, 2007.
- [274] P. S. Nikam, M. C. Jadhav, and M. Hasan. Density and Viscosity of Mixtures of Dimethyl Sulfoxide +Methanol, +Ethanol, +Propan-1-ol, +Propan-2-ol, +Butan-1-ol, +2-Methylpropan-1-ol, and +2-Methylpropan-2-ol at 298.15 K and 303.15 K. *J. Chem. Eng. Data*, 41:1028–1031, 1996.
- [275] J. G. Baragi, M. I. Aralaguppi, T. M. Aminabhavi, M. Y. Kariduraganavar, and S. S. Kulkarni. Density, Viscosity, Refractive Index, and Speed of Sound for Binary Mixtures of 1,4-Dioxane with Different Organic Liquids at (298.15, 303.15, and 308.15) K. *J. Chem. Eng. Data*, 50:917–923, 2005.
- [276] M. Contreras S. Densities and Viscosities of Binary Mixtures of 1,4-Dioxane with 1-Propanol and 2-Propanol at (25, 30, 35, and 40) °C. *J. Chem. Eng. Data*, 46:1149–1152, 2001.
- [277] B. González, N. Calvar, E. Gómez, and Á. Domínguez. Density, dynamic viscosity, and derived properties of binary mixtures of methanol or ethanol with water, ethyl acetate, and methyl acetate at  $T = (293.15, 298.15, \text{ and } 303.15)$  K. *J. Chem. Thermodyn.*, 39:1578–1588, 2007.
- [278] Y. Maham, T. T. Teng, L. G. Hepler, and A. E. Mather. Densities, Excess Molar Volumes, and Partial Molar Volumes for Binary Mixtures of Water with Monoethanolamine, Diethanolamine, and Triethanolamine from 25 to 80°C. *J. Solution Chem.*, 23:195–205, 1994.
- [279] Y. Maham, C.-N. Liew, and A. E. Mather. Viscosities and Excess Properties of Aqueous Solutions of Ethanolamines from 25 to 80°C. *J. Solution Chem.*, 31:743–756, 2002.
- [280] M. Yasmin and M. Gupta. Density, Viscosity, Velocity and Refractive Index of Binary Mixtures of Poly(Ethylene Glycol) 200 with Ethanolamine, m-Cresol and Aniline at 298.15 K. *J. Solution Chem.*, 40:1458–1472, 2011.

- [281] A. Blanco, A. García-Abuín, D. Gómez-Díaz, J. M. Navaza, and O. L. Villaverde. Density, Speed of Sound, Viscosity, Surface Tension, and Excess Volume of N Ethyl-2-pyrrolidone + Ethanolamine (or Diethanolamine or Triethanolamine) from  $T = (293.15 \text{ to } 323.15) \text{ K}$ . *J. Chem. Eng. Data*, 58:653–659, 2013.
- [282] T. M. Aminabhavi, H. T. S. Phayde, R. S. Khinnavar, B. Gopalakrishna, and K. C. Hansen. Densities, refractive indices, speeds of sound, and shear viscosities of diethylene glycol dimethyl ether with ethyl acetate, methyl benzoate, ethyl benzoate, and diethyl succinate in the temperature range from 298.15 to 318.15 K. *J. Chem. Eng. Data*, 39:251–260, 1994.
- [283] T. M. Aminabhavi, S. K. Raikar, and R. H. Balundgi. Densities, viscosities, refractive indices, and speeds of sound in methyl acetoacetate + methyl acetate + ethyl acetate, + n-butyl acetate, + methyl benzoate, and + ethyl benzoate at 298.15, 303.15, and 308.15 K. *J. Chem. Eng. Data*, 38:441–445, 1993.
- [284] Y. W. Sheu and C.-H. Tu. Densities and Viscosities of Binary Mixtures of Isoamyl Acetate, Ethyl Caproate, Ethyl Benzoate, Isoamyl Butyrate, Ethyl Phenylacetate, and Ethyl Caprylate with Ethanol at  $T = (288.15, 298.15, 308.15, \text{ and } 318.15) \text{ K}$ . *J. Chem. Eng. Data*, 51:496–503, 2006.
- [285] W. Hayduk and V. K. Malik. Density, Viscosity, and Carbon Dioxide Solubility and Diffusivity in Aqueous Ethylene Glycol Solutions. *J. Chem. Eng. Data*, 16:143–146, 1971.
- [286] D. Bohne, S. Fischer, and E. Obermeier. Thermal Conductivity, Density, Viscosity, and Prandtl-Numbers of Ethylene Glycol-Water Mixtures. *Ber. Bunsenges. Phys. Chem.*, 88:739–742, 1984.
- [287] A. Pal, G. Dass, and A. Kumar. Excess Molar Volumes, Viscosities, and Refractive Indices of Triethylene Glycol Dimethyl Ether with Dimethyl Carbonate, Diethyl Carbonate, and Propylene Carbonate at 298.15 K. *J. Chem. Eng. Data*, 43:738–741, 1998.
- [288] M. N. Roy, B. K. Sarkar, and R. Chanda. Viscosity, Density, and Speed of Sound for the Binary Mixtures of Formamide with 2-Methoxyethanol, Acetophenone, Acetonitrile, 1,2-Dimethoxyethane, and Dimethylsulfoxide at Different Temperatures. *J. Chem. Eng. Data*, 52:1630–1637, 2007.
- [289] A. M. Cases, A. C. Gómez Marigliano, C. M. Bonatti, and H. N. Sólamo. Density, Viscosity, and Refractive Index of Formamide, Three Carboxylic Acids, and Formamide + Carboxylic Acid Binary Mixtures. *J. Chem. Eng. Data*, 46:712–715, 2001.

- [290] A. C. Gómez Marigliano and H. N. Sólamo. Density, Viscosity, Excess Molar Volume, Viscosity Deviation, and Their Correlations for Formamide + Three Alkan-1-ols Binary Systems. *J. Chem. Eng. Data*, 47:796–800, 2002.
- [291] B. Orge, M. Iglesias, A. Rodríguez, J. M. Canosa, and J. Tojo. Mixing properties of (methanol, ethanol, or 1-propanol) with (n-pentane, n-hexane, n-heptane and n-octane) at 298.15 K. *Fluid Phase Equilib.*, 133:213–227, 1997.
- [292] N. V. Sastry and M. K. Valand. Densities, Speeds of Sound, Viscosities, and Relative Permittivities for 1-Propanol + and 1-Butanol + Heptane at 298.15 K and 308.15 K. *J. Chem. Eng. Data*, 41:1421–1425, 1996.
- [293] R. A. Clará, A. C. Gómez Marigliano, and H. N. Sólamo. Density, Viscosity, and Refractive Index in the Range (283.15 to 353.15) K and Vapor Pressure of r-Pinene, d-Limonene, ( $\pm$ )-Linalool, and Citral Over the Pressure Range 1.0 kPa Atmospheric Pressure. *J. Chem. Eng. Data*, 54:1087–1090, 2009.
- [294] M. T. Zafarani-Moattar and R. Majdan-Cegincara. Viscosity, Density, Speed of Sound, and Refractive Index of Binary Mixtures of Organic Solvent + Ionic Liquid, 1-Butyl-3-methylimidazolium Hexafluorophosphate at 298.15 K. *J. Chem. Eng. Data*, 52:2359–2364, 2007.
- [295] G. S. Gokavi, J. R. Raju, T. M. Aminabhavi, R. H. Balundgi, and M. V. Mudda-purt. Viscosities and Densities of Binary Liquid Mixtures of Dimethyl Sulfoxide with Chlorobenzene, Pyridine, and Methyl Ethyl Ketone at 25, 35, 45, and 55°C. *J. Chem. Eng. Data*, 31:15–18, 1986.
- [296] I-H. Peng and C.-H. Tu. Densities and Viscosities of Acetone, Diisopropyl Ether, Ethanol, and Methyl Ethyl Ketone with a Five-Component Hydrocarbon Mixture from 288.15 K to 308.15 K. *J. Chem. Eng. Data*, 47:1457–1461, 2002.
- [297] T. M. Aminabhavi and B. Gopalakrishna. Density, Viscosity, Refractive Index, and Speed of Sound in Aqueous Mixtures of N,N-Dimethylformamide, Dimethyl Sulfoxide, N,N-Dimethylacetamide, Acetonitrile, Ethylene Glycol, Diethylene Glycol, 1,4-Dioxane, Tetrahydrofuran, 2-Methoxyethanol, and 2-Ethoxyethanol at 298.15 K. *J. Chem. Eng. Data*, 40:856–861, 1995.
- [298] V. K. Rattan, S. Singh, and B. P. S. Sethi. Viscosities, Densities, and Ultrasonic Velocities of Binary Mixtures of Ethylbenzene with Ethanol, 1-Propanol, and 1-Butanol at (298.15 and 308.15)K. *J. Chem. Eng. Data*, 49:1074–1077, 2004.
- [299] G. Moumouzias, D. K. Panopoulos, and G. Ritzoulis. Excess properties of the binary liquid system propylene carbonate + acetonitrile. *J. Chem. Eng. Data*, 36:20–23, 1991.

- [300] P. K. Muhuri, B. Das, and D. K. Hazra. Viscosities and Excess Molar Volumes of Binary Mixtures of Propylene Carbonate with Tetrahydrofuran and Methanol at Different Temperatures. *J. Chem. Eng. Data*, 41:1473–1476, 1996.
- [301] Y. Oshmyansky, H. J. M. Hanley, J. F. Ely, and A. J. Kidnay. The Viscosities and Densities of Selected Organic Compounds and Mixtures of Interest in Coal Liquefaction Studies. *Int. J. Thermophys.*, 7:599–608, 1986.
- [302] B. Das, M. N. Roy, and D. K. Hazra. Densities and viscosities of the binary aqueous mixtures of tetrahydrofuran and 1, 2-dimethoxyethane at 298, 308 and 318 K. *IJCT*, 1:93–97, 1994.
- [303] D.R. Lide. *CRC Handbook of Chemistry and Physics*. CRC, Boca Raton. Florida., 85th edition edition, 2004.
- [304] C.-J. Hsieh, J.-M. Chen, and M.-H. Li. Dielectric Constants of Aqueous Diisopropanolamine, Diethanolamine, N-Methyldiethanolamine, Triethanolamine, and 2-Amino-2-methyl-1-propanol Solutions. *J. Chem. Eng. Data*, 52:619–623503, 2007.
- [305] J. P. Teas. Graphic analysis of resin solubilities. *J. Paint Technol.*, 40:19–25, 1968.
- [306] L. Gorb, A. Asensio, I. Tu n3n, and M. F. Ruiz-L3pez. The Mechanism of Formamide Hydrolysis in Water from Ab Initio Calculations and Simulations. *Chem. Eur. J.*, 11:6743–6753, 2005.
- [307] G. R. Leader and J. F. Gormley. The Dielectric Constant of N-Methylamides. *J. Am. Chem. Soc.*, 73:5731–5733, 1951.
- [308] H. Zarei, S. A. Golroudbari, and M. Behroozi. Experimental studies on volumetric and viscometric properties of binary and ternary mixtures of N,N-dimethylacetamide, N-methylformamide and propane-1,2-diol at different temperatures. *J. Mol. Liq.*, 187:260–265, 2013.
- [309] M. Kaushik, W. C. Chen, T. G. M. van de Ven, and A. Moores. An improved methodology for imaging cellulose nanocrystals by transmission electron microscopy. *Nord. Pulp Pap. Res. J.*, 29:77–84, 2014.
- [310] S. Park, J. O. Baker, M. E. Himmel, P. A. Parilla, and D. K. Johnson. Cellulose crystallinity index: measurement techniques and their impact on interpreting cellulase performance. *Biotechnol. Biofuels*, 3:10, 2010.
- [311] M. Morra, E. Occhiello, and F. Garbassi. Knowledge about polymer surfaces from contact angle measurements. *Adv. Colloid Interface Sci.*, 32:79–116, 1990.
- [312] M. Strobel, V. Jones, C. S. Lyons, M. Ulsh, M. J. Kushner, R. Dorai, and M. C. Branch. A comparison of corona-treated and flame-treated polypropylene films. *Plasmas Polym.*, 8:61–95, 2003.

- [313] D. Y. Kwok and A. W. Neumann. Contact angle measurement and contact angle interpretation. *Adv. Colloid Interface Sci.*, 81:167–249, 1999.
- [314] D. H. Kaelble. Dispersion-Polar Surface Tension Properties of Organic Solids. *J. Adhes.*, 2:66–81, 1970.
- [315] H. Y. Erbil and R. A. Meriç. Determination of surface free energy components of polymers from contact angle data using nonlinear programming methods. *Coll. Surf.*, 33:85–97, 1988.
- [316] B. Jadczyk, W. Wbjcik, A. Zdziennicka, and J. M. Bruque. Components of the surface free energy of low rank coals in the presence of n-alkanes. *Powder Technol.*, 86:229–278, 1996.
- [317] P. Marliacy, J.-B. Bourdet, L. Schuffenecker, and R. Solimando. Dissolution enthalpy of anhydrous sodium sulfate in water. Experimental measurements and treatment with the electrolyte-NRTL model. *J. Chem. Thermodyn.*, 34:579–591, 2002.
- [318] R. G. Picknett and R. Bexon. The evaporation of sessile or pendant drops in still air. *J. Colloid Interface Sci.*, 61:336, 1977.
- [319] D.C. Boffito, P.A. Patience, B. Srinivisan, M. Perrier, and G.S. Patience. How do you Write and Present Research Well? 10-State the Uncertainty, but Not Too Precisely. *Can. J. Chem. Eng.*, 94:1425–1430, 2016.

## APPENDIX A LIST OF CONTRIBUTIONS

This annex lists the contributions (publications, oral&poster presentations) carried in the context of this Ph.D. project. Awards are highlighted in bold. The list is up to date as of 2020/07/10.

### A.1 LIST OF PUBLICATIONS

#### Publications in peer-reviewed journals

- **C. Bruel**, T. S. Davies, P. J. Carreau, J. R. Tavares, and M.-C. Heuzey. Self-assembly behaviors of colloidal cellulose nanocrystals: A tale of stabilization mechanisms. *Journal of Colloid and Interface Science*, 574:399-409, 2020.
- C. S. Torres Castillo, **C. Bruel**, and J. R. Tavares. Chemical affinity and dispersibility of boron nitride nanotubes. *Nanoscale Advances*, 2:2497-2506, 2020.
- **C. Bruel**, J. R. Tavares, P. J. Carreau, and M.-C. Heuzey. The structural amphiphilicity of cellulose nanocrystals characterized from their cohesion parameters. *Carbohydrate Polymers*, 205:184-191, 2019.
- **C. Bruel**, S. Queffeuilou, T. Darlow, N. Virgilio, J. R. Tavares, and G. S. Patience. Experimental methods in chemical engineering: Contact angles. *Canadian Journal of Chemical Engineering*, 97(4):832-842, 2019 (**Top downloaded paper 2018-2019 in the Can. J. Chem. Eng.**).
- **C. Bruel**, Q. Beuguel, J. R. Tavares, P. J. Carreau, and M.-C. Heuzey. Apparent structural hydrophobicity of cellulose nanocrystals. *J-FOR – Journal of Science & Technology for Forest Products and Processes*, 7(4):13-23, 2018.
- Q. Beuguel, D. Bagheriasl, **C. Bruel**, J. R. Tavares, P. J. Carreau, and M.-C. Heuzey. Comportement rhéologique à l'état fondu de nanocomposites à base de nanocristaux de cellulose (CNCs). *Rhéologie*, 34:10-16, 2018.

#### Publications in conference journals

- **C. Bruel**, J. R. Tavares, P. J. Carreau, and M.-C. Heuzey. Impact of Colloidal Stability on Cellulose Nanocrystals Self-Ordering in Thin Films, *TechConnect Briefs*, 1:61-64, 2019.

## Manuscripts submitted to peer-reviewed journals

- **C. Bruel**, S. Queffeuilou, P. J. Carreau, J. R. Tavares, and M.-C. Heuzey. Orienting cellulose nanocrystal functionalities tunes the wettability of air/samples interfaces. Submitted to *Langmuir* on 2020/06/17, in peer-review.
- M. Mohammadi, **C. Bruel**, M.-C. Heuzey, and P. J. Carreau. CNC dispersion in PLA and PBAT using two solvents: Morphological and rheological properties. Submitted to *Cellulose* on 2020/05/21, in peer-review.

## A.2 LIST OF PRESENTATIONS

### Oral presentations

- **C. Bruel**, T. Davies, J. R. Tavares, P. J. Carreau, and M.-C. Heuzey. Non-aqueous dispersion and self-ordering of cellulose nanocrystals. Presented at the *69th Canadian Chemical Engineering Conference*, Halifax, NS, Canada, 22nd October 2019.
- **C. Bruel**. On the dispersibility and self-ordering properties of cellulose nanocrystals (CNCs). Presented at the *CREPEC Industrial Forum (Invited speaker)*, Montreal, QC, Canada, 9th October 2019.
- **C. Bruel**, J. R. Tavares, P. J. Carreau, and M.-C. Heuzey. Impact of Colloidal Stability on Cellulose Nanocrystals Self-Ordering in Thin Films. Presented at the *TechConnect World Innovation Conference & Expo*, Boston, MA, U.S.A., 19th June 2019.
- **C. Bruel**. La dispersion et l'auto-organisation de cellulose nanocristalline. Presented at the *87th ACFAS Congress* for Canada's finals of *Ma thèse en 180 secondes* (MT180), Gatineau, QC, Canada, 29th May 2019.
- **C. Bruel**. Les matériaux composites de demain : de la nanocellulose dans nos plastiques. Presented at the finals of Polytechnique Montreal's internal contest of *Ma thèse en 180 secondes* (MT180) (**1st prize** and **Public award**), Montreal, QC, Canada, 4th April 2019.
- **C. Bruel**, J. R. Tavares, P. J. Carreau, and M. C. Heuzey. Dispersion and self-ordering of cellulose nanocrystals. Presented at the *7th Joint Chemical Engineering Research Days*, Montreal, QC, Canada, 20th March 2019.
- **C. Bruel**, T. Darlow, S. Queffeuilou, J. R. Tavares, P. J. Carreau, and M.-C. Heuzey. Cellulose nanocrystals: structure-dispersibility-wettability relationships. Presented at the *XXIX Interamerican Congress of Chemical Engineering & 68th Canadian Chemical Engineering Conference*, Toronto, ON, Canada, 29th October 2018.
- Q. Beuguel, D. Bagheri, C. Bruel, M. C. Heuzey, J. R. Tavares, and **P. J. Carreau**.



Rheological Behavior of Cellulose Nanocrystals (CNCs) in Molten Polymers. Presented at the *Annual European Rheology Conference* (AERC 2018), Sorrento, Italy, 20th April 2018.

- **C. Bruel**, Q. Beuguel, J. R. Tavares, P. J. Carreau, and M. C. Heuzey. The Apparent Structural Hydrophobicity of Cellulose Nanocrystals. Presented at the *McGill-Polytechnique Research Day* (**Outstanding contribution-Ph.D., 1st prize**), Montreal, QC, Canada, 27th March 2018.
- **C. Bruel**, D. Khandal, J. R. Tavares, P. J. Carreau, and M. C. Heuzey. Understanding, Enhancing, and Characterizing CNC Dispersion in Non-polar Media. Presented at *Paperweek 2018*, Montreal, QC, Canada, 8th February 2018.
- **C. Bruel**, Q. Beuguel, J. R. Tavares, P. J. Carreau, and M. C. Heuzey. The Apparent Structural Hydrophobicity of Cellulose Nanocrystals. Presented at *BIOFOR 2018*, Montreal, QC, Canada, 7th February 2018.
- C. Bruel, **Q. Beuguel**, J. R. Tavares, P. J. Carreau, and M. C. Heuzey. Gas phase modification of cellulose nanocrystals for improved hydrophobicity. Presented at the *6th International Conference on Biobased and Biodegradable Polymers* (BIOPOL-2017), Mons, Belgium, 13th September 2017.

## Poster presentations

- C. Bruel, **T. Davies**, J. R. Tavares, P. J. Carreau, and M.-C. Heuzey. Promotion of CNC self-ordering in non-aqueous solvents. Presented at the *CREPEC Student Colloquium* (**Outstanding contribution, 3rd prize**) 6th June 2019.
- **C. Bruel**, T. Davies, J. R. Tavares, P. J. Carreau, and M.-C. Heuzey. Promotion of CNC self-ordering in non-aqueous solvents. Presented at *GDRI Nanomatériaux Multifonctionnels Contrôlés: de la dispersion du nano-objet aux propriétés multifonctionnelles*, Jouvence, QC, Canada, 22nd-24th May 2019.
- **C. Bruel**, J. R. Tavares, P. J. Carreau, and M.-C. Heuzey. Promotion of CNC self-assembly in non-aqueous solvents. Presented at *Paperweek 2019*, Montreal, QC, Canada, 7th February 2019.
- **C. Bruel**, S. Queffeuilou, J. R. Tavares, P. J. Carreau, and M.-C. Heuzey. Wettability and chemical affinity of CNC lattice planes. Presented at the *13th CREPEC Annual Colloquium* (**Outstanding contribution, 2nd prize**), Montreal, QC, Canada, 6th December 2018.
- **C. Bruel**, S. Queffeuilou, J. R. Tavares, P. J. Carreau, and M.-C. Heuzey. Wettability and chemical affinity of CNC lattice planes. Presented at the *CREPEC Industrial Forum*, Montreal, QC, Canada, 25th September 2018.

- **C. Bruel**, S. Queffeuilou, J. R. Tavares, P. J. Carreau, and M.-C. Heuzey. Wettability and chemical affinity of CNC lattice planes. Presented at *Nanomaterials for Devices*, Varennes, QC, Canada, 10th-12th September 2018.

## **APPENDIX B    SUPPLEMENTARY INFORMATION TO ARTICLE 1: THE STRUCTURAL AMPHIPHILICITY OF CELLULOSE NANOCRYSTALS CHARACTERIZED FROM THEIR COHESION PARAMETERS**

Charles Bruel, Jason R. Tavares, Pierre J. Carreau, and Marie-Claude Heuzey. The structural amphiphilicity of cellulose nanocrystals characterized from their cohesion parameters. *Carbohydrate Polymers*, 205 (2019) 184-191.

This appendix gathers the density and viscosity data that were employed to calculate relative sedimentation times in pure solvents and binary mixtures as well as the Hansen solubility parameters of the solvents, mixtures, and polymer matrices. The dielectric constants of the pure solvents are also provided. Finally, it includes the pictures of the vials, and the table of results from which Figs. 5.2&5.3 were drawn.



Figure B.1 Sedimentation tests in the set of pure solvents: pictures of the vials were taken after a relative sedimentation time ( $RST$ ) of  $11.8 \times 10^{11} \text{ s}^2\text{m}^{-2}$  on 2 different backgrounds: a colorful one (**a&c**), and a text (**b&d**). The only exception being triethanolamine, for which the sedimentation test was interrupted after  $t_{\text{sed}}=5540 \text{ h}$ , corresponding to a  $RST$  of  $1.59 \times 10^{10} \text{ s}^2\text{m}^{-2}$  (13.5 % of the standard  $RST$ ), because the sedimentation was already finished. Solvents are from left to right in (**a&b**): acetone (0), benzene (0), benzyl alcohol (0), 2-butanol (0), chloroform (1), cyclohexane (0), dichloromethane (1), dimethyl sulfoxide (2), 1,4-dioxane (0), ethanol (0), ethanolamine (2), ethyl acetate (0), ethyl benzoate (0) and ethylene glycol (0). And in (**c&d**): formamide (2), heptane (0), d-limonene (0), methanol (0), methyl ethyl ketone (0), N,N-dimethyl formamide (0), 1-propanol (0), 2-propanol (0), propylene carbonate (0), tetrahydrofuran (0), toluene (0), triethanolamine (0), and water (2). Values between parenthesis correspond to their respective grades, from 0 to 2, and are summarized in Table B.1.

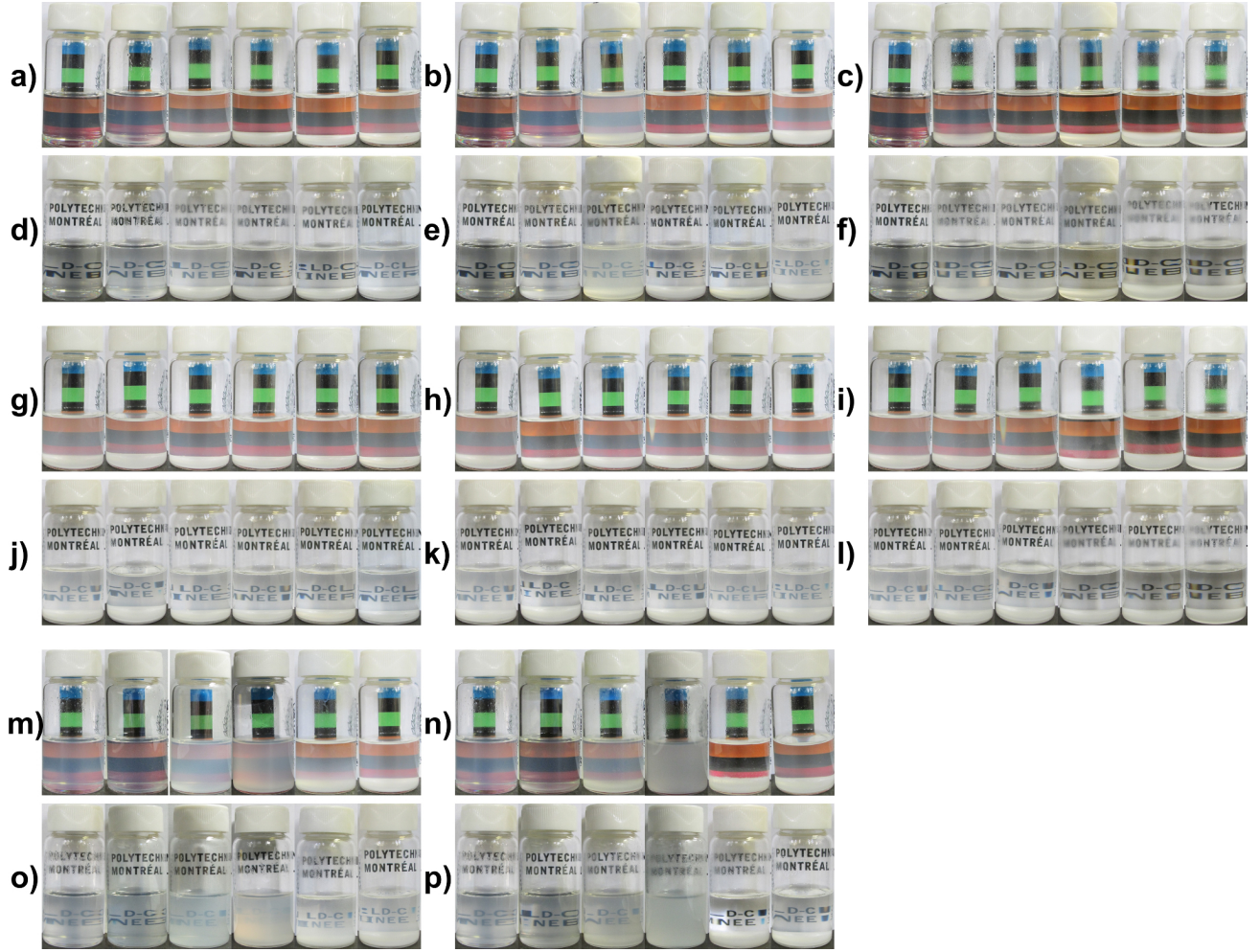


Figure B.2 Sedimentation test in the set of binary mixtures: pictures of the vials were taken after a relative sedimentation time ( $RST$ ) of  $11.8 \times 10^{11} \text{ s}^2 \text{m}^{-2}$  on 2 different backgrounds: a colorful one (a; b; c; g; h; i; m & n), and a text (d; e; f; j; k; l; o & p). If  $\Phi_A$  and  $\Phi_B$  are the volumic fractions in solvents A and B, respectively, then each line of 6 vials corresponds from left to right to the compositions  $(\Phi_A/\Phi_B) = (1/0)$ ,  $(0.8/0.2)$ ,  $(0.6/0.4)$ ,  $(0.4/0.6)$ ,  $(0.2/0.8)$ , and  $(0/1)$ . The couples of solvents studied are: DMSO/acetone (a&d), DMSO/methanol (b&e), DMSO/toluene (c&f), EtOAc/acetone (g&j), EtOAc/methanol (h&k), EtOAc/toluene (i&l), formamide/methanol (m&o), and formamide/1-propanol (n&p). DMSO and EtOAc stand respectively for dimethyl sulfoxide and ethyl acetate. Grades, from 0 to 2, are summarized in Table B.1 for the pure solvents and in Table B.2 for the binary mixtures, respectively.

Table B.1 Properties of the solvent set at 25 °C. Purities are reported as provided by the different commercial suppliers. Dielectric constants,  $\epsilon_{\text{solv}}$ , densities,  $\rho_{\text{solv}}$ , and viscosities,  $\eta_{\text{solv}}$ , were extracted from the literature and averaged between the different sources. The absolute time of sedimentation,  $t_{\text{sed}}$ , was calculated with Eq. 5.1 for a relative sedimentation time ( $RST$ ) of  $1.18 \times 10^{11} \text{ s}^2 \text{m}^{-2}$ . Dispersibility grades, from 0 to 2 (Fig. 5.2.a) were attributed for each solvent once  $t_{\text{sed}}$  had elapsed. HSP values were extracted from the HSPiP database [131].  $RED_{\text{p-s}}$  and  $RED_{\text{np-s}}$ , calculated with Eq. 5.5, are the reduced energy differences of the solvent with the center of the polar sphere and of the non-polar sphere (see Table 5.1 and Fig. 5.2), respectively.

Solvent set		Physical properties (25 °C)				Sedimentation		HSP values (25 °C)			HSP analysis	
Solvent	Purity	$\epsilon_{\text{solv}}^a$	$\rho_{\text{solv}}$ g cm <sup>-3</sup>	$\eta_{\text{solv}}$ mPa s	Ref. <sup>b</sup>	$t_{\text{sed}}$ h	Grade 0 to 2	$\delta_{\text{D}}$ MPa <sup>1/2</sup>	$\delta_{\text{P}}$ MPa <sup>1/2</sup>	$\delta_{\text{H}}$ MPa <sup>1/2</sup>	$RED_{\text{p-s}}$	$RED_{\text{np-s}}$
acetone	99.90 %	21.0(20)	0.785	0.302	[257, 258, 259]	12.1	0	15.5	10.4	7.0	1.80	3.24
benzene	> 99.90 %	2.28(20)	0.874	0.601	[260, 261, 262]	26.9	0	18.4	0.0	2.0	3.13	3.26
benzyl alcohol	> 99.0 %	11.9(30)	1.04	5.34	[263, 264, 265]	310	0	18.4	6.3	13.7	1.82	3.65
2-butanol	99.90 %	17.3(20)	0.801	3.17	[266, 267, 268]	129	0	15.8	5.7	14.5	1.98	4.15
chloroform	99.25 %	4.81(20)	1.47	0.539	[266, 259, 269]	127	1	17.8	3.1	5.7	2.54	0.960
cyclohexane	99.90 %	2.02(20)	0.774	0.888	[257, 270, 259]	35	0	16.8	0.0	0.2	3.27	3.80
dichloromethane	99.90 %	8.93	1.32	0.397	[271, 272, 273]	45.1	1	17.0	7.3	7.1	2.00	1.29
dimethyl sulfoxide	99.90 %	47.2(20)	1.10	1.99	[274, 258, 260]	128	2	18.4	16.4	10.2	0.840	5.88
1,4-dioxane	> 99.0 %	2.22(20)	1.03	1.20	[258, 275, 276]	67.9	0	17.5	1.8	9.0	2.52	1.88
ethanol	95 %	25.3(20)	0.785	1.09	[274, 277, 259]	43.5	0	15.8	8.8	19.4	1.68	6.63
ethanolamine	≥ 99.0 %	31.9(20)	1.01	18.9	[278, 279, 280, 281]	1050	2	17.0	15.5	21.0	0.998	8.61
ethyl acetate	99.90 %	6.08(20)	0.895	0.425	[257, 261, 277]	19.6	0	15.8	5.3	7.2	2.28	1.60
ethyl benzoate	99.0 %	6.20(20)	1.04	1.83	[282, 283, 284]	106	0	17.9	6.2	6.0	2.18	0.832
ethylene glycol	≥ 99.0 %	41.4(20)	1.11	17.2	[285, 286, 287]	1140	0	17.0	11.0	26.0	1.84	9.77
formamide	99.0 %	111(20)	1.13	3.29	[288, 289, 290]	226	2	17.2	26.2	19.0	0.907	11.8
heptane	99.0 %	1.92(20)	0.679	0.393	[291, 292, 262]	13.9	0	15.3	0.0	0.0	3.35	4.33
d-limonene	96 %	2.37	0.841	0.897	[293]	38.4	0	17.2	1.8	4.3	2.78	1.77
methanol	99.90 %	33.0(20)	0.787	0.547	[274, 277, 294]	21.9	0	14.7	12.3	22.3	1.62	8.74
methyl ethyl ketone	99.90 %	18.6(20)	0.800	0.386	[257, 295, 296]	15.7	0	16.0	9.0	5.1	2.04	2.49
N,N-dimethyl formamide	99.90 %	38.3(20)	0.945	0.801	[264, 297, 272, 273]	39.7	0	17.4	13.7	11.3	1.02	4.82
1-propanol	> 99.7 %	20.8(20)	0.800	1.98	[274, 298, 276]	80.5	0	16.0	6.8	17.4	1.84	5.47
2-propanol	> 99.0 %	20.2(20)	0.781	2.04	[274, 266, 268, 259]	80.9	0	15.8	6.1	16.4	1.93	5.02
propylene carbonate	99.5 %	66.1(20)	1.20	2.49	[299, 300, 287]	201	0	20.0	18.0	4.1	1.55	6.84
tetrahydrofuran	> 99.0 %	7.52	0.877	0.461	[301, 297, 294, 302]	20.7	0	16.8	5.7	8.0	2.13	1.04
toluene	99.90 %	2.38(23)	0.862	0.550	[257, 261, 260]	24.2	0	18.0	1.4	2.0	2.98	2.73
triethanolamine	≥ 99.0 %	28.1(30)	1.12	606	[278, 279, 281]	5540 <sup>c</sup>	0	17.3	7.6	21.0	1.80	7.06
water	<sup>d</sup>	80.1(20)	0.997	0.891	[277, 285, 302]	48.0 <sup>e</sup>	2	15.1 <sup>f</sup>	20.4 <sup>f</sup>	16.5 <sup>f</sup>	0.778	9.10

<sup>a</sup> When different from 25 °C, the temperature is provided between parenthesis in °C. Values are extracted from Lide [303], excepted for triethanolamine [304]. <sup>b</sup> References provided here are for  $\rho_{\text{solv}}$  and  $\eta_{\text{solv}}$ . <sup>c</sup> Sedimentation in triethanolamine was interrupted after  $t_{\text{sed}}=5540 \text{ h}$ , corresponding to a  $RST$  of  $1.59 \times 10^{10} \text{ s}^2 \text{m}^{-2}$  — it is 13.5 % of the standard  $RST$  for other solvents. Indeed, sedimentation was not susceptible to continue further as triethanolamine was already awarded 0 for a grade. <sup>d</sup> Distilled water. <sup>e</sup> An absolute sedimentation time of 48 h in water was chosen as a reference to calculate the  $t_{\text{sed}}$  in the other solvents. <sup>f</sup> Water has three sets of HSP, those provided are for “1 % soluble in” — the most appropriate to describe diluted aqueous suspensions [127].



Table B.2 Binary mixture properties at 25 °C. Each line corresponds to a mixture of solvents A and B of respective volumic fractions  $\Phi_A$  and  $\Phi_B$  (vol%). Purities of the different solvents are those reported in Table B.1. Densities and viscosities were interpolated from values found in the literature and averaged between the different sources. The absolute time of sedimentation,  $t_{\text{sed}}$ , was calculated with Eq. 5.1 for a relative sedimentation time ( $RST$ ) of  $1.18 \times 10^{11} \text{ s}^2 \text{m}^{-2}$ . Dispersibility grades, from 0 to 2 (Fig. 5.2.a) were attributed for each solvent once  $t_{\text{sed}}$  had elapsed. HSP values were calculated with Eq. 5.4 from the HSP of pure solvents (Table B.1).  $RED_{\text{p-s}}$  and  $RED_{\text{np-s}}$ , calculated with Eq. 5.5, are the reduced energy differences of the binary mixture with the center of the polar sphere and of the non-polar sphere (see Table 5.1 and Fig. 5.2), respectively.

Solvent A	Binary mixtures			Densities & viscosities (25 °C)			Sedimentation		HSP values (25 °C)			HSP analysis	
	$\Phi_A$ vol%	$\Phi_B$ vol%	Solvent B	$\rho_{\text{mixt}}$ $\text{g cm}^{-3}$	$\eta_{\text{mixt}}$ mPa.s	Ref.	$t_{\text{sed}}$ h	Grade 0 to 2	$\delta_D$ $\text{MPa}^{1/2}$	$\delta_P$ $\text{MPa}^{1/2}$	$\delta_H$ $\text{MPa}^{1/2}$	$RED_{\text{p-s}}$	$RED_{\text{np-s}}$
dimethyl sulfoxide	0.20	0.80	acetone	0.916	0.615	[258]	29.2	0	16.1	11.6	7.6	1.59	3.51
	0.40	0.60		0.993	0.960	[258]	51.4	0	16.7	12.8	8.3	1.38	3.97
	0.60	0.40		1.04	1.32	[258]	76.1	0	17.2	14.0	8.9	1.19	4.53
	0.80	0.20		1.07	1.67	[258]	101	2	17.8	15.2	9.6	0.997	5.18
dimethyl sulfoxide	0.20	0.80	methanol	1.01	1.09	[274]	59.7	0	15.4	13.1	19.9	1.30	7.77
	0.40	0.60		1.05	1.47	[274]	87.4	0	16.2	13.9	17.5	1.001	6.91
	0.60	0.40		1.07	1.73	[274]	105	1	16.9	14.8	15.0	0.780	6.28
	0.80	0.20		1.09	1.89	[274]	120	2	17.7	15.6	12.6	0.716	5.92
dimethyl sulfoxide	0.20	0.80	toluene	0.924	0.794	[260]	38.2	0	18.1	4.4	3.6	2.55	1.52
	0.40	0.60		0.978	1.06	[260]	55.4	0	18.2	7.4	5.3	2.11	1.54
	0.60	0.40		1.02	1.35	[260]	75.9	0	18.2	10.4	6.9	1.68	2.77
	0.80	0.20		1.06	1.65	[260]	99.9	0	18.3	13.4	8.6	1.25	4.30
ethyl acetate	0.20	0.80	acetone	0.828	0.341	[257]	14.4	0	15.6	9.4	7.0	1.88	2.80
	0.40	0.60		0.856	0.372	[257]	16.2	0	15.6	8.4	7.1	1.97	2.45
	0.60	0.40		0.873	0.395	[257]	17.7	0	15.7	7.3	7.1	2.08	2.05
	0.80	0.20		0.884	0.412	[257]	18.7	0	15.7	6.3	7.2	2.18	1.82
ethyl acetate	0.20	0.80	methanol	0.866	0.423	[277]	18.7	0	14.9	10.9	19.3	1.55	7.18
	0.40	0.60		0.881	0.417	[277]	18.9	0	15.1	9.5	16.3	1.60	5.65
	0.60	0.40		0.885	0.424	[277]	19.3	0	15.4	8.1	13.2	1.74	4.06
	0.80	0.20		0.893	0.417	[277]	19.2	0	15.6	6.7	10.2	1.98	2.65
ethyl acetate	0.20	0.80	toluene	0.872	0.491	[257, 261]	21.9	0	17.6	2.2	3.0	2.82	2.07
	0.40	0.60		0.880	0.457	[257, 261]	20.6	0	17.1	3.0	4.1	2.67	1.45
	0.60	0.40		0.886	0.439	[257, 261]	20.0	0	16.7	3.7	5.1	2.54	1.08
	0.80	0.20		0.891	0.430	[257, 261]	19.7	0	16.2	4.5	6.2	2.40	1.18
formamide	0.20	0.80	methanol	0.906	1.05	[290]	49.0	0	15.2	15.1	21.6	1.28	8.97
	0.40	0.60		0.993	1.59	[290]	85.2	2	15.7	17.9	21.0	0.9999	9.46
	0.60	0.40		1.06	2.16	[290]	129	2	16.2	20.6	20.3	0.797	10.1
	0.80	0.20		1.10	2.75	[290]	179	2	16.7	23.4	19.7	0.764	10.9
formamide	0.20	0.80	1-propanol	0.892	2.53	[290]	116	0	16.2	10.7	17.7	1.37	6.16
	0.40	0.60		0.970	3.04	[290]	157	2	16.5	14.6	18.0	0.912	7.26
	0.60	0.40		1.04	3.29	[290]	189	2	16.7	18.4	18.4	0.586	8.64
	0.80	0.20		1.09	3.31	[290]	210	2	17.0	22.3	18.7	0.566	10.2

Table B.3 Polymer Hansen Solubility Parameters at 25 °C. Polymers' HSP are notably functions of their molecular weight and degree of crystallinity [127] and the parameters reported here are average values as provided in the HSPiP polymer dataset [131].  $RED_{p-s}$  and  $RED_{np-s}$ , calculated with Eq. 5.5, are the reduced energy differences of the polymer with the center of the polar sphere and of the non-polar sphere (See Table 5.1 and Fig. 5.2), respectively.

Polymer matrices		HSP values (25 °C)				HSP analysis	
		$\delta_D$ MPa <sup>1/2</sup>	$\delta_P$ MPa <sup>1/2</sup>	$\delta_H$ MPa <sup>1/2</sup>	$R_0$ MPa <sup>1/2</sup>	$RED_{p-s}$	$RED_{np-s}$
PE	poly(ethylene)	16.9	0.8	2.8	8.0	3.00	2.63
PEG	poly(ethylene glycol)	17.0	10.0	5.0	8.0	1.90	2.60
PLA	poly(lactic acid)	18.5	8.0	7.0	8.0	1.92	1.85
PMMA	poly(methyl methacrylate)	18.6	10.5	5.1	8.0	1.83	3.00
PP	poly(propylene)	18.0	0.0	1.0	8.0	3.20	3.51
PVOH	poly(vinyl alcohol)	15.0	17.2	17.8	8.0	0.944	8.33



## APPENDIX C SUPPLEMENTARY INFORMATION TO ARTICLE 2: SELF-ASSEMBLY BEHAVIORS OF COLLOIDAL CELLULOSE NANOCRYSTALS: A TALE OF STABILIZATION MECHANISMS

Charles Bruel, Tom S. Davies, Pierre J. Carreau, Jason R. Tavares and Marie-Claude Heuzey. Self-assembly behaviors of colloidal cellulose nanocrystals: A tale of stabilization mechanisms. *Journal of Colloid and Interface Science*, 574 (2020) 399-409.

This supplementary information (SI) gathers the extended protocols - including those for sample analysis - and the physical data used within this work (Tables C.1&C.2). Some additional results on the behavior of CNCs in standing vials and upon solvent casting are also presented and discussed. Finally, Table C.3 summarizes our findings and provides guidelines about how to classify a suspension's stabilization mechanisms based on its behavior in standing vials and upon solvent casting.

### C.1 SI to “2- Materials and methods”

#### C.1.1 SI to “2.1- Materials”

**Solvent selection:** Solvents were selected for their widely representative chemistries based on the Hansen solubility parameters (HSP) theory. Fig. C.1 is a Teas graph [305], in which HSP coordinates  $\{\delta_D; \delta_P; \delta_H\}$  are plotted as their percent fraction  $\{f_D; f_P; f_H\}$  (e.g.,  $f_D = 100 \times \delta_D / (\delta_D + \delta_P + \delta_H)$ ). The empty black circle represents the chemical affinity of CNCs [106] and the 16 others are for the solvents probed in our work (numbered as a function of their dielectric constant from the highest to the lowest, see Table C.1, the color code is the same than those employed in Figs. 6.2&C.3). The chemical affinity between CNCs and a solvent,  $R_a$ , may be expressed as a function of the distance between the CNC circle and the solvent's symbols. The dotted grey line highlights the threshold  $R_0 = 7.8 \text{ MPa}^{1/2}$  of stability against sedimentation; good solvents for CNCs are located within this area [106]. Regions of the graphs corresponding to  $f_D < 20\%$ ,  $f_P > 50\%$ , or  $f_H > 50\%$ , are empty as these criteria cannot be met by common solvents [127]. As may be seen, the probed solvents cover most of the remaining area.

**Solvent parameters:** Solvent parameters employed in this work are provided in Table C.1. It is worth noting that, while our experiments were conducted at 60 °C, HSP values are

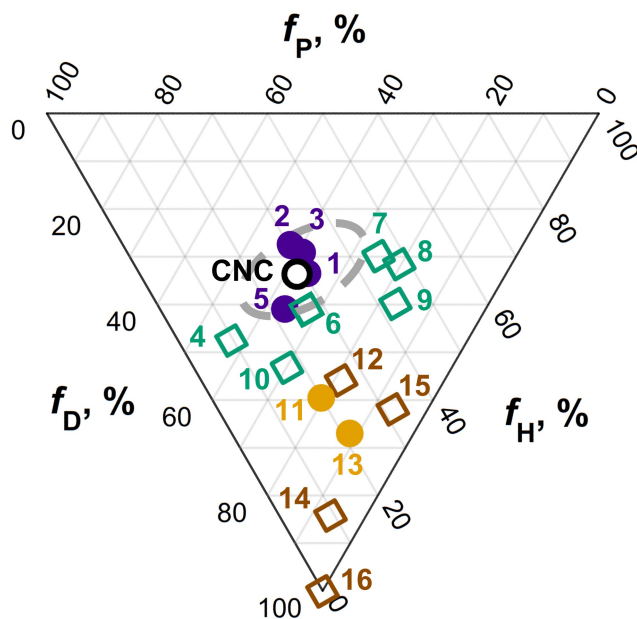


Figure C.1 Teas graph of the solvents employed in this study. Axes represent the potential for interaction of a chemical with its environment in terms of dispersive ( $f_D$ ), dipole-dipole ( $f_P$ ), and H-bonding ( $f_H$ ) interactions, as a percentage of the total potential for interaction. Solvents are ranked from 1 to 16 as a function of their dielectric constant (from high to low, see Table C.1). The color code is the same than that of Figs. 6.2&C.3. The chemical affinity of CNC polar surfaces is shown by an empty black circle and the grey dotted line represents the threshold  $R_0=7.8 \text{ MPa}^{1/2}$  of good chemical affinity for the CNCs: solvents within this area adsorb significantly on CNC polar surfaces (see section 3.2).

tabulated for 25 °C and dielectric constants at 20 °C. This is because HSP theory has been elaborated at 25 °C [127], while the work of van der Hoeven and Lyklema [119] on which we based our criteria for the dielectric constants was led at room temperature. A discussion on the influence of the temperature on the validity of our criteria may be found in the main article (Section 4.3, *Limitations and extrapolability*).

**Polytetrafluoroethylene (PTFE) evaporating dishes:** As mentioned in the article, these evaporating dishes had a spiral pattern imprinted at their bottom that arises from the production process. The spiral is clearly visible at the center of the dish (Fig. C.2.a) and its curvature decreases when it is observed farther from the center and closer to the edge (Fig. C.2.b&c). The width of the spiral pattern is of roughly  $\sim 80 \mu\text{m}$ , which matches the imprinting witnessed on the bottom sides of the DMSO and formamide-cast thin films (Fig. 6.3).

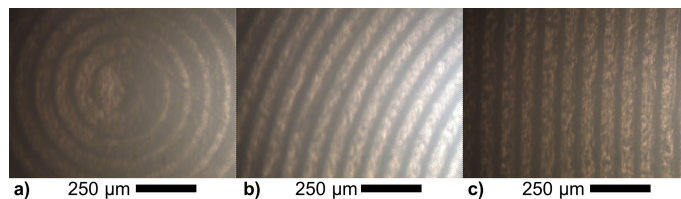


Figure C.2 Optical microscopy images of the PTFE evaporating dish. The imprinted spiral motive is clearly visible at the center of the dish **(a)**. Its curvature decreases as it is observed farther from the center **(b)**, up to being almost not visible close to the edge **(c)**.

### C.1.2 SI to “2.2- Protocols”

**Solvent addition to the CNCs:** While manipulating, we found it easy to identify which media would provide a combination of electrostatic and solvation-induced stabilization to the nanoparticles based on CNC behavior upon addition of the first drops of solvent. If the desired quantity of spray-dried CNCs has been weighed in a vial, adding a drop of good solvent ( $R_a \leq 7.8 \text{ MPa}^{1/2}$ : formamide, MF, water, or DMSO) on top of it indeed leads to the immediate formation of a sticky gel that does not break upon addition of further solvent: the gel remains stuck at the bottom of the vial, which makes the ultrasonication more challenging since this large agglomerate first needs to be put in suspension (using a spatula to detach it from the walls of the vial for instance). The addition of a poor solvent ( $R_a > 7.8 \text{ MPa}^{1/2}$ ) does not result in the formation of a gel, making ultrasonication easier. Working with binary mixtures consisting of a good and a poor solvent (as presented in Fig. 6.5 of the main article, for instance), it is thus rather counter-intuitively that we found it easier to add the poor solvent first to wet the spray-dried powder without forming a gel, and then add the good solvent in a second step.

**Ultrasonication:** As we optimized our protocol for dispersion, we found it significantly more efficient to vary the position of the probe within the vial during the process to ensure a more homogeneous treatment. It was especially relevant in highly viscous solvents such as ethylene glycol in which the high viscosity is expected to decrease the efficiency of the mixing generated by the ultrasonic probe. In practice, the probe was kept immobile but the position of the vial (together with that of its ice-bath) was varied to ensure that the whole suspension was covered by the treatment.

**Evaporation time:** The samples were left to dry for 72 h, unless the solvent had a boiling point over 180 °C, in which case additional time was provided for a complete evaporation. At 60 °C, suspensions in DMSO and MF were left to evaporate for 6 days. It was 9, 13, and 14 days in EG, F, and PC, respectively (Table C.1).

**Vials tests for gelation:** Gelation was assessed through vial inversion in tabletop rheology [218]. Vials were sealed right after sonication and placed vertically in a controlled room at the desired temperature for a period of 24 h, unless otherwise mentioned. The vials were then inclined horizontally and a picture was taken after 60 s. Vials were kept in that position for a longer time to make sure that what was observed was a yield stress and not the result of a high viscosity fluid [218]. For a fluid, gravity is expected to lead to a horizontal air/media interface (angle of 0° between the interface and the horizontal). The presence of a yield stress, in the case of a gel, means that the system will stabilize at an angle greater than 0° as the gravity induced force falls below the yield stress. An angle of 90° corresponds to a scenario in which inclining the vial does not move the gel at all. It is, hence, possible to detect gelation and roughly rank the strength of the gels (on a comparative basis) based on vial tests such as those [218]. In our interpretation of these tests, we assumed that the detection of a yield stress based on tabletop rheology, even a faint one, was likely to mean that the system was at kinetic arrest with regards to CNC self-ordering.

**Optical microscopy:** Optical microscopy (OM) imaging was performed with a hyperspectral microscope (Olympus BX51, CytoViva®), which operated with a 150 W quartz halogen light source (Fiber-Lite DC-950, Dolan Jenner Industries) and an optical camera (Retiga-2000R Fast 1394, QImaging). Imaging was performed employing a 10X lens set in either reflective or transmission mode. In the latter case, polarizers were placed before and after the sample and the angle between them was either set at 0° (light polarized only once) or at 90° (cross-polarizer) to highlight the optical activity of the sample.

**Scanning electron microscopy:** Analysis of the thin films' cross section was performed with a Tabletop Hitachi TM3030+ scanning electron microscope (SEM) operating at 15 kV and with a magnification ranging from  $\times 150$  to  $\times 12,000$ . The samples were prepared by exposing the cross section of the thin films using a razor blade. The cut was performed with an angle of 45°. A 6 nm-thick layer of chromium was then deposited on the cross-section by metal sputtering in order to improve the contrast of the SEM images.

## C.2 SI to “3- Analysis of the stabilization mechanisms”

### C.2.1 SI to “3.3- A diagram for stability mechanisms”

**DISA in standing colloidal suspensions** In our previous work [106], vial tests exploring CNC behavior in suspensions were performed at a concentration of  $10 \text{ mg}_{\text{CNC}}/\text{mL}_{\text{solvent}}$ . Reinterpreting these results in terms of stabilization mechanisms (using the classification presented in Fig. 6.1.c) provides a clear picture of CNC solvent dispersibility and resistance against DISA. In Fig. C.3, suspensions that are stable against sedimentation are plotted as filled circles, and those that sediment as empty diamonds. The color code refers to the expected nature of the stabilization mechanism (see Fig. 6.1): none (brown), electrostatic (sea green), solvation (yellow), solvation and electrostatic (purple).

Three distinct behaviors could be observed [215, 106] as CNC suspensions were either:

1. clear and stable against sedimentation (as in water, DMSO, formamide, and N-methylformamide);
2. cloudy and stable against sedimentation (as in chloroform and dichloromethane);
3. cloudy (with different shades) and that sedimented overtime (other solvents of our set).

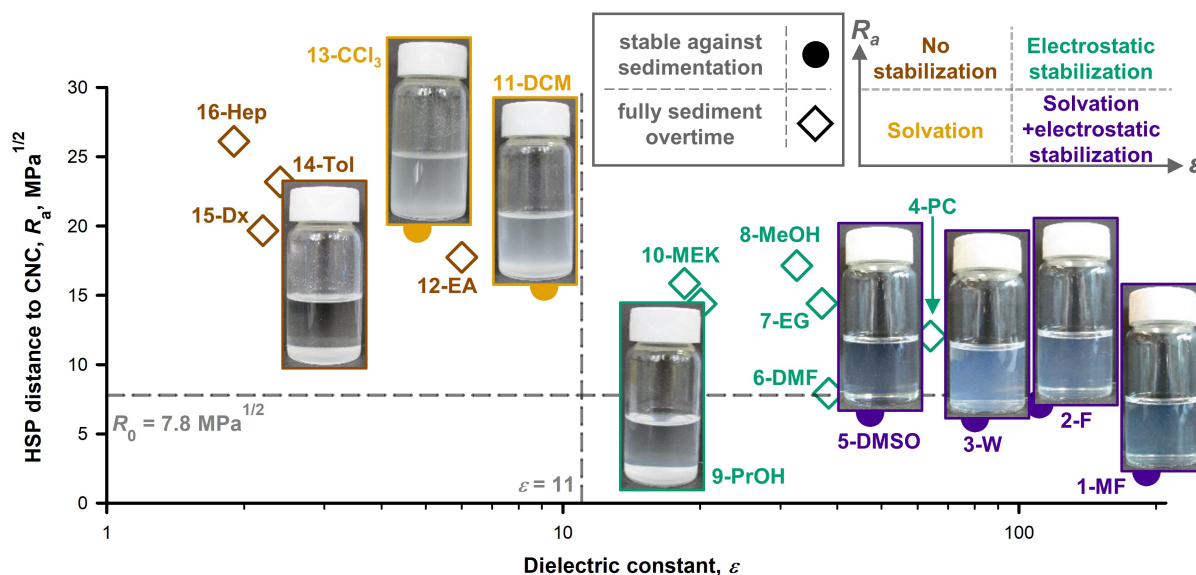


Figure C.3 Dispersion tests of 16 CNC suspensions ( $10 \text{ mg}_{\text{CNC}}/\text{mL}_{\text{solvent}}$ ) as a function of the dielectric constant,  $\epsilon$ , of the solvent and of its chemical affinity for the CNC particles,  $R_a$ . Figure adapted from the results published by Bruel et al. [106], in which vial pictures are observed at kinetic equilibrium. All chemical abbreviations are defined in Table C.1.

The two first categories correspond to suspensions stabilized by a combination of solvation and electrostatic (Fig. C.3, purple filled circles) and solvation-only (yellow filled circles) effects, while the third engulfs suspensions that are expected to be electrostatically (green empty diamonds) stabilized and those that should not benefit from any form of stabilization (brown empty diamonds). While the resistance against sedimentation (filled circles) appears to be correlated to the presence of solvation-induced stabilization (purple and yellow symbols), it should not be treated as a result: it is precisely this lack of sedimentation that led us to conclude that the adsorption of solvent molecules on the nanocrystal surfaces was significant in these media, thus enabling us to map CNC chemical affinity [106] and formulate Eq. 6.2 for  $R_a$ .

The dielectric constant, and thus the electrostatic stabilization, seems to have a significant effect on the turbidity of the suspension and over the sedimentation time: while both CNC suspensions in dichloromethane ( $\epsilon=9.1$ ) and chloroform ( $\epsilon=4.8$ ) were cloudy, which indicates a tendency for DISA and agglomeration, the former were found to be notably clearer than the latter. Other solvents with a dielectric constant below 5 sedimented within seconds instead of the hours or days displayed by those with a higher dielectric constant [215, 106]. No clear transition in sedimentation behavior was observed around  $\epsilon \approx 11$  as sedimentation rate is hugely influenced by other factors such as solvent viscosity and density [127].

In terms of self-assembly mechanism, these results imply that all CNC suspensions, except the ones undergoing a combination of electrostatic and solvation-induced stabilizations, are subject to DISA at low concentrations ( $10 \text{ mg}_{\text{CNC}}/\text{mL}_{\text{solvent}}$ ) and over a short period of time (ranging from a few seconds to a few days). In practice, it means that upon evaporation, a competition is expected to take place in these media between EISA and DISA, and thus between thin film formation and bulk nucleation.

### C.3 SI to “4- Results and discussion”

#### C.3.1 SI to “4.1.1- Combined influence of solvation-induced and electrostatic stabilizations”

Lagerwall et al. [147] discussed the balance in aqueous suspensions between “glass-like” gelation and chiral nematic domains formation, the latter leading to the appearance of the helicoidal structure that brings iridescence. While they did not use the terminology employed in the broader field of nanocrystals self-assembly, the competition they describe corresponds to that between DISA and EISA, respectively: when evaporation occurs, CNC concentration increases and chiral nematic domains eventually form (onset of EISA). As the viscosity of

the system increases, the mobility of CNC particles is reduced up to the point where gelation happens (onset of DISA) and kinetically it prevents any further self-ordering. Described as the gelation point, or as the point of kinetic arrest, it is usually expressed as a critical concentration threshold,  $C_{\text{gel}}$  [147, 122]. The time span between the onset of EISA and the kinetic arrest represents an operation window for chiral nematic domain formation. Since the latter may lapse over several tens of hours [122], failure to provide a long enough operation window results in incomplete self-ordering and casting of “glass-like” systems [147]. Extending the operating window, by slowing down the evaporation rate in this critical phase, can improve the outcome by enabling further self-ordering to take place [153].

In order to estimate  $C_{\text{gel}}$  for the suspensions stabilized by electrostatic and solvation effects, we performed tabletop rheology analysis [218]. Vials of CNC suspensions at 10, 30, 50, 70, and 100 mg<sub>CNC</sub>/mL<sub>solvent</sub> were prepared in DMSO, water, MF, and formamide, and assessed gel formation at room temperature ( $\sim 25^\circ\text{C}$ ) after 24 h. In formamide, a dispersion at 100 mg<sub>CNC</sub>/mL<sub>solvent</sub> could not be achieved under our protocol: the vials broke repeatedly before the treatment could be completed. It is probably because the high viscosity of this system eases the propagation of the ultrasonic waves, thus causing more damages to the walls of the vial.

Immediately after sonication (Fig. C.4.a), all the suspensions were fluid, including the most concentrated ones (100 mg<sub>CNC</sub>/mL<sub>solvent</sub>): it is only after a certain period of time that a gel eventually forms as DISA progressively takes place in the media. For a given solvent, the turbidity of the suspension increased with CNC concentration. However, and contrarily to what was observed for poorer solvents (see the text related to Fig. C.3), we did not find turbidity to be directly correlated with the dielectric constant of the solvents as the suspensions in DMSO and F were the two clearest at high concentrations. It suggests that the dielectric constant alone cannot explain the full extent of CNC agglomeration. In systems stabilized by a combination of solvation and electrostatic effects, the link between turbidity and potential for self-ordering thus remains to be investigated. Quantitative turbidity data will probably be required to elucidate self-ordering.

After 24 h (Fig. C.4.b), aqueous suspensions formed a weak gel from 70 mg<sub>CNC</sub>/mL<sub>water</sub> and a strong gel from 100 mg<sub>CNC</sub>/mL<sub>water</sub>, which corresponds to the usually reported thresholds. MF behaved similarly, but the gel was slightly stronger at 70 mg<sub>CNC</sub>/mL<sub>solvent</sub>. DMSO and formamide suspensions, however, displayed strong gels from 70 mg<sub>CNC</sub>/mL<sub>solvent</sub> and weak ones from as low as 50 mg<sub>CNC</sub>/mL<sub>solvent</sub>. Both gels had similar strengths (orientation of the gel/air interface) at 50 mg<sub>CNC</sub>/mL<sub>solvent</sub>.

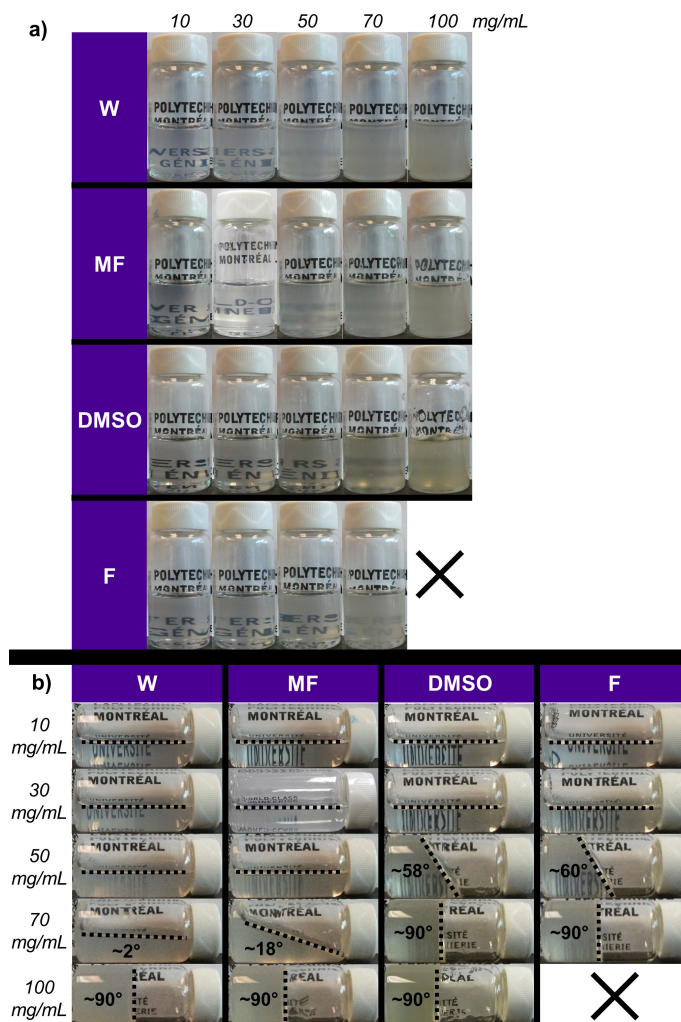


Figure C.4 Vial tests at  $\sim 25^\circ\text{C}$  for CNC suspensions in water (W), N-methylformamide (MF), dimethylsulfoxide (DMSO), and formamide (F) at concentrations ranging from 10 to  $100 \text{ mg}_{\text{CNC}}/\text{mL}_{\text{solvent}}$ . The test at  $100 \text{ mg}_{\text{CNC}}/\text{mL}_{\text{solvent}}$  could not be performed in formamide. Right after ultrasonication, the suspensions were fluid (a). After a 24 h period, the vials were inclined (b) to assess gel formation based on tabletop rheology [218]. The air/media interface is highlighted by a dotted line on the images, its angle with the horizontal is specified when it deviates from zero.

Bruckner et al. [122] reported that the gelation point was higher in formamide ( $> 9 \text{ wt\%}$ ) than in MF or water (both at  $\sim 8 \text{ wt\%}$ ). At first sight, these results contradict our own observations: we observed a lower gel point in formamide than in MF or water. We believe that the apparent contradiction arises from differences in the respective experimental protocols to prepare highly concentrated suspensions. In our work, the desired amount of CNCs was added to the target amount of solvents and a strong ultrasonication treatment was applied. Bruckner et al. [122] first prepared dilute suspensions (at  $\sim 1.5 \text{ wt\%}$ ) that were



then evaporated until reaching the targeted CNC concentration. The latter protocol enables for some EISA to happen before any DISA takes place. During evaporation the initially randomly oriented CNCs will self-order and optimize their interparticular distance through chiral nematic domain formation, while our protocol provides a direct measure of DISA at a given concentration by suppressing the competition from EISA.

After being stored for 5 months at  $\sim 25^\circ\text{C}$ , CNC suspensions in formamide and DMSO actually formed a strong gel from  $30\text{ mg}_{\text{CNC}}/\text{mL}_{\text{solvent}}$  (Fig. 6.3.a). Ultrasonication was unable to return them to their initial fluid state, which points towards a permanent change being made to the system beyond agglomeration. In DMSO, desulfation is likely to be the cause as reported by Sojoudiasli et al. [154]. By lowering the surface charge of CNC particles, desulfation indeed weakens electrostatic stabilization overtime, thus promoting DISA. At  $70^\circ\text{C}$ , significant desulfation and gel formation occurred within 4 to 6 h (no intermediate temperature between  $25^\circ\text{C}$  and  $70^\circ\text{C}$  was probed) [154]. In aqueous suspensions, sealed in an autoclave, Na-neutralized CNCs do not experience any desulfation, and its induced gelation, below  $110^\circ\text{C}$  [228]. In formamide, it could be direct desulfation of the CNC particles as in DMSO, or it could be hydrolysis of the formamide into ammonia and formic acid [306]. This reaction may even occur at  $25^\circ\text{C}$ , although at a slow rate, in presence of water (captured from the atmosphere for instance since formamide is hygroscopic). Formamide hydrolysis, if significant, would slowly lower the chemical affinity of CNCs for the solvent, a factor known to trigger DISA [160]. By generating formic acid, hydrolysis may also acidify the media, which has been reported to catalyze desulfation [228].

### C.3.2 SI to “4.1.2- Electrostatic-only stabilization”

Given the potential influence of thermal energy on the self-assembly mechanisms [160], we investigated the solvent-casting of electrostatically-stabilized suspensions at higher temperature ( $80^\circ\text{C}$  instead of  $60^\circ\text{C}$ ) and in an evaporating dish that offers a better heat transfer (aluminum instead of PTFE).

Increasing the thermal energy available to the system is expected to counter-balance gravity and favor deagglomeration, thus favoring EISA over DISA upon solvent-casting [160]. It matches with our observation for CNC suspensions in DMF, an electrostatically-stabilized system (Fig. 6.4). There, switching the material of the evaporating dish from PTFE to aluminum to improve the heat transfer resulted in a significant improvement in the continuity of the film recovered from the solvent casting (Fig. refArt2:Figure4 & C.5). In EG, this test also led to a greater continuity in the film (Fig. C.5). In PC, no improvement could be noticed and the casting yielded a powder. We described in the main text the balance of

interactions to be very favorable to sedimentation (DISA) in this solvent. Improving the heat transfer does not seem to be enough to shift it in favor of EISA. Increasing the heat transfer, by favoring evaporation and reducing the time span available for self-ordering, was not expected to improve the outcome and it did not.

In our work, we hence report temperature to have an overall positive effect on the outcome of solvent casting for electrostatically-stabilized suspensions by mitigating the influence of agglomeration and of sedimentation. It is worth noting that researchers working with aqueous CNC suspensions (a system benefiting from electrostatic and solvation-induced stabilization) have, however, reported temperature to have a negative effect on EISA: films casted at higher temperature notably have larger helicoidal pitches [152]. It was proposed that increasing the evaporation rate reduced the time available to self-ordering, thus favoring early gelation [152, 153]. It is thus likely that increasing the temperature is only an asset as far as agglomeration and sedimentation are concerned. By speeding up kinetic arrest, temperature may have a negative impact on EISA in systems whose stability relies on a combination of electrostatic and solvation-induced stabilization.

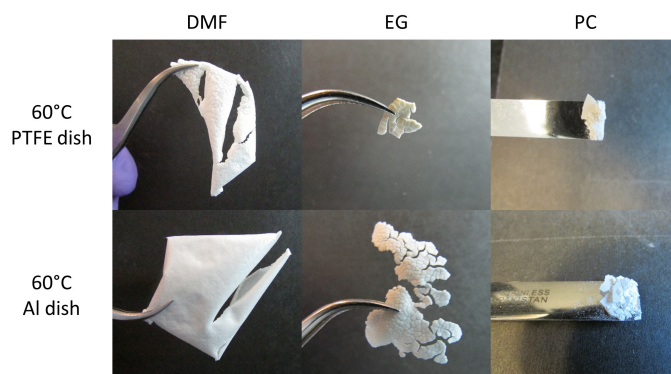


Figure C.5 Effect of the evaporating dish, PTFE or Al, on the continuity of the thin film casted from some electrostatically-stabilized suspensions (DMF, EG, PC). The greater continuity observed with Al dishes is attributed to the better heat transfer in this material.

### C.3.3 SI to “4.1.4- Casting of CNC suspensions in binary mixtures”

For films casted from CNC suspensions in binary mixtures, it is interesting to note that in configurations in which the good solvent has the highest boiling point (DMSO, MF, formamide), drying does not result in the formation of cracks but in a self-wrapping of the films (Fig. 6.5: 10 to 20 vol% for DMSO, 1 to 2.5 vol% for MF, and 1 to 5 vol% for formamide in DMF). Cracks form when the cohesion is lowered by the formation of voids [220]: the presence of CNC agglomerates potentially results in an unoptimized packing of the agglomerates

and solvent evaporation creates voids. In this configuration, crack formation seems to be the favored outcome to release the mechanical stress generated by the evaporation throughout the material. But when intercohesion is strong, the stress generated by evaporation is not enough to break CNC-CNC interactions and the gradient in composition between the bottom and the top layers of the film (presence or absence of agglomerates) seems to result in its wrapping rather than in its cracking. In circumstances where the good solvent has a higher boiling point than the poor solvent, evaporation is expected to improve the quality of the media overtime, and it looks like the agglomerates that form in the initial poorer media end up being more strongly bonded to one another.

Table C.1 Solvents and their properties. “Rkg” stands for solvents’ ranking in term of dielectric constants,  $\varepsilon$  (highest to lowest), and “Abbr.” for the abbreviations with which solvents are referred to throughout the work. Purities are reported as provided by the different commercial suppliers. Dielectric constants,  $\varepsilon$ , boiling points,  $T_{\text{bp}}$ , HSP values  $\{\delta_{\text{D},\text{s}}; \delta_{\text{P},\text{s}}; \delta_{\text{H},\text{s}}\}$ , densities,  $\rho_{\text{s}}$ , and viscosities,  $\eta_{\text{s}}$ , were extracted from the literature.  $R_{\text{a}}$  was calculated from  $\{\delta_{\text{D},\text{s}}; \delta_{\text{P},\text{s}}; \delta_{\text{H},\text{s}}\}$  using Eq. 6.2.

Rkg	Abbr.	Solvent set		Parameters		Solvent-casting		HSP values (25 °C)			Other properties (25 °C)	
		Solvent	Purity	$\varepsilon^a$ (20 °C)	$R_{\text{a}}$ (25 °C) MPa <sup>1/2</sup>	$T_{\text{bp}}^b$ °C	$t_{\text{evap}}^c$ d	$\delta_{\text{D},\text{s}}^b$ MPa <sup>1/2</sup>	$\delta_{\text{P},\text{s}}^b$ MPa <sup>1/2</sup>	$\delta_{\text{H},\text{s}}^b$ MPa <sup>1/2</sup>	$\rho_{\text{s}}^d$ g cm <sup>-3</sup>	$\eta_{\text{s}}^d$ mPa s
13	CCl <sub>3</sub>	chloroform	99.25 %	4.8	19.8	61	3	17.8	3.1	5.7	1.47	0.539
11	DCM	dichloromethane	99.90 %	8.9(25)	15.6	40	3	17.0	7.3	7.1	1.32	0.397
6	DMF	N,N-dimethylformamide	99.90 %	38.3	7.9	152	3	17.4	13.7	11.3	0.945	0.801
5	DMSO	dimethylsulfoxide	99.90 %	47.2	6.5	191	~6	18.4	16.4	10.2	1.10	1.99
15	Dx	1,4-dioxane	> 99.0 %	2.2	19.7	101	3	17.5	1.8	9.0	1.03	1.20
12	EA	ethyl acetate	99.90 %	6.1	17.7	77	3	15.8	5.3	7.2	0.895	0.425
7	EG	ethylene glycol	≥ 99.0 %	37.0	14.4	245	~9	17.0	11.0	26.0	1.11	17.2
2	F	formamide	99.0 %	111	7.1	220	~13	17.2	26.2	19.0	1.13	3.29
16	Hep	heptane	99.0 %	1.9	26.1	98	3	15.3	0.0	0.0	0.679	0.393
8	MeOH	methanol	99.90 %	33.0	17.1	65	3	14.7	12.3	22.3	0.787	0.547
10	MEK	methyl ethyl ketone	99.90 %	18.6	15.9	80	3	16.0	9.0	5.1	0.800	0.386
1	MF	N-methylformamide	99.0 %	191 [307]	2.2	200	~6	17.4	18.8	15.9	0.999 [308]	1.75 [308]
9	PrOH	1-propanol	> 99.7 %	20.8	14.4	97	3	16.0	6.8	17.4	0.800	1.98
4	PC	propylene carbonate	99.5 %	66.1	12.1	242	~14	20.0	18.0	4.1	1.20	2.49
14	Tol	toluene	99.90 %	2.4(23)	23.2	111	3	18.0	1.4	2.0	0.862	0.550
3	W	water	<sup>e</sup>	80.1	6.1 <sup>f</sup>	100	3	15.1 <sup>f</sup>	20.4 <sup>f</sup>	16.5 <sup>f</sup>	0.997	0.891

<sup>a</sup> When different from 20 °C, the temperature is provided between parenthesis in °C. Unless another reference is provided, values are extracted from Lide [303].

<sup>b</sup> Values extrated from the HSPiP database [131].

<sup>c</sup> Samples were left 72 h (= 3 d) in the oven, depending on which occurred last. Values displayed here refer to the solvent casting experiments performed in an oven pre-heated at 60 °C.

<sup>d</sup> Unless a reference is provided, values are extracted from the Appendices of our previous work [106].

<sup>e</sup> Distilled water.

<sup>f</sup> Water has three sets of HSP, those provided are for “1 % soluble in” — the most appropriate to describe diluted aqueous suspensions [127].

Table C.2 Binary mixtures and their properties. Each line corresponds to a mixture made of solvents A and B of respective volume fractions  $\Phi_A$  (vol%) and  $\Phi_B$  (vol%). The purities and the dielectric constants of the pure solvents are reported in Table C.1. HSP values  $\{\delta_{D,mix}; \delta_{P,mix}; \delta_{H,mix}\}$  were calculated with Eq. 6.3 based on those of the pure solvents (Table C.1)  $R_a$  was calculated from  $\{\delta_{D,mix}; \delta_{P,mix}; \delta_{H,mix}\}$  using Eq. 6.2. To the best of our knowledge, DMF is perfectly miscible with DMSO, W, F, and MF, and does not form any azeotrope upon mixing with these solvents.





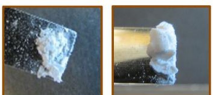
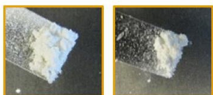
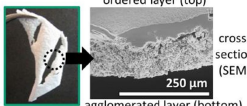
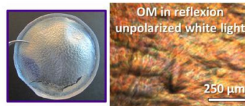
Binary mixtures				Parameters		Solvent-casting	HSP values (25 °C)		
Solvent A	$\Phi_A$	$\Phi_B$	Solvent B	$\varepsilon^a$ (20 °C)	$R_a$ (25 °C)	$t_{evap}^b$	$\delta_{D,mix}^c$	$\delta_{P,mix}^c$	$\delta_{H,mix}^c$
	vol%	vol%			MPa <sup>1/2</sup>	d	MPa <sup>1/2</sup>	MPa <sup>1/2</sup>	MPa <sup>1/2</sup>
DMSO	1.0	99.0	DMF	~38	7.9	3	17.4	13.7	11.3
	2.5	97.5		~39	7.9	3	17.4	13.8	11.3
	5.0	95.0		~39	7.8	3	17.5	13.8	11.2
	10.0	90.0		~39	7.7	3	17.5	14.0	11.2
	20.0	80.0		~40	7.5	3	17.6	14.2	11.1
W	0.5	99.5	DMF	~39	7.9	3	17.4	13.7	11.3
	1.0	99.0		~39	7.9	3	17.4	13.8	11.4
	2.5	97.5		~39	7.7	3	17.3	13.9	11.4
	5.0	95.0		~40	7.6	3	17.3	14.0	11.6
	10.0	90.0		~42	7.2	3	17.2	14.4	11.8
F	0.5	99.5	DMF	~39	7.9	3	17.4	13.8	11.3
	1.0	99.0		~39	7.8	3	17.4	13.8	11.4
	2.5	97.5		~40	7.6	3	17.4	14.0	11.5
	5.0	95.0		~42	7.2	3	17.4	14.3	11.7
	10.0	90.0		~46	6.5	~4	17.4	15.0	12.1
MF	0.5	99.5	DMF	~53	5.1	~6	17.4	16.2	12.8
	1.0	99.0		~39	7.9	3	17.4	13.7	11.3
	2.5	97.5		~40	7.9	3	17.4	13.8	11.3
	5.0	95.0		~42	7.8	3	17.4	13.8	11.4
	10.0	90.0		~46	7.6	3	17.4	14.0	11.5
	0.5	99.5	DMF	~54	7.3	3	17.4	14.2	11.8
	1.0	99.0		~54	7.3	3	17.4	14.2	11.8
	2.5	97.5		~54	7.3	3	17.4	14.2	11.8
	5.0	95.0		~54	7.3	3	17.4	14.2	11.8
	10.0	90.0		~54	7.3	3	17.4	14.2	11.8
	0.5	99.5	DMF	~69	6.6	3	17.4	14.7	12.2
	1.0	99.0		~69	6.6	3	17.4	14.7	12.2
	2.5	97.5		~69	6.6	3	17.4	14.7	12.2
	5.0	95.0		~69	6.6	3	17.4	14.7	12.2
	10.0	90.0		~69	6.6	3	17.4	14.7	12.2

<sup>a</sup> Estimated based on the dielectric constants of the mixture's constituents, weighted by their respective volume fraction.

<sup>b</sup> Samples were left 72 h (= 3 d) in the oven or until complete evaporation, depending on which occurred last. Values displayed here refer to the solvent casting experiments performed in an oven pre-heated at 60 °C.

<sup>c</sup> Calculated through Eq. 3.

Table C.3 Summary of colloidal CNC behavior in standing suspensions and upon solvent-casting as a function of their stabilization mechanisms. Illustrations are adapted from Figs. 6.1,6.2,6.3,6.4&C.3.

Stabilization	No stabilization	Solvation	Electrostatic	Solvation+Electrostatic
Analysis of CNC stabilization mechanisms: (illustrations adapted from Fig. 1)				
Specific interactions solvent/CNCs	-	significant solvent adsorption on CNC surfaces	significant counter-ion dissociation	significant solvent adsorption on CNCs & counter-ion dissociation
Forces acting to stabilize the CNCs	-	structural force	electrostatic repulsion (from $-OSO_3^-$ groups) & osmotic pressure (from $Na^+$ )	structural force, electrostatic repulsion ( $-OSO_3^-$ ) & osmotic pressure ( $Na^+$ )
Experimental criteria <sup>a</sup>	$\epsilon < 11$ and $R_a > 7.8 \text{ MPa}^{1/2}$ <sup>b</sup>	$\epsilon < 11$ and $R_a \leq 7.8 \text{ MPa}^{1/2}$ <sup>b</sup>	$\epsilon > 11$ and $R_a > 7.8 \text{ MPa}^{1/2}$ <sup>b</sup>	$\epsilon > 11$ and $R_a \leq 7.8 \text{ MPa}^{1/2}$ <sup>b</sup>
In a standing colloidal suspension: (illustrations adapted from Fig. SI.3)				
Colloidal CNC behavior	<b>CNC suspension in toluene (10 mg/mL, 25°C)</b>  CNCs fully sediment within seconds/minutes of their ultrasonication fully sediment over time (within seconds or minutes)	<b>CNC suspension in chloroform (10 mg/mL, 25°C)</b>  CNCs form agglomerates (cloudiness) that remain in suspension (no sedimentation) for months cloudy suspension, stable over time	<b>CNC suspension in propan-1-ol (10 mg/mL, 25°C)</b>  CNCs fully sediment within hours/days of their ultrasonication fully sediment over time (within hours or days)	<b>CNC suspension in water (10 mg/mL, 25°C)</b>  The suspension remains clear and stable for months (no obvious sign of agglomeration or sedimentation) clear suspension, stable over time <sup>c</sup>
Competing phenomena <sup>c</sup>	sedimentation agglomeration	agglomeration	sedimentation agglomeration	none below gelation point ( $C_{gel}$ ), <sup>c</sup> agglomeration above $C_{gel}$
Self-assembly mechanisms	DISA (nucleation of agglomerates)	DISA (nucleation of agglomerates)	DISA (nucleation of agglomerates)	none below $C_{gel}$ , <sup>c</sup> DISA (gelation) above $C_{gel}$
Upon solvent-casting of a colloidal suspension: (illustrations adapted from Figs. 2,3&4)				
Solvent-casting's outcome	<b>Casting of a CNC suspension in 1,4-dioxane (left)/toluene (right) (60°C, 72 h, PTFE mold)</b>  powder	<b>Casting of a CNC suspension in chloroform (left)/DCM (right) (60°C, 72 h, PTFE mold)</b>  powder	<b>Casting of a CNC suspension in DMF (60°C, 72 h, PTFE mold)</b>  powder (no EISA) or opaque bilayer film (EISA competes with DISA) <sup>d</sup>	<b>Casting of a CNC suspension in water (60°C, 72 h, PTFE mold)</b>  continuous & transparent film (glass-like or iridescent) <sup>e</sup>
Competing phenomena <sup>c</sup>	sedimentation, agglomeration, evaporation <sup>f</sup>	agglomeration evaporation <sup>f</sup>	sedimentation, agglomeration, evaporation <sup>g</sup> , self-ordering <sup>h</sup>	evaporation, self-ordering <sup>h</sup> , agglomeration above $C_{gel}$
Self-assembly mechanisms	DISA (nucleation of agglomerates)	DISA (nucleation of agglomerates)	DISA (nucleation of agglomerates) + potential EISA <sup>i</sup>	EISA (nematic domains form) below $C_{gel}$ , DISA (gelation) above $C_{gel}$

<sup>a</sup> The criterion on  $\epsilon$  is theoretical and empirical [119], while it is empirical for  $R_a$  [106].

<sup>b</sup> This criterion stands for CNC polar surfaces, adsorption may also happen on CNC non-polar surfaces as in chloroform and dichloromethane [106].

<sup>c</sup> Does not take into account the eventual chemical alteration of the system (such as desulfation, solvent hydrolysis, etc.). Note that even CNCs stabilized by a combination of solvation and electrostatic effects will eventually agglomerate over extended periods of time.

<sup>d</sup> Or any outcome in between depending on the degree to which EISA is competitive with respect to DISA (see Figs. 6.4&C.5).

<sup>e</sup> The film may form iridescent domains if gelation (kinetic arrest) occurs after the onset of self-ordering. Increasing the time span in between favors chiral nematic domain formation [153].

<sup>f</sup> Evaporation is slow in front of agglomeration and/or sedimentation.

<sup>g</sup> Evaporation may be kinetically competitive with agglomeration and sedimentation.

<sup>h</sup> Self-ordering refers here to the process of chiral nematic domains formation, whose rate appears to be controlled by  $\epsilon$  [122].

<sup>i</sup> EISA seems possible when evaporation is competitive or fast in front of DISA and that the rate of self-ordering is not limiting.

## APPENDIX D SUPPLEMENTARY INFORMATION TO ARTICLE 3: ORIENTING CELLULOSE NANOCRYSTAL FUNCTIONALITIES TUNES THE WETTABILITY OF AIR/SAMPLES INTERFACES

Charles Bruel, Salomé Queffeuilou, Pierre J. Carreau, Jason R. Tavares and Marie-Claude Heuzey. Orienting cellulose nanocrystal functionalities tunes the wettability of air/samples interfaces. Submitted to *Langmuir* on 2020/06/17, in peer-review.

This supplementary information (SI) includes a nomenclature of the abbreviations, symbols, and variables used in the main text. It also gathers: extended protocols; CNC structural characterization (purity, Zeta-potential, dimensions, crystallinity, and cross-sectional shape); the methodology that was used to minimize kinetic and roughness-induced contact angle hysteresis; considerations over the surface tension parameters of the fluid and over the influence of surface charges (ionic dissociation) on the mechanisms proposed in the main text; and the description of a typical advancing/receding contact angle (ARCA) experiment. Finally, Table D.5 summarizes ARCA results and their statistical analysis.

### D.1 Extended protocols

**Transmission electron microscopy:** A Jeol JEM-2100F field emission electronic microscope performed imaging (acceleration voltage of 200 kV) of nanocrystals deposited on copper-based TEM grids (CF200-Cu, Electron Microscopy Sciences) coated by 5-6 nm of pure carbon. The grids were dipped in an aqueous CNC suspension diluted at  $10 \mu\text{g}_{\text{CNC}}/\text{mL}$  and dried for 24 h under the hood. TEM images were analyzed manually using the software ImageJ [1]. Standard deviations are reported.

**Elemental analysis:** A Tabletop Hitachi TM3030+ scanning electron microscope performed quantitative elemental analysis on the oven-cast thin films through energy-dispersive X-ray spectroscopy (EDX). Acquisition was achieved for 60 s on three different locations with an electron beam generated from a 15 kV source. Standard deviations were below  $\sim 1\%$  and are not reported.

**Zeta-potential:** A Malvern Zetasizer Nano-ZS, operated with a DTS1070 cell, performed Zeta-potential measurements on dilute CNC suspensions ( $3 \text{ mg}_{\text{CNC}}/\text{mL}$ ). Zeta-potential was determined based on 3 successive measurements (10 runs of 15 s each) performed on 3 different samples (total of 9 measurements). The standard deviation is reported.

**X-ray diffraction:** A X’pert instrument (Philips) performed X-ray diffraction (XRD) on the CNC spray-dried powders and on the oven-cast thin films. It operated with  $\text{Cu K}\alpha$  radiations (wavelength of  $0.1542 \text{ nm}$ ) that were generated at  $50 \text{ kV}$  by a current of  $40 \text{ mA}$ . The  $2\theta$  angle was varied from  $5.01^\circ$  to  $49.99^\circ$  at a step of  $0.02^\circ$  per scan (scan time of  $1 \text{ s/step}$ ).

**Atomic force microscopy:** An ICON Microscope (Bruker Santa Barbara, CA) performed atomic force microscopy (AFM) on the spin-coated and oven-cast films. Analyses were carried at room temperature in air in Peak Force Tapping mode operated at a scan rate of  $1 \text{ Hz}$  with silicon nitride cantilevers (model: ScanAsyst-Air from Bruker). Acquisition was assisted by a scan Asyst parameter optimization routine. The cantilever resolves height resolution within  $0.2 \text{ nm}$ . Planar resolution is, however, limited by the geometry of its tip and falls in the range of  $\sim 10 \text{ nm}$ .

## D.2 CNC structural characterization

### D.2.1 Purity and surface charge

The purity of our CNC samples and their level of sulfatation was assessed by an elemental analysis performed on oven-cast films through energy-dispersive X-ray (EDX) analysis. CNCs have a S/C ratio of  $0.0061$ , which correspond to  $3.6$  sulfate half-ester groups per  $100$  anhydroglucose units according to the equation by Hamad and Hu [16]. These sulfate half-ester groups introduce negative charges at the surface of the nanocrystals that result in a Zeta potential of  $-45.5 \pm 3.8 \text{ mV}$ . The O/C ratio is of  $0.85$ , which, once corrected for the oxygen atoms that belong to the sulfate half-ester groups, yields a value of  $\sim 0.83$  for the unsulfated CNC backbone. This is because each sulfur is bonded to  $4$  oxygen atoms, three of which do not belong to cellulose backbone. It coincides with the theoretical O/C ratio of  $0.83$  for cellulose chains and is indicative of a high level of purity: the presence of impurities, especially lignin, is expected to decrease this ratio since cellulose is the oxygen-richest component in plant cell walls [190].



### D.2.2 Dimensions

TEM images displayed an obvious mix of individual CNC particles and agglomerates so that the differentiation may be hard to tell. Counting 250 CNCs bundles (without making any size discrimination) leads to an average length,  $L_{\text{CNC}}$ , of 150 nm and an average diameter,  $D_{\text{CNC}}$ , of 10.0 nm with respective standard deviations of 70 nm and 4.5 nm. In our former work, where TEM grids were prepared by depositing and drying a drop on the surface, a bundle's length of  $\sim 165$  nm and a width of  $\sim 13$  nm were reported for the same CNCs [145]. Here, the grids were immersed in the suspension and withdrawn, resulting in a smaller thickness of liquid being deposited on the surface. That the protocol influences the average size of CNC bundles has already been reported [309]. This influence arises from the reagglomeration that takes place upon preparation of the TEM grids and illustrates the need to perform a more in-depth analysis such as the one published by Elazzouzi-Hafraoui et al. [96]. Therefore, the distribution in terms of width $\times$ length was plotted to discriminate agglomerates from individual CNC particles (Fig. D.1). A peak appears in the range of  $L_{\text{CNC}} \approx 105\text{-}120$  nm and  $D_{\text{CNC}} \approx 7\text{-}8$  nm. The smallest particles are, however, about 4-5 nm in diameter, which is in the range of what has been reported for plant-based  $I_\beta$  elementary microfibrils [23, 46, 41].

### D.2.3 Cristallography

**CNC alignment in the films:** Fig. D.2.a plots the X-ray diffraction spectra for both spray-dried CNC powders and oven-cast films. Spin-coated films were too thin to be analyzed properly. 5 main peaks, labeled accordingly to their Miller indices (hkl) [21], may be observed in cellulose  $I_\beta$  nanocrystal samples. They correspond to the lattice planes (1 $\bar{1}$ 0), (110), (012), (200), and (004); their respective peak maxima are expected at angles,  $2\theta$ , of 15.1, 16.8, 21.0, 22.8, and 34.6°, respectively [96, 97], where  $\theta$  is the Bragg angle. These 5 peaks appear in the spectrum of the powder. Note that the peak for the lattice plane (012) appears as a shoulder to the (200) peak. It is however interesting to note that peaks (012) and (004) disappear in the film spectrum. This is attributed to the alignment of the CNCs within the films: while CNCs are randomly oriented within spray-dried agglomerates, they align upon solvent casting in water. As a consequence, they lie in the film with their long axis parallel to the air/film interfaces. This is coherent with the AFM images presented in Fig. 7.1 of the main text. Elazzouzi-Hafraoui et al. [96] reported similar results by analyzing CNC films from their top side or from their cross-section: the peaks (012) and (004), visible from the cross sectional observation, disappeared in the analysis performed from the top side. Fig. D.2.b plots the cross-section of cellulose  $I_\beta$  crystal cell and displays its lattice planes (schemes in background represent individual cellulose chains [106]).

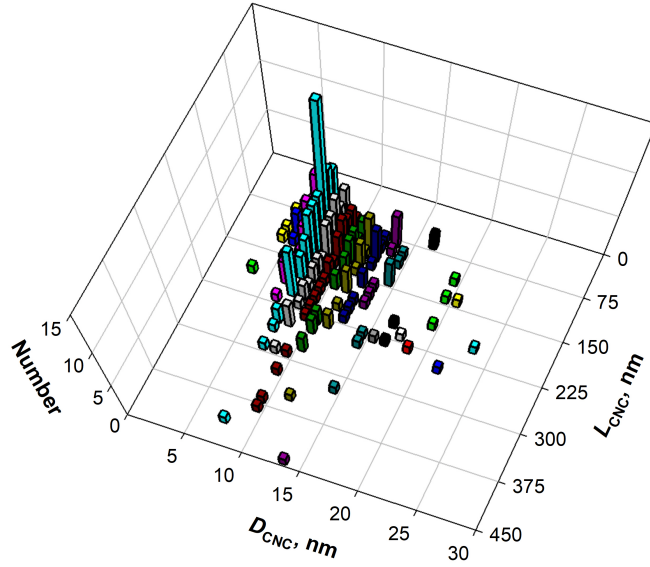


Figure D.1 Length ( $L_{\text{CNC}}$ ) times diameter ( $D_{\text{CNC}}$ ) distribution of CNC bundles on TEM images based on an analysis with ImageJ [1]. Each bar represents an interval of 15 nm for the length and 1 nm for the diameter. The height of a bar is proportional to the number of counts (out of 250) for the corresponding  $L_{\text{CNC}} \times D_{\text{CNC}}$  interval. The distribution is centered around a peak corresponding to  $D_{\text{CNC}} \approx 7-8$  nm and  $L_{\text{CNC}} \approx 105-120$  nm, which are assumed to correspond to the dimensions of an individual nanocrystal.

**Crystallinity index:** Using Segal's equation (Eq. D.1) [191, 310], we estimated the crystallinity index,  $CI$ , of our sample to be of  $\sim 81$  % in the powder and of  $\sim 87$  % in the films. Segal's formula is an empiric equation that relies on the determination of the maximum intensity of the peak (200),  $I_{(200)}$ , and of the maximum intensity of the amorphous peak,  $I_{\text{AM}}$ . The latter is measured as the minimum observed between (110) and (200) peaks.

$$CI = 100 * \frac{I_{(200)} - I_{\text{AM}}}{I_{(200)}} \quad (\text{D.1})$$

This slight increase in  $CI$  between the powder and the film may be attributed to the disappearance of the peak (012), that creates a shoulder in the (200) peak of the powder. This probably helps in determining  $I_{\text{AM}}$  by clearing the gap between the (110) and (200) peaks. A real increase in crystallinity cannot, however, be totally ruled out: in their model for the cross section of  $I_\beta$  nanocrystals, Ding and Himmel [41] proposed that surface chains, being influenced by their environment, are only para-crystalline. It is thus possible that solvent casting favors the overall crystallinity of the sample by providing an optimized vis-à-vis to surface chains, thus limiting their motility. Indeed, solvent casting enables a strong ordering

between CNC particles through an evaporation-induced self-assembly mechanism [173].

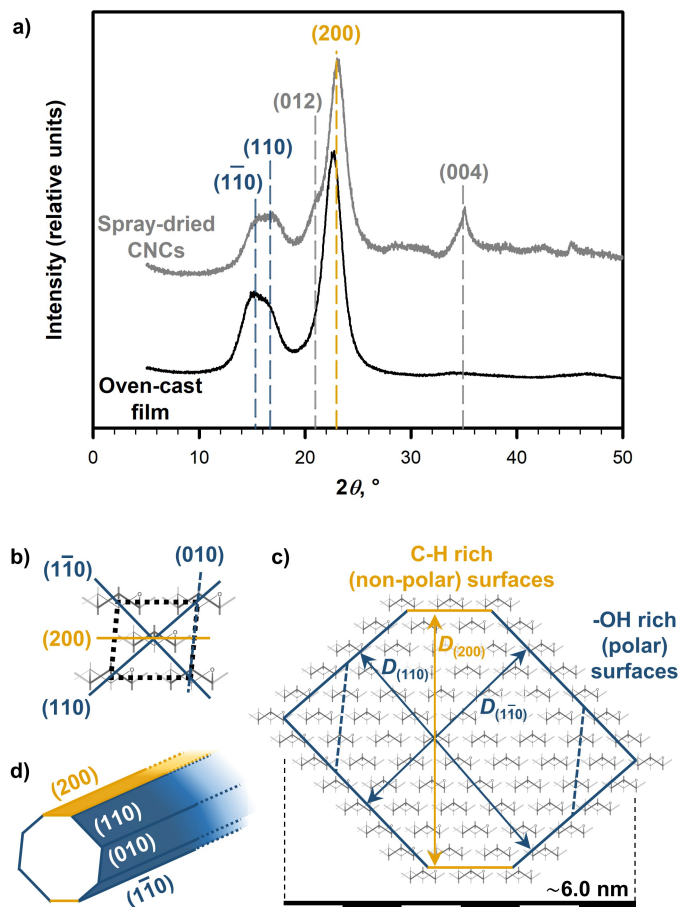


Figure D.2 XRD spectra of spray-dried CNCs (top grey line) and oven-cast films (bottom black line) **(a)**. The spectrum is typical of cellulose  $I_\beta$  nanocrystals. 5 peaks corresponding to the lattice planes (110),  $(1\bar{1}0)$ , (012), (200), and (004) are visible on the spectrum of the spray-dried sample which denotes a random orientation of the nanoparticles within the powder. The spectrum of the film, however, only shows the 3 peaks of the nanocrystal's cross-section: (110),  $(1\bar{1}0)$  and (200), which points towards an alignment of the nanocrystals within the film. The corresponding cross-section of the crystalline cell unit is plotted in **(b)**: hydroxyl groups rich lattice planes are plotted in blue, C-H bond rich ones are in yellow. Molecule schemes, in background, each representing the cross-section of a cellulose chain viewed from its long-axis. In **(c)**, the nanocrystal cross-sectional shape is triangulated from the XDR-determined estimates of  $D_{(110)}$ ,  $D_{(1\bar{1}0)}$ , and  $D_{(200)}$ . The presence of (010) surfaces (dashed blue lines), often hypothesized for CNCs [161], cannot be proven by XRD. However, this bears little consequences on the overall chemistry of the nanocrystal. The octagonal cross-sectional shape considered in this work is displayed in **(d)**.

**Cross-sectional shape** Through a deconvolution of the peaks, XRD data also enables for an estimation of the apparent crystallite size,  $D_{(hkl)}$ , using Scherrer's equation (Eq. D.2) [95, 96, 97].

$$D_{(hkl)} = K * \lambda_{\text{XRD}} / (\beta_{(hkl)/2} * \cos(\theta_{(hkl)})) \quad (\text{D.2})$$

Its parameters are the angular width of the (hkl) peak mid-height,  $\beta_{(hkl)/2}$ , the Bragg angle of its maximum,  $\theta_{(hkl)}$ , and the wavelength of the XRD beam,  $\lambda_{\text{XRD}}$  (=0.1542 nm in our case). Note that  $\beta_{(hkl)/2}$  needs to be expressed in radian.  $K$  is a dimensionless shape factor, whose typical value is between 0.9 and 1.  $K=0.9$  was considered as a measurement of  $D_{(hkl)}$  lower bound. Three values, each corresponding to a lattice plane, may hence be calculated:  $D_{(1\bar{1}0)}$ ,  $D_{(110)}$ , and  $D_{(200)}$ . No large deviations could be observed between the values derived from the powder spectrum and those derived from the film: their average was thus considered.  $D_{(110)}$ ,  $D_{(1\bar{1}0)}$ , and  $D_{(200)}$  were hence estimated at 4.5, 3.8, and 4.4 nm, respectively. Table D.2 summarizes all the parameters relevant to the peak deconvolution and Fig. D.2.c shows the triangulation of a nanocrystal cross section from  $D_{(hkl)}$  values.

Knowing the parameters of a cellulose  $I_\beta$  cell unit ( $a=0.778$  nm,  $b=0.820$  nm,  $c=1.038$  nm,  $\gamma=96.5^\circ$ ) [21], it is possible to calculate the  $d$ -spacings,  $d_{(hkl)}$ , between lattice planes:  $d_{(1\bar{1}0)}$  (0.61 nm),  $d_{(110)}$  (0.53 nm), and  $d_{(200)}$  (0.39 nm) [23]. From there, the number of cellulose chains,  $N_{(hkl)}$  along each crystallographic plane may be calculated from the ratio between  $D_{(hkl)}$  and  $d_{(hkl)}$  (Eq. D.3).  $N_{(hkl)}$  values are not integers, probably due to a combination of sample polydispersity and method uncertainty. Indeed, cross-sectional shape determination is a multi-step process whose uncertainty increases at each stage: XRD data acquisition, peak deconvolution, shape factor  $K$ . Cellulose chains are drawn in background of Fig. D.2.c.

$$N_{(hkl)} = \frac{D_{(hkl)}}{d_{(hkl)}} \quad (\text{D.3})$$

Hence, the cross-sectional shape that can be derived from XRD is hexagonal and predict the existence of (200) surface for CNCs (Fig. D.2.c). In terms of surface area, and despite the uncertainty of the method, a large majority of polar (110) and (110) surfaces is expected. This is coherent with CNCs being reported as displaying a primarily hydrophilic behavior [106]. The presence of small (200) surfaces however comfort expectations that CNCs, as amphiphilic particles, should be able to display some preferential orientations at the air/water interface. It is also worth noting that the projected diameter of the nanocrystal found by XRD is, independantly of the shape factor ( $K=0.9$  or 1) smaller than that determined through TEM for individual nanocrystals ( $\sim 7\text{-}8$  nm). Previous works also reported such a difference [98, 96].

Literature often considers the presence of (010) surfaces (dashed blue lines on Fig. D.2.b&c), which provide an octagonal shape to the nanocrystals [161]. Their presence cannot be proven through XRD due to the lack of a (010) peak that would allow an estimation of  $D_{(010)}$ . However, this bears little consequences on the expected behavior of CNC particles: (010) lattice planes, when exposed, come to the detriment of (110)&(1 $\bar{1}$ 0) surfaces with which they share the same hydroxyl rich chemistry. The crucial part is that, whatever the shape hypothesis (hexagonal or octagonal), CNCs keep displaying a majority of hydroxyl groups rich surfaces that are combined with a minority of C-H bonds rich ones. This work considered octagonally-shaped nanocrystals (plotted in Fig. D.2.d) in the main text to abide by the convention found in most references on the interfacial behavior of cellulose nanocrystals in Pickering emulsions [161].

### D.3 Model applicability

The following sections summarize the precautions that were taken in order to make non-surface tension related phenomena negligible and to minimize kinetic and surface roughness-induced hysteresis. This ensures that experimental data can be fitted with the model presented in Eq. 7.7 of the main text. The influence of liquid surface tension parameters on model predictions and of ionic dissociation on the energies calculated in the main text (Fig. 7.4) are also discussed.

#### D.3.1 Capillary and Bond numbers

The ratio between the hydrodynamic forces (viscosity of the liquid,  $\eta^l$ , times its rate of progression over the surface,  $v^l$ ) and the surface tension forces of the liquid,  $\gamma^l$ , is defined as the capillary number,  $N_{Ca}$  (Eq. D.4). In our case, the upper bound of  $v^l$ , which is controlled by the rate at which the liquid is injected/withdrawn, was measured at  $\sim 0.05 \text{ mm s}^{-1}$ . It corresponds to a  $N_{Ca}$  of  $\sim 2 \times 10^{-5}$  for EG and  $\sim 3 \times 10^{-6}$  for DIM, a range at which hydrodynamic forces can be neglected. According to Strobel and Lyons [240],  $N_{Ca} < 10^{-5}$  generally ensures that the CA measured at the moving three-phase boundary is equal to that measured just after it stops, i.e. that it corresponds to a thermodynamic state. Overall, this condition was verified during our experiments.

$$N_{Ca} = \frac{\eta^l v^l}{\gamma^l} \quad (\text{D.4})$$

The ratio between the gravitational forces (liquid density,  $\rho^l$ , times gravitational acceleration,  $g$ , times the square of a characteristic length,  $D^{\text{drop}}$ ) and the surface tension forces,  $\gamma^l$ , is defined as the Bond number,  $N_{\text{Bo}}$  (Eq. D.5). The upper bound of  $D^{\text{drop}}$  was measured below 5 mm in all circumstances. It means that  $N_{\text{Bo}}$  remained below  $\sim 6 \times 10^{-3}$  for EG and  $\sim 2 \times 10^{-2}$  for DIM.

$$N_{\text{Bo}} = \frac{\rho^l g (D^{\text{drop}})^2}{\gamma^l} \quad (\text{D.5})$$

$N_{\text{Ca}}$  and  $N_{\text{Bo}}$  values prove that surface tension largely dominates (by 2 to 3 orders of magnitude) the force balance in our systems.

### D.3.2 Minimization of kinetic hysteresis

Selecting an appropriate probe liquid is the main step that may be taken in order to minimize kinetic hysteresis [311, 312]. Considering our aim, at least two solvents must be selected: one predominantly polar and the other non-polar. Their surface tension,  $\gamma^l$ , must be in the same range or greater than that of the solid in order to obtain non-zero contact angles. Van Oss *et al.* [244] proposed that targeting a liquid surface tension above  $\sim 44 \text{ mN m}^{-1}$  was a safe threshold to carry the analysis of polar surfaces. Water ( $\gamma^l = 72.8 \text{ mN m}^{-1}$ ), glycerol ( $64 \text{ mN m}^{-1}$ ), formamide ( $58 \text{ mN m}^{-1}$ ), ethylene glycol (EG,  $48 \text{ mN m}^{-1}$ ), and dimethylsulfoxide (DMSO,  $43.5 \text{ mN m}^{-1}$ ), are the most common polar liquids. The threshold is hard to clear for non-polar liquids and in practice diiodomethane (DIM,  $50.8 \text{ mN m}^{-1}$ ) or  $\alpha$ -bromonaphthalene ( $44.4 \text{ mN m}^{-1}$ ) are selected [244]. They are two of the few non-polar liquids suitable for the analysis of polar surfaces.

In terms of kinetic hysteresis, the liquid must have a high boiling point (a criteria met by all the aforementioned solvents) to minimize evaporation and a low chemical affinity for the surface. Based on our previous manuscript on the chemical affinity of CNCs for solvents [106], water, formamide, and DMSO are unsuitable: their chemical affinity for CNCs is too strong. This causes a near instantaneous swelling of the film that was confirmed by performing dewetting tests in which these liquids failed to recede properly. The swelling was significant enough to be detected by the camera of the optical goniometer. It only left glycerol and EG as potential candidates. However, the high viscosity of glycerol (nearly two decades larger than that of EG) makes it hard to use for a dynamic CA experiment: it significantly increases the duration of the test, thus increasing the likelihood of kinetic phenomena (such as swelling) taking place. Previous investigations indeed suggested that any polar solvent may, up to a certain point, swell CNC thin films [140]. Keeping the overall

duration of each test within a few minutes is thus a top-priority and EG was selected as our polar probe liquid. Despite these precautions to select the polar liquid that causes the fewer swelling to the film, dewetting tests carried with EG remained difficult to analyze (see section “Wettability results and uncertainties” in SI). Regarding the non-polar probe solvent, DIM was selected for its higher surface tension and its low chemical affinity for CNCs.

### D.3.3 Thermodynamic hysteresis

Thermodynamic hysteresis arises from a combination of chemical and topographical heterogeneities at the surface of the sample [241, 242]. Since measuring thermodynamic hysteresis caused by chemical heterogeneities is precisely the focus of this work, surface roughness needs to be controlled. Roughness influences contact angle measurements in at least 3 ways in drop-based methods [241]. Macroscale roughness (defined as being visible with the instrument’s camera) favors instrumental error by creating an uncertainty on the sample baseline. At smaller scale, it turns the theoretical Young contact angle into an apparent (“Wenzel”) contact angle. Finally, it favors the transition from an homogeneous (liquid in contact with the surface) to an heterogenous wetting regime, in which the liquid is only partially in contact with the sample due to some air bubbles remaining trapped in surface cavities [241]. Estimating, and eventually minimizing, surface roughness is thus critical in making sure that what is measured is the real (by opposition to “apparent”) contact angle of the drop in direct contact with the surface (homogeneous regime). Only in these circumstances may the results be interpreted in terms of surface tension of the substrate.

Macroscale roughness is expected to be nearly null for CNC films, which can be confirmed from their cross-sectional image observed with the optical goniometer: it eliminates any instrumental uncertainty regarding the detection of the baseline. Mesoscale roughness was measured according to two metrics:  $r_{\text{surf}}$ , which is the ratio between the surface area of the film and its projected surface area (see Eq. 7.5 of the main text); and  $R_q$ , which is defined as the standard deviation in term of sample height. Both were calculated based on AFM measurements operating in tapping mode over a  $5 \times 5 \mu\text{m}^2$  area:  $r_{\text{surf}}$  and  $R_q$  were respectively smaller than 1.02 and 15 nm in all our samples. Microscale roughness was assessed by measuring the standard deviation in term of sample’s height,  $R_q$ , over flattened micrographs: the surface is corrected by a baseline (second order polynomial) that accounts for the mesoscale roughness ( $r_{\text{surf}}$  is not reported for these flattened surfaces).  $R_q$  ranged from 2.0 to 8.5 nm for all our sample, independently of the surface area analyzed, which is in the range of a single nanocrystal diameter,  $D_{\text{CNC}}$  ( $\sim 7\text{-}8\text{ nm}$ ).

This level of roughness remains large with regards to the size of a liquid molecule. However, being in the range of  $D_{\text{CNC}}$ , it is as flat as may be hoped for a surface made of self-assembled nanoparticles and we did not try to reduce it further. Indeed, while there is no consensus on the level of flatness that a sample must meet for its thermodynamic hysteresis to become neglectable [313, 240], it is commonly accepted that a roughness below  $\sim 0.05\text{-}0.1\text{ }\mu\text{m}$  is unlikely to yield a significant hysteresis [311]. These results also highlight the lack of any cavities susceptible to trap air bubbles on the films. It is worth noting that the tip of the cantilever as a geometry roughly  $10\text{ nm}$  wide. It means that any feature whose width would be smaller than that, such as potential interstices between the self-assembled nanocrystals, cannot be detected by AFM.

### D.3.4 Surface tension coefficients

#### Probe liquids coefficients

One of the tedious aspect of the Owens-Wendt-Rabel-Kaelble (OWRK) model is the accurate partition of the surface tension between a dispersive and a polar component (Eq. 7.2 of the main text). Indeed, while the total surface tension is easy to determine and consistent across the literature, it splits differently as a function of the source. For instance, diiodomethane ( $\gamma^{\text{l}}=50.8\text{ mN m}^{-1}$ ) is often considered as a purely dispersive solvent ( $\gamma_{\text{D}}^{\text{l}} \approx \gamma^{\text{l}}$ , and  $\gamma_{\text{P}}^{\text{l}} \approx 0$ ) [244, 243]: this approximation simplifies solid surface tension calculations from CA measurements. However, and like other liquid dihalogenomethanes ( $\text{CH}_2\text{Cl}_2$ ,  $\text{CH}_2\text{Br}_2$ ), DIM has a small permanent dipole moment that results in a polar component for the surface tension. Hence this work considers the coefficients  $\gamma_{\text{D}}^{\text{l}}=48.5\text{ mN m}^{-1}$ , and  $\gamma_{\text{P}}^{\text{l}}=2.3\text{ mN m}^{-1}$  for DIM as per Kaelble [314].

Variations observed in the literature for ethylene glycol ( $\gamma^{\text{l}}=48.0\text{ mN m}^{-1}$ ) are more significant.  $\gamma_{\text{P}}^{\text{l}}$  vary from  $19\text{ mN m}^{-1}$  [315] to  $29.3\text{ mN m}^{-1}$  [316]. This work considers an in-between value of  $\gamma_{\text{P}}^{\text{l}}=25.4\text{ mN m}^{-1}$  (and  $\gamma_{\text{D}}^{\text{l}}=22.6\text{ mN m}^{-1}$ ) [237]. This hypothesis bears no real influence on the  $f^{\text{nps}}$  values determined for the spin-coated films through Eq. 7.7 of the main text. However, they shift the predictions by  $\sim 0.05\text{-}0.07$  for the oven-cast films. Considering EG as a lowly polar liquid  $\gamma_{\text{P}}^{\text{l}}=19\text{ mN m}^{-1}$  [315] slightly increases  $f^{\text{nps}}$  (0.49 instead of 0.42), while considering EG as a more polar liquid  $\gamma_{\text{P}}^{\text{l}}=29.3\text{ mN m}^{-1}$  slightly lowers it (0.37). Table D.3 summarizes the influence of EG surface tension coefficients on model predictions for the oven-cast films. Our conclusions are unaffected.

It is worth mentioning that using Eqs. 7.11&7.12 of the main text, it is possible to estimate the surface tension coefficients of the probe liquids based on their HSP [237]:



- DIM has HSP of  $\{22.0; 3.9; 5.5\}$  MPa<sup>1/2</sup>, which yields  $\gamma_D^l=48.5 \text{ mN m}^{-1}$  and  $\gamma_P^l=2.2 \text{ mN m}^{-1}$ .
- For EG ( $\{17.0; 11.0; 26.0\}$  MPa<sup>1/2</sup>), it is  $\gamma_D^l=26.5 \text{ mN m}^{-1}$  and  $\gamma_P^l=23.9 \text{ mN m}^{-1}$ .

These predictions are close to the surface tension coefficients we considered (Table D.3).

## CNC coefficients

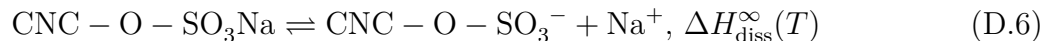
Table D.4 provides a comparison between the surface tension coefficients determined in this work for CNCs and those reported in the literature. Previous characterization either failed to report the split of  $\gamma$  in terms of dispersive and polar components, or to differentiate between CNC polar and non-polar surfaces. This is discussed in the main text (section “CNC’s surface tension parameters”).

### D.3.5 Influence of ionic dissociation

Energy calculations presented in Fig. 7.4 of the article do not consider the enthalpy of dissociation between the sulfate half-ester groups of CNCs and their Na<sup>+</sup> counter ions (Eq. D.6). However, upon CNC adsorption at the air/interface or upon CNC agglomeration, some stabilization brought by this counter-ion dissociation may be lost.

Based on elemental analysis, CNCs have a sulfur content of  $\sim 0.75$  wt% (the balance excludes the hydrogen, the true content is hence slightly smaller). Hence, CNCs have a sulfur molality of  $m_{S-CNC} \approx 0.23 \text{ mmols/g}_{CNC}$ , and a  $\sim 3$  wt% aqueous suspensions of CNCs has a molality of  $m_{S-w} \approx 7.0 \text{ } \mu\text{molS/mL}_w$ . The enthalpy of dissociation,  $\Delta H_{diss}(T, m)$ , of an ionic bond is a function of the temperature,  $T$ , and of the molality of the suspension,  $m$  [317]. A molality of  $\sim 7.0 \text{ } \mu\text{molS/mL}_w$  may, however, be considered as an infinite dilution:  $\Delta H_{diss}(T, m) \approx \Delta H^{\infty}_{diss}(T)$ .

To our knowledge, there is no report of  $\Delta H_{diss}(T)$  for the sulfate group of CNCs. However, the dissolution of Na<sub>2</sub>SO<sub>4</sub> in water is well reported: at infinite dilutions and 298 K,  $\Delta H_{diss} \approx -2 \text{ kJ mol}^{-1}$  [317]. This probably represents an overestimation for CNCs since Na<sub>2</sub>SO<sub>4</sub> has twice the number of cations per sulfate group. Hence, CNC’s counter-ion dissociation has an enthalpy of dissociation that probably lies below  $\sim -0.47 \text{ J/g}_{CNC}$  ( $=m_{S-CNC} \times \Delta H_{diss}(298 \text{ K})$ ) or about  $\sim -1.3 \text{ mJ m}^{-2}$  considering a CNC specific surface area of  $\sim 350 \text{ m}^2/\text{g}_{CNC}$ . This is more than one order of magnitude below the energy variations reported in Fig. 7.4 for surface adsorption ( $\sim -13$  to  $\sim -71 \text{ mJ m}^{-2}$ ).





Therefore, while the influence of counter-ion dissociation is not totally negligible, it remains secondary and should not alter the mechanisms proposed in the main text of the article. It is worth mentioning, however, that CNC surface charges have been reported to alter the interfacial stability of oil in water Pickering emulsions [98]. It is indeed likely that electrostatic repulsion influences the maximum density of CNC particles at the oil/water interface. This work characterizes dried films whose interface is entirely made of CNCs and the influence that surface charges may have over CNC orientation during the casting process itself remains to be investigated.

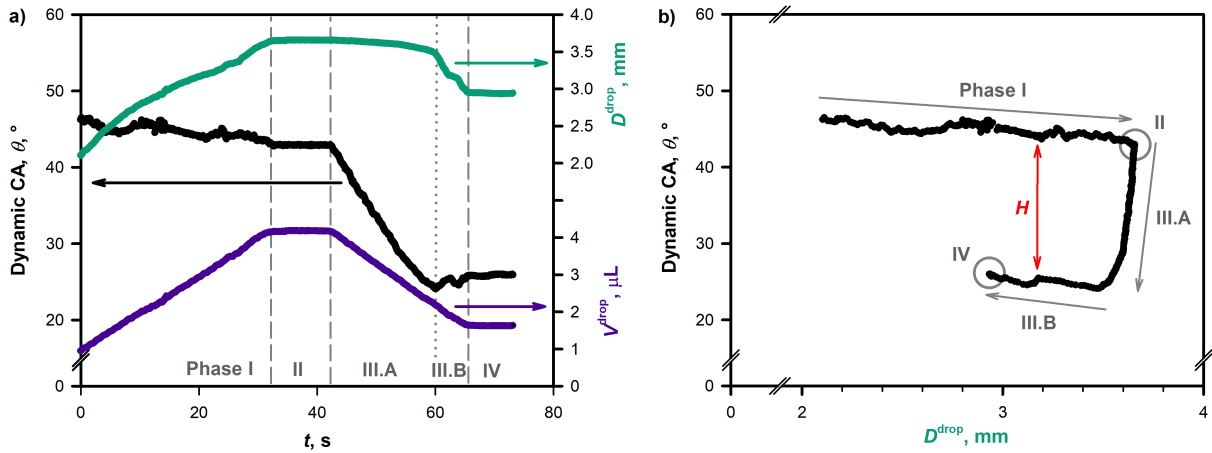


Figure D.3 Evolution of the drop parameters (volume,  $V^{\text{drop}}$ , contact diameter,  $D^{\text{drop}}$ , and dynamic contact angle,  $\theta$ ) over the course of an ARCA experiment conducted with diiodomethane on an oven-cast film (a). A typical experiment comprises 4 phases that correspond to liquid injection and withdrawal (phases I and III, respectively), each followed by a break of at least 5 s (Phases II and IV) in order to monitor the behavior of the drop at rest. In phase I,  $\theta$  remains roughly constant while  $D^{\text{drop}}$  grows. Phase III is subdivided between two phases: III.A during which  $D^{\text{drop}}$  remains constant while  $\theta$  decreases; and III.B, during which the reverse occurs. These phases are better evidenced (grey arrows) by plotting  $\theta$  as a function of  $D^{\text{drop}}$  (b). In this plot, all the data points corresponding to phases II and IV are superimposed (within the grey circles). This representation also highlights the magnitude of the CA hysteresis,  $H$  (red arrow).

## D.4 Wettability testing

### D.4.1 ARCA experiments and analyses

The video analysis of ARCA experiments returns three main parameters: the instantaneous contact angle,  $\theta$  ( $^\circ$ ), the apparent contact diameter of the drop,  $D^{\text{drop}}$  (mm), and its volume,  $V^{\text{drop}}$  ( $\mu\text{L}$ ). Their evolution during a typical test, performed with diodomethane, is presented on Figure D.3. The zero-time,  $t=0$ , is set arbitrarily, short after the liquid enters in contact with the sample.  $V^{\text{drop}}$  calculations are based on the hypothesis that the drop is axissymmetric (and that its volume may thus be estimated from its cross-section). Small deviations between the calculated  $V^{\text{drop}}$  value and the real amount of injected liquid may hence occur. Figure D.3 shows four distinct phases:

- Phase I – Liquid is injected at a constant rate:  $V^{\text{drop}}$  and  $D^{\text{drop}}$  increase. The liquid is advancing on the surface and  $\theta$  is thus an advancing contact angle,  $\theta_a$ . Small variations in  $\theta_a$  may be attributed to surface heterogeneities, while its slight overall declining trend reflects the effect of gravity (as the drop grows, so does the Bond number,  $N_{\text{Bo}}$ ).
- Phase II – Liquid injection is stopped for at least 5 s for the drop to stabilize:  $V^{\text{drop}}$  and  $D^{\text{drop}}$  reach a plateau value. A constant  $\theta$  during this phase indicates a proper minimization of kinetic phenomena and viscous forces. It also validates the hypothesis that the moving contact angle can be considered as being equal to the static contact angle.
- Phase III – Liquid is sucked at a constant rate:  $V^{\text{drop}}$  decreases. Initially  $D^{\text{drop}}$  remains constant and the loss of volume results in a decrease of the contact angle (phase III.A). This is until  $\theta$  reaches a new plateau value, from which  $D^{\text{drop}}$  starts to decrease. In this second part (phase III.B), the liquid is in receding conditions and a receding contact angle,  $\theta_r$ , is measured. The slight increasing trend in contact angle values over time can be attributed to the reducing effect of gravity.
- Phase IV – Liquid sucking is stopped for at least 5 s in order for the drop to stabilize. It has the same effects and objectives than those described for the phase II.

The distinction between phases III.A and III.B is analogous to that made between the constant contact area and the constant contact angle modes during the evaporation of a sessile droplet, respectively [318]. Plotting the contact angle as a function of the drop diameter (Fig. D.3.b) highlights the CA hysteresis between advancing and receding conditions:  $H$  is measured as the average distance (measured in  $^\circ$  for a given diameter) between the data points of the phases I and III.B (red arrow on Fig. D.3.b). The uncertainty of the drop-based methods is commonly estimated in the range of  $\pm 2^\circ$ , to which may be added the influence

of the drop-size effect. Induced by the weight of the drop, it is expected to be small at low  $N_{Bo}$ . Nonetheless, and as evidenced in Fig. D.3.b, the advancing CA values were found to decrease by  $\sim 3-4^\circ$  between the moment where the droplet was small ( $D^{drop} \approx 2 \text{ mm}$ ) and that where it became larger ( $D^{drop} \approx 3.5 \text{ mm}$ ). It is especially noticeable for DIM that has a high density. To enable for a comparison between the samples, experimental  $\theta_a$  and  $\theta_r$  values are hence reported as the average  $\theta$  during phases I and III.B, respectively, for  $D^{drop} > 3 \text{ mm}$  ( $\sim 6$  times the diameter of the needle).

#### D.4.2 Wettability results and uncertainties

Table D.5 summarizes the results plotted in Figs. 7.2.a&c and in Fig. 7.3.a of the main text. To account for the local nature of drop-based measurements (analyses of few  $\text{mm}^2$  only), ARCA experiments were performed on at least three locations of at least three different films (minimum of 9 tests per condition). Uncertainties reported in the text and error bars plotted on the graphs are standard deviations,  $\sigma_{SD}$ . Additionally, 95 % confidence intervals,  $\sigma_{95\%}$  [319], are also provided in Table D.5.

Receding measurements for EG were harder to acquire: in the the case of the spin-coated films, there was no receding at all; on the oven-cast films, most of the video footages were unexploitable and only three could be analyzed with satisfying precision. Since a film by film breakdown is impossible in these conditions, only an average CA value is reported for the receding of EG on oven-cast films and the statistical analysis was performed on 3 measurements only (instead of 9).

Table D.1 Nomenclature. As a general rule for variables, while superscripts point to the substrate characterized by the variable, subscripts refers to variable specifications. Elements that appear in SI but not in the main text (such as crystallographic variables) are not listed.

<b>List of abbreviations and acronyms</b>	
AFM	Atomic force microscopy
ARCA	Advancing/receding contact angle
CA	Contact angle
CNC	Cellulose nanocrystal
DIM	Diiodomethane
EDX	energy-dispersive X-ray spectroscopy
EG	Ethylene glycol
OC	Oven-cast
SC	Spin-coated
TEM	Transmission electron microscopy
XRD	X-ray diffraction
<b>List of variables</b>	
$\delta$	Hansen solubility parameter ( $\text{MPa}^{1/2}$ )
$\gamma$	Surface tension ( $\text{mN m}^{-1}$ )
$\theta$	Contact angle ( $^\circ$ )
$\rho$	Density ( $\text{g cm}^{-3}$ )
$\eta$	Viscosity ( $\text{Pa s}$ )
$\Delta E$	Surface energy variations ( $\text{mJ m}^{-2}$ )
$D$	Diameter (m)
$f$	Surface fraction ( $0 \leq f \leq 1$ , dimensionless)
$H$	Contact angle hysteresis ( $=\theta_a - \theta_r$ , $^\circ$ )
$v$	Rate of progression over a surface ( $\text{m s}^{-1}$ )
<b>List of variables' superscripts</b>	
drop	Drop, applies to $D^{\text{drop}}$
l	liquid, applies to $\gamma^l$ , $\rho^l$ , $\eta^l$ , $v^l$
nps	non-polar surfaces, applies to $\delta^{\text{nps}}$ , $\gamma^{\text{nps}}$ , $\theta^{\text{nps}}$ , $f^{\text{nps}}$
ps	polar surfaces, applies to $\delta^{\text{ps}}$ , $\gamma^{\text{ps}}$ , $\theta^{\text{ps}}$ , $f^{\text{ps}}$
s	solid, applies to $\gamma^s$
w	water, applies to $\gamma^w$
<b>List of variables' subscripts</b>	
a	Advancing, applies to $\theta_a$
comp	Composite, applies to $\theta_{\text{comp}}$
r	Receding, applies to $\theta_r$
D	Dispersive, applies to $\delta_D$ , $\gamma_D$
H	Hydrogen-bonding, applies to $\delta_H$
P	Polar, applies to $\delta_P$ , $\gamma_P$
T	Total, applies to $\delta_T$
W	Wenzel, applies to $\theta_W$
Y	Young, applies to $\theta_Y$
<b>Other symbols</b>	
$g$	Gravitational force constant ( $\sim 9.81 \text{ m s}^{-2}$ )
$N_{\text{CA}}$	Capillary number (dimensionless)
$N_{\text{Bo}}$	Bond number (dimensionless)
$r_{\text{surf}}$	Surface roughness coefficient (dimensionless)
$R_q$	Standard deviation in terms of surface's height (m)

Table D.2 Parameters of the crystallographic analysis.  $\lambda_{\text{XRD}}=0.1542\text{ nm}$  and  $K=0.9$  were considered to calculate  $D_{(\text{hkl})}$  using Scherrer's equation (Eq. D.2).

			Lattice planes (hkl)		
			(1 $\bar{1}$ 0)	(110)	200)
<b>Cellulose I<math>_{\beta}</math> crystal unit (from literature)</b>					
$2\theta_{(\text{hkl})}$	[96, 97]	$^{\circ}$	15.1	16.8	22.8
$d_{(\text{hkl})}$	[23]	nm	0.61	0.53	0.39
<b>Spray-dried CNC powder (XRD analysis)</b>					
$2\theta_{(\text{hkl})}$	$a$	$^{\circ}$	15.4	17.2	23.0
$\beta_{(\text{hkl})}/2$	$a$	rad	0.0389	0.0297	0.0321
$D_{(\text{hkl})}$	$b$	nm	3.60	4.73	4.41
<b>Oven-cast film (XRD analysis)</b>					
$2\theta_{(\text{hkl})}$	$a$	$^{\circ}$	14.9	16.6	22.8
$\beta_{(\text{hkl})}/2$	$a$	rad	0.0348	0.0328	0.0325
$D_{(\text{hkl})}$	$b$	nm	4.02	4.28	4.36
<b>Averaged values<sup>c</sup></b>					
$D_{(\text{hkl})}$	$d$	nm	3.81	4.50	4.39
$N_{(\text{hkl})}$	$e$	-	6.2	8.5	11.2

<sup>a</sup> Measured from Fig. D.2.a. <sup>b</sup> Calculated from Eq. D.2. <sup>c</sup> These average values were used to plot the cross-sectional shape displayed in Fig. D.2.c. <sup>d</sup> Average of  $D_{(\text{hkl})}$  measured from the spray-dried powder and the oven-cast thin films. <sup>e</sup> Calculated from Eq. D.3.

Table D.3 Influence of the surface tension coefficients of EG on  $f^{\text{nps}}$  predictions (Eq. 7.7 of the main text). Predictions are issued for advancing contact angle values of  $\theta_a=41.0\pm 4.3^{\circ}$  for EG and  $\theta_a=46.1\pm 1.2^{\circ}$  for DIM. Values in bold are those that are reported in the main text. "Ref." points to the references for the surface tension coefficients.

Liquid	Ref.	$\gamma$	$\gamma_D$	$\gamma_P$	$f^{\text{nps}}$
Diiodomethane	[314]	<b>50.8</b>	<b>48.5</b>	<b>2.3</b>	<b>0.44<math>\pm</math>0.06</b>
Ethylene glycol	[315]	48.0	29.0	19.0	0.49 $\pm$ 0.09
-	[237]	<b>48.0</b>	<b>22.6</b>	<b>25.4</b>	<b>0.42<math>\pm</math>0.08</b>
-	[316]	48.2	18.9	29.3	0.37 $\pm$ 0.07

Table D.4 Surface tension parameters for various cellulose  $I_\beta$  nanocrystals' samples and surfaces as a function of the method of determination. Computer simulation enables for a discrimination between the various lattice planes (see Fig. D.2.b). Our approach distinguishes polar surfaces (attributed to hydroxyl rich (110),  $(1\bar{1}0)$ , and (010) lattice planes) from non-polar ones (C-H bonds rich (200) lattice planes) [106]. Other methodologies amalgamate CNC surfaces and report a single apparent surface tension whose value varies with the substrate morphology.

	$\gamma$ $\text{mN m}^{-1}$	$\gamma_D$ $\text{mN m}^{-1}$	$\gamma_P$ $\text{mN m}^{-1}$	Ref.
<b>Computer simulations</b>				
(110) surfaces	155	-	-	[110]
$(1\bar{1}0)$ surfaces	155	-	-	[110]
(200) surfaces	92	-	-	[110]
<b>Inverse gas chromatography</b>				
Powder <sup>a</sup>	-	45.6-68.5	-	[235]
<b>Contact angle measurements</b>				
Oven-cast film <sup>b</sup>	68.9	40.9	28.0	[207]
	69.5	42.0	27.5	[233]
Spin-coated film <sup>b</sup>	78.9	45.8	33.1	[233]
CNC pellets <sup>b</sup>	62.1	40.9	21.2	[207]
<b>This work: HSP modeling + CA measurements</b>				
Polar surfaces	53.1 <sup>c</sup>	30.7 <sup>c</sup>	22.4 <sup>c</sup>	
	47.8-55.2 <sup>d</sup>	-	-	-
Non-polar surfaces	31.0 <sup>c</sup>	28.0 <sup>c</sup>	3.0 <sup>c</sup>	
	30.3-32.2 <sup>d</sup>	-	-	-

<sup>a</sup> Measurements performed at 30 °C, the range corresponds to the difference between spray-dried and air-dried samples. <sup>b</sup> Estimated from CA measurements through the Owens-Wendt-Rabel-Kaelble (OWRK) model. <sup>c</sup>  $\gamma = \gamma_D + \gamma_P$ , with  $\gamma_D$  and  $\gamma_P$  calculated from Eqs. 11&12 of the article, respectively. <sup>d</sup> Range calculated from Eqs. 9&10 of the article

Table D.5 ARCA results for spin-coated and oven-cast samples analyzed with EG and DIM (Figs. 7.2.a&c and in Fig. 7.3.a of the main text). Results are reported for each of the films (at least 3 measurements per film) and for the average of the 3 films. Standard deviations,  $\sigma_{\text{SD}}$ , and 95 % confidence intervals,  $\sigma_{95\%}$ , are reported. Uncertainties reported in the main text and error bars plotted on the graphs are standard deviations.

		Spin-coated films				Oven-cast films			
		Film 1	Film 2	Film 3	SC-average	Film 1	Film 2	Film 3	OC-average
EG	$\theta_{\text{a}}$	10.1	10.7	9.7	10.2	35.6	45.7	40.1	41.0
	$\sigma_{\text{SD}}$	0.6	0.4	0.5	0.6	0.9	1.7	2.4	4.3
	$\sigma_{95\%}$	1.5	0.9	1.2	2.8	2.2	4.3	3.7	6.6
	$\theta_{\text{r}}$	0 <sup>a</sup>	0 <sup>a</sup>	0 <sup>a</sup>	0 <sup>a</sup>	- <sup>b</sup>	- <sup>b</sup>	- <sup>b</sup>	19.5 <sup>c</sup>
	$\sigma_{\text{SD}}$	-	-	-	-	-	-	-	0.9 <sup>c</sup>
	$\sigma_{95\%}$	-	-	-	-	-	-	-	1.4 <sup>c</sup>
DIM	$\theta_{\text{a}}$	39.4	32.0	32.9	34.8	46.7	46.1	45.6	46.1
	$\sigma_{\text{SD}}$	0.9	0.9	1.2	3.4	0.8	0.7	1.6	1.2
	$\sigma_{95\%}$	2.2	2.4	3.1	8.7	1.9	1.8	4.1	3.1
	$\theta_{\text{r}}$	13.3	11.0	10.6	11.6	24.8	24.8	24.2	24.6
	$\sigma_{\text{SD}}$	1.7	1.7	0.5	1.8	0.6	0.3	1.1	0.8
	$\sigma_{95\%}$	4.2	4.2	1.3	4.6	1.5	0.6	2.9	2.1

<sup>a</sup> No receding for EG and the spin-coated films. <sup>b</sup> Not enough data for a film by film breakdown. <sup>c</sup> Based on 3 data points only (instead of 9 for the other averages).